1D NANOMATERIALS FOR ENERGY STORAGE APPLICATIONS

A Dissertation
Presented to
The Academic Faculty

by

James M. Benson

In Partial Fulfillment
of the Requirements for the Degree
Doctor of Philosophy in the
School of Materials Science and Engineering

Georgia Institute of Technology
December 2016

1D NANOMATERIALS FOR ENERGY STORAGE APPLICATIONS

Approved by:

Dr. Gleb Yushin, Advisor
School of Materials Science and Engineering
Georgia Institute of Technology

Dr. Thomas Fuller
School of Chemical and Biomolecular Engineering
Georgia Institute of Technology

Dr. Faisal Alamgir
School of Materials Science and Engineering
Georgia Institute of Technology

Dr. Matthew McDowell
School of Materials and Science Engineering
Georgia Institute of Technology

Dr. Alexander Alexeev
School of Mechanical Engineering
Georgia Institute of Technology

Date Approved: October 20th, 2016

ACKNOWLEDGEMENTS

There are several people who I would like to acknowledge for their guidance and support in completing this work. First I'd like to thank my Advisor, Dr. Gleb Yushin. Your willingness to let me explore my passions has been a blessing and has enabled me to grow more fully as a scientist, researcher, and entrepreneur. Thank you for letting me be a part of you group and I feel grateful for the knowledge, experience, and guidance you have provided throughout the years. I'd also like to thank the members of my thesis committee Dr. Alamgir, Dr. Fuller, Dr. Aleexev, and Dr. McDowell for their expertise and time and for their valuable feedback.

Next I'd like to thank our group's post-doctoral research associates, Dr. Igor Kovalenko, Dr. Alexandre Magasinski, Dr. Feixiang Wu, and Dr. Vojtech Svoboda for their assistance in maintaining order during my time with Dr. Yushin. I'd also like to thank the other graduate students current and past who have been there for me when needed. Specifically I'd like to thank Dr. Yair Korenblit and Dr. Ben Hertzberg for teaching me how to build lab equipment, Dr. Kara Evanoff, and Dr. Sofiane Boukhalfa for hours of companionship and for accompanying me to my first conferences, Danni Lei for her hours of discussions and collaborations, Dr. Nox Nitta for providing perspective and friendship while analyzing ToF-SIMS data and life, and Dan Gordon for listening and helping keep the lab stocked with donuts.

To my collaborators from around the world thank you for your time and support. I'd like to thank David Lashmore and Mark Schauer from Nanocomp Technologies Inc. for providing CNT samples for evaluation and discussion thereof. Thanks also go to Dr. Marta Hatzell for her kind donation of her time and equipment for last minute prototype validation. I'd like to thank Dr. John Reynolds as well for his donation of his time and lab space towards the end of my research at GT.

Thanks to the TIGER Fellowship and professors Marie Thursby, Margi Berbari, and Anne Rector for getting me excited about life, and showing me how to connect with people to change the world. Particularly thanks to my PaniPure team Brett Goodman, Divya Vepakomma, Mason Raphaelson, and Vaibhav Sharma for being patient with me as I learned to overcome my fear of phones.

I'd like to send a sincere thanks to the staff at the IEN facility, Eric Woods, Walter Henderson, and David Tavakoli, for their expertise and suggestions for characterization and acquisition of new tools and their constant support of the research at GT.

Finally I'd like to thank my parents, Arthur and Linnett Benson for keeping me going during these last weeks of writing and wedding, my sisters Kayla Carswell and Chelsea Vinings for doing everything first, Aunty M for "helping me to write more smarter," and thanks to Lola for keeping my feet warm while typing away. I'd also like to send my deepest thanks to my new wife Sara who put up with me as I floundered my way through college. I will always love you babe and will try my best to be there when you need me like you have been for me.

TABLE OF CONTENTS

	Page
ACKNOWLEDGEMENTS	iv
LIST OF FIGURES	viii
SUMMARY	xvi
CHAPTER	
1 Introduction	1
1.1 Motivation	1
1.2 Dissertation Format	2
2 Background Matter	4
2.1 Electrochemical Reactions	4
2.2 Electrochemical Storage Devices (ECSDs)	9
2.3 Characterization Methods	44
2.4 1D Nanomaterial Synthesis Techniques	70
2.5 Multifunctional Energy Storage	91
3 AlNW Synthesis for Supercapacitor Substrates	100
3.1 Introduction and Motivation	100
3.2 Results and Discussion	103
3.3 Conclusions	113
3.4 Experimental Details	114
4 Aluminum Oxide Nanowire Separators from Al-Li Alloys	117
4.1 Introduction	117
4.2 Conversion of Aluminum to Alkoxide Nanowires	119
4.3 Alkoxide Nanowire Growth Mechanism	123

4.4 High Performance Battery Separator Synthesis 128
4.5 Conclusions 133
4.6 Experimental Details 134
5 PANI-CNT Composites for Multifunctional Supercapacitor Applications 137
5.1 Introduction and Motivation 137
5.2 Pulsed Electrodeposition of PANI on CNT Fabrics 140
5.3 PANI-CNT Fabrics as Supercapacitor Electrode 143
5.4 PANI-CNT Fabric as Capacitive Desalination Electrode 147
5.5 Static and Dynamic Mechanical Properties 150
5.6 Conclusions 151
5.7 Experimental Details 152
6 CoF_2-CNT Composites as Multifunctional Cathode 156
6.1 Introduction 156
6.2 Synthesis and Characterization 158
6.3 Electrochemical Testing 163
6.4 Post-Mortem Analysis 167
6.5 Conclusion 168
6.4 Experimental Details 169
7 Conclusions 172
7.1 Research Impact 173
7.2 Recommendations 174
REFERENCES 176
VITA 199

LIST OF FIGURES

Page

Figure 1. The proposed model for the electrical double layer showing the distribution of specifically adsorbed anions and cations in relation to the inner and outer Helmholtz planes (IHP and OHP). ψ_o and ψ are the potentials at the electrode surface and throughout the electrode/electrolyte boundary.[14] 8

Figure 2. Schematic comparison of the specific power *vs.* specific energy of different commonly used electrochemical energy storage devices.[17] 10

Figure 3. ECSD form factors used for both battery and supercapacitor devices include a) cylindrical cells, b) coin cells, c) prismatic cells, and d) pouch cells.[2] 13

Figure 4. Schematic showing a) the dimensions of a typical current collector with a tab connection, and b) the configuration of the electrodes and the resulting resistance contributions from the electrochemical reaction, the bulk electron transport, and the constricting resistance at the tab.[23] 15

Figure 5. Electrochemical stability of Al surface in non-aqueous electrolytes used in LIB systems.[27] 17

Figure 6. Lithium location in the graphite crystal structure during intercalation for secondary LIB applications.[2] 21

Figure 7. Potential stability of graphite during constant current lithiation in a non-aqueous LIB; a) charge and discharge curves with intercalation starting at 0.5V *vs.* Li; and b) differential capacity of the multistage Li insertion process during reduction of the graphite and oxidation of the Li-Gr intercalation compound.[38] 21

Figure 8. SEM images of typical tri-layer LIB separator Celgard 2325 a) surface images, and b) shows cross sectional image of the tri-layer structure.[59] 27

Figure 9. Configuration of secondary Li-ion battery (LIB) composed of cathode (+) and anode (-). The electron and Li+ flow directions are indicated during charging and discharging. 31

Figure 10. Comparison of intercalation and conversion materials with typical constant current discharge curves for a variety of a) intercalation cathodes, b) conversion cathodes. c) Typically observed experimental capacities for intercalation and conversion cathode and anodes. d) Intercalation of Li into LCO cathode. e) Conversion of FeF_2 cathode.[7] .. 32

Figure 11. Capacity for commonly used elements in secondary LIBs. Elements which are faded indicate relative abundance in the earth.[7] 33

Figure 12. Possible aging mechanisms at the anode/electrolyte surface.[62] 34

Figure 13. Representative energy diagram for an ideal EDLC showing the applied potential as a function of device charge/discharge in relationship to the stability window.[63] 36

Figure 14. Typical cyclic voltammetry performance of a pseudocapacitive material (MnO_2 in 0.1 M K_2SO_4) showing the continuous potential range of redox reactions. [16] . 38

Figure 15. Chemical structures of selection of most popular conductive polymer species showing the linear and aromatic and S, N and heteroatom free varieties.[86] 42

Figure 16. Different reaction pathways for the redox reactions of polyaniline and polyaniline salts and the corresponding optical colors of the different forms.[88] 44

Figure 17. X-ray emission of a molybdenum target as a function of electron bombardment at a variety of accelerating voltages from 5-25kV.[89] 45

Figure 18. Bragg-Brentano geometry for a typical XRD experiment with the X-ray tube (T), crystal (C) located at the origin (O), diffracting towards the detector (D).[89] 46

Figure 19. Schematic representation of the absorption effect for a thin film or information depth from angle resolved GA-XRD. This simplifies to the traditional θ-2θ geometry when α=θ.[92] 48

Figure 20. Comparison of the SEM and the TEM.[95] 49

Figure 21. Typical 1st cycle of a constant current charge-discharge experiment performed on a LFP-graphite based lithium ion battery, a) the current and voltage profile *vs.* time, b) the same cycle presented as voltage *vs.* specific capacity, c) the same battery material tested for multiple cycles and at different constant current values denoted by the C-rates 0.1-5C..... 52

Figure 22. Examples of typical cyclic voltametry experiments demonstrating a) the voltage *vs.* time profile of an experiment using a scan rate of 10mV/s and a voltage window of ±0.75V. The resulting current *vs.* voltage profile of a symetric cell showing, b) reversible faradaic reaction, and c) the electrostatic energy storage commonly observed in capacitor materials. 54

Figure 23. The current response to an applied AC voltage signal of frequency *f* and the resulting phase shift referenced to the voltage signal used in EIS experiments a) with respect to time, and b) with respect to applied voltage.[87] 57

Figure 24. Equivalent electrical circuits commonly used to model a) basic supercapacitor behavior, and b) complex faradaic reactions including battery and pseudocapacitor behavior.[99,100] 59

Figure 25. The idealized response of a Randle equivalent circuit commonly used to evaluate electrochemical impedance response of ECSDs.[100] 60

Figure 26. Four point probe details with a) showing a commercially available four point probe station. Schematics of b) a two point probe measurement and c) a linear four point probe array with equal tip spacing.[106] 63

Figure 27. Tensile test geometry for non-woven fabrics using a) cut strip sample and b) grab test showing the beginning of out of plane buckling at high elongation.[111] c) Schematic tensile tests of polymer samples showing different failure modes with respect to temperature.[109] 65

Figure 28. Skematic of a PerkinElmber DMA8000 dynamic mechanical analyzer (DMA) with a) showing the sample geometry and fixture in bending mode with the resulting oscillation indicated by arrows and b) showing the applied force and resulting displacement and phase lag.[114] 67

Figure 29. DMA results of a constant stress amplitude test of NMP-free 30um thick polyaniline film from 25-400 ºC with a heating rate of 5 ºC min^{-1}.[115] 69

Figure 30. Comparison of the typical pressure and temperature required for different processing methods.[117] 71

Figure 31. PVD system for production of 1D nanomaterials. The schematic on the left shows AlNW grown at θ=85º with no substrate rotation on the top right and slow substrate rotation on the bottom right.[120] 73

Figure 32. Schematic of the mechanisms involved in CVD reactions.[123] 74

Figure 33. Reaction mechanism for a) chemical vapor deposited films, and b) surface limited atomic layer deposited films.[126] 75

Figure 34. Schematic diagram illustrating the different control regimes and deposition rate as a function of temperature, pressure, and kinetics.[123] 76

Figure 35. Nanowire growth mechanisms commonly described as VLS growth with a) showing tip, root, and catalyst-free CVD growth mechanisms, b) three methods of tip growth including the location of the liquid (L), and solid (S) phases and the diffusion paths of the source atoms, c) root growth VLS mechanism with the diffusion path of source gasses shown, d) geometry relationship between the contact angle of the liquid solid interface and the radius of the resulting nanowire.[126] 78

Figure 36. Commonly used water properties to predict conditions during hydrothermal synthesis. a) Iso-dielectric constant lines for water as a function of temperature and pressure. b) P-T curves for different autoclave fill fractions.[138] 83

Figure 37. Example waveform for a reverse pulse deposition method for deposition of Cu in a through hole on a printed circuit board.[145] 87

Figure 38. Typical conductive polymer electrochemical reaction path including radicle formation, coupling, and propagation.[88] 89

Figure 39. Room temperature ionic conductivity for a variety of potential electrolyte polymers *vs.* their compressive modulus.[158] 94

Figure 40. AlNWs grown on a rough Cu foil at 125 °C: a) optical micrograph showing uniform large-area deposition of AlNWs, b) SEM micrograph showing a high resolution image of curved AlNWs produced, and c) a typical EDS spectrum taken at a region containing AlNWs.[32] 103

Figure 41. SEM micrographs of CVD deposition of AlNWs onto rough Cu foils at different temperatures: a) 100 °C, b) 125 °C, c) 150 °C, d) 200 °C, e) 300 °C, and f) 400 °C.[32] 104

Figure 42. Diameter and deposition rate of Al nanowires on metal foil substrates: a) mass of Al nanowires deposited on metal foil substrates at different temperatures for 1h, b) average diameter of Al nanowires grown on several metal substrates as a function of deposition temperature; c) diameter distribution of Al nanowires deposited on Cu foil at 125 °C.[32] 105

Figure 43. a) Low and b) high resolution TEM micrographs showing a twin boundary within an AlNW grown on the Cu surface at 125 °C; c) EDS spectra taken from a single AlNW.[32] 107

Figure 44. Patterned Al nanowire growth: a) schematic of the process, b) SEM micrograph of a patterned Al nanowire growth on a rough Cu foil at 125 °C. In this case the growth on a portion of the Cu foil was prevented by the deposition of a thin layer of a methylmethacrylate-based polymer.[32] 109

Figure 45. XRD pattern of Al nanowires grown on a rough Cu foil at 125 °C.[32] 110

Figure 46. Electrochemical activity of Al nanowires in Li half cells: cyclic voltammetry recorded at 1 mV/s showing reversible electrochemical interaction of Li^+ ions with Al nanowire electrodes and flat Al sheets.[32] 111

Figure 47. Al nanowire - based supercapacitor: a) simplified schematic of the electrode; b) SEM and c) TEM micrographs of VO_x-coated Al nanowires; d) EDS spectrum of VO_x-coated Al nanowires; e) cyclic voltammetry recorded at 0.1 mV/s for VO_x-coated Al nanowire electrode in comparison to that of porous carbon (capacitance is normalized by the active mass); f) average capacitance as a function of a slew rate for 50 nm VO_x coatings in comparison to that of activated carbon.[32] 112

Figure 48. Qualitative summary of the experimental results: a) formation products upon exposure or β-AlLi alloys to water and selected alcohols, NW stands for nanowire morphology of the samples; b) selected XRD spectra of the produced samples, showing formation of Al and remaining AlLi alloy for H_2O, MeOH, *i*-PrOH, t-BuOH, and PhOH solvents. *Phenol is solid at RT thus delithiation was only performed at 60 °C. 120

Figure 49. Formation of Al ethoxide nanowires: SEM micrographs showing a) the initial grain structure of the as produced β-AlLi alloy, b-d) low and high resolution SEM

micrographs showing formation of the aligned $Al(EtO)_3$ nanowire forest on the surface of the β-AlLi particles after exposure to dry ethanol at room temperature for 30 sec; f) misaligned re-dispersed $Al(EtO)_3$ nanowires produced after completion of the conversion reaction; g) schematic representation of the nanowire formation. 121

Figure 50. Characterization of Al ethoxide nanowires produced at room temperature: a) HR-TEM micrograph and SAED pattern showing their amorphous structure, b) EDS spectrum, showing its elemental composition, c) XRD spectrum of the nanowires suspended in EtOH (with the background subtracted), d) FTIR spectra of as-produced nanowires (blue) and commercial $Al(EtO)_3$ powder (black), showing identical vibrational modes. 122

Figure 51. Schematic of the proposed $Al(EtO)_3$ nanowire formation mechanism: a) major process steps, such as (a.1) selective oxidation of Li from the β-AlLi alloy and its dissolution in ethanol resulting in the formation of strained delithiated Al surface layer, the stresses in which induce formation of nano-islands of amorphous Al, separated by surface cracks; (a.2) chemical transformation of the Al nano-islands into $Al(EtO)_3$ inducing formation of nucleation cites for (a.3) further growth of $Al(EtO)_3$ nanowires upon continuous dissolution of Li from β-AlLi alloy until (a.4) all β-AlLi is consumed and transformed into suspended $Al(EtO)_3$ nanowires; b) detailed initial steps of the $Al(EtO)_3$ nanowire formation, such as (b.1) shape change in Al upon formation of the initial $Al(EtO)_3$ nuclei and (b.2-b.4) $Al(EtO)_3$ nanowire growth caused by minimization of the strain energy at the $Al(EtO)_3$/Al (and possibly Al/AlLi) boundaries, which aligns the transformation-induced expansion with the direction normal to these boundaries. 125

Figure 52. Selected characterization of the $Al(MeO)_3$ powder produced upon exposure of β-AlLi alloy to MeOH at 60 °C: a) FTIR, b) XRD (with the background subtracted), c) SEM micrographs recorded at low and high magnifications. 126

Figure 53. Selected characterization of the Al(*i*-PrO)$_3$ nanowires produced upon exposure of β-AlLi alloy to *i*-PrOH at 60 °C: a) FTIR in comparison with that of the commercial Al(*i*-PrO)$_3$ powder, b) XRD (with the background subtracted), c) SEM micrograph. ... 127

Figure 54. Diameter of nanowires tunable by synthesis temperature and alcohol used: a,b,c,d) image analysis of nanowire diameter distribution, e) average nanowire diameter for four synthesis conditions. 128

Figure 55. Transformation of $Al(EtO)_3$ nanowires into AONWs: a) *in-situ* HT-GIXRD study of $Al(EtO)_3$ nanowires upon heating in air at the heating rate of 4 ^oC/min; b) SEM micrograph of free-standing nonwoven Al_2O_3 fabric produced upon annealing of $Al(EtO)_3$ nanowires at 800 °C for 2 h and c) its optical images. Diffraction spectrum from the amorphous $Al(EtO)_3$ nanowires is weak and thus is almost not visible. 129

Figure 56. Selected tests conducted on AONW separator in comparison to that of commercial polypropylene and cellulose separators: a) wettability test showing time-resolved optical images of a 5 µl drop of 1M $LiPF_6$ in EC:DEC:DMC (1:1:1) on the separator surface and revealing faster and more uniform electrolyte wetting on AONW

separator; b) thermal stability test showing optical images of the separators after 2 min exposure to selected temperatures in the range from 25 to 800 °C and demonstrating dramatically higher thermal stability of the of AONW separator..... 131

Figure 57. Electrolyte wetted area in AONW separator as a function of time in comparison with that of commercial cellulose fiber and polypropylene separator (as shown in Figure 56). 132

Figure 58. Selected electrochemical characterization of the AONW separator in comparison with that of commercial propylene and cellulose fiber separators: a) rate performance and b, d) typical charge-discharge profile of a full cell comprised of identical graphite anode and $LiFePO_4$ (LFP) cathode in 1M $LiPF_6$ / EC:DEC:DMC electrolyte at 0.5C and 2C rates; c) ionic conductivity of the separators filled with 1M $LiPF_6$ / EC:DEC:DMC electrolyte, as measured in symmetric stainless steel-stainless steel cells using an electrochemical impedance spectroscopy technique. 133

Figure 59. Photographic and SEM images of CNT fabric before (a,c) and after (b, d-f) coating with PANI electro-deposited at different current densities.[280]..... 141

Figure 60. Chemical characterization of the deposited PANI: a) energy dispersive spectroscopy of a PANI-coated CNT and b) typical Raman spectra of CNT and PANI-coated CNT fabrics.[280] 142

Figure 61. Electrochemical characterization of PANI-coated CNT fabrics in 1M H2SO4 electrolyte in symmetric two-electrode cells: a) cyclic voltammetry of the CNT fabric samples with PANI deposited at different current densities, b) effect of sweep rate on the capacitance retention for the sample produced at 2 mA cm-2 current density, c) effect of the sweep rate on the capacitance retention of PANI-CNT samples in comparison with a commercial activated carbon YP17-D and as-produced CNT fabric, d) effect of the current density in charge-discharge tests on the specific capacitance of PANI-CNT samples in comparison with as-produced CNT fabric, e-f) specific capacitance of the PANI component of the composite as a function of sweep rate and current density.[280] 144

Figure 62. Electrochemical characterization of PANI-coated CNT fabrics in comparison with other materials in 1M H_2SO_4 electrolyte in symmetric two-electrode cells: a) frequency response of the PANI-CNT electrodes in comparison with a commercial activated carbon YP17-D and as-produced CNT fabric, b) cycle stability of a PANI-CNT electrode produced at 2 $mA \cdot cm^{-2}$ current density in comparison with that of pure PANI (chemically synthesized) electrode in charge-discharge testes performed in the voltage range from -0.6 to +0.6V, c) energy and power density of PANI-CNT electrodes discharged from different maximum voltages.[280] 146

Figure 63. Electrochemical characterization of PANI-coated CNT fabrics in 1M NaCl electrolyte in symmetric two-electrode cells: a) effect of sweep rate on the capacitance retention for the sample produced at 2 mA cm^{-2} current density, b) typical shape of the charge-discharge profiles, c, e) effect of the current density in charge-discharge tests on the specific capacitance of PANI-CNT samples and the PANI component of these

samples in comparison with as-produced CNT fabric, d, f) cycle stability of a PANI-CNT electrode and the PANI component of this sample produced at 2 $mA \cdot cm^{-2}$ current density.[280] 149

Figure 64. Mechanical characterization of PANI-coated CNT fabrics: a) tensile tests, b) specific ultimate strength, c) storage modulus and d) modulus of toughness of PANI-CNT in comparison with other materials.[280] 151

Figure 65. Schematics of CoF_2/CNTs composite fabrication.[350] 158

Figure 66. The morphology and structural characteristics of the CoF_2/CNTs composite fabric: a) SEM micrograph of the composite surface (inset-photograph of the composite, scale bar of 5 cm); b) high resolution SEM micrograph of the interface of CoF_2-decorated CNTs with a close-up of a single CoF_2 nanoparticle on a CNT (inset, scale bar of 50 nm); c) TEM micrograph of the CoF_2-decorated CNTs; d) XRD spectrum of the composite.[350] 160

Figure 67 Cross-section images of prepared CoF_2-CNTs nanocomposite: a) SEM image of layer-by-layer structure of the composite and b) SEM image of CoF_2 large aggregation between layers.[350] 161

Figure 68 Component analysis of CoF_2/CNTs nanofibrous composite: a) EDS analysis and b) XPS survey, showing the presence of cobalt, fluoride and slight impurity of silicon from absorbed silicon fluoride gas.[350] 161

Figure 69. Selected mechanical characteristics of the CoF_2/CNTs composite fabric: a) tensile test results and a comparison of the produced material with selected materials for b) the specific ultimate tensile strength, and c) the modulus of toughness.[350] 162

Figure 70. TGA analysis of prepared CoF_2-CNTs nanocomposite in air from room temperature to 700 ^oC, indicating the content of CoF_2 to be 40 wt. %. The heating rate is 2 $^oC\ min^{-1}$.[350] 163

Figure 71. Rate performance and cycle stability of CoF_2/CNT composites in 1M $LiPF_6$, FEC/EMC (3:7) electrolyte. a) charge discharge performance and complete capacity recovery, b) the charge/discharge profiles at different current densities, c) capacity retention and columbic efficiency at current density of 100 and 500 mA g^{-1}, d) Capacity contribution from CNT fabric at different current densities.[350] 165

Figure 72. Impact of electrode morphology for the stability, capacity, and impedance of the CoF_2-based composite cathodes: a) comparison of cycling stability of CoF_2/CNT composite *vs.* CoF_2/CNT mixture with a current density of 100 mA g^{-1}, b) EIS spectrum (0.01Hz to 100kHz) comparing half cells of CoF_2-CNT fabric with CoF_2-CNT mixture. 166

Figure 73. Morphology and composition of the cycled Li anodes: a) SEM micrograph and b) EDS spectrum of the anode foil in 1M $LiPF_6$, FEC/EMC (3:7) electrolyte, showing smooth morphology as well as a lack of Co precipitates.[350] 168

SUMMARY

Electric propulsion technology has been advancing rapidly, primarily driven by electric vehicles and unmanned aerial vehicles (UAVs). In both cases, the energy storage technologies available are limited in capacity, power capability, and cost. A great amount of work has been done in developing nanomaterials (NM) to improve the energy density of anode and cathode active materials; however, growth in this field has kept a steady pace with battery energy density increasing only 3% per year over the last 60 years.

Although extensive research has been done on utilizing one dimensional (1D) NM as the energy storage device's active material, current collector and separators have received little attention. This dissertation focuses on improving energy storage devices by using 1D NM, including Al nanowires, Al_2O_3 nanowires, and carbon nanotubes, for collectors and separators instead of main electrical storage material. Much work has been done studying nanoparticles and nanoporous materials; however, 1D structures have faced less utilization due to the difficult and limited synthesis routes currently available. Thus this dissertation also focuses on developing and characterizing new synthesis methods for the production of such 1D NM and the resulting performance of composites produced using them.

Materials that can simultaneously serve as energy storage and structural applications would be valuable in applications where minimizing system mass and volume are needed. Today's electrode materials are particle based and have inherently low strength and conductivities compared to 1D materials that can transfer loads. This feature allows the creation of porous, mechanically strong current collectors needed for structural batteries. By substituting a purely structural component of a UAV with a dual-purpose structural battery, the flight time could increase by as much as 26%.

One dimensional nanomaterials (1D-NM), such as nanowires and nanotubes, may offer significant performance benefits for a broad range of energy storage technologies due to their high surface area, high aspect ratio and high structural flexibility. Conductive 1D-NM such as aluminum nanowires (AlNW) and carbon nanotubes (CNTs) offer high strength and high electrical conductivity, which make them attractive as high-performance current collectors. Non-conductive 1D-NM, such as aluminum oxide (Al_2O_3) nanowires (AONW), offer high strength, excellent wettability by a broad range of organic and aqueous electrolytes and remarkable thermal stability, which make them ideal for use in high performance separators. The high costs of the currently employed synthesis methods for these (nano)materials limit the progress in their applications and studies. This dissertation details two new lower-cost 1D-NM synthesis methods suitable for large scale mass production of AlNW and AONW based on chemical vapor deposition (CVD) and novel solution-based processing, respectively. These studies reveal the impact of processing / synthesis parameters on the properties of such nanomaterials as well as the impact of material properties on their performance in energy storage applications, such as batteries and supercapacitors. The growth mechanisms for AlNW and AONW are discussed. Finally, the promising applications of CNT current collectors are demonstrated in multi-functional Li-ion battery anodes and cathodes as well as in supercapacitor electrodes.

CHAPTER 1

INTRODUCTION

1.1 Motivation

Energy storage is an increasingly important field today. In addition to enabling higher performance consumer electronics it also facilitates reduction in fossil fuel usage through usage in renewable resources, grid storage, and electric vehicles. One of the benefits of incorporating energy storage devices into the energy mix is that they can help to support intermittent renewable energy sources, such as solar and wind. The Li-ion battery market alone is expected to reach $46 billion worldwide, by 2022 driven primarily by sharp growth in electric vehicle demand and tightened environmental emissions standards.[1] Energy Storage Association's U.S. Energy Storage Monitor 2015 Year in Review suggests that energy storage will be a $2.5 billion market in the US by 2020. Much of the growth in these fields recently have been driven by advancements in material research and more specifically the development of nanomaterial synthesis. Nanomaterials have been researched extensively for use in battery active materials to increase the rate capability, energy density, and cycle stability while also enabling the use of materials with otherwise unsuitable electrical resistance.[2-7]

Much work has been placed into increasing the energy storage capability through careful design of the active materials, however this work has been slow with an increase in capacity on the order of 5-8% per year over the last 20 years.[8] While these active materials are important, the research into other cell components including current collectors and separator materials could lead to advances separate from the active material development efforts. Work on nanostructured Cu current collectors has shown a six fold improvement in the energy density compared to a planar electrode in a lithium

ion battery (LIB).[9] Additionally a doubling of the area-normalized capacitance (1.5 F cm^{-2}) was observed for a MnO_2 based pseudocapacitors using a modified current collector.[10] Further, by increasing the performance of the current collectors while maintaining the same mechanical properties, multifunctional energy storage devices can be developed which have been shown by DARPA to increase flight time in unmanned aerial vehicles by 26%.[11]

Battery separators are an important though often neglected part of battery design, as demonstrated recently with the Samsung Galaxy Note 7 recall which decreased their stock price by $25 Billion in two weeks.[12] High-performance separator materials are important for achieving high rate capability in cells and for preventing the unplanned rapid discharge and resulting fires which may occur. Recent efforts to utilize ceramic nanomaterial coatings to prevent device shorting under elevated temperatures have shown promise. Unfortunately, though, solid ceramic separators with suitable flexibility, weight, electrochemical performance, and cost have not been demonstrated so far.

Using nanomaterials for novel applications has been investigated in the recent decades despite the challenge of scaling up production. Investigation of nanomaterial performance and inclusion into mass market products has been hindered by the limited scalability of many synthesis methods. This requires that the development of any high performance material also be coupled with scalable synthesis methods. This dissertation documents several new nanomaterial synthesis methods and their application in a large array of energy storage devices, such as separator and current collector materials for both batteries and supercapacitors.

1.2 Dissertation Format

This dissertation has been structured to provide both an introduction to the topics discussed, as well as to evaluate the work in detail. This dissertation details two new lower-cost 1D nanomaterial synthesis methods suitable for large scale mass production of

aluminum nanowires, AlNWs (Chapter 3) and aluminum oxide nanowires, AONWs (Chapter 4) based on chemical vapor deposition (CVD) and novel solution-based processing, respectively. This study reveals the impact of processing / synthesis parameters on the properties of such nanomaterials as well as the impact of material properties on their performance in energy storage applications, such as batteries and supercapacitors. The growth mechanisms for AlNW and AONW are discussed. The promising applications of CNT current collectors are demonstrated in multi-functional supercapacitor electrodes (Chapter 5) and Li-ion battery cathodes (Chapter 6) with a focus on electrical and mechanical multifunctionalities. Finally, a summary of the work and recommendations for future research is included in Chapter 7.

CHAPTER 2

BACKGROUND MATTER

2.1 Electrochemical Reactions

Faradaic Reactions

Faradaic reactions, also known as electrochemical reactions, are a subset of chemical reactions relying on the transfer of electrons for completion. This electron transfer process harnesses the electrical work from the chemical reaction and, thus, forms the fundamentals of many energy storage systems. These reactions are generally split into half reactions based on whether the oxidation state of the species involved is being increased (oxidation) or reduced (reduction). The labeling convention specifies that electrodes upon which reduction reactions occur be labeled the cathode and that electrodes upon which oxidation reactions occur be labeled the anode. Examples are shown in (1) and (2), with v_i being the stoichiometric coefficient for species *i* and *n* being the electron mole equivalent for the half reaction. When Faradaic reactions are paired, the electron transfer step is often omitted, as shown in (3), and called redox reactions.

$$Reduction: v_a A + ne^- \rightarrow v_b B \tag{1}$$

$$Oxidation: v_c C \rightarrow v_d D + ne^- \tag{2}$$

$$Full\ Cell\ Reaction: v_a A + v_c C \rightarrow v_b B + v_d D \tag{3}$$

Since redox reactions are a subset of chemical reactions, they can be described by thermodynamic analysis involving the free energy of reaction. This is shown in (4) for the full cell reaction described in (3). The Gibbs free energy, ΔG_{rxn}, of reaction is the maximum energy that is generated at equilibrium. The sign of ΔG_{rxn} determines the spontaneity of reaction: negative values of ΔG_{rxn} for spontaneous reactions and positive values showing an input of external energy for the reaction to occur.

$$\Delta G_{rxn} = \Delta G^o + RT \ln \frac{a_B^{v_b} a_D^{v_d}}{a_A^{v_a} a_C^{v_c}} \quad (4)$$

Where ΔG^o is the standard state Gibbs free energy, R is the universal gas constant, T is temperature, and a_i is the chemical activity of species *i*. The term $\frac{a_B^{v_b} a_D^{v_d}}{a_A^{v_a} a_C^{v_c}}$ is described as the reaction constant in non-standard states or the equilibrium constant in the standard state.

For a battery system in equilibrium, the electrical work (W_{elec}) which is available is equal to the chemical energy available (ΔG_{rxn}). Electrical work is defined as the amount of charge (nF) moved through a potential field (E).

$$W_{elec} = -\Delta G_{rxn} = nFE \quad (5)$$

where F is Faraday's constant, or 96,485 coulombs per mole of electrons. Thus positive cell potentials correspond with negative ΔG_{rxn} and suggest spontaneous redox reactions. This equation holds for reactions under equilibrium and when standard state is used and can be represented as in (6).

$$\Delta G_{rxn} = -nFE_{rxn}; \text{ and } \Delta G^o_{rxn} = -nFE^o_{rxn} \quad (6)$$

Dividing equation (4) by nF and incorporating equation (6) yields the Nernst equation. The Nernst equation describes the relationship between electrochemical potential, species activity, and temperature of a redox reaction.

$$E_{rxn} = E^o_{rxn} - \frac{RT}{nF} \ln \frac{a_B^{v_b} a_D^{v_d}}{a_A^{v_a} a_C^{v_c}} \quad (7)$$

Most faradaic reactions for energy storage applications do not occur at thermodynamic equilibrium. These reactions are controlled by electron transfer from the anode and cathode to the solution species. The electrical current (I, in A) is used to estimate the rate of the electrochemical reaction (dN/dt, in mol s^{-1}) with the following:

$$\frac{dN}{dt} = \frac{I}{nF} \tag{8}$$

As current is applied to the system, the operating voltage deviates from equilibrium because of irreversible occurrences caused by charge transfer, mass transfer, and joule heating.

In the case of charge transfer, controlled half-cell reactions such as (1), the current is a function of the applied voltage. The Butler-Volmer equation relates the applied potential of a system with the resulting current response. This equation includes both the thermodynamic properties and the kinetic reaction rates.[13]

$$I = I_o \left[\frac{C_A}{C_A^*} \exp\left(\frac{\alpha_1 F \eta}{RT}\right) - \frac{C_B}{C_B^*} \exp\left(\frac{\alpha_2 F \eta}{RT}\right) \right] \tag{9}$$

where I_o is the equilibrium exchange current, C_A and C_B are the concentrations at the electrode surface of species A and B, C_A^* and C_B^* are the concentrations in the bulk of the electrolyte of species A and B , and α_1 and α_2 are the reduction and oxidation charge transfer coefficients with $\alpha_a + \alpha_c = 1$. This relationship assumes an Arrhenius type relation between the electrochemical reaction and the activation energy being described by the difference between the equilibrium voltage $\left(E_{eq}\right)$ and the measured voltage (E) and is called the over potential (η).

$$\eta = E - E_{eq} \tag{10}$$

Electrostatics/Double Layer Theory

An alternative energy storage mechanism can be based on the electrostatic forces generated by bringing charged objects in close proximity. This is demonstrated simply in the case of a dielectric capacitor which is formed by two conductors separated by an insulator. When a potential is applied across the conductors the charge inside must balance this electrical field to achieve charge neutrality as governed by Gauss's law

($\oiint E \cdot dA = Q/\varepsilon_o$). This provides a relationship between the applied potential (V) and charge (Q in coulombs) inside the capacitor as shown in (11).

$$V = \frac{Qd}{\varepsilon A} \tag{11}$$

Where ε is the permittivity constant of the electrolyte in F/m, A is the specific surface area in m^2/g, and d is the thickness of the dielectric material in m. The capacitance (C in farads) is defined as shown below in (12) and is the primary indicator of energy storage capabilities for capacitors with both volumetric and specific capacitance also commonly compared.

$$C = \frac{Q}{V} \tag{12}$$

If (12) is substituted into (11) the general capacitance equation for a dielectric capacitor is obtained as shown in (13).

$$C = \frac{\varepsilon A}{d} \tag{13}$$

The total energy stored (U in Joules) in the capacitor can be obtained by integrating the charge as it moves across the applied potential of the capacitor and can be described by (14) which uses (12) to show common equivalent forms.

$$U = \int_0^Q V dQ = \int_0^Q \frac{Q}{C} dQ = \frac{1}{2}\frac{Q^2}{C} = \frac{1}{2} C V^2 \tag{14}$$

This result suggests two mechanisms for increasing the capacitance (increase the available surface area, decrease the charge separation distance) and an additional mechanism for increasing the energy density of these dielectric based capacitors (increase the applied voltage across the capacitor). For dielectric capacitors where the surface area is primarily controlled by the device geometry, the energy density is controlled primarily by the breakdown voltage of the dielectric.

If instead of using a solid dielectric material a liquid electrolyte is used, the available surface area and charge separation distance can be drastically improved. This improvement occurs due to the formation of a layer of electro-adsorbed ions at the

solution-electrode interface and creates small charge separation distances on the order of atomic radii. When two conductive electrodes are placed in an electrolyte solution and a voltage is applied, the ions of the opposite charge migrate to the electrodes and accumulate without electron transfer to the species in solution. This accumulated region is called the electrical double layer, and it was first described by Helmholtz and later modified by Gouy-Chapman and Stern with the Stern model being commonly used today.13 This double layer is depicted in Figure 1 and the contributions can be broken down into the Stern layer which is composed of specifically adsorbed ions and the diffuse layer which is composed of non-specifically adsorbed ions. To help define these layers the location of the specifically adsorbed charge centers is called the inner Helmholtz plane (IHP) and the charge center of the closest solvated ion is called the outer Helmholtz plane (OHP).

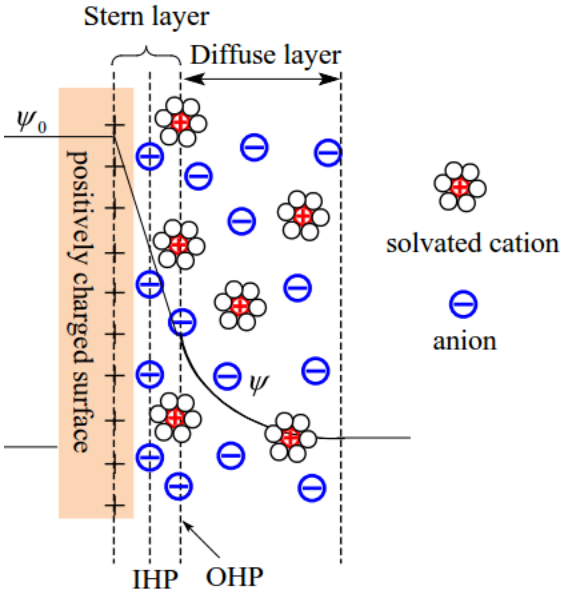

Figure 1. The proposed model for the electrical double layer showing the distribution of specifically adsorbed anions and cations in relation to the inner and outer Helmholtz planes (IHP and OHP). ψ_o and ψ are the potentials at the electrode surface and throughout the electrode/electrolyte boundary.[14]

Although no electron transfer occurs across the double layer, these interfaces store charge through electrostatic adsorption of charged ions on their surfaces which can allow

for utilization of non-planar, highly porous surfaces for charge storage. In dielectric capacitors the separation distance is on the order of 1 μm, however for electrical double layer capacitors the charge separation distance for the double layer depends on the ionic concentration of the solution and is typically 2-8 Å. This reduced separation coupled with the non-geometric electrode area provided by a porous electrode accounts for much of the increased capacitance.[15]

Because the capacitance of double layer capacitors can make use of porous surfaces, much work has been performed on optimization of these surfaces. Because ions in solution are accompanied by a layer of electrostatically attracted solvent molecules called the solvation shell, the effect size of the ion is much larger than suggested by the ion alone. This size was thought to limit the size of the pore which was able to be utilized for the double layer effect. However, further research showed it was possible for this solvated shell to be partially stripped to allow access to pores which possessed sizes the same size or smaller than one ion with a single attached solvent molecule.[16] This shedding of part of the solvation shell was thought to increase the confinement of the ions in the pore and thus lead to increased capacitance.

2.2 Electrochemical Storage Devices (ECSDs)

The production and storage of renewable energy sources has become one of the largest hurdles in aggressively reducing environmental degradation. Energy storage devices includes a broad category of devices including pumped hydro compressed air, fly wheel, with electrochemical storage being a smaller but more common subset. Electrochemical storage devices (ECSDs) operate by converting chemical energy into electrical energy through faradaic or electrostatic methods as previously described. This energy is available as a function of electrical current at a certain voltage and time. ECSDs show advantages compared with other energy storage systems as they require only one

step (chemical to electrical) whereas chemical or thermal energy storage require multiple steps (steam generation followed by kinetic energy conversion to electrical).

Even within this subset, however, there are many different devices commonly used with the two most popular being batteries and supercapacitors. ECSDs are used to provide electrical power in situations where moderate energy requirements occur and large power is needed with charge and discharge times on the order of milliseconds to hours. Due to their ability to operate at low temperatures and their closed system nature, ECSDs offer large benefits for portable power applications such as mobile electronics, electric vehicles, and even grid storage. Selection of a specific device can be done by many parameters including cost, operating temperature, energy storage, operating lifetime, etc. The most common of these parameters are the maximum amount of energy which can be stored (proportional to capacity/capacitance) or the maximum rate of charge/discharge (power). These device selections and comparisons are shown in the form of a Ragone Plot as shown in Figure 2.

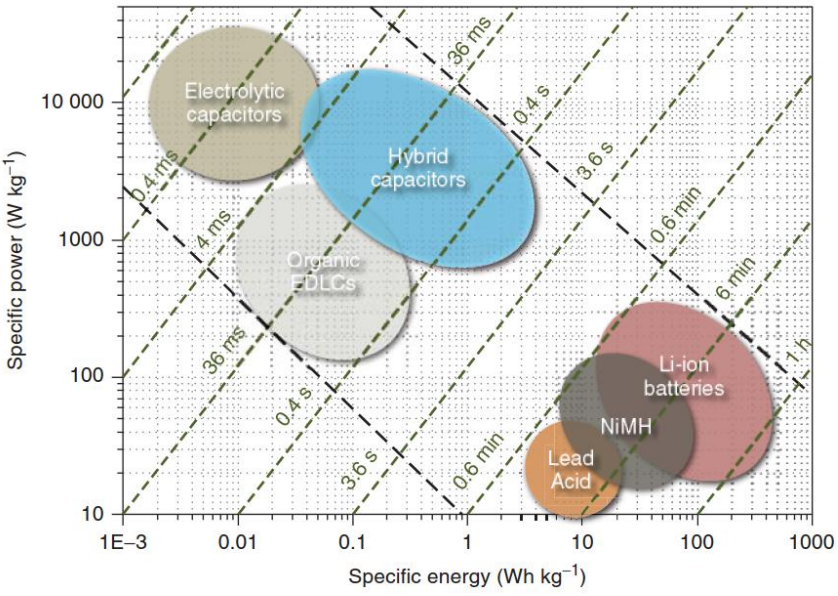

Figure 2. Schematic comparison of the specific power *vs.* specific energy of different commonly used electrochemical energy storage devices.[17]

Common Cell Components

Though the charge storage mechanisms of capacitors and batteries are different, their constructions are somewhat similar. This similarity stems both from the physical requirements of applying a voltage to a large volume of electroactive materials and to the processing and manufacturing requirements of these systems. This similarity means that there are many shared cell components between the different types of ECSDs. The electrodes for these different devices are in practice complex composites composed of active materials, polymeric binders to hold the particulate structure together, and conductive additives such as carbon black to provide electronic conductivity.[18] Additionally these components must be combined to leave sufficient porosity for the liquid electrolyte to penetrate the composite and allow the ions to reach the reaction sites. While the electrodes of these ECSDs are different, all cells share the need for a current collector, electrolytes, separators, and cell casings and their distribution throughout a typical cell can be seen in Figure 3. 1D nanomaterials show potential benefits in current collector and separator applications and will be detailed later in this section after a brief summary of the other common cell components.

The first concern of any ECSD is the electrode which is typically composed of the active material casted or deposited on a current collector. The role of the current collector is to transport electrons to the active material for energy storage. The active materials are typically attached to the current collector (e.g., metal foils) using an adhesive polymeric binder, which is uniformly mixed with the active materials and conductive additives before being cast onto the current collector. Because the electrical conductivity of many active materials is low, most battery electrodes include conductive additives to help increase the electron transport throughout the electrode. Usually carbon black is chosen as the additive however other conductive particles can also be used such as carbon nanotubes, graphene, or conductive polymers. These alternative conductive additives provide increased performance by providing a continuous path for electron transport

instead of the particle to particle transport that is required in the case of carbon black.[5] Because a conductive path is needed from the current collector to the active material the connectivity of this network of conductive additives is important. Deterioration of this conductive pathway can occur due to mechanical separation of particles or resistive film formation which leads to capacity fading, increased electrode polarization, and reduced cycling rates.

An electrically insulative material called a separator is inserted between the electrodes and an ionically conductive electrolyte (liquid, solid, or gel) is infiltrated into the electrodes and separator. Electrodes can be coated with active material either on a single or double side depending on if the electrodes are assembled in a single pair or if they are rolled or layered together to achieve higher energy density. Finally everything is enclosed in a cell container to avoid evaporation of the electrolyte and prevent unwanted side reactions or contaminants from entering during use or storage. Many different form factors for the cell casing and electrode geometry can be seen in Figure 3. Different form factors are used for different capacity and device volumetric requirements.

While operating under different physical energy storage mechanisms and thereby having large variation in performance, there are many common components required for both secondary batteries, EDLC's, and pseudocapacitors other than the active material. Due to the common requirement for ionic and electronic conductivity and the requirement for charge separation between an anode and cathode many of these components can be shared to some degree with special considerations being taken care for chemical compatibility and manufacturing requirements. As these components are non-active materials, the performance of the entire device efficiency can be greatly reduced on a per-cost and per-specific energy density basis by poor selection.

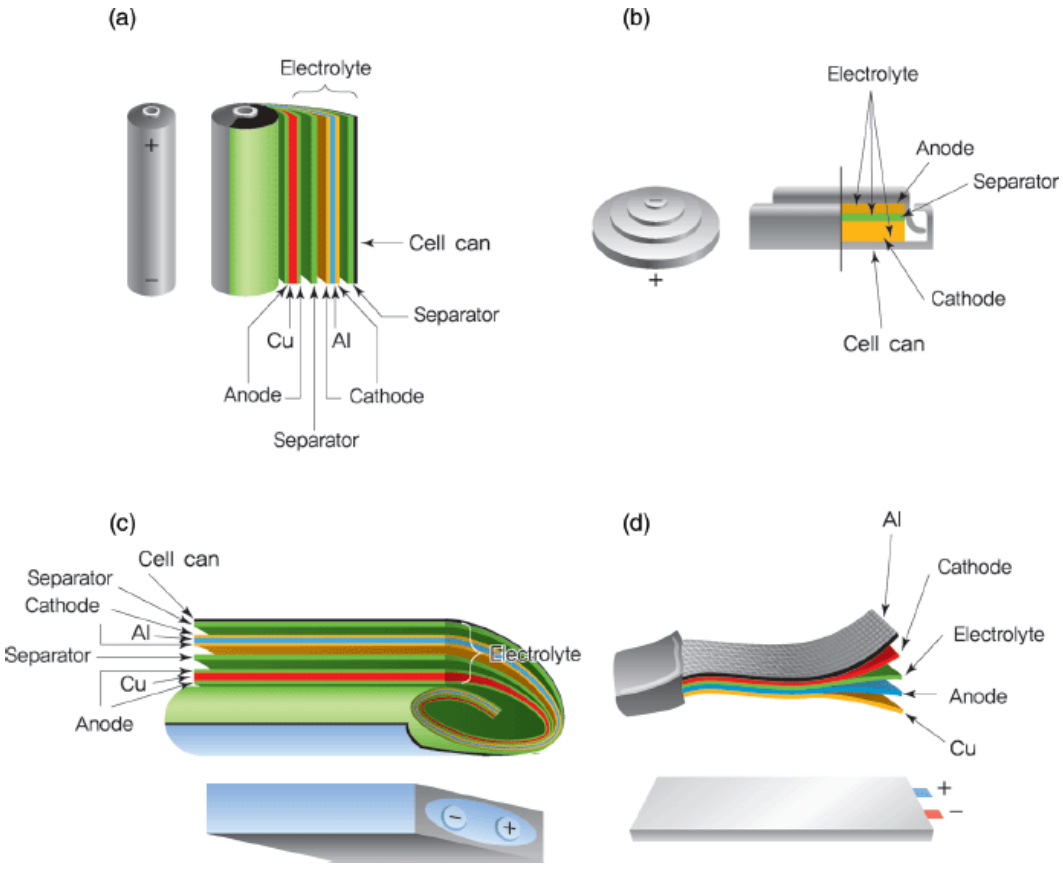

Figure 3. ECSD form factors used for both battery and supercapacitor devices include a) cylindrical cells, b) coin cells, c) prismatic cells, and d) pouch cells.[2]

Current Collectors

Current collectors need to be sufficiently conductive to allow efficient electron transport to the active materials without inducing significant voltage drop at the required current densities and local heating. They also typically need to be electrochemically inert to the chemicals (e.g., electrolytes and active materials) involved and at the potentials used. This electrochemical stability is important at both the highest electrode potentials (where oxidation reactions, such as dissolution, may occur) and at low potentials (where reduction reactions, such as ion insertion, may take place). Due to the stresses commonly involved in roll to roll production of commercial battery anodes and cathodes the current collectors also must have moderate tensile strength and flexibility. Further these current collectors must provide good bonding with the active materials to prevent delamination

and allow efficient electron transport. This is often done with surface layer engineering to increase roughness, and chemical compatibility. In the supercapacitor field where high power applications make the minimization of electrode resistance a priority, surface coatings by conductive paints and even sol-gel processes have been used.[16,19]

The current collector is a non-active part of the battery, meaning it does not contribute to the total capacity, thus its thickness is typically reduced to the order of 7-20 μm to provide suitable mechanical stability.[20,21] While metal foils have traditionally been used, an increase in research into high performance current collectors has begun with an emphasis on enabling 3D structured current collector materials. Non-metal current collectors based on carbon and carbon nanomaterials have also been investigated as the material prices decrease and production rates increase.[22]

In order to determine if a new material is suitable for replacement of a current collector, the resistance contribution for that component must be fully understood. There are three main contributions to the cell resistance which are also displayed schematically in Figure 4b: electrochemical resistance (R_{ec}), constriction resistance at the electrodes tabs (R_c), and the current collector bulk electrical resistance (R_b). While the constriction resistance is closely related to the current collector and the resistivity contribute, it is more dictated by cell geometry (*a*, *b*, and *c*) and tab location (*e*). Thus the bulk electrical resistance is the only direct contribution to cell resistance from the current collector. Often the in plane current is assumed to be carried only by the current collector due to the relatively low resistivity compared with the active electrode materials. Taheri *et al.*, 2013 have provided an analytical solution to the resistance contributions of the current collector as well as relating them to the tab geometry for a working cell,[23]

$$R_b = \frac{c\rho}{2at} \tag{15}$$

where *a*, *c*, and *t* are geometry terms representing the width, length, and thickness of the current collector respectively as shown in Figure 4a, and ρ is the bulk resistivity

(Ω-cm). While important, R_b has been calculated to be only 3% of the total cell resistance when typical geometry and material selection is used.[23] While these contributions are small, this estimated value will change for carbon based current collectors. Further, this resistance calculation does not ensure the uniformity of the current distribution which will also need to be ensured for high rate capabilities.

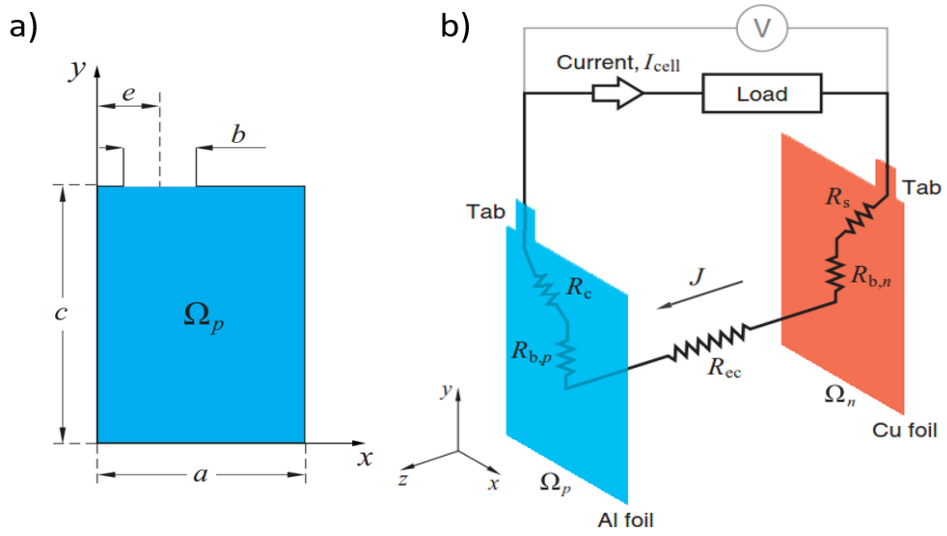

Figure 4. Schematic showing a) the dimensions of a typical current collector with a tab connection, and b) the configuration of the electrodes and the resulting resistance contributions from the electrochemical reaction, the bulk electron transport, and the constricting resistance at the tab.[23]

Metal Current Collectors

Many metals have been investigated for use in these applications with Al, Cu, Pt, Au, and Ag showing promise due to their low electrical resistivity (1.6 to 10.6x10^{-8} Ω m). Unfortunately the costs and weight of Pt and Au make commercial cells impossible, though their uses in research scale testing is significant due to their relative chemical stability in a broad range of electrolytes and potentials. Even for conventional batteries, Al and Cu metal current collectors can make up about 10% of the total battery weight.[24] Simply making thinner current collectors provides a limited solution as thinning also results in more fragile electrodes prone to breaking during handling with most metal foil current collectors limited to above ~7 µm at the thinnest for Cu.[21] Despite this, efforts to

sputter 1 µm metals films onto active materials and separators have been able to produce working devices[24] however the added costs of the metal deposition methods (PVD or CVD) currently prevent wide scale use. Metal mesh and foams are another way to reduce the weight of these current collectors and due to their 3D nature and good electrical conductivity they allow the potential use of active materials with low electrical conductivity.

Aluminum is an ideal current collector due to its low cost, high strength, light weight properties (2.70 g cm^{-3}), and low electrical resistivity (2.65 x 10^{-8} Ω m) and is commonly used for non-aqueous LIB cathodes with operating voltages between 3.5-5 V *vs.* Li.[25] The use of Al for these high potential applications may be surprising as the thermodynamic stability of Al at high potentials (>3.5 V *vs.* Li) is very low. This stability is due to the chemical stability and non-porous nature of the surface films which form, with a native oxide Al_2O_3 layer naturally forming in the presence of air. While this native oxide layer greatly increases the current collector's natural stability, the additional growth of passivating films of aluminum hydroxide, oxyhydroxide, and even fluoride allow increased stability.[26] Further, electrochemical experiments which have disrupted these films in-situ have shown that these passive films (Al_2O_3, and $Al(OH)_3$) can reform while submerged in non-aqueous electrolytes primarily due to the reduction of most carbonate based electrolytes.[27] AlF_3 in particular has been shown to be crucial in providing passivation and preventing pitting corrosion in electrolytes such as $LiPF_6$. Experiments using non-fluoride containing salts such as organic imide-based salts ($Li(CF_3SO_2)_2N$ (LiTFSI), $Li(C_2F_5SO_2)_2N$ (LiBETI)) show a reduction of 0.5-1 V in oxidation onset and a three order of magnitude increase in corrosion current when compared with electrolytes containing $LiPF_6$ salts.[28] Thus the use of $LiPF_6$ as an additive in these electrolyte systems has been proposed to develop a stable AlF_3 layer and enhance Al current collector stability as shown in Figure 5.

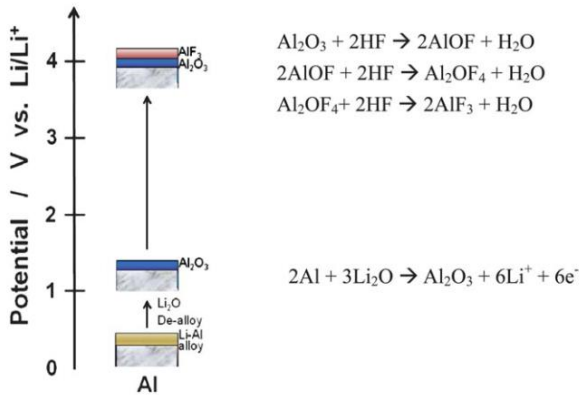

Figure 5. Electrochemical stability of Al surface in non-aqueous electrolytes used in LIB systems.[27]

While commonly used, $LiPF_6$ can also provide an issue for the Al stability as any residual water species can react with the $LiPF_6$ to form HF with this process being facilitated at higher potentials.[26] The HF species thus generated can accelerate corrosion of metal oxides through attack of the passivation layer (Al_2O_3 or $Al(OH)_3$) on the Al current collector or by attacking the transition metal oxides commonly used for active cathode materials. Additionally the reaction of HF with the transition metal oxides can also lead to the formation of H_2O as a reaction product thus leading to a self-catalytic reaction. When corrosion is observed it is often in the form of pitting corrosion after extensive cycling which can progress to electrode delamination and electrical isolation over time.[20]

While suitable for high potential LIB cathode applications, most anode active materials are based on graphite which operate close to 0 V *vs.* Li. Al readily alloys with Li at 0.27 V *vs.* Li to form first β-AlLi followed by more Li rich phases at lower potentials as shown in Figure 5.[29] When most metals alloy electrochemically with Li the resulting Li_xM compounds tend to be of highly ionic character and are therefore usually fairly brittle and not electrically conducting.[30] Thus the lithiation of the metal current collector must be avoided to prevent pulverization and thus electronic contact of the active electrode above. This issue is further complicated by the large volume expansions

(100-400% by volume) which are often observed for Li-metal alloying reactions. This results in rapid current collector crumbling and is commonly studied as this reaction is a possible high capacity anode material with a theoretical capacity of 996 mAh g^{-1} for LIB. Unfortunately efforts to impede this crumbling by reducing the aluminum dimensions to nanometer thin films,[31] particles, and even nanowire structures[32] have failed to increase the cycle stability to more than a few electrochemical charge discharge cycles.

Because copper is resistant to electrochemical alloying with Li at potentials even at 0 V *vs.* Li, it is commonly used for anode current collectors in LIB.[27] Evidence for environmentally assisted cracking of copper films due to intergranular Li attack has been observed for large grained work hardened materials however these conditions have not been observed in commercially available Cu foils.[20] Despite the lower electrical resistivity of Cu (1.72×10^{-8} Ω m) compared with Al, Cu has a much higher density (8.96 g cm^{-3}) which greatly reduce the gravimetric energy density of Cu containing cells. A review of the mechanical properties of commercial Cu current collector foils show a strength over 245 MPa and 5% elongation to fail even for the high purity 99.95% pure alloys typically required.[21] Thus for anodes, copper foil is more commonly used for anode current collectors in LIB despite the higher cost and extra weight reducing the total cell energy density. While Cu current collectors are stable at low potentials they oxidize at voltages above 3.3 V *vs.* Li^+/Li and are therefore limited in their use as high voltage cathode current collectors.[27] For supercapacitors Cu is rarely used as the operating voltage range in these systems can be controlled to avoid redox reactions of the Al current collector and the higher resistivity do not balance the increased cost and density.

Carbon Current Collectors

Carbon has attracted interest in electrochemical devices due to its low cost, electrical properties, light weight, and chemical stability and for many applications it would be difficult to find a suitable replacement. Carbon comes in many allotropes with

the allotropes exhibiting majority of sp^2 bonds show the most interest in electrochemical devices due to their high conductivities. A wide variety of densities have been reported depending on the porosity and degree of crystallinity of the sp^2 carbon being studied. These densities range from 2.25 g cm^{-3} for highly crystalline graphites to 1.12 g cm^{-3} for graphite foils, which compare favorably to Al and especially Cu foil current collectors.[33] Graphite has very anisotropic properties with low electrical resistivity and good mechanical properties in the basal plane direction due to the covalently bonded carbon sp^2 bonds. Crystallization of amorphous and defect containing carbons has been shown to increase conductivity of carbons by annealing in inert atmospheres and extreme temperatures with the electrical conductivity beginning to increase at 600-700 ºC and final graphitization occurring at over 2500 ºC, where conductivity increase saturates.[17] This makes highly oriented pyrolytic graphite (HOPG), graphene, carbon nanotubes and nanofibers good candidates for current collectors in some ECSDs.

The usage of carbon as a current collector has faced difficulty primarily due to the inflexibility and difficulty achieving resistance values comparable with metal foils. Inflexible carbon rods and plates are used as current collectors for the positive electrode in dry cells and in redox flow batteries however these materials cannot be incorporated into commercial LIB production due to their rigidity. In order to achieve the flexibility needed carbon composites or fabrics are required which reduce the inherent conductivity of the carbon due to particle to particle or fiber to fiber contact resistances. The electrical conductivity of carbon materials can vary greatly depending on the microstructure and crystallinity of the material of interest with low temperature CVD grown carbon films showing 20-1000 mΩ cm, partially ordered PECVD carbons showing 5 mΩ cm, and well-ordered graphite (in plane) showing 0.3 mΩ cm.[34] More recently commercially available flexible graphite sheets such as Grafoil® have been produced that have in plane conductivity of 0.7 mΩ cm.[22,35] Even lower resistivity has been achieved by metallization of submicron thick layers of Cu or Al using physical vapor deposition onto the graphite

papers, though at a significant impact to the manufacturing cost.[20] These un-metalized graphite foils are not as flexible as other forms of conductive carbons (CNT, graphene, carbon fiber) and issues with exfoliation have been observed in some electrolyte systems.[36] Further challenges included delamination of active material due to graphite layers flaking off during manufacture, assembly, and testing. Some of these issues could be addressed by texturing the graphite foil surface which also improved electrolyte access and Li^+ ion transfer through the thickness of the foil but further work was needed to improve charge and discharge rate (<50 mAh/g at C/20) as well as cycle stability.[22]

Once a flexible carbon current collector is chosen there are still stability concerns with use in LIB with electrochemical activity of these carbons at low voltages and solvent co-intercalation at high voltages. The electrochemical alloying is well studied as this is the charge storage mechanism commonly used for LIB graphite anode materials,

$$C + xLi + xe^- \leftrightarrow Li_xC \tag{16}$$

During this electrochemical alloying the Li^+ ions intercalate between the basal planes of the graphite particles at low potentials (0-0.25 V *vs.* Li/Li^+). Diffusion through the graphitic planes is difficult however defects in the graphite lattice or holes in the planes can increase this reaction.[37] During the intercalation the Li completely occupies one inter planar space in the graphite lattice leaving unlithiated planes on either side of the Li filled layers. As the Li concentration is increased in the graphite, the numbers of unlithiated layers between the Li filled graphene layers decreases gradually to zero for fully saturated LiC_6 and is known as staging.

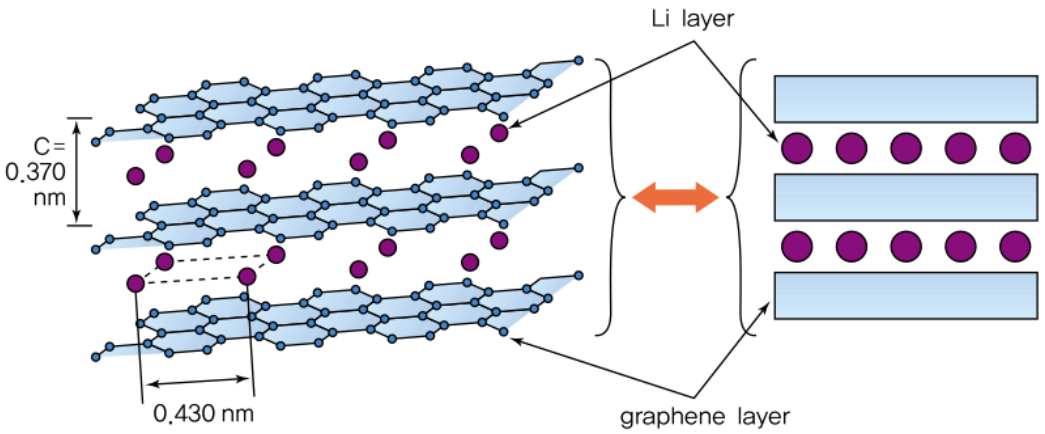

Figure 6. Lithium location in the graphite crystal structure during intercalation for secondary LIB applications.[2]

The multistage insertion process also results in multiple voltage plateaus during constant current charge and discharge as shown in Figure 7. The difference in potential of these different redox potentials are related to the different staging potentials of the Li insertion in the graphite lattice.

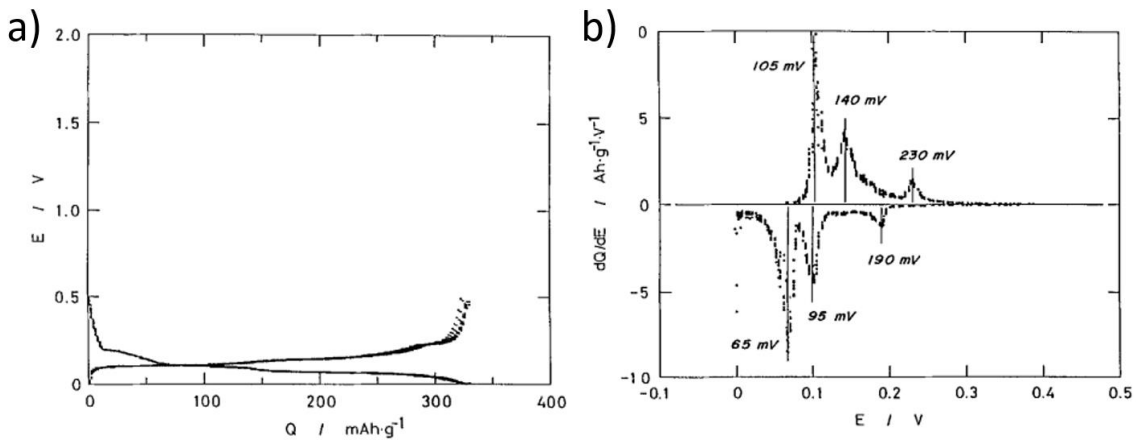

Figure 7. Potential stability of graphite during constant current lithiation in a non-aqueous LIB; a) charge and discharge curves with intercalation starting at 0.5 V *vs.* Li; and b) differential capacity of the multistage Li insertion process during reduction of the graphite and oxidation of the Li-Gr intercalation compound.[38]

This Li insertion is ideal for charge storage in a battery active material however it can cause great difficulties for using graphite as an anode current collector. This lithiation can cause delamination and embrittlement,[39] but an increase in electrical conductivity.[40]

These issues can be avoided by using high potential anodes such as LTO, SnO_2, or Si which operate above 0.25 V *vs.* Li/Li^+ however this comes at the expense of energy density.[25]

For high potential current collector applications anion and solvent intercalation are potential issues. Solvent co-intercalation with the cation insertion was observed by Besenhard in 1976 during his work with alkali metal graphite alloys in ammonia.[41] Since then other solvents including propylene carbonate (PC) and ethylene carbonate (EC) have been shown to intercalate graphite causing extreme volumetric expansion (>100%) and subsequent exfoliation.[25,36] Experiments using graphitic carbon fibers with different textures have shown that solvent intercalation initiates at the edges of basal planes and thus can be reduced for highly oriented graphites and by reducing the graphite flake thickness.[42] Work has been done to design surface films through electrolyte and additive reduction which form blocking layers to solvent co-intercalation and are in common use.

Another issue with carbon substrates is the poor wetting that is often observed for pristine carbon surfaces with contact angles with water as high as 85º observed for freshly cleaved HOPG surfaces ranging to 55º for polycrystalline graphite.[43] This problem is also observed for C-H terminated carbon surfaces found in CVD produced carbons.[34] This can make solution based synthesis methods such as infiltration, electrodeposition, and hydrothermal difficult as well as prevent effective contact with many electrolytes. The surface of carbonaceous materials can contain numerous chemical species which form during the material synthesis process or introduced during post processing. These surface groups are typically oxygen based and include carboxyl, carbonyl, lactone, quinone, and phenol groups and can be found both on the basal plane of the graphite or on the edge planes.[25] Further, the wetting behavior or highly curved carbon surfaces found in nanofibers, nanotubes, or porous carbons can be much different due to increased sample curvature.

CNT Current Collectors

Carbon nanotubes are a commonly studied carbon allotrope which can be described by rolling a single atomic layer of graphite into a cylinder. Like graphite it has many of the same physical properties which make for attractive current collector materials. Compared to metals the density of CNTs is much lower as even the most dense vertically aligned CNT arrangements report densities around 1.6 g cm^{-3} with typical values for CNT non-woven fabrics being 0.2-0.5 g cm^{-3}.[44] These tubes can be single, double, or multi-walled and range in diameter from 2-100 nm. While the resistivity of single CNTs is very low and even bundles of individual CNTs perform on the order of 10^{-4} Ω cm,[45] large scale composites and fabrics show much lower performance (10^{-2} Ω cm)[46] due to the inter-particle contact resistance and porosity which is often observed.

The lithiation process in these materials proceeds identically to their graphite counterparts however due to the reduced presence of graphite edge sites for Li and solvent intercalation they exhibit more stable behavior.[42] This effect is observed for CNTs with high defect concentrations including acid functionalized, ball milled, and un-annealed CVD grown CNTs where the Li insertion and extraction can occur through the defects in the CNT walls.[47] Because of the large diameter of MWCNTs the volume expansion during lithiation (~6% lattice expansion from 3.40 to 3.60 Å) typically does not cause fracture.[39] Biggest effect of the Li insertion is a drastic change in the mechanical properties of the CNTs with a transition from a flexible behavior with failure dominated by sword-in-sheath failure modes to a sharp brittle failure.[39] This brittle failure mode was studied using molecular orbital based modeling and was shown to be due to a "point-force" effect of the Li atoms trapped between the CNT walls which contract radially upon being axially strained in tension.[39]

CNT fabrics tend to not realize the full potential mechanical properties when assembled into non-woven fabrics due to the weak bonding between CNTs. This forces much of the mechanical strength of a non-modified CNT fabric to be transferred via van

der Waals bonding between fibers, friction between crossed or entangled tubes if the aspect ratio and flexibility are high enough, and possible branched growth processes either through Y/T joins or through "nanowelding" which may occur from co-deposited amorphous carbons to join the CNTs.[48] Additional mechanical bonding can be enhanced through active material deposition onto the CNT fabric. In fact if the active material is non-conducting and is deposited before CNT fabric formation the electrical conductivity between the CNTs can be greatly decreased due to poor contact between the CNTs through the deposited active materials.

One side-effect of using CNTs as a current collector is the potential contribution to the double layer capacitance due to the high surface area and electrically active surface. This has suggested the use of CNTs as both the current collector and active material for an EDLC. Because the surface area of MWCNTs is much lower than SWCNTs (~50 $m^2 g^{-1}$ compared to 1300 $m^2 g^{-1}$)[49] more work has been done to try to synthesize free standing SWCNT networks[50] and have achieved modest results of 40-120 F g^{-1} and these values have been increased to 200 F g^{-1} by backing the SWCNT films with cellulose paper.[51] These values are still much lower than that capable for a pseudocapacitor which suggests a better use of these expensive nanomaterials as a substrate rather than an active material, though the cycle stability of the CNTs double layer capacitors tends to be much higher than that for pseudocapacitors.

Effects of High Surface Area

Much research has shown the importance of current collector surface features on the performance of the metal current collectors. While the surface chemistry has been shown to be important for tailoring the electronic transport the surface roughness is also an important parameter for electrode adhesion during long term cycling. For high rate capability ECSDs the internal resistance must be kept as low as possible to prevent unnecessary heating and electrical polarization during operation. Nano-architectured

electrodes enable high performance by providing a high specific surface area for thin films of a faradaic active materials for battery[9] or capacitor applications.[10] By allowing electron access to large areas of thin films materials which suffer from low electronic or ionic conductivities can be more efficiently utilized. Surface patterning with features on the order of 3-10 μm helps with electrode adhesion and prevents premature cracking and delamination of the active materials by providing increased surface area for proper adhesion.[21,52] Current collectors have been developed which provide these surface finishes and use a variety of methods including electrodeposition, reactive-ion etching, sputtering, and chemical vapor deposition.[24,53]

Progress has been made in demonstrating the advantage of these high surface area current collectors in recent years and a variety of materials have been synthesized using an equally broad selection of deposition methods. Work on LIB current collectors has shown a six fold improvement in the energy density compared to a planar electrode [9] and a doubling of the area-normalized capacitance (1.5 F cm^{-2}) was observed for a MnO_2 based pseudocapacitor.[10] Electrodeposition has also been used to produce high surface area Al and Cu current collectors.[54,55] Sol-gel coatings of conductive carbonaceous materials have been used to increase the rate capability and electrode adhesion of Al foils for carbon-carbon supercapacitors. Carbon nanotubes have been widely used as flexible current collectors and active materials in both battery and capacitor applications even with low surface areas of 50 m^2 g^{-1}.[53]

Separators

For any ECSD to function, ions must be allowed to transport between the anode and cathode without direct electrical connection and while maintaining proper ionic contact through well wet electrolytes. These competing goals are met by using a porous insulating material and polymers are typically used because they allow good formability and low cost. Separator materials are used to ensure reliable electrical insulation and

optimal ionic conductivity and must be chemically and electrochemically compatible with the materials used. This challenge has been more severe in the case of LIB compared with supercapacitors as the operating voltages, mechanical stress due to active material dimension changes, and the safety concerns from possible fire are higher. These issues coupled with an increasing market for LIBs has led to more investment to develop high performance separators. The majority of the cost of the separator material is in the manufacturing methods not the material costs[56], and separator costs can represent ~10-15% of the total material costs of a battery.[57]

The production of LIB separator materials is commonly done using dry or wet processes, both of which use the combination of extrusion and stretching of polyolefin films. In the dry process the extruded polymer films are heat treated to increase the crystallinity and crystal size before the membrane is mechanically stretched about 150-250%.[58] This stretching causes the crystalline regions to fracture into regions connected with nanosized polymer chains. This typically result in a slit-like pore structure as shown in Figure 8a. Not all polymers are easily crystallized however and this makes the dry process limited in the materials it is compatible with. The wet process involves the mixing of the polyolefin with a plasticizer or wax particles which are washed out after the extruding and biaxial stretching process leaving more spherical pores.[57] While this allows a much greater flexibility in the chemical composition of the membranes, there is also a much higher cost associated with fully removing the wax and plasticizers which can impact the final cell components if left behind. In both cases the morphology can be controlled by the stretching ratio, speed, and temperature of the stretching process.

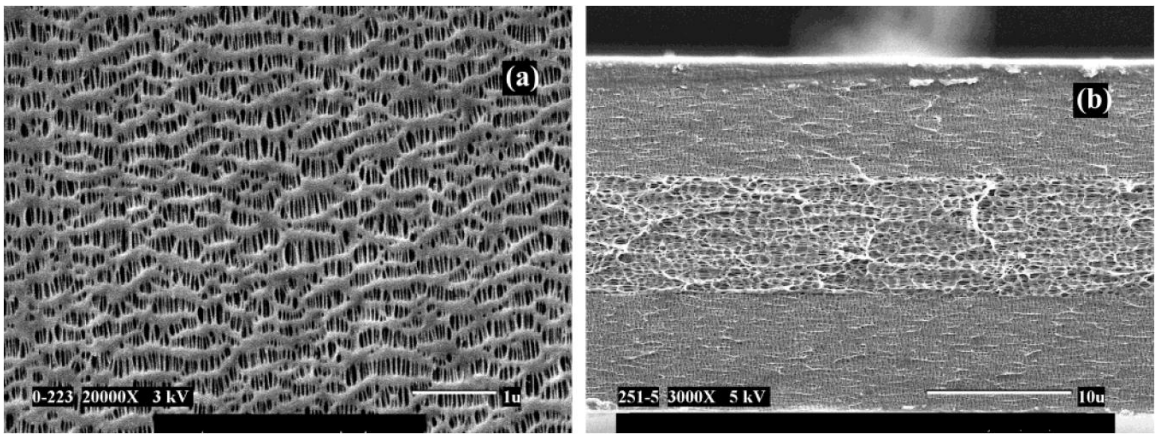

Figure 8. SEM images of typical tri-layer LIB separator Celgard 2325 a) surface images, and b) shows cross sectional image of the tri-layer structure.[59]

For LIBs, non-aqueous electrolytes are required to prevent reactions with active materials and to provide higher operating voltages and energy densities. Unfortunately, the low ionic conductivity of these non-aqueous electrolytes causes large solution resistances for a comparable separation distance in an aqueous cell. This has resulted in efforts to minimize internal cell resistance and the minimization of separator thickness for LIB applications is one method to achieve this. Separator film thicknesses of 25 and 16 μm are common. For these LIB applications polyolefins such as polypropylene (PP), polyethylene (PE), and other polymers such as polyvinylidene fluoride (PVDF) and polyethylene terephthalate (PET) are typically used due to their chemical stability, wettability, and process ability. Their high tensile strength (>100 MPa) allows for rapid cell assembly using automated high speed winding machines.[58] In order to achieve these goals microporous polymer films (Figure 8) are normally used instead of the non-woven fabrics commonly used in aqueous systems such as lead acid and alkaline cells.

Due to the sensitivity of LIBs to water it is common to vacuum dry these materials at 60-80 °C, which makes thermal stability important. Thermal shrinkage is a challenge even for highly porous polymer based separators as there is a large difference in density between the amorphous and crystalline phases of the polyolefin materials which are commonly used.[58] This shrinkage should be less than 5% in the transverse or

manufacturing directions when exposed to 90 °C for 1 h. In addition to temperature stability for drying purposes, these separators can be exposed to localized heating due to microshorts caused by either particle puncture or dendrite growth. This localized shorting can cause runaway heating as the polymer melts and a higher current density forms.[58] Microporous layered PP-PE-PP composites (Figure 8b) are used in order to provide a thermal safety feature by melting at 130 ºC and blocking ion transport at that location.[59] Porosity is typically 40%, pore sizes need to be small enough (<1 μm) to prevent penetration by the micron size active material particles during assembly and to help block dendrite growth which can lead to microshorts.[25]

Separator ionic resistance must be decoupled from the inherent ionic resistance of the electrolyte used in order to properly compare performance. This can be done by measuring the resistance of a separator filled with electrolyte (R_{sep}) and subtracting the resistance contribution from only the electrolyte (R_{el}, determined by an empty cell test). The ratio of these values is known as the MacMullin number ($N_M = R_{sep}/R_{el}$) and is used to characterize the resistance contribution to the system solely from the separator with values of 4-5 being typical.[56,58] The ionic resistivity for a medium power LIB separator typically ranges below 1 kΩ cm which for a typical 25 μm separator results in an area specific resistance of <2.5 Ω cm^2.[60] Because ion transport through separators rarely involves a linear path the concept of tortuosity (T) has been developed which is a ratio of the actual ion's path length with the direct distance between electrodes and typically varies from 1.3 for porosities around 60% and approaches unity for high porosity samples.[25] The tortuosity and porosity of a separator are the primary terms used to describe the separator ionic resistance as follows:

$$R_{sep} = R_{el}\left(\frac{T^2}{P} - 1\right) \tag{17}$$

where R_{sep} is the ionic resistance of the separator, R_{el} is the electrolyte ionic resistance, T is the tortuousity, and P is the porosity. Porosity values of separators

materials are often measured according to ASTM D2873 using solvent absorption using non-reactive low surface tension solvents such as hexadecane. This measurement can be done by weighing the sample before and after dipping in the solvent of choice with the surface excess solvent being removed by blotting. The porosity (P) is then calculated according to the following,

$$P = \frac{w_T - w_S}{\rho_{solv} V_S} * 100 \quad (18)$$

where w_T is the weight of the separator with absorbed solvent, w_S is the weight of the pristine separator, ρ_{solv} is the solvent density, and V_S is the separator volume.

As energy and power density increases in commercial Li-ion batteries, a higher demand for safety has developed with special interest from car manufacturers and airline operators. Many of these safety issues stem from melting of the polymer separator and rapid discharge through short circuiting causing thermal runaway events (fires). The incorporation of ceramic particles with high thermal stability (>1000 ºC) into the polymer separator is one approach to addressing this issue. Additionally, the ceramic particles also improve the puncture resistance of these films (>300 g with a given needle)[58] with their high hardness values thus increasing the damage tolerance of the battery to outside forces as well as to penetration by the micron size particles which compose the electrodes. These films can be created in many ways, including coating the surface of traditional separators, mixing ceramic particles directly into the wet extrusion process, or applying the ceramic particles to the electrode surface.[56] Work has also been done to produce ceramic filled nonwoven materials with wet laid PET microfibers being used as a polymer support upon which ceramic particles are applied in a paste and subsequently dried.[57]

Al_2O_3, SiO_2, TiO_2, ZrO_2, and MgO particles have been shown to be suitable for use in high performance separators and due to their low density, low cost, and good electrochemical stability Al_2O_3 and MgO are popular materials for such studies.[57] By

incorporating ceramic nanoparticles, the ionic transport properties of separator materials can be increased by disrupting the crystallization of the polymer, encouraging the formation of amorphous regions with higher ionic conductivity, and increasing the wettability of the polyolefins with the highly hydrophilic ceramic materials.[59] While not all of these materials show electrochemical stability in contact with Li metal in half cell testing, stable performance may be obtained in full cell testing using graphite anode materials, particularly with an additional polymer layer on the graphite side. This has led to the development of commercial ceramic particles' containing separators by companies, including Celgard, Targray, Dreamweaver, DuPont, Sony, LG Chemical, Evonik-Degussa, Hitachi Maxell, among others.[57] Another advantage to using the ceramic separators is their ability to scavenge the trace hydrofluoric acids which form due to the reaction of the lithium salt ($LiPF_6$) with residual water thus increasing the battery stability.[58]

Secondary Batteries

Batteries offer the largest energy storage capacity of all of the electrochemical storage devices, which normally comes at the expense of lower charge and discharge rates compared with capacitors. This tradeoff is due to the faradaic charge storage mechanism and hence are limited by the diffusion time of the redox species through either liquid or solid state. Batteries can be classified into primary batteries, which are used once and discarded or recycled, and secondary batteries, which can be recharged and used multiple times. In recent years large growth in secondary battery research has occurred driven by the development of secondary LIB technology, which operates at high discharge voltage of 3.7 V *vs.* Li and shows greatly improved energy density (200 Wh/kg compared to 30 Wh/kg for lead acid, or 70 Wh/kg for nickel metal hydride batteries).[25] This has increased secondary battery usage in a large variety of devices, including mobile electronics, electric vehicles, robots, renewable energy storage solutions. Other types of

future applications for LIB include microcell batteries, flexible batteries, and structural batteries. The synthesis methods, material composition, and manufacturing methods for these new battery formats are very different from currently used methods.

Unlike general faradaic reactions, the simple assignment of anode/cathode based on oxidation/reduction occurring at the electrode can be confusing for the reversible reaction typical of rechargeable/secondary batteries. This confusion occurs because reduction and oxidation reactions occur at both electrodes of the battery depending on the charging or discharging state of the battery. For this reason, the electrodes are labeled according to the spontaneity of their reaction (discharge state): cathode being the positive (+) electrode and the anode being the negative (-) electrode as shown in Figure 9.

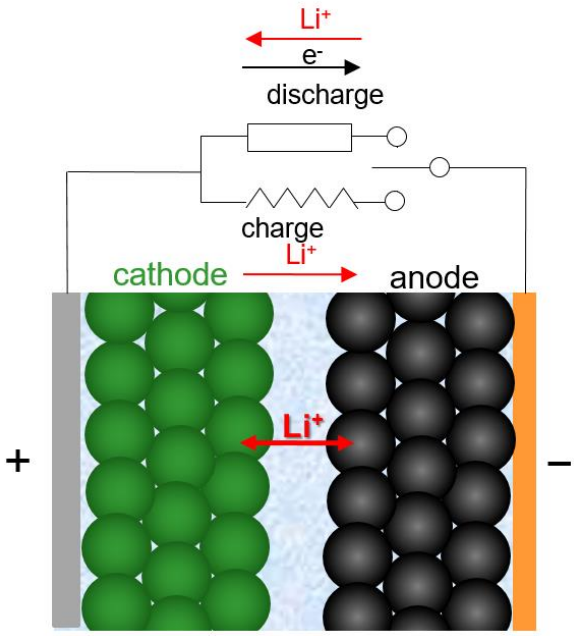

Figure 9. Configuration of secondary Li-ion battery (LIB) composed of cathode (+) and anode (-). The electron and Li^+ flow directions are indicated during charging and discharging.

The capacity of a LIB is governed by how much Li can be reversibly transferred between the anode and cathode. Because the charge transfer is done by Li ions, materials which can store large amounts of Li reversibly while maintaining useful potential differences are ideal for these applications. In commercially available LIBs, graphite and

metal oxides such as (SnO_2 and Li_2TiO_3) are usually used as the anode materials[6] and $LiCoO_2$, $LiFePO_4$, $LiNiCoAlO_2$, $LiNiMnCoO_2$, and $LiMn_2O_4$ as the cathode materials.[61] These materials operate as intercalation materials which can store Li-ions between the crystalline planes without undergoing significant crystallographic restructuring as shown in Figure 6d. While these materials have high cycle stability (>500 cycles) due to the small degree of atomic reordering which occurs, they also have smaller theoretical capacities (~120-200 mAh/g) compared to other storage mechanisms such as conversion materials as shown in Figure 10a-c.[7]

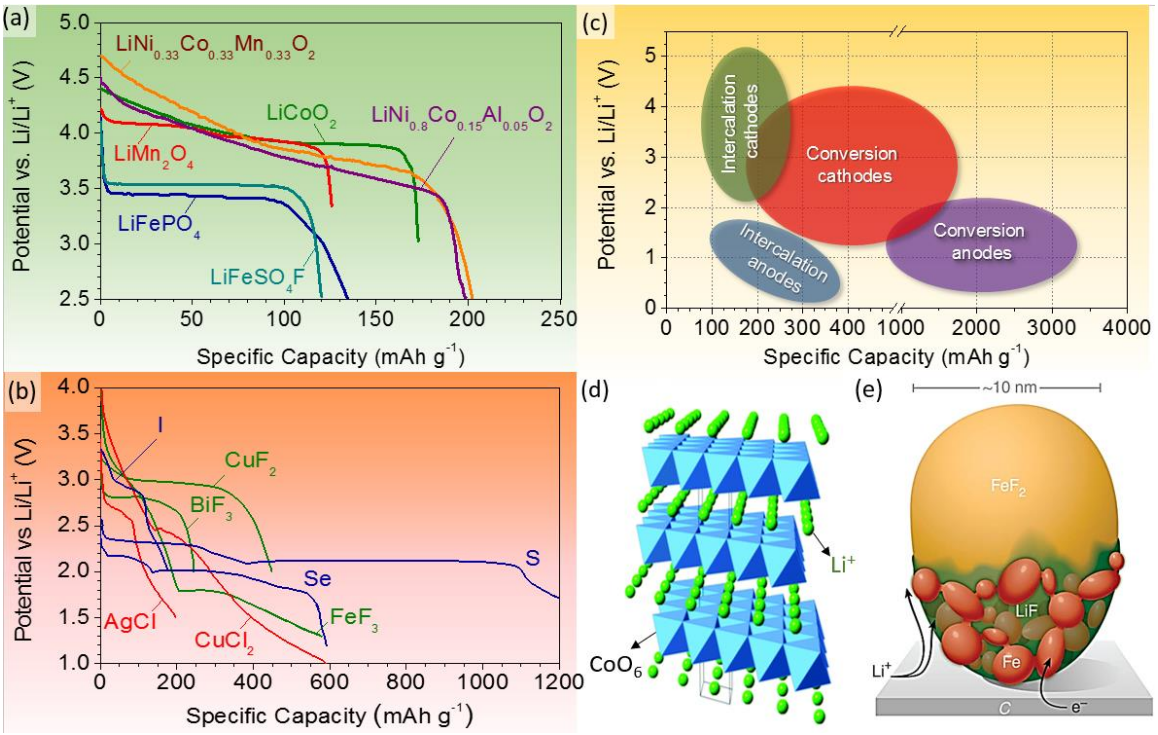

Figure 10. Comparison of intercalation and conversion materials with typical constant current discharge curves for a variety of a) intercalation cathodes, b) conversion cathodes. c) Typically observed experimental capacities for intercalation and conversion cathode and anodes. d) Intercalation of Li into LCO cathode. e) Conversion of FeF_2 cathode.[7]

Of the intercalation anode materials, carbon based materials are the most attractive due to their low cost, high stability, and electrical conductivity and have been used the most for both commercial and military lithium ion batteries.

$$xLi^+ + xe^- + 6C \leftrightarrow Li_xC_6 \quad (19)$$

One approach to increasing the capacity of a battery involves using higher capacity active materials, which include conversion-type reactions instead of intercalation-type reactions. A conversion cathode or anode is defined as a material which undergoes significant crystallographic reorientation upon solid state redox reaction often with the nucleation and growth of additional phases and sharp accompanying volumetric changes which can be anywhere between 2% to 400%. These conversion reactions can further be grouped into two types (A and B) as described below,[7]

Type A: $yLi + MX_z \leftrightarrow M + zLi_{y/z}X$ (20)

Type B: $yLi + X \leftrightarrow Li_yX$ (21)

Examples of Type A conversion materials under current investigation include metal fluorides and chloride cathodes (MX_2 and MX_3 where M= Fe, Co, Cu and X=F, Cl) cathodes and metal oxide anodes such as SnO_2, MnO. Similarly, commonly studied Type B conversion materials include Chalcogen cathodes (S, Se) and alloy anode materials (Al, Sn, Si).[6]

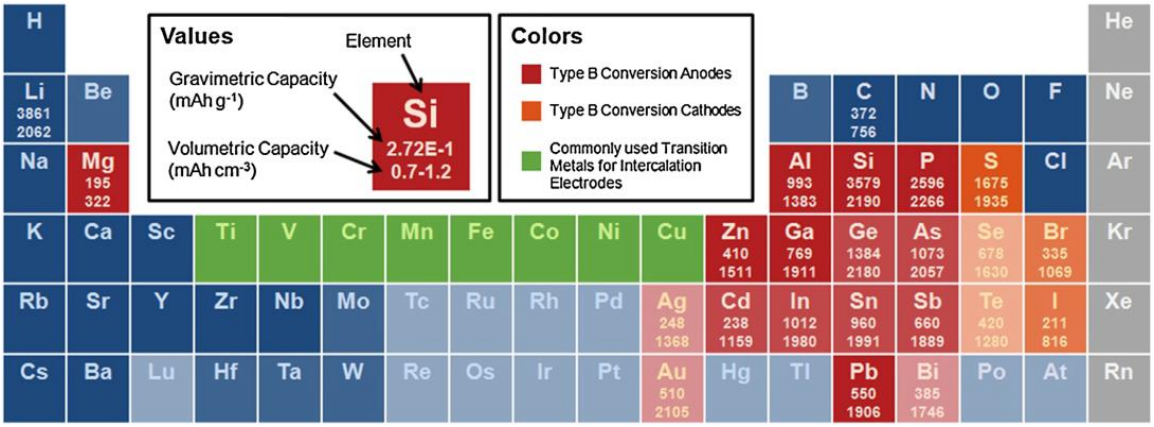

Figure 11. Capacity for commonly used elements in secondary LIBs. Elements which are faded indicate relative abundance in the earth.[7]

Due to the variety of chemicals necessary to battery operation and the delicate interplay between the thermodynamic instability of these systems and the kinetic reaction

pathways it is unsurprising that batteries may undergo a variety of degradation mechanisms as shown in Figure 12. In fact, carbon is unstable in most common electrolytes causing electrolyte reduction and a surface film to form called the solid electrolyte interphase (SEI). This surface layer remains impermeable to additional electrolyte solvents while maintaining Li ion conductivity and it is the careful formation of this SEI layer that has allowed the popularization of graphite as a LIB anode.

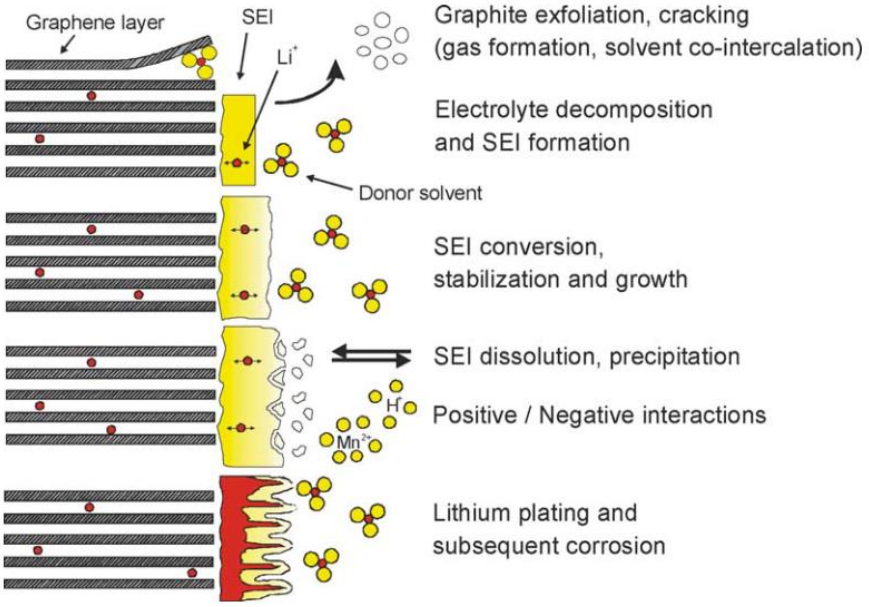

Figure 12. Possible aging mechanisms at the anode/electrolyte surface.[62]

Electrochemical Capacitors

Electrochemical capacitors (also called supercapacitors) nearly bridge the existing gap in performance between secondary batteries and traditional capacitors, as shown in a Ragone plot (Figure 2), by offering moderate energy and power characteristics. When supercapacitors are designed to use electrostatic charge separation as the primary energy storage mechanism in the form of the double layer, they are called electrochemical double layer capacitors (EDLCs). Electrochemical capacitors that have a high degree of faradaic capacitance contribution are called pseudocapacitors, however unlike a battery the faradaic reactions are typically localized to the material's surface. These rapid surface localized faradaic reactions often result from oxidation state changes in the surface

functional groups, transition metals, or electrochemically active polymers. In contrast to batteries, supercapacitors additionally offer significantly longer cycle stability (>50,000 cycles) and a broader operation temperature (-40 to 60 ºC).[3] The cycle stability of pseudocapacitors typically falls between an EDLC and a battery as the redox reactions tend to allow for side reactions in comparison to electrostatic charge storage however the pseudocapacitor typically forms redox reactions at the surface.

Electrochemical Double Layer Capacitors

Due to the small charge separation distance allowed by the electrochemical double layer, the energy stored in an EDLC can be much higher than a solid state dielectric capacitor. The limiting factor to the energy stored in these devices is the ionically accessible surface area ($U \propto A$) and the voltage stability window of the electrolyte ($\Delta V_{max}^{electrolyte}$) of choice ($U \propto \Delta V^2$). In order to maximize the energy stored the maximum operating voltage of the EDLC (ΔV_{max}^{EDLC}) should ideally be equal to $\Delta V_{max}^{electrolyte}$ with higher potentials leading to electrochemical decomposition of the electrolytes, gas evolution, and possible cell rupture.

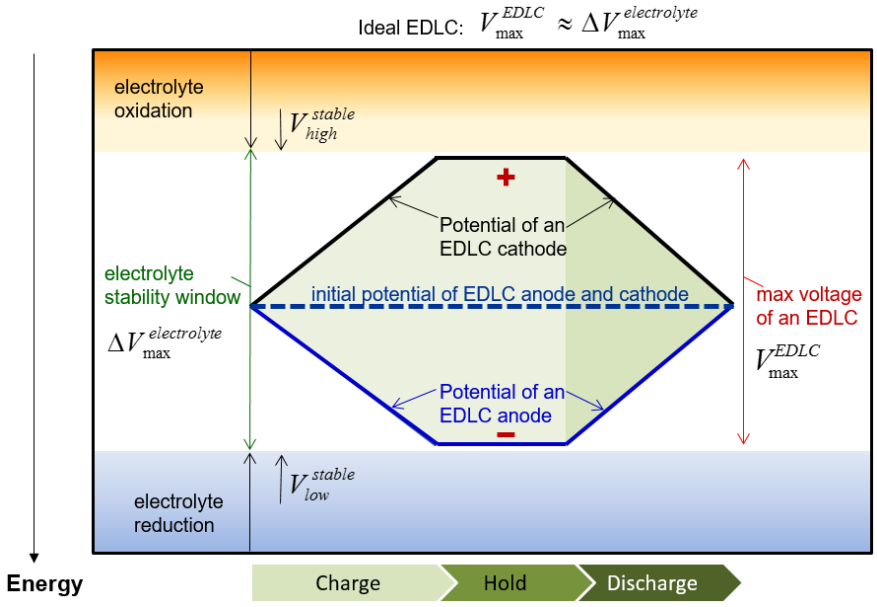

Figure 13. Representative energy diagram for an ideal EDLC showing the applied potential as a function of device charge/discharge in relationship to the stability window.[63]

While these devices suggest higher performance at ever increasing specific surface area (SSA), this is not strictly observed in practice with a plateau of performance around 1200-3000 m^2 g^{-1}.[63] Increasing the surface area by creating smaller and smaller pores is effective until the ionic resistance due to torturous ion paths increases, or the access of electrolyte or volumetric density is reduced. The pore shape and average pore size has also been shown to have large effects on the contribution of the surface area to the measured capacity of the cell.[64] An anomalous increase in EDLC capacitance for pores with diameters <1 nm was observed due to the disturbance of the solvation shell around the ions present in the double layer in these pores.[64] For a carbon supercapacitor the charging time can be reduced by three orders of magnitude by changing the pores within individual porous carbon particles from tortuous to straight.[65]

Pseudocapacitors

While EDLCs have captured a majority of the electrochemical capacitor market, pseudocapacitors have begun growing at a substantial rate with adoption primarily in

high capacitance applications. The definition of a pseudocapacitor has been loosely used in the literature to indicate any material which produces the electrochemical signature of a double layer electrode (constant capacitance over different voltage ranges, rectangular cyclic voltammetry, current decay upon voltage hold, etc.) but which uses a charge storage mechanism based on a faradaic reaction.[66] There are many different mechanisms for pseudocapacitive contributions with the three most common including underpotential deposition, redox reaction, and intercalation.[67] Typical pseudocapacitance materials can be classified as inorganic (VOx, RuO_2, MnO_2) or polymeric (polyaniline (PANI), polypyrrole (PPy), polythiophene (PTh), and polyethylenedioxythiophene (PEDOT))[4,68] and will be covered in more detail in this section. Additional classifications of pseudocapacitance include intrinsic pseudocapacitance where the material shows the electrochemical response in its bulk form, or extrinsic pseudocapacitance where material engineering (increasing the surface area or reducing the diffusion distance) induces pseudocapacitance behavior in an otherwise faradaic material.[67]

Conway explains the similarity between pseudocapacitance and EDLC behavior by including the thermodynamics of a system with continually varying density of states. He defined a property *y* which can be many thermodynamically related parameters including the extent of surface coverage of an electrode, fractional absorption of H^+, extent of conversion of oxidized species in solution or in a hydroxide.[3] All of these terms are proportional to the charge passed through a surface based redox reaction and are related it to the electrode potential through a Langmuir-type electrosorption isotherm. By taking the derivative of this property with respect to electrode potential (V) the following is attained,[3]

$$\frac{dy}{dV} = \frac{F}{RT}\frac{Kexp(\frac{VF}{RT})}{\left[1 + Kexp\left(\frac{VF}{RT}\right)\right]^2} \tag{22}$$

where K is the reaction rate constant which can be different in the forward or backward reaction and impacts the capacitance upon charge or discharge, and F, R, and T

have their traditional electrochemical definitions. Because *y* is proportional to charge (Q), dy/dV is proportional to capacitance (dQ/dV). A typical pseudocapacitor behavior during cyclic voltammetry testing is demonstrated for the MnO_2 system as seen in Figure 14 and is a well-studied pseudocapacitor material where the continuous variable *y* is the fractional hydration of the metal oxide.[16]

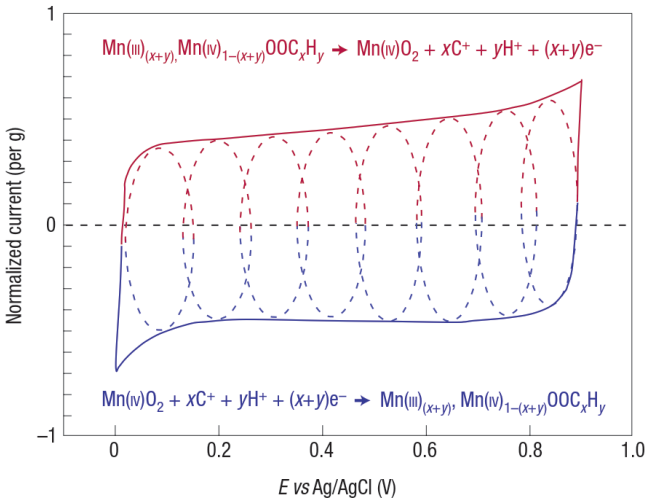

Figure 14. Typical cyclic voltammetry performance of a pseudocapacitive material (MnO_2 in 0.1 M K_2SO_4) showing the continuous potential range of redox reactions. [16]

Inorganic Pseudocapacitors

The RuO_2 system has been strongly studied due to the low electronic resistivity (40 μΩ cm for bulk films),[69] which allows for thicker film dimensions and more efficient material utilization in an electrode composite. Commonly reported performance capacitance values range from 600-700 F g^{-1} and an electrode energy density of 25 Wh kg^{-1}.[70] This advantage is limited however by the high price and rarity of ruthenium itself ($1,350 kg^{-1} in 2016). While this electrochemical response is often attributed to multiple overlapping redox peaks which is observed in the ruthenium oxide (RuO_2) system the same behavior is also observed in other metal oxide/hydroxide systems as well as conductive polymer applications. This discrepancy can be explained by a continuous change in the electrode materials chemical activity during operation which occurs over a large compositional range. For RuO_2 this process can be described as,

$$RuO_2 + xH^+ + xe^- \leftrightarrow RuO_{2-x}(OH)_x \quad (23)$$

where $0 \leq x \leq 2$ and the oxidation state smoothly changes from Ru^{2+} to Ru^{4+}.[16]

Other low cost transition metal systems have been studied both in aqueous systems which are limited to 1 V electrolyte stability window and inorganic systems with much broader stability windows allowing for activation of different redox reactions. This increase in voltage window is especially useful for supercapacitor applications as the energy storage increases as ΔV^2. Additionally the larger voltage stability windows in inorganic solvents can allow the activation of redox couples in more abundant materials or activate multiple redox reactions in the same material thus increasing the charge storage and capacitance achievable.[3] Manganese oxide (MnO_2) has been studied as a low cost pseudocapacitor material to replace RuO_2 however the high resistivity (ranging from 10^3-10^7 Ω cm depending on the crystallinity)[71] only allows for charge storage in a thin layer on the surface even though it is considered an intrinsic pseudocapacitor material.[67] This has led to the use of ultrathin films and material engineering to increase the capacitance instead of traditional slurry based electrodes. This method has allowed an increase of capacitance from ~250 F g^{-1} for thick film to >1000 F g^{-1} which approaches the theoretical value of 1233 F g^{-1} for a one electron transfer in the MnO_2 system.[67,71]

MnO_2 charge storage mechanism is different than the RuO_2 case even though they both operate in aqueous environments. While RuO_2 involves the hydration of its crystal structure MnO_2 is an intercalation type material which operates as follows,[67]

$$MO_2 + xA^+ + xe^- \leftrightarrow A_xMO_2 \quad (24)$$

where M=Mn and A is an alkali metal cation, typically Li or Na. Typically this redox reaction involves only the transition between the Mn^{4+} and Mn^{3+} states. Unfortunately the Mn^{3+} species that is formed decomposes in acidic or even neutral conditions which limits the electrolytes which can be used as well as the cycle stability and device lifetime.[72]

Vanadium oxide (VO_x) has attracted interest as an active pseudocapacitive material due its wide availability, low cost (~\$12 kg^{-1}), and the large potential window for oxidation/reduction reactions to occur (1.5-3.5 V *vs.* Li/Li^+).[73-80] In order to make use of this large potential window inorganic electrolytes are typically used which allow activation of the V^{2+} to V^{5+} oxidation states. Similarly to MnO_2, VO_x uses intercalation as its charge storage mechanism in the same form as (24) with M=V and A=Li or Na and $A_yV_2O_5$ materials are known as vanadium bronzes. VO_x has been shown to be an extrinsic pseudocapacitor where nanostructuring efforts or amorphous materials are required to achieve pseudocapacitance behavior.[67] Bulk VO_x compounds show multiple well defined voltage plateaus which have provided much interest for use in LIB cathode materials as well.[25]

The highest oxide containing VO_x phase is V_2O_5 (VO_x, x=2.5) with the α-V_2O_5 phase having the highest theoretical capacity of the VO_x family which can contain three Li^+ ions and reaches a rock salt (NaCl) structure upon complete lithiation to $Li_3V_2O_5$.[25] V_2O_5 forms a series of phases as lithiation progresses (α, ε, δ, γ, ω) with an irreversible transition from the initial layered oxide(α, ε, δ,- V_2O_5) to the rock salt structure(γ, ω-V_2O_5) occurring.[25] This NaCl structure is not suitable for pseudocapacitor applications as the lack of well-defined conduction pathways for the Li ions decreases the rate capability and provide large overpotentials upon delithiation.

The electronic conductivity of these materials are sometimes an issue and an increasing in oxygen deficiency during deposition has achieved resistivity values of 30 mΩ cm for x<0.8 however the stable VO_x phase at this composition has a NaCl crystal structure which is not conducive to Li^+ ion intercalation.[81,82] Other attempts to overcome the high resistivity have included the nanostructuring of VO_x materials to form nanowires, aerogels, and nanotubes however the resistivity of these materials remains greater than 20 Ω cm.[79,83] Further research has produced thin films of VO_x onto high surface area conductive carbons including carbide derived carbons (120 F g^{-1}),[84] CNTs

(300 F g^{-1}),[79] and carbon aerogels (2000 F g^{-1}).[80] Unfortunately like Mn, even trace amounts of acid have been shown to reduce the cycle life of VOx based pseudocapacitors due to vanadium dissolution.[85] Efforts to reduce this dissolution include the addition of gel polymer electrolytes and providing electrolyte additives which form passivating surface films however cycle life is still a concern for these material systems.

Organic Pseudocapacitors

Organic pseudocapacitor materials have been researched extensively due to the low materials and manufacturing costs compared with inorganic options. These organic options are typically composed of conductive polymers which have a large degree of π-conjugated bonds in the polymer backbone which allow easier electron transport through the π-electron mobility. This allows for the combination of chemical and mechanical properties of polymers with the electronic properties of metals or semi-conductors with a wide variety of resistivities available (10^{-5} to 10^{10} Ω cm).[3,86,87] These materials can be classified by the presence of different non-carbon heteroatoms in the backbone with the most popular being nitrogen and sulfur containing as well as the type of double bonds present including aromatic and linear bonds. The chemical structure of a selection of these polymers can be seen in Figure 15 such as polyacetylene (PA), polyaniline (PANI), polypyrrole (PPy), and polythiophene (PTh). Conductive polymers have become of high interest due to their chemical stability, corrosion resistance, low cost, and charge storage mechanisms due to reversible redox couples. In addition to their electrochemical activity these polymers can be chemically oxidized and reduced and are frequently doped in order to increase the electrical conductivity.

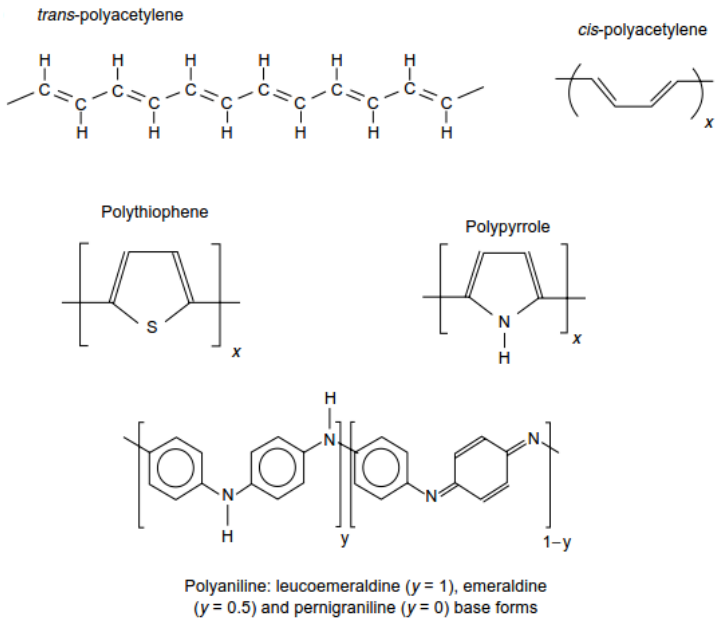

Figure 15. Chemical structures of selection of most popular conductive polymer species showing the linear and aromatic and S, N and heteroatom free varieties.[86]

Polyaniline is a nitrogen substituted cyclic conductive polymer which has been extensively studied due to its optical response, chemical stability, ease of formation, wide range of resistivity, low monomer costs, multiple oxidation states, and redox reversibility. Additionally the ability to both chemically or electrochemically polymerize this material under a wide array of ambient conditions provides a variety of synthesis methods for device creation.[88] While Figure 15 shows the polymers as one molecule, they all undergo a series of partial oxidation steps each of which induces a deprotonation. For PANI, the deprotonation occurs at the nitrogen containing group and the degree of oxidation is determined by the fraction of polymer which is oxidized (*y*) which subsequently leaves a fraction (*y*-1) unoxidized or in the reduced state. The fully protonated form is called the leucoemeraldine form which has all nitrogen groups as –NH- (*y*=1) and progresses continuously to the pernigraniline form which has all nitrogen groups dehydrated leaving –NH= groups (*y*=0) as shown in Figure 16. As the degree of conjugation changes during this process the electrical conductivity also changes with the pernigraniline form showing high resistivity which often results in electrical isolation and capacitance loss during

excessive oxidation. This limits the operational *y* that can be used with the intermediate emeraldine form (*y*=0.5) being commonly used due to its non-solubility and good electrical conductivity.

Conductivity in PANI is also dependent on the incorporation of anions, which are electrostatically attracted to the nitrogen groups with the anion free polyaniline form called bases and the anion containing form called salts. Anions are typically added through a doping process by addition of acids such as HCl, H_2SO_4, HNO_3, etc. and they can be removed by de-doping typically through the use of a base such as NH_3 as shown in Figure 16.[3] The size of these anions were found to have an impact on the polymer structure with small ions such as ClO_4^-, and BF_4^- showing a more compact structure during deposition. PANI can exhibit mechanical stresses due to the shrinking and swelling from anion incorporation during the redox cycling of the polymer which can cause degradation.[88] The emeraldine salt form is the most conductive of all polyaniline forms due to the formation of unpaired electrons at the nitrogen atoms in conjunction with cations. These cation electron pairs behave as polarons and allow increased conductivity by their increased mobility through the polymer backbone.[88] These polarons tend to move in pairs called bipolarons and require non-anion associated nitrogen groups to propagate thus explaining the low conductivity of the fully doped form of pernigraniline.[88]

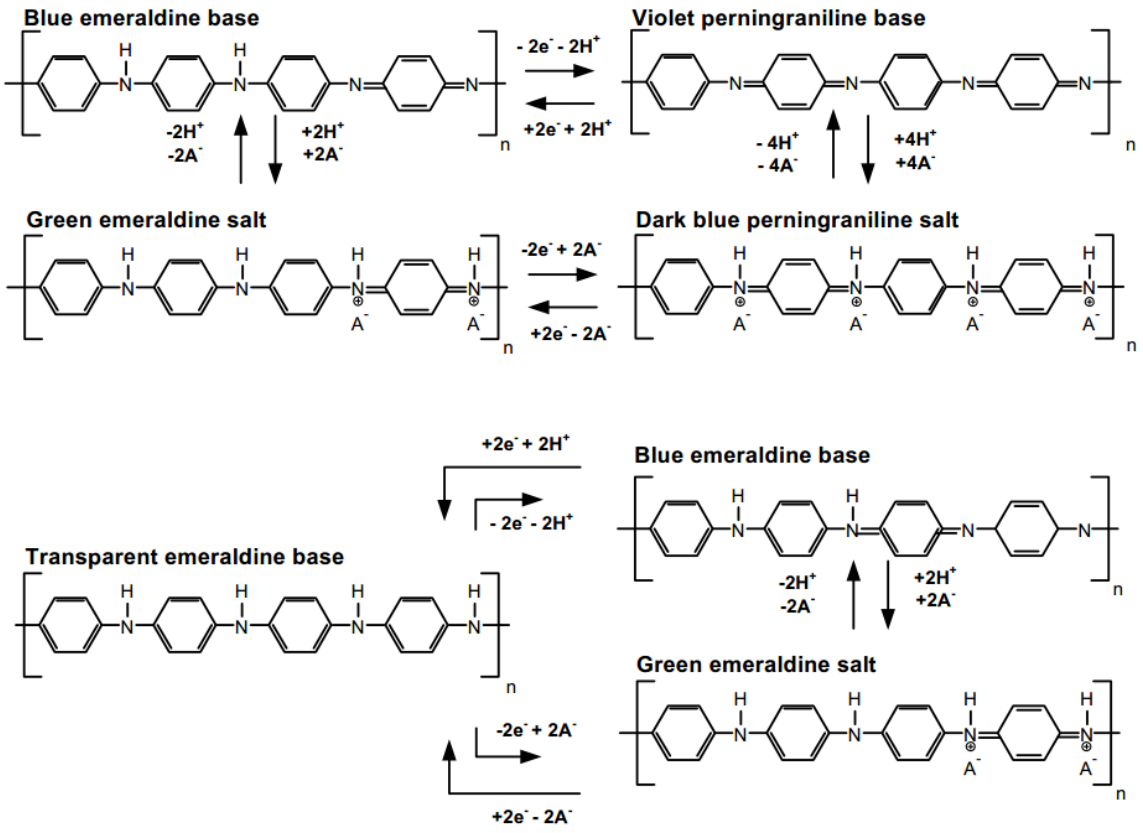

Figure 16. Different reaction pathways for the redox reactions of polyaniline and polyaniline salts and the corresponding optical colors of the different forms.[88]

2.3 Characterization Methods

X-Ray Diffraction

X-rays have been used for many years to study the crystal structure of solids due to the wavelength of the light having similar length scales as the interatomic distances commonly seen in crystalline solids. Because light can be explained as a wave property and X-rays interact strongly with the charged electron cloud in the atom causing scattering, the diffraction equations for constructive and destructive wave interactions can be applied to X-rays. The wavelength of electromagnetic radiation is related to the energy of the wave through the plank/de Broglie relationship. X-rays are typically generated by electron bombardment of a high Z transition metal target with good thermal stability such as Cu or Mo. These electron collisions generate a continuous range of white spectrum

radiation called continuous background which occurs from the deceleration of the electrons in the material. In addition to this broad spectrum radiation there is also a characteristic radiation which has sharp spikes at wavelengths corresponding to the core energy levels of the material being bombarded as shown in Figure 17. When an electron reverts to a lower energy state this causes the emission of a photon with the same energy as the difference in the electron energy levels. This is typically 1.54 Å for Cu $K\alpha_1$ or 0.709 Å for Mo $K\alpha_1$ X-ray sources.[89] Filters and monochrometers are often used to remove the unwanted wavelength of X-ray radiation and prevent multiple diffraction peaks from the same crystal plane.

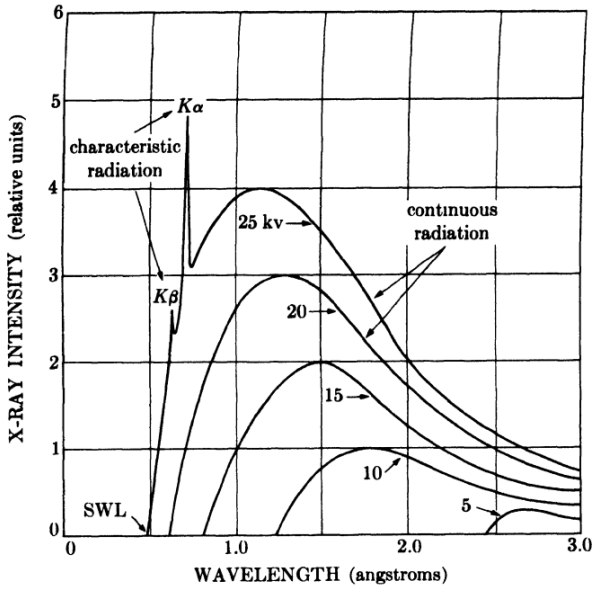

Figure 17. X-ray emission of a molybdenum target as a function of electron bombardment at a variety of accelerating voltages from 5-25 kV.[89]

A crystal lattice is a mathematical relationship which describes a repeating, volume filling pattern in space. These relationships can be defined with three vectors which describe the repeated translations required to generate the entire lattice and are typically described by three magnitudes (a, b, and c) with angles between them of (α, β, and γ). Bragg's Law was developed in 1913 to describe the path of a wave capable of

constructive/destructive interference (X-rays) through a set of periodically arranged scattering centers (the atoms in a crystal) and is seen below,

$$n\lambda = 2d_{hkl}\sin(\theta) \tag{25}$$

where $n\lambda$ is an integer multiple of the wavelength of light, d_{hkl} is the distance between the diffracting objects (crystal planes in the case of crystallography), and θ is half the angle between the diffracted and transmitted beam. Because the wavelength of X-rays are similar to the atomic distances common in crystalline materials the interplanar distance of crystalline materials can be measured by the geometry of the system during active diffraction. Because the values for d_{hkl} are fixed by the possible lattice positions for a certain crystal they can be used to identify crystalline phases by scanning θ for observable X-ray intensities and correlating diffracted intensities in a database or predicted via crystal symmetry. For large volume powder diffraction experiments the Bragg-Brentano geometry (θ-2θ) is often used as shown in Figure 18.

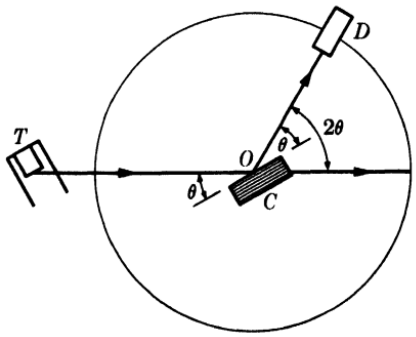

Figure 18. Bragg-Brentano geometry for a typical XRD experiment with the X-ray tube (T), crystal (C) located at the origin (O), diffracting towards the detector (D).[89]

In addition to the diffracting θ, the peak width is of interest for XRD analysis as this can be an indication of crystals of the same lattice type having slight variations in d-spacing. These variations result in a broadening in the observed peak with respect to 2θ periodic dislocations induced by a strained lattice (microstrain, ε), and crystal structure relaxation due to particle size reduction. Scherrer first modeled the effect of the crystallite

size and Williamson-Hall improved upon this model by including the effects of microstrain,[90]

$$B_{FWHM} * cos(\theta) = \frac{K\lambda}{d_\theta} + \varepsilon \sin(\theta) \quad (26)$$

where B_{FWHM} is the sample broadening measured from the full width of the peak of interest measured at half the total intensity in radian, K is a particle shape factor and is normally 0.9 for spherical particles, and d_θ is the crystallite particle size estimated by the diffraction planes of interest. This solution leads to a treatment which includes multiple diffraction line analysis and by the application of a linear regression to the plot of $B_{FWHM} * cos(\theta)$ *vs.* $\sin(\theta)$ the intercept can provide the average crystallite size and the slope, the microstrain.[90]

In the synthesis of crystalline nanomaterials it is often difficult to produce large enough volumes of material to avoid X-ray penetration to the substrate when measured using traditional θ-2θ geometries. This is due to the low absorption of X-rays by materials, with this problem being exacerbated upon analysis of low Z materials common in LIB such as C, Al, Si, Li, and oxides thereof with penetration depths on the order of 100 μm being typical. In order to reduce the information depth of the measured X-rays a technique called grazing incidence XRD (GIXRD) is performed where the incident angle (α) is chosen to be small (>5º) and constant and the 2θ of the detector is scanned as shown in Figure 19.[91] The penetration depth ($\tau_{1/e}$) is defined as the depth at which the X-rays lose 1/e=63% of their original intensity. For GIXRD this penetration depth is calculated as,

$$\tau_{1/e} = \frac{\sin \alpha}{\mu} \quad (27)$$

where μ is the linear attenuation coefficient and depends on the radiation used, the Z of the elements in the sample, and the density of the sample. These values can be found in reference tables and for composites or mixtures of materials accurate estimates can be calculated. For calculation of the mass absorption coefficient of a compound (μ_{comp}) a

weighted average of the individual mass absorption coefficients can be used with the coefficient for air being used for porous samples,

$$\mu_{comp} = \rho_{comp} \sum_{i=1}^{n} \left[\left(\frac{\mu}{\rho} \right)_i w_i \right] \tag{28}$$

where w_i is the weight fraction of material i in the compound containing n total materials.

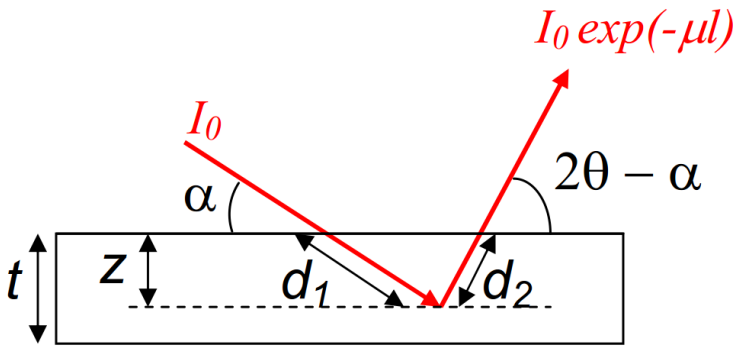

Figure 19. Schematic representation of the absorption effect for a thin film or information depth from angle resolved GA-XRD. This simplifies to the traditional θ-2θ geometry when α=θ.[92]

Electron Microscopy

Electron microscopy has long been a primary tool for investigating nanomaterial synthesis and behavior due to the wavelength of electrons allowing imaging below the resolution of light combined with their ease of manipulation through magnetic lenses and generation methods. Scanning electron microscope (SEM) and transmission electron microscopes (TEM) use a magnetically focused electron beam rastered across a material in order to image either the elastically scattered (backscattered) electrons or the secondary electrons which are generated with the primary beam collision (Figure 20). Electrons can be generated by many different techniques ranging from cold field emission, thermal field emission, and thermionic emission with cold field emission being primarily used due to its higher beam intensity, smaller probe size, and operational stability.[93] The first TEM was constructed in the 1930s and as the name suggests the

electrons used pass through the sample requiring careful sample preparation in order to thin the material and prevent total absorption of the electrons.[94]

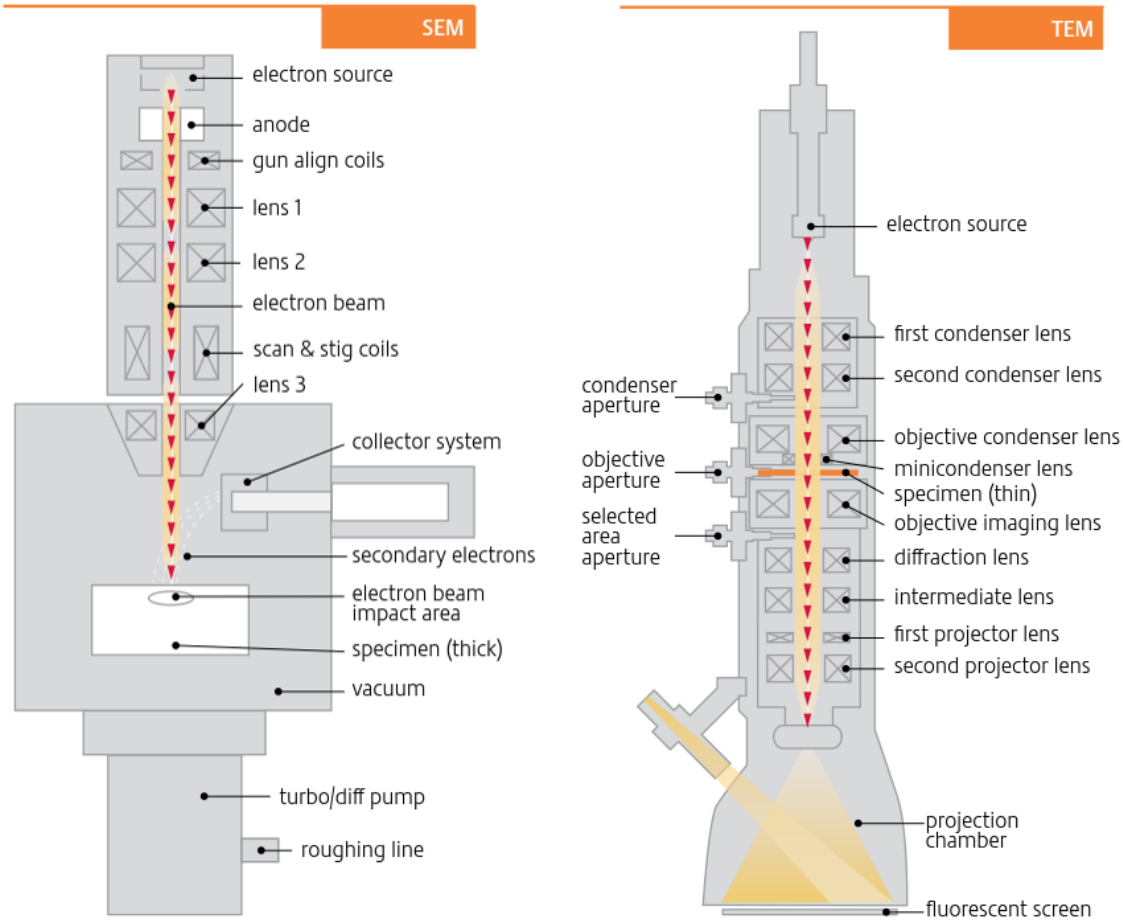

Figure 20. Comparison of the SEM and the TEM.[95]

Because both light and electrons behave as waves, it is not possible to focus them into a perfect dot. Instead concentric rings of constructive and destructive interference occur which prevents resolution between two points which are two wavelengths apart. This was first realized by Ernst Abbe and the maximum resolution in a perfect optical/electron imaging system is described mathematically as Abbe's equation,

$$d = \frac{0.612\lambda}{n \sin \alpha} \tag{29}$$

where d is the maximum resolution (minimum distance which two objects can be distinguished), λ is the wavelength of the probing wave (light or electromagnetic), n is

the index of refraction for the medium through which the wave must travel, and α is the half angle of the aperture. As shown here, assuming typical experimental conditions in a SEM with $n = 1$ for a perfect vacuum and a highly collimated electron source, $\sin(\alpha) \approx \alpha$. Because λ is related to the electron energy through the De Broglie relation which for an electron with non-relativistic speeds suggests $\lambda \propto KE^{-1/2}$ and that the maximum resolving power for a typical SEM increases as the electron energy increases. This principle explains the increased sub-nanometer resolution possible with 200-300 keV TEMs compared to the 1-30 keV SEM.

Another analysis method frequently used in conjunction with electron microscopy techniques makes use of the characteristic X-rays which are generated through energy level transitions in the core shell electrons generated by the primary electron beam. This occurs when the primary electron beam causes the ejection of an inner core shell electron upon which an electron from an outer shell (typically the K, L, or M shells) transitions to fill this vacancy emitting an X-ray in the process. This X-ray's energy is directly related to the energy difference of the electron orbitals involved. Energy dispersive X-ray spectroscopy (EDS) is performed by analyzing the energy of these characteristic X-rays and comparing the intensity to calibrated standards the atomic composition of a material can be determined. Because the characteristic X-rays require a minimum energy of incoming electrons to excite the core shell electrons, EDS analysis requires that the primary electron beam have an energy of typically 2-3 times the core shell transition energy.[93] Another complicating effect is the increasing electron beam interaction volume which occurs at higher operating voltages and the absorption of low energy X-rays produced at a deeper location inside the material of interest. This effect can be used to determine the approximate depth of certain layers in well controlled sample geometries with Monte Carlo simulation software such as CASINO or DTSA-II being freely available to assist in these calculations.

Constant Current Charge Discharge

Constant current charge discharge tests are the most basic electrochemical tests and are performed on battery materials and supercapacitors as they represent a good approximation to the performance achieved during device operation. The current and voltage profile *vs.* time for a typical battery during charge discharge testing is shown below in Figure 21a. By integrating the current with respect to time to obtain charge (Q=It for constant current experiments) the voltage *vs.* charge profile can be created as shown in Figure 21b. This type of plot shows clearly the electrochemical potential of the primary energy storage mechanisms (E_o), the irreversible capacity losses (ΔQ_{loss}) occurred during electrochemical cycling, and the electrode polarization (η) which occurs due to non-equilibrium concentration variations as well as other mass transfer related components. This voltage *vs.* capacity plot is also used to calculate the energy density ($U = \int EdQ$) of the cell.

In order to allow accurate comparison between cells of different sizes, specific current (i) is often used (A/g and A/cm^2). The total current (I) can also be represented by the C-rate which is the time it takes (h) to charge or discharge a given capacity rated battery (C_{bat}) at that current.

$$h = \frac{C_{bat}}{I} = \frac{1}{C_{rate}} \tag{30}$$

For example, a 1C rate means that the discharge current will discharge the entire battery in 1 h and similarly a 0.5C rate suggests a 2 h charge/discharge. Figure 21c shows a rate capability study, where multiple charge-discharge cycles are analyzed for cell capacity and plotted *vs.* cycle number. Further insight into the rate capability of the cells can be gained by performing multiple cycles at a variety of C-rates as shown in Figure 21c. In this particular example a cycle stability test can also be performed by looking at the slope of the capacity *vs.* cycle curve (fading rate) during the repeated 0.5C rate cycling to determine the percent degradation per cycle.

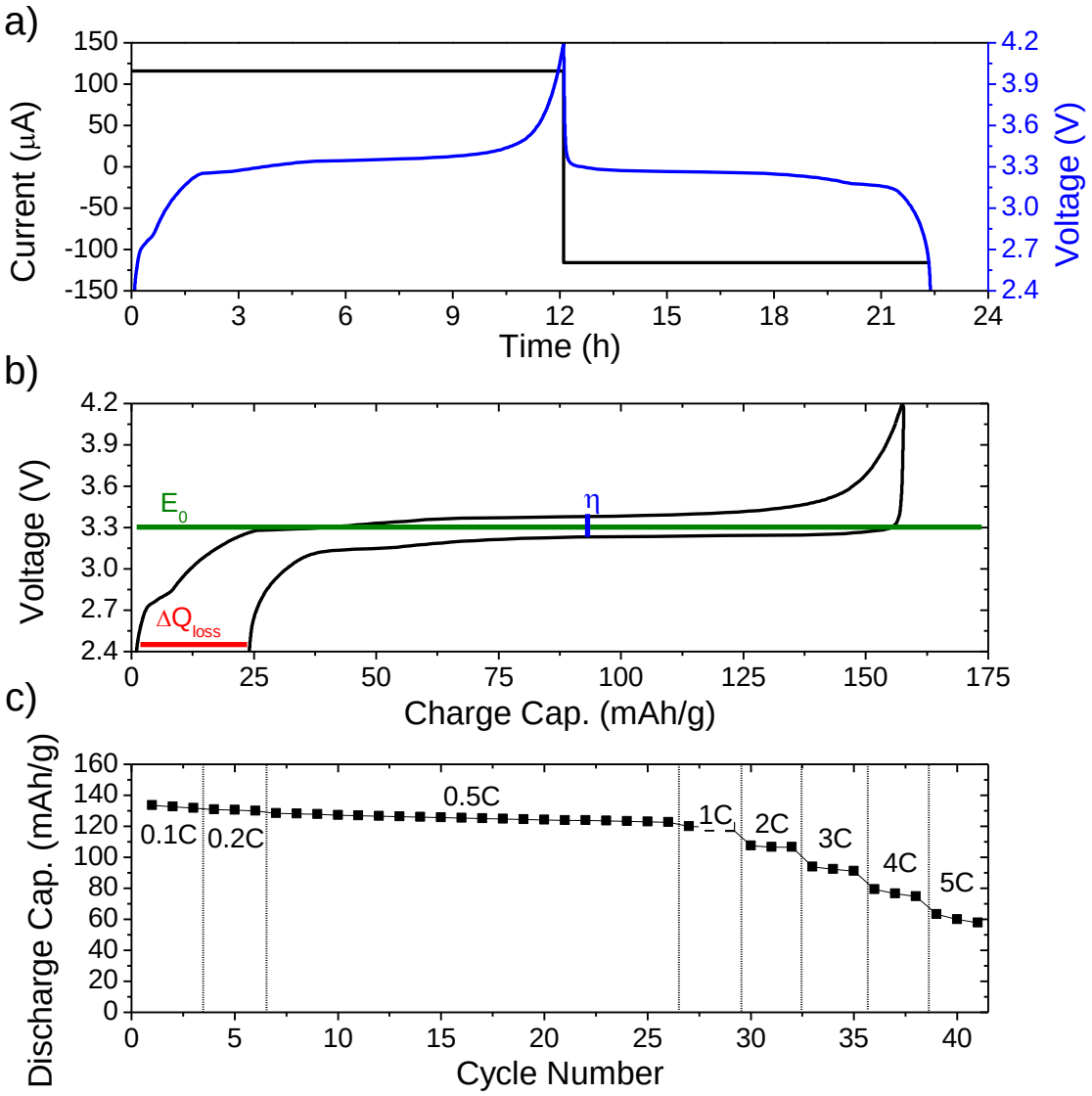

Figure 21. Typical 1st cycle of a constant current charge-discharge experiment performed on a LFP-graphite based lithium ion battery, a) the current and voltage profile *vs.* time, b) the same cycle presented as voltage *vs.* specific capacity, c) the same battery material tested for multiple cycles and at different constant current values denoted by the C-rates 0.1-5C.

Cyclic Voltammetry

Cyclic voltammetry (CV) is used to study the fundamentals of electrochemical reactions by determining the reaction potential. This technique utilizes a potentiostat to apply a non-constant voltage waveform, which is described by,

$$E = E_i + vt \tag{31}$$

Where E is the applied potential [V], E_i is the initial starting potential [V], v is the scan rate [mV/s], and t is the experiment time in [s]. Once the final potential is reached, the linear sweep is reversed by changing the sign of the scan rate. Multiple cycles may be repeated to study electrochemical stability or establish reproducible results. Potential scan windows depend on the electrolyte and materials electrochemical stability window with aqueous electrolyte based experiments ranging from -0.4-0.8 V *vs.* SHE and organic electrolytes in LIB systems ranging from 0-5 V *vs.* Li/Li^+. Scan rates also vary based on the mechanism of interest with liquid state redox reactions occurring much faster than many solid state Li diffusion/intercalation processes and a large range of scan rates may be needed to fully characterize a new system with rates as high as 2000 mV s^{-1} for fast reactions. Slow electrochemical reactions in solids may be studied with scan rates around 1 μV s^{-1} however for liquid analysis care must be taken that natural convection does not interfere the double layer composition during the measurement.

A potential waveform generated from this method using a 10 mV/s scan and a scan window from -0.75 V to 0.75 V is shown in Figure 22a. The “duck shaped” feature of this figure is characteristic of a reversible faradaic reaction where the current is low below the voltage required to initiate the faradaic reaction of interest. By increasing the over potential past this point the reaction rate increases rapidly and the resulting current increases to a maximum called the peak current. Further increase in voltage consumes all of the available reactants and the reaction becomes concentration limited by the rate of diffusion of new species through the surface boundary layer leading to a decline in current. This process is then repeated in the opposite direction during the reverse sweep producing a symmetric plot for a reversible reaction.

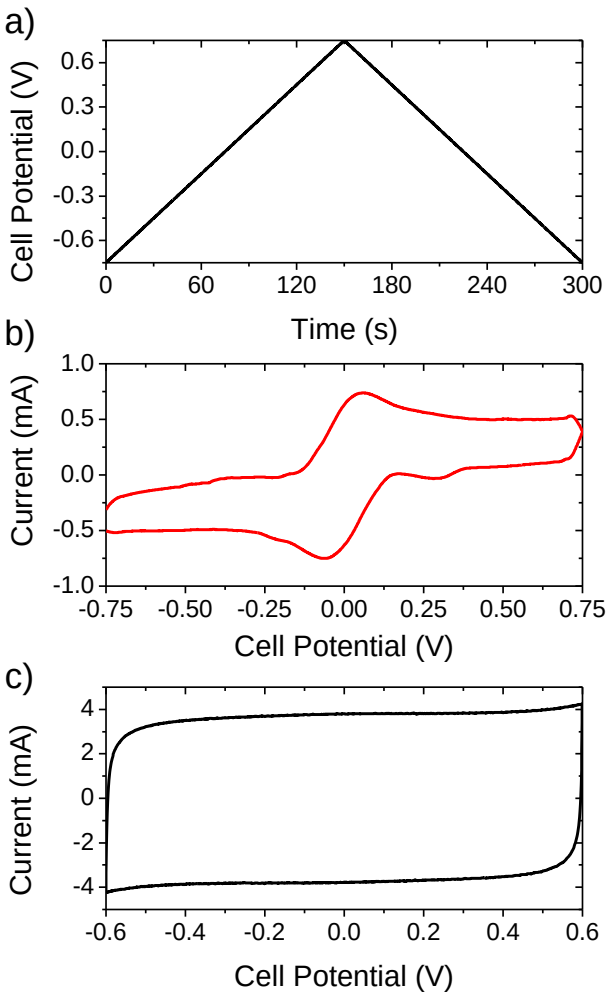

Figure 22. Examples of typical cyclic voltametry experiments demonstrating a) the voltage *vs.* time profile of an experiment using a scan rate of 10 mV/s and a voltage window of ±0.75 V. The resulting current *vs.* voltage profile of a symetric cell showing, b) reversible faradaic reaction, and c) the electrostatic energy storage commonly observed in capacitor materials.

When the potential applied provides enough free energy for a faradaic/redox reaction, such as described in (1) or (2) to occur, the concentration of reactants and products changes as a function of time. In 1964 Nicholson and Shain derived the relation between current with respect to potential during CV experiments for a variety of electrochemical reactions, including reversible, irreversible redox reactions, and coupled chemical reactions.[96] The two most studied for battery and pseudocapacitor research are the reversible reaction (32) and the irreversible reaction (33). The reversible case is

required for the charge storage mechanism in a high cycle stability battery and irreversible reactions for battery degradation mechanisms.

$$Ox + ne^- \rightleftarrows Red \tag{32}$$

$$Ox + ne^- \overset{k}{\rightarrow} Red \tag{33}$$

The current voltage relationship are shown below for reversible i_{rev} and irreversible currents i_{irev} ,

$$i_{rev} = n^{3/2}F^{3/2}AC_o\sqrt{\frac{\pi D_o v}{RT}}\chi(at) \tag{34}$$

$$i_{irev} = nF^{3/2}AC_o\sqrt{\frac{\pi \alpha_a D_o v}{RT}}\chi(bt) \tag{35}$$

with n being the number of electrons transferred per electrochemical equivalent, A being the electrode surface area, C_o and D_o being the bulk concentration and diffusion coefficient of the Ox species, v being the scan rate during CV, α_a being the anodic charge transfer coefficient, and $\chi(at)$ and $\chi(bt)$ being unitless, tabulated values which can be looked up in the literature. [13,96]

In the absence of a faradaic reaction, which is the case for EDLCs, the system is modeled as a resistor and capacitor in parallel (RC circuit) and the typical current voltage response is shown in Figure 22c. Based on this model, the current response is calculated by adding the charge *vs.* voltage response of the capacitor ($q = C_d E_c$) and resistor ($E_R = R(dq/dt)$). The assumption that q=0 at t=0 coupled with this model yields:

$$i = vC_d - vC_d e^{-t/(RC_d)} \tag{36}$$

Where I is the current (A), v is the scan rate (V/s), and C_d and R are the capacitance and resistance of the equivalent circuit model. When the capacitor reaches steady state during the CV experiment (t>>0) and $i = vC_d$. This provides a simple method of determining the capacitance of a non-faradaic ECSD and works well for an ideal electrochemical double layer capacitor.

For non-ideal capacitors or pseudocapacitors, C_d may change as a function of applied voltage. This is the case with pore or ion size effects or for capacitors which have faradaic components. In order to provide a reproducible measurement of capacitance for these systems an average current ($\bar{I}$) for one cycle is used to calculate an average value of C_d from the CV experiment.

$$C_d = \frac{1}{v}\bar{I} = \frac{1}{v}\frac{\int_{V_i}^{V_f} IdV + \int_{V_f}^{V_i} IdV}{2(V_f - V_i)} \tag{37}$$

CV tests are performed in a symmetric cell configuration, where the anode and cathode are composed of the same electrode with the same mass and the same anodic and cathodic capacitance. Additionally, normalization by mass is done for more accurate comparison to other systems. Then using the mass of one electrode (m_{elec}) to provide the specific capacity yields:

$$C_{elec} = \frac{1}{v}\frac{\int_{V_i}^{V_f} IdV + \int_{V_f}^{V_i} IdV}{m_{elec}(V_f - V_i)} \tag{38}$$

To study the mass transfer effects on energy storage in supercapacitors, the average capacitance is plotted as a function of scan rate over several orders of magnitude.

Electrochemical Impedance Spectroscopy

Electrochemical impedance spectroscopy (EIS) is an electrochemical analysis method, which utilizes small sinusoidal signals for analysis. Previously described electrochemical analysis methods make use of large perturbations of the cell which result in a wide range of applied/resulting voltage. EIS avoids these large voltage changes in the system by applying an alternating voltage of small magnitude. This has some advantages as the experiment's response is steady over time thus allowing high-precision measurements and averaging. Additionally knowledge of the cell response over a wide overpotential range is not necessary for extracting many useful cell performance

parameters such as solution resistance. Such an AC voltage signal (V(t)) can be expressed as follows in equation (39) and is illustrated in Figure 23,

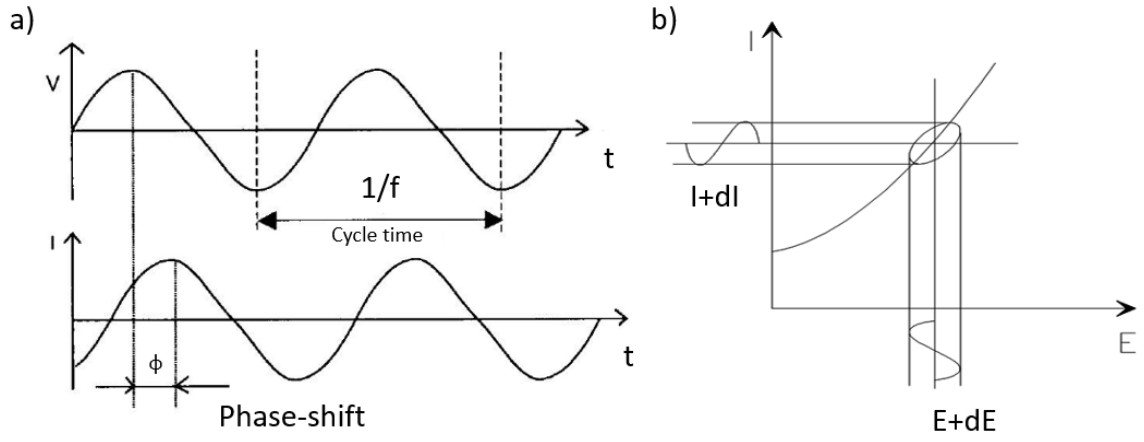

Figure 23. The current response to an applied AC voltage signal of frequency *f* and the resulting phase shift referenced to the voltage signal used in EIS experiments a) with respect to time, and b) with respect to applied voltage.[87]

$$V(t) = V_A \sin(\omega t) = V_A e^{j\omega t} \tag{39}$$

where V_A is the voltage amplitude (typically 10 mV), t is time, ω is the radial frequency which is related to the AC frequency f as ω=2πf, and j is the imaginary number $\sqrt{-1}$. This expression is often written in the exponential form using Euler's relationship for complex analysis. Similar relationships for the current response, I(t), can be expressed including a phase shift component (ϕ) to account for different system behaviors,

$$I(t) = I_A \sin(\omega t + \phi) = I_A e^{j\omega t - j\phi} \tag{40}$$

The impedance (Z) of a linear electrical system is analogous to the complex statement of Ohm's Law and can be reported as the ratio of V(t) to I(t) as shown below.

$$Z^* = \frac{V(t)}{I(t)} = Z_A e^{j\phi} = Z_A\big(\cos\phi + jsin(\phi)\big) = Z' - jZ'' \tag{41}$$

Where Z' is the real component of impedance also known as resistance and Z'' is the imaginary component of impedance also known as reactance. The form of equation (66) suggests the two common methods of presenting impedance data with the Nyquist plot (Z'' *vs.* Z') and the Bode plot ($\log(Z_A)$ *vs.* $\log(\omega)$).

EIS applies a sinusoidal voltage waveform and measures the current response over a range of frequencies. Because the different electrical responses occur at different frequencies (dipole interactions at high frequency, bulk properties at intermediate frequencies, and surface and mass transport properties at low frequencies)[87] the frequency response of a system can provide information on all of these aspects in one experiment. This allows for the study of the total impedance of the cell and, by developing model equivalent circuits, a better understanding of the electrochemical responses can be developed. By comparing the magnitude of the response and the phase shift of the resulting current, the electrical response of an ECSD can be measured and values of resistance and capacitance can be obtained.

As in many fields of science there are many approaches to interpreting collected EIS data and attempts to develop accurate models to predict experimental behavior have been frequent. The mathematical basis for analyzing the results of EIS were first developed by Heaviside between 1880-1900 which Dolin and Ershler[97] and Randles[98] used to develop equivalent electrical circuit (EEC) analysis methods. The most basic of these models includes a resistor and capacitor in series (Figure 24a) which can be used to describe a planar electrochemical double layer capacitor with no faradaic reactions (pseudocapacitance) and no mass transport limitations.[99] This includes the solution resistance (R_s) and the double layer capacitance (C_{dl}) and leads to an impedance described by,

$$Z = R_s + \frac{1}{jC_{dl}\omega} \tag{42}$$

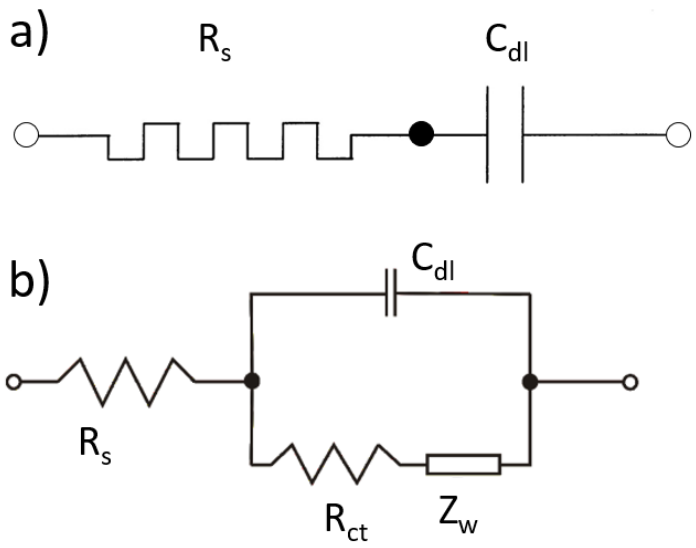

Figure 24. Equivalent electrical circuits commonly used to model a) basic supercapacitor behavior, and b) complex faradaic reactions including battery and pseudocapacitor behavior.[99,100]

The Randles equivalent circuit, shown in Figure 24b, has been widely used in EIS EEC analysis for modeling faradaic reactions with fast charge transfer kinetics on a planar electrode. R_s is the solution resistance and depends on the electrode separation, ionic concentration and conductivity, and temperature. R_{ct} is described as the charge transfer resistance and is determined by the reaction kinetics. C_{dl} is the double layer capacitance. The Randles circuit also includes an element developed in 1899 by Warburg to address the mass transport/diffusional aspect of these reactions called the Warburg impedance element (Z_w),

$$Z_w = \left(\frac{2}{\omega}\right)^{1/2} \sigma \tag{43}$$

Where σ is the Warburg coefficient which includes contributions of diffusion of the oxidation species and the reduction species as described below,[101]

$$\sigma = 2^{-\frac{1}{2}} R_{ct} \left(\frac{k_{ox}}{D_O^{\frac{1}{2}}} + \frac{k_{red}}{D_R^{\frac{1}{2}}} \right) \tag{44}$$

With k_{ox} and k_{red} being the forward and backwards kinetic rate of the redox reaction and D_O and D_R being the diffusion coefficients for the oxidized and reduced reactants. While

components such as resistors and capacitors are familiar, the Warburg element has no physical analog and is instead represented by a semi-infinite resistive-capacitive transmission line with a series resistance per unit length and a shunt capacity per unit length.[101]

Figure 25 shows a representative faradaic reaction predicted by a Randles circuit as represented in a Nyquist plot of the real and imaginary impedance contributions. At high frequencies the resistance contributions due to the solution (R_s) are easily seen with the kinetically controlled semicircle (R_{ct}) being observed at more moderate frequencies. At lower frequencies the diffusion of ionic species is observed through the straight 45° line commonly described as the Warburg tail.[100]

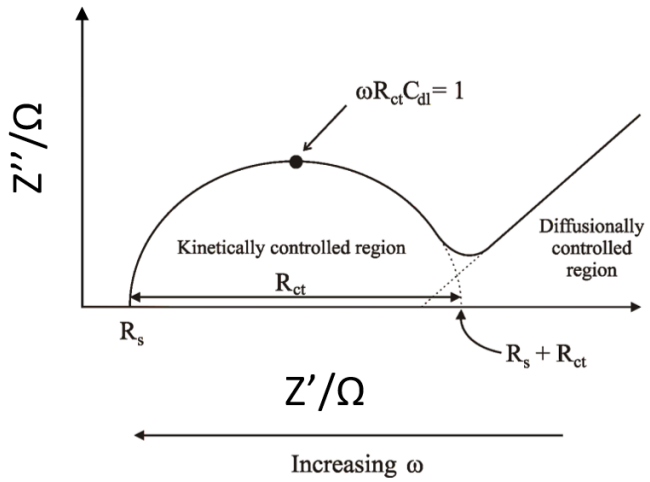

Figure 25. The idealized response of a Randle equivalent circuit commonly used to evaluate electrochemical impedance response of ECSDs.[100]

It must be mentioned that due to the ease of which models can be developed using EECs, care must be taken to minimize the number of elements used to match the data to avoid large standard errors in the models.[101,102] In fact, there are an infinite possible arrangement of EEC which can provide the same impedance output, thus care should be taken to use models based on physical analogs and not simply good fit to the data. One method commonly used to evaluate the validity of the suggested EEC is the application of a Kramers-Kronig transformation, which requires that the impedance be finite-valued

for ω approaching zero and infinity, and the impedance must be continuous and finite valued function.[103] The present day application of Kramers-Kronig transformations is commonly provided in software through complex nonlinear least squares (CNLS) analysis programs such as ZView, Gamry Echem Analyst, and EQUIVALENT CIRCUIT and the mathematical details are widely available in the literature.[101-103]

Four Point Probe Resistivity

Electrical resistivity (ρ) is a material property which describes the resistance of electrons to flow under an applied electrical field and ranges from 10^{-8} to 10^{16} Ω cm for a variety of materials.[104] It can be described in the form of Ohm's law,

$$\rho = \frac{E}{J} \tag{45}$$

where E is the electric field (V cm^{-1}), and J is the current density (A cm^{-2}). The relationship between resistivity and resistance requires a definition of the plane of current flow and the sample size,

$$R = \frac{\rho L}{A} \tag{46}$$

where R is the measured resistance in the plane of the current flow, ρ is the bulk resistivity, L is the length of the electron path, and A is the area perpendicular to the current flow. While ρ is a material property and sample geometry independent other measures of resistance are often used for the characterization of films and foils and change based on the sample geometry. The sheet resistance, R_{sheet} (Ω sq^{-1}, or Ω/□) is often used as a process control parameter and describes the resistance of electron motion in the plane of the film (not perpendicular to the film),

$$R_{sheet} = \frac{\rho}{t} \tag{47}$$

where t is the thickness of the film or electrode being measured in cm. This results in decreased sheet resistance with increased film thickness for the same material as expected from an analogy with a wire diameter. R_{sheet} is reported in units of Ω sq^{-1} to

avoid confusion with simple sample resistance R. Values of R_{sheet} for CNT films have been produced with R_{sheet} of 5-10 Ω sq^{-1}.[105]

Four point probe was first developed in 1915 by Wenner to measure the resistivity of the earth by soil resistivity measurements.[106] The accurate measurement of a high resistance sample was difficult using a two probe approach as the variable contact resistance would cause current dependent measurement errors. Four point measurements eliminate this issue as the current is passed with the outer probes and the voltage is measured through a high impedance probe anywhere within the current flow region. The first paper describing the four point probe method for use in semiconductors was by Valdes for analyzing germanium for transistors in 1954 and the technique has been widely used since.[107]

A commercially available four point probe station is shown in Figure 26a with the linear probe arrangement, current flow, and voltage measurement position shown in Figure 26c.[106] While it is not necessary to have a linear arrangement or equally spaced probes this configuration greatly simplifies manufacturing as well as mathematics during analysis. In order to insure repeatable measurements the probe tip spacing (s), and tip radius are carefully controlled. The probes are also typically on a controlled force spring to prevent damage to the sample surface and the probe tips themselves. The tip spacing should be selected in relation to the sample geometry and for energy storage materials such as electrodes and current collectors the analysis will likely be performed on films of thickness t, and for $t < s/5$ the measurement errors will be ~1%.[106] A typical probe spacing is 1 mm which means samples on the order of 200 μm can be tested while remaining in thin film geometry.

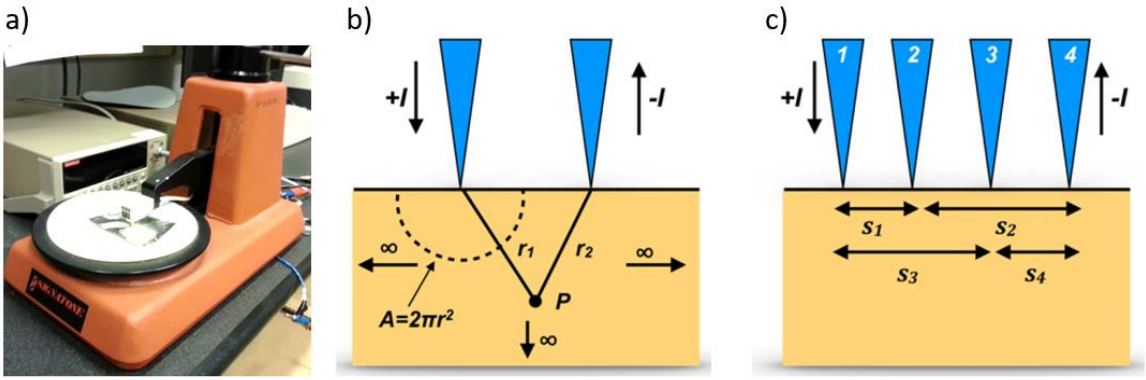

Figure 26. Four point probe details with a) showing a commercially available four point probe station. Schematics of b) a two point probe measurement and c) a linear four point probe array with equal tip spacing.[106]

As described above, measurements are performed by applying a current I to probes 1 and 4, and measuring voltage ΔV between 2 and 3. For a thin film geometry with $t < s/5$ the relationship between ΔV / I and resistivity are,[108]

$$\rho = \frac{\pi}{\ln 2} t \frac{\Delta V}{I}; R_{sheet} = \frac{\pi}{\ln 2} \frac{\Delta V}{I} \quad (48)$$

Interestingly, this result is independent of probe spacing (s). Commonly this measurement would be repeated over a range of I-V measurements to ensure reliable results. Common measurement errors include poor contact leading to Schottky contact behavior, high currents leading to heating and resistance drift, and carrier injection through light interactions or high electric field between the inner probes (<25 mV).

Additionally, resistivity can be an anisotropic value even though it is a bulk material property. This can occur due to crystal symmetries and is true for bulk graphite with the resistivity through the plane compared to in the plane being lower.[33] While CNTs also exhibit this anisotropy, typical bulk measurements are performed on non-woven unaligned CNT fabric which will have isotropic properties due to particle averaging effects. This also causes the measured resistivities on the bulk CNT fabric to differ significantly from the values of the individual CNTs.[33,106]

Mechanical Measurements

The measurement of the mechanical properties of electrochemical devices is not as developed as for other material systems. This is due to the inherently low strength requirements and low mechanical stresses that energy storage cells are generally exposed. With the increasing introduction of battery packs into electric vehicles and with some systems even being built into the structural frame of the car, the mechanical properties of these ECSDs will proportionally become important. The mechanical properties of most interest include the young's modulus (E), yield strength (σ_y), ultimate tensile strength (σ_{UTS}), elongation at failure (ε_f), and poison's ratio (ν_{xy}). The most commonly used test method for acquiring these values is the tensile test where a sample of known geometry (cross sectional area, A) is applied with a controlled load (F) and the resulting displacement (Δl) is measured. For materials such as metals with low degree of strain before plastic deformation occurs the yield strength is commonly defined as the stress observed using a 0.2% offset, while for materials with higher degrees of elongation Young's modulus is measured through the linear region of the stress strain curve during the tensile measurements. For materials such as polymers or non-woven fabrics which do not have a well-defined linear stress strain response region the instantaneous slope may be used.[109] It must be noted that the Young's modulus is different than the general elastic modulus tensor and is described as follows,

$$E = \frac{\sigma}{(\Delta l/l)} \tag{49}$$

Tensile Test Methods

Composite electrodes produced from 1D materials are effectively composite fabrics and as such there are many possible types of tensile tests and different specimen preparations which can be employed many which differ from bulk material preparation for metals or ceramics. The most common include a strip test and a grab test both which utilize a tensile test frame. A strip test uses a specimen where the grip size is larger than

the sample width and a grab test where the sample size is larger than the grip size as shown in Figure 27.[110] These test methods have been used extensively in textile characterization and standard test methods have been developed for each with the strip test being described by ASTM D5035 and the grab test being described by ASTM D5034.

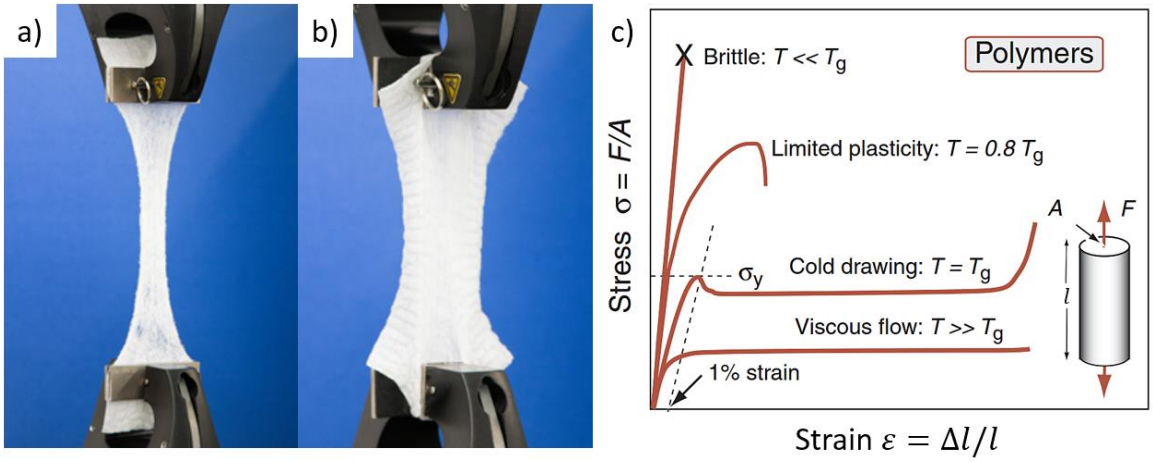

Figure 27. Tensile test geometry for non-woven fabrics using a) cut strip sample and b) grab test showing the beginning of out of plane buckling at high elongation.[111] c) Schematic tensile tests of polymer samples showing different failure modes with respect to temperature.[109]

Modulus of toughness is a value that is used to estimate the damage tolerance of a composite. This value is measured in J m^{-3} and is easily measured by integrating the area under a standard tensile test stress-strain curve and represents the sum of the energies consumed by various microfailure processes, namely, fiber fracture, matrix cracking or yielding, debonding, and fiber pullout.[112]

Each of these methods has its advantages and drawbacks which make test selection important for accurate measurement of a specific material. Investigations have been performed to compare these methods and allow comparison of these different tests via empirical and theoretical approaches. Grab tests have been shown to provide tensile test measurements which are higher than strip specimens due to the mechanical contributions which occur outside of the gripped area.[113] Grab tests are also not suitable

for fabrics made of brittle fibers such as glass fiber mats. Further for samples which exhibit elongation at failure greater than 11% out of plane fabric buckling can distort results which excludes many polymer based non-wovens and CNT composites.[110] This makes cut strip tests more suitable for CNT composite based electrodes which tend to be non-woven fabrics with high elongation.

For most nanowire based non-woven fabrics the orientation of the fibers can be approximated as random due to the solution/fluid based laying process. When a non-woven material is placed under load the material response is similar to the polymer case described in Figure 27c. It first strains linearly with respect to the stress in the linear elastic region. After this region a non-linear yielding of the curve is observed which may plateau or decrease until failure is observed. In some cases an increase in observed stress occurs immediately before fabric failure. This plateau behavior is different to that expected from a bulk material and has been shown through SEM failure analysis to be caused by fiber alignment followed by pullout and for nanowires slippage between wires aligned in a bundle. The strengthening behavior observed close to failure occurs after fiber realignment has completed and the increased fiber fraction which has been aligned parallel to the tensile stress causes strengthening.

Sample dimensions are determined by the degree of accuracy of testing needed with reproducible sample preparation. ASTM specifications recommend sample dimensions exceed 100 mm x 5 mm for cut strip samples with large elongations. This ensures suitable parallel edges and reproducible sample width area for stress calculations. Sample edges should be inspected to avoid tears and samples which fail at the grips should be discarded.

Dynamic Mechanical Analysis

As in many fields additional data can be acquired through the use of a sinusoidal waveform to study the dynamic properties of a system and this is also true for the

mechanical properties. This is particularly useful for the study of materials which are not strictly viscoelastic and show flow behavior in addition to the stiffness which is commonly studied using tensile test methods. During the 70's several companies produced commercially available dynamic mechanical analyzers (DMA) for the thermal and rheological fields which helped propel the use of DMA for material characterization.[114] DMA applies a sinusoidal force using a load cell and measures the resulting displacement using a linear variable differential transformer (LDVT) as shown in Figure 28a.

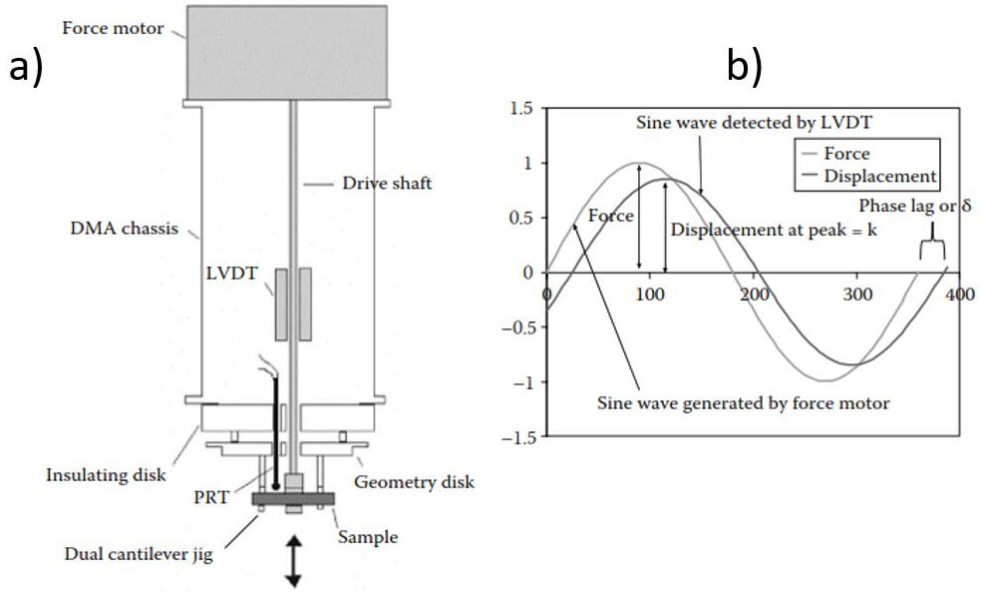

Figure 28. Skematic of a PerkinElmber DMA8000 dynamic mechanical analyzer (DMA) with a) showing the sample geometry and fixture in bending mode with the resulting oscillation indicated by arrows and b) showing the applied force and resulting displacement and phase lag.[114]

The sinusoidal stress which is applied is typically small in order to maintain a linear viscoelastic response. Resulting strains of 0.5% are commonly used. The stress waveform can be defined as,

$$\sigma(t) = \sigma_o \sin(\omega t) \tag{50}$$

where σ_o is the stress amplitude, ω is the radial frequency of the applied force, and t is time. This applied stress induces a time dependent strain function which can either be in phase or out of phase (Figure 28b) as described below,

$$\varepsilon(t) = \varepsilon_o \sin(\omega t + \delta) \tag{51}$$

where ε_o is the amplitude of the resulting strain response and δ is the phase angle/lag in radians between the stress and the strain signal. By applying Euler's law this expression can also be formed into a complex equation as described below,

$$\varepsilon^* = \varepsilon' + i\varepsilon'' = \varepsilon_o \sin(\delta) + i\varepsilon_o \cos(\delta) \tag{52}$$

where ε' is the real strain component and is related to the storage of energy and ε'' is the imaginary strain component and is related to the loss of energy and *i* is the imaginary number. These definitions can be combined to provide a real and complex modulus also called the storage modulus (E') and loss modulus (E'') respectively.

$$E' = \frac{\sigma_o}{\varepsilon_o}\cos(\delta)\,; E'' = \frac{\sigma_o}{\varepsilon_o}\sin(\delta) \tag{53}$$

The storage modulus E' (also called the elastic modulus or real modulus) is similar to the Young's modulus previously described however differences are often observed as Young's modulus is measured over a linear region with the storage modulus being measured only at a single point. The loss modulus E'' is often associated with internal friction and is used to study molecular motion and relaxation processes in polymers as well as phase transitions and other structural heterogeneities.

In many instances the tangent of the phase angle, tan(δ), is of interest as it provides a sample geometry independent correlation between the storage and loss modulus as shown below,

$$\tan\delta = \frac{\sin(\delta)}{\cos(\delta)} = \frac{\varepsilon'}{\varepsilon''} = \frac{E'}{E''} \tag{54}$$

DMA experiments are typically run at 1 Hz and measurements of modulus can be performed every complete sine wave thus allowing for rapid data acquisition and

averaging to increase measurement reproducibility. This rapid measurement capability allows for measurements to be performed while changing the temperature of the system and is sometimes called thermomechanical analysis (TMA) or dynamic thermomechanical analysis (DTMA). This method is used frequently in the polymer field to help identify different mechanical strengthening mechanisms, glass transition and other phase transition temperatures as shown in Figure 29. Because these phase transitions mark a change in the viscoelastic properties of the materials, they often show clearly in a tan δ *vs.* temperature plot. In the case below, a 50 ºC temperature phase change is observed, which is attributed to a β transition temperature often confused with the evaporation of small amounts of moisture. This is followed by a large change in all properties at ~220 ºC, which is a clear indication of the glass transition temperature followed by an increase in storage modulus due to the onset of oxidation and carbonization above 350 ºC in air.[115]

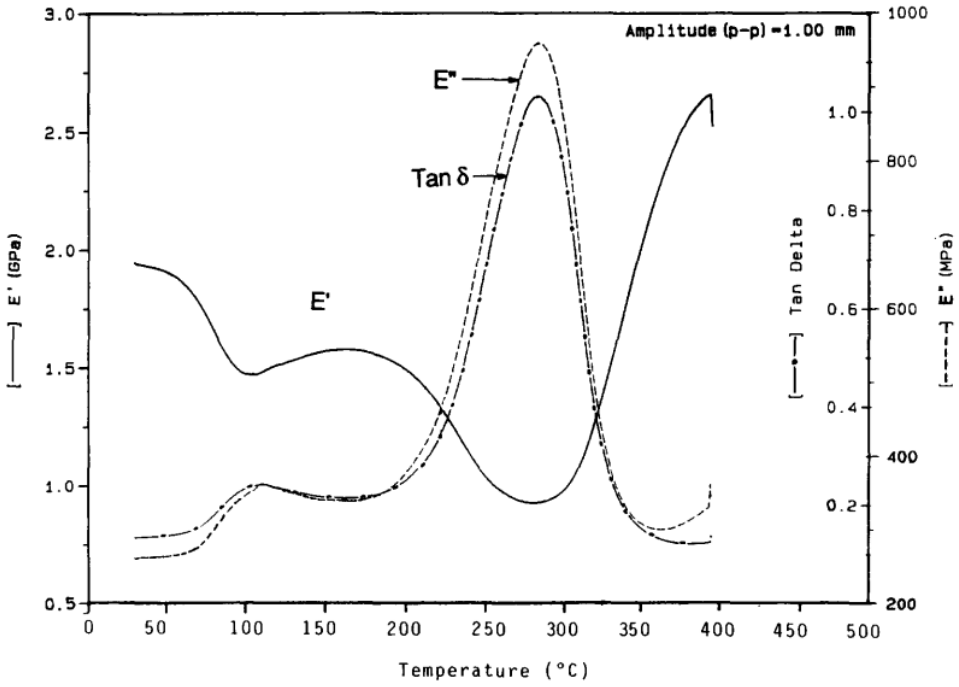

Figure 29. DMA results of a constant stress amplitude test of NMP-free 30 μm thick polyaniline film from 25-400 ºC with a heating rate of 5 ºC min^{-1}.[115]

2.4 1D Nanomaterial Synthesis Techniques

1D nanomaterials have become an important area of research for many years with the number of types of materials and synthesis methods explored increasing every year. Nanomaterials in this classification are high aspect ratio wire-like or tube-like structures with dimensions less than 100 nm in at least one dimension. Many of these same methods are also commonly used for thin film processing however the conditions required to produce a higher surface area nanomaterial are quite different. For 1D nanomaterials to have wide practical applications many areas of research still need to be addressed.

Three main synthesis approaches have been investigated for the growth of 1D nanomaterials, all which require the facilitation of anisotropic growth to prevent 2D film formation. The first is the natural crystallographic growth of solid materials such as exhibited by many naturally forming materials such as kaolinite, brucite etc. asymmetrically along the c-axis. Template-controlled growth is also commonly used with both hard and soft materials. Finally kinetically controlled growth is used with supersaturation, catalysts, or an appropriate capping agent.[116] These processes can also be further classified by the environmental conditions required for synthesis with the temperature and pressure dictating much of the growth mechanisms possible as shown in Figure 30. While ambient temperatures and pressures are generally preferred due to the lower cost and increased safety, much 1D nanomaterial synthesis occurs outside of these parameters.

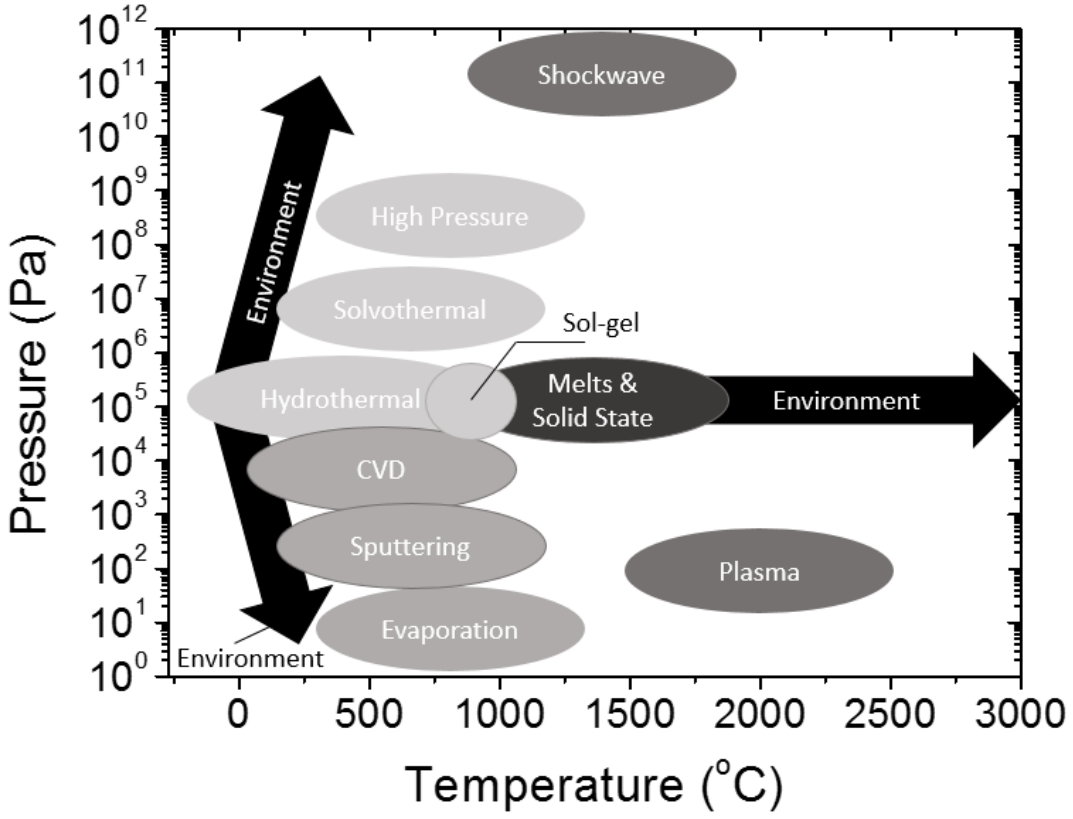

Figure 30. Comparison of the typical pressure and temperature required for different processing methods.[117]

Vapor Deposition Methods

The two most popular vapor deposition methods are physical vapor deposition (PVD) and chemical vapor deposition (CVD). Both are compatible with a wide range of materials used for energy storage applications, as well as 1D material synthesis. PVD involves the transfer of atoms from a source to a substrate using physical processes such as thermal energy (evaporation) or through impact via gaseous ions (sputtering). The substrates used for PVD are maintained at room temperature to coat a large range of materials, which is the case with metallization of polymers. PVD may be done by heating a metal to form a vapor and directing the metallic vapors to a low temperature substrate and condensing the vapor onto the surface. At these low pressures, the molecular gas flow moves linearly with few atomic collisions, leading to line of sight deposition. For

applications in electrochemistry where high surface area is needed, line of sight deposition is not suitable for the porous materials that need to be coated.

Some success has been achieved with deposition of 1D materials using PVD; however, the mechanisms required to form anisotropic depositions in this case are different than those used for simple film formation. Glancing angle deposition (GLAD) is a modified PVD method used to create 1D materials. This technique uses a vapor source at a shallow/glancing angle (<70°) to the substrate during deposition.[118] During growth, the glancing angle geometry causes faster deposition at taller features, such as the nanowire tip, and the shorter features become blocked and stop growing. By changing the rotation rate of the substrate, the growth angle of the wires with respect to the substrate are controlled. Additionally, intermittent rotation yield helical nanowires growth. During substrate rotation, columnar growth can be observed due to extreme shadowing effects. These shadowing effects combined with limited surface mobility of the deposited material are used to adjust the diameter of the nanowires with diameters as low as 10 nm and as long as ~10 μm. Unfortunately, the quality of the nanowires produced is low with non-uniform diameter, polycrystalline or amorphous composition. ITO, CNT, Si, Ge, Si, SiO2, Al, Ni, Co, Mn W, and Cu[118-120] nanowires have been grown using this GLAD coupled with a catalyst and a heated substrate and has resulted in more desirable single crystal nanowires thought still at low growth rates (0.1-0.5 nm s^{-1}).

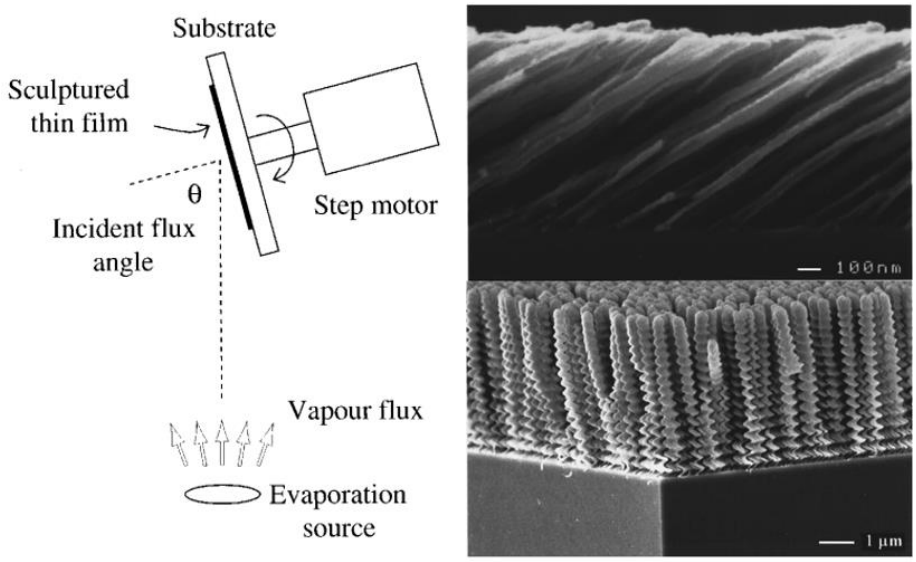

Figure 31. PVD system for production of 1D nanomaterials. The schematic on the left shows AlNW grown at θ=85° with no substrate rotation on the top right and slow substrate rotation on the bottom right.[120]

Chemical Vapor Deposition

CVD on the other hand allows much more complexity due to the coupling of a chemical reaction to the deposition process. These chemical reactions can take many forms, with the most commonly used in industry being pyrolysis and compound formation. Pyrolysis using only thermal decomposition of the precursor and compound formation using a secondary gas to react with the precursor or precursor decomposition products. Both processes use a gas phase precursor flown into a reaction vessel with the gaseous byproducts continuously removed. Unlike PVD which is typically performed at high vacuum (10^{-6} Torr), CVD is typically performed at rough vacuum to atmospheric pressure (0.1-760 Torr) where the gas is in a viscous flow range.[121] High pressure and low gas flow velocity create thick boundary layers with low pressure and high flow rates creating thinner boundary layers. The thickness of these boundaries layers are important to the mass transfer properties of the system as the reactants and products must diffuse through this layer to interact with the surface and leave. The boundary layer is defined as the region in which the gas flow has 99% of the free-stream velocity.[122]

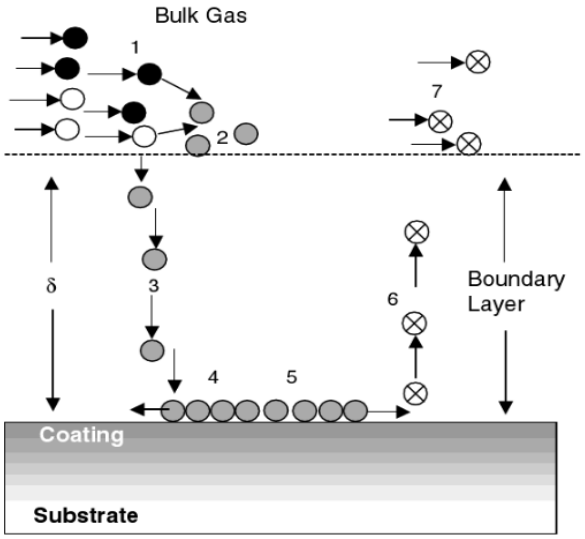

Figure 32. Schematic of the mechanisms involved in CVD reactions.[123]

Figure 32 depicts the primary deposition mechanisms involved in CVD reactions. These steps include 1) transport of the precursor vapor into the reaction chamber, 2) precursor decomposition/reaction to form reactive components, 3) diffusion through the boundary layer to the surface, 4) surface adsorption of reactive components, 5) final surface reaction of the adsorbed species, 6) diffusion through boundary layer of reaction product gases, 7) exhaust gas removal from reactor system. All of these steps can have different kinetics depending on the precursor and substrates used, and the deposition conditions (temperature and mass flow) with the surface reactions (steps 4 and 5) tending to have the highest activation energies. Identifying the slowest reaction step in this system (rate determining step, RDS) is important for predicting growth rates, surface film contaminants, coverage uniformity, and gas phase precipitates.

CVD allows for a deposition of a large variety of materials however the continuous mass deposition can cause issues for processes that require uniform coatings on complex geometry substrates. For these applications a surface limited reaction can be used which typically uses an initial precursor which chemisorbs strongly to the substrate in a monolayer with no further reaction. When the residual precursor for the first step is completely removed a second precursor is added which only react with the first

chemisorbed precursor to form another monolayer. Thus by alternating these precursors, atomic control can be attained if suitable purging is performed between steps and time is allowed for full surface coverage. Examples of suitable ALD precursors include $AlCl_3$ and H_2O for Al_2O_3 formation, vanadyl tri-isopropoxide and H_2O for VO_x formation.[124] Figure 33 shows the difference between the traditional CVD and the atomic layer deposition (ALD) which was developed in 1974 by Suntola.[125]

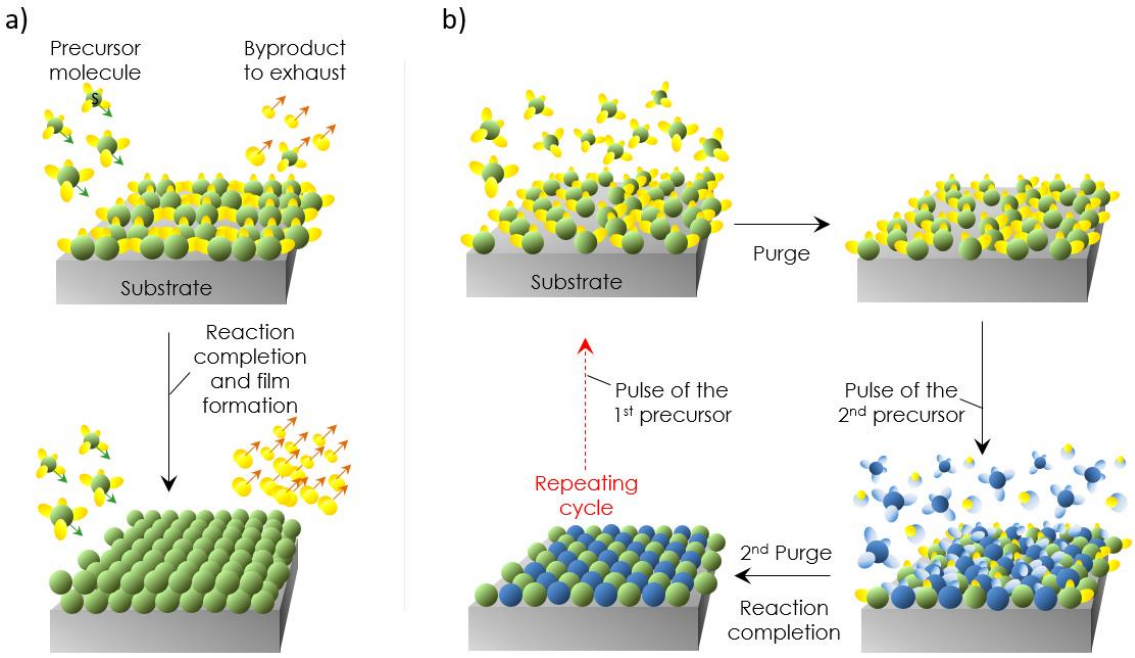

Figure 33. Reaction mechanism for a) chemical vapor deposited films, and b) surface limited atomic layer deposited films.[126]

If we consider the mass flow of materials during a traditional CVD environment we have two main categories. Reaction precursors have to diffuse through the boundary layer to reach the surface and once there they have to react and desorb. The diffusion through the boundary layer can be described as follows,[123]

$$j_\delta = \frac{D}{\delta}(C_g - C_s) \tag{55}$$

where j_δ is the molar flux through the boundary layer (mol s^{-1} cm^{-2}), D is the diffusion coefficient for the reactive gas of interest (cm^2 s^{-1}), δ is the boundary layer thickness (cm), and C_g and C_s are the gas concentrations in the bulk gas and at the

substrate surface respectively (mol cm^{-3}). The flux of gas which deposits at the surface and desorbs is controlled by an Arrhenius surface reaction rate described as,[123]

$$j_s = k_s C_s \tag{56}$$

where and j_s is the molar flux to the surface and k_s is the surface reaction rate constant (cm s^{-1}). If we assume the flux through the boundary layer is the same as the flux deposited at the surface we can solve (56) for the gas concentration at the surface (C_s) and substitution into (55) yields,[123]

$$j_s = \frac{C_g}{1/k_s + \delta/D} \tag{57}$$

Because the deposited flux is proportional to the growth rate, this relation is useful to predict the temperature relationship of growth rate, and can help identify whether the rate determining step is surface limited or mass transfer limited as shown in Figure 34.

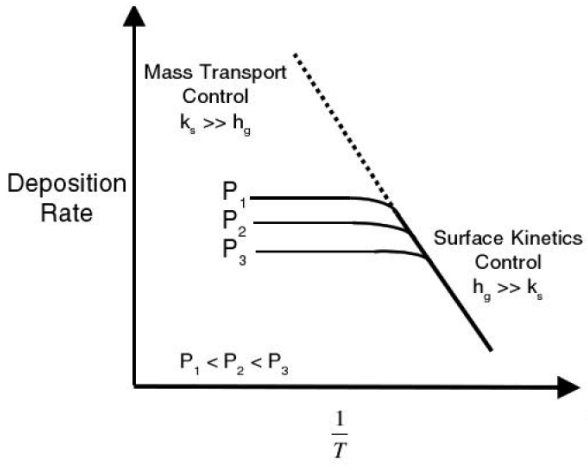

Figure 34. Schematic diagram illustrating the different control regimes and deposition rate as a function of temperature, pressure, and kinetics.[123]

CVD of 1D Nanomaterials

Historically, CVD research has attempted to provide conditions for the growth conformal thin films with controlled, reproducible, and high growth rates. Because these conditions are not always suitable for production of 1D nanomaterials, modifications are

often needed. CVD has become a powerful method to produce conductive nanowires, nanotubes, and other high surface area materials useful for current collectors for ECSDs including Cu, Al, and CNTs.[126]

By far the most common growth mechanism for producing controlled diameter high quality 1D materials is the vapor-liquid-solid (VLS) method, which was first demonstration for the production of micron scale whiskers of SiO_2 and Si by Wagner in the 1960s.[127] It is currently most widely used in the production of large scale volumes of CNTs and the primary indication for its occurrence is the presence of a catalyst particle of roughly the same diameter as the nanowire found on the end of the wire.[128] VLS growth uses a catalyst material which easily alloys/reacts with the source gasses. This catalyst is typically a liquid at the temperatures used for the growth thus the vapor from the reaction gas interacts with the liquid catalyst depositing the solid nanomaterials, hence called VLS growth. This source gas is absorbed and increases in concentration until the material gets redeposited after reaching the saturation point. Often catalysts are chosen which form eutectic compositions with the source gas of interest, with Ag catalysts for Si NW and Fe/Co/Ni catalysts for CNTs. These catalyst particles can form either at the tip of the nanowire and move away from the substrate surface during growth or they can form at the root of the nanowire where the nanowire is pushed up away from the substrate surface as shown in Figure 35a,b. The different growth methods depend on the relative diffusivity of the reaction products at the boundary of the gas-liquid or gas solid interface as well as the solubility limits for the catalysts as shown in Figure 35b,c.

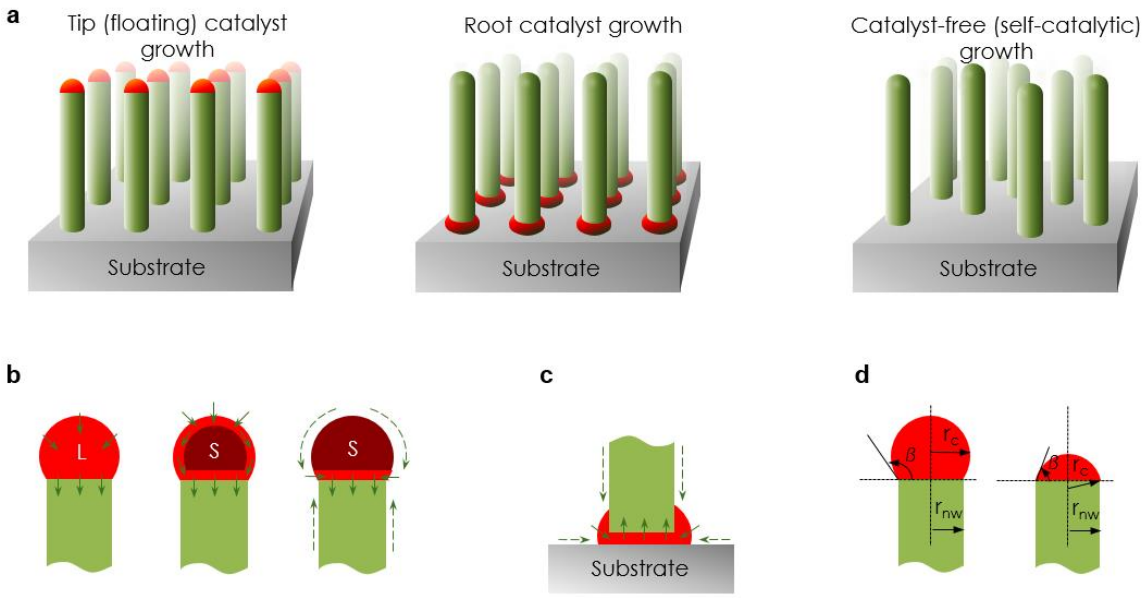

Figure 35. Nanowire growth mechanisms commonly described as VLS growth with a) showing tip, root, and catalyst-free CVD growth mechanisms, b) three methods of tip growth including the location of the liquid (L), and solid (S) phases and the diffusion paths of the source atoms, c) root growth VLS mechanism with the diffusion path of source gasses shown, d) geometry relationship between the contact angle of the liquid solid interface and the radius of the resulting nanowire.[126]

These catalysts can be deposited on the substrate prior to reaction or generated in situ via evaporation as is observed for $FeCl_2$ in CNT productions.[129] Substrate based CNT growth methods have been shown to produce very uniform diameter and length MWCNTs and in many cases vertically aligned dense CNT forests can be grown. These forests can be removed from the substrate and used as free standing materials or the CNTs can be collected by fiber pullout with the van der Waals bonding between CNTs allowing yarns of pure CNT to be produced.

Due to the need for large scale nanomaterial production for use in device manufacturing, continuous flow production methods have been developed. One promising method for this synthesis has been the use of fluidized bed CVD (FB-CVD) reactors. A fluidized bed is a group of particles, which, due to a fluid flow (typically gas), maintains a fluid like characteristic with particles suspended in the carrier gas during the high temperature deposition. This carrier gas is typically an inert gas such as methane,

helium, nitrogen, or argon. For CNT synthesis this FB-CVD method is more efficient as the traditional CVD systems are severely limited by inhomogeneous gas/solid contacts and temperature gradients. The intense mixing found in FB-CVD systems ensures high carbon utilization per catalyst.[130] During deposition the catalyst is fluidized along with the continuously growing CNTs. Once the particles are suspended, proper process control is required to maintain the suspension as improper gas velocities may either blow the particles out of the reactor or allow the particles to fall into the gas inlet. For 1D nanomaterial synthesis this is critical as during the growth process the size, shape, and mass of the particles change drastically. Size is a particularly important parameter as the gas velocity required for proper fluidization varies as the square of the particle size however this allows for simple separation of the produced CNTs from the residual catalysts.[130] Typical catalysts for CNT growth include Ni, Fe, Co, Mo, and W which are typically infiltrated onto high surface area heterogeneous catalyst support materials such as Al_2O_3, MgO, TiO_2 etc.[130] The catalyst mass loading has been shown to influence the form of carbon produced with moderate 2.5-15 wt. % producing primarily MWCNTs and SWCNTs generally produced with loadings less than 2.5 wt. %.[121]

Due to the presence of the catalyst in the final product during VLS type growth, these nanowires typically require post processing to purify them before use in other devices. Vapor-solid (VS) reactions avoid contamination through having a third phase however they are less well understood in CVD systems. While the VS growth mechanism is less understood than VLS the three main mechanisms are anisotropic growth, defect induced growth, and self-catalytic growth. Self-catalytic growth mechanisms have been observed, yet these are more difficult to control due to the balance required between the nucleation and growth requirements and the sensitivity to local environmental conditions. Some examples of 1D nanomaterials grown using self-catalytic VS include SnO_2 nanowires grown on quartz through pyrolytic CVD,[131] ZnO, SnO_2, In_2O_3, and CdO nanowires grown using a sublimation method at temperatures dependent on the melting

point of the corresponding oxides,[132] and binary nanowires GaN, InAs, InN and ternary nanowires InGaAs, InGaN grown using CVD of NH_3 and pure metals at 800-1100 ºC and low pressure.[133] An interesting subset of self-catalyzed nanowire formation is called oxide assisted growth (OAG), which starts with an oxide based material, such as SiO_2 or GeO_2 and involves heating them in a vacuum, producing reduced Si, or Ge wires.[134] CuNWs have also been deposited without a catalyst by the use of twinned defects in an organometallic precursor deposition onto Si at 200 ºC.[135,136] While there are many examples of self-catalytic growth for nanowires, more research is needed to better understand the mechanisms more directly and control the properties of these produced materials.

Hydrothermal/Solvothermal Synthesis

The term hydrothermal originated from the natural geological processes, which involve high temperature and pressure reactions underground, which facilitate the formation of a variety of rocks and minerals. Since its origination the usage of the term has been highly uneven with definitions. The broadest definition suggests that a hydrothermal reaction is any homogeneous or heterogeneous reaction which occurs in a solvent at temperatures or pressures, which allow the dissolution and precipitation of materials that are not obtainable under ordinary conditions. This field has been further divided based on the solvents used with many researchers reserving hydrothermal to aqueous systems and other terms, such as solvothermal systems (with terms such as alcothermal, glycothermal, ammonothermal etc. being used for alcohol, glycol, and ammonia solvent systems respectively).[137] Additional divisions have been made using the harshness of the environment with low temperature and pressure, methods being classified as soft solution processing methods. This is normally accomplished by combining a solvent, mineral, and/or mineralizer in a sealed container called an autoclave which is then heated. By using an enclosed system, the synthesis of low temperature

phases with high vapor pressure can be performed while allowing greater compositional control.[138]

This is a broad field with its roots based in geology, mineralogy, and even petrology and was popularized due to its uses in producing high quality single crystal quartz and zeolites and progressed to the synthesis of artificial gemstones such as ruby, emerald, sapphire, and diamonds. Additional attention was applied when it was shown that purification of bauxite ores for industrial aluminum production could be performed efficiently using hydrothermal methods.[137] While water is by far the most commonly used solvent due to its excellent solvation properties, low cost, and low environmental impact, other solvents such as CO_2, NH_3, HF, HCl, HBr, Br_2, S_2Cl_2, H_2S, C_2H_5OH, CS_2, CCl_4, C_6H_6 are also commonly used.[139] All of these solvents can be forced into a supercritical fluid at high temperatures and pressures which allows for more processing options due to the difference in dielectric constant and solvent density compared to the liquid or gas phase. For materials that do not have high enough solubility in the solvent of choice at experimentally achievable temperatures and pressures, mineralizers such as NaOH, Na_2CO_3, NH_4F, and K_2HPO_4 are sometimes used to form more soluble complexes.

Hydrothermal synthesis often creates regularly shaped crystals due to the equilibria conditions under which growth is conducted. In order to force the asymmetric growth required to form 1D nanomaterials surfactants, chelates, and other organic capping molecules are used to control the nucleation of the desired phase and to increase the size, shape, and dispersibility of the particles.[139] These shaping materials are typically surfactants which are organic molecules that contain both hydrophobic and hydrophilic surface functional groups. Surfactants that are commonly used include sodium dodecylsulfonate (SDS), sodium dodecylbenzene sulphonate (DBS), cetyltrimethyl ammonium bromide (CTAB), and hexadecylpyridinium chloride (HPC).[117] Surfactants can be selected with a variety of parameters in mind including pH *vs.* pKa, isoelectric

point, and chemical compatibility with desired phases. High pressures temperatures tend to produce higher crystallinity samples with lower defect concentrations than other solution processing methods due to the higher energies available.[140]

Solubility can be studied by looking at the thermodynamic predictions as well as the solvation energy. For solubility predictions of ionic solids the solvation energy must overcome the attractive forces in the crystal lattice. This solvation occurs without an electron transfer thus can be treated using approaches from electrostatics based on the Poisson equation. The Born model was developed in 1920 and provides a good estimation of the free energy of solvation (ΔG_{Born}).[141]

$$\Delta G_{Born} = -\frac{q^2}{2r}\left(1 - \frac{1}{\epsilon}\right) \tag{58}$$

where q is the charge of the ion being dissolved, r is the effective Born radius of both of the dissolved species, and ϵ is the dielectric constant for the solvent. This $\left(1 - \frac{1}{\epsilon}\right)$ term is thus very important in allowing solubility of species with higher dielectric materials such as water (ϵ =75). For water the dielectric constant is known to decrease with rising temperature and to increase with rising pressure with the temperature effect dominating and these values are readily available in literature as shown in Figure 36.[138] Despite the simplicity and lack of quantum contributions the Born model has been shown to provide accurate measurements for equilibrium solvation energies and is often used in determination of pKa, redox potentials, and the electrostatic contribution to molecular solvation energies.

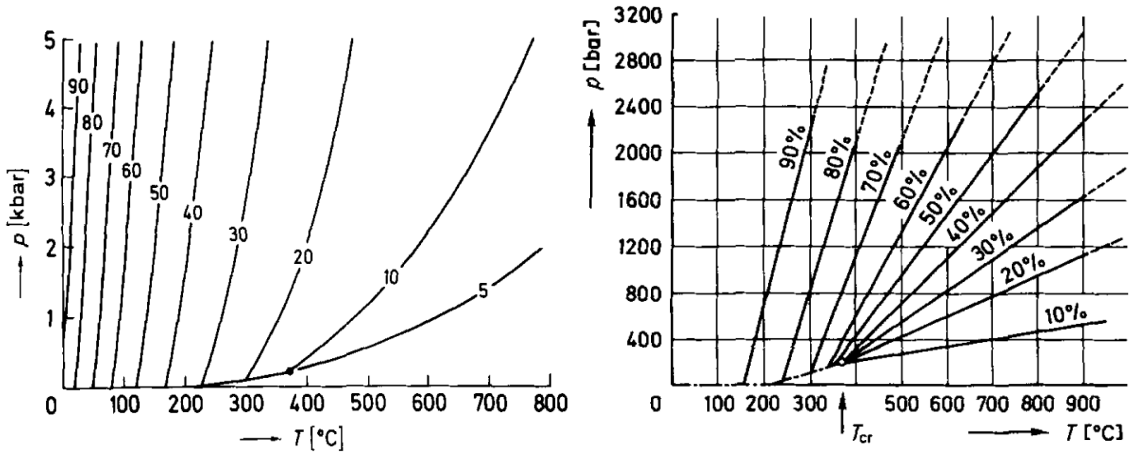

Figure 36. Commonly used water properties to predict conditions during hydrothermal synthesis. a) Iso-dielectric constant lines for water as a function of temperature and pressure. b) P-T curves for different autoclave fill fractions.[138]

Electrodeposition

Electrodeposition is a film growth process which produces a coating onto a conductive base material through the use of an electrochemical redox reaction to deposit materials from the electrolyte and is often called electroplating. Water is the most commonly used electrolyte as it has good ionic conductivity and good solubility for many materials of interest. The part which is to be plated into is typically submerged into a bath containing the electrolyte and a counter electrode. The part and the counter electrode are then connected to a power supply which supplies the electrons need for reduction of the metal ion species. Electrodeposition has long been used due to the wide range of materials which can be produced and the detailed patterning which can achieved in ambient conditions. Some examples of usage include gold plating of electrical contacts, Cu deposition of microelectronics interconnects, and even purification of high purity metals.

Fundamentals of Electrodeposition

The fundamentals of electrodeposition are similar in nature to the faradaic reactions which occur in battery systems however because the desired outcome is control of metal deposition quality. The general electrochemical equation for electroplating is shown below,

$$\left(M_x L_y\right)^z + nxe^- \rightarrow xM^\circ + yL \tag{59}$$

where M is the metal which is being deposited, L is a ligand species which can be a molecule or ionic species which is tightly bound to the ionic metal species forming a complex species $\left(M_x L_y\right)^z$. This reaction may or may not be reversible however because the end goal is for mass deposition reversibility is often not required. This equation shows the stoichiometric deposition of x mols of M° with the exchange of n mols of e^-. Faraday's law is shown in (60) and is used to show the relation between the amount of charge passed and the mass of material deposited assuming perfect efficiency.

$$\Delta m = \frac{Q M_w}{nF} \tag{60}$$

where Δm is the mass of material deposited, Q is the charge passed calculated from $Q = \int I dt$, M_w is the molecular weight of the metal species, n is the molar equivalent of electrons, and F is Faraday's constant. For reversible reactions with no coupled chemical reactions or side reactions this provides a highly accurate relation between the mass deposited and the charge passed which can be controlled and measured easily using balances and potentiostats. For reactions with coupled chemical reactions or parasitic side reactions such as hydrogen evolution, co-deposition of competing ionic species, partial ion reduction, and even oxide formation there is a significant fraction of charge (Q_p) which is not involved in the deposition process directly. By measuring the actual mass change (Δm) and comparing this with the total charge passed (Q_T) we can describe the current efficiency (CE) of the system as shown in (61). Current efficiency is often represented as a percentage.

$$CE = \frac{Q_p}{Q_T} = \frac{\Delta mnF}{Q_T M_w} \quad (61)$$

Values can vary widely depending on the temperature, deposition rate, pH, metal and electrolyte of choice and typically range from 70-100%. Poor values for CE can be indicators of electrolyte oxidation/reduction, co-deposition of unwanted species, and reduction of surface contaminants such as oxides which may form spontaneously during the deposition.[142] This reduces the fraction of electrons involved in the electrodeposition and is important particularly for cost reduction in high current or large production volume applications as well is for isolating production inefficiencies.

Frequently for electrodeposition Faraday's law is combined with the density and geometry of the sample to estimate the thickness of the deposited films as shown below for planar coatings,

$$t = \frac{\Delta m}{S\rho} = \frac{Q_p M_w}{nFS\rho} \quad (62)$$

where t is the deposited film thickness, S is the actual surface area, and ρ is the density of the deposited material.

Generally, the electron transfer process in electrodeposition systems is much faster than the mass transport of metal ion species 0.1-1 ms compared with (1-10 s).[142] Thus, for high overpotential experimental conditions the deposition rate is limited by mass transport. Mass transport is the sum of the convection, migration, and diffusion contributions and a good approximation for this is shown below,[142]

$$i = \frac{nFD(C^* - C^o)}{\delta} \quad (63)$$

where *i* is the maximum current, D is the diffusion coefficient, C^* and C^o are the concentration of metal ion in the bulk and at the surface respectively, and δ is the diffusion layer thickness often 0.03-0.05 cm in aqueous systems or ~0.001 cm during stirring. In the mass transfer limited case the bulk concentration C^* will remain constant but the surface concentration C^o will drop effectively to zero providing the limiting current density (i_d),

$$i_d = \frac{nFDC^*}{\delta} \tag{64}$$

Typical deposition rates occur at current values of $i \leq 0.4 i_d$ to avoid surface roughening and possible dendrite formation which may occur if there are local non-uniformities in the current density over the surface of the electrode being deposited.[142]

Pulse Deposition and Waveform Selection

Direct current (DC) and direct voltage (DV) plating were the first large scale electrodeposition methods used primarily due to the low equipment requirements for producing a constant deposition waveform. DC was commonly used as the calculation of the charge passed was simply $Q = It$ and thickness of the deposited coatings were linear with respect to the deposition time.[143] Electroplating with pulse current (PC) is becoming increasingly popular because it offers several advantages over direct current plating, such as mass transfer enhancement and the availability of additional process parameters (on-time, off-time and pulse current density) which can be varied independently to influence deposit properties including hardness, grain size, and morphology.[142,144] An example current waveform for a reverse current pulse cycle is shown in Figure 37 with the peak current (i_p) and reverse peak current (i_{rev}) as well as the on time (t_{on}), off time (t_{off}), and reverse time (t_{rev}) indicated for two complete deposition cycles.[142] Rectangular waveforms without reverse pulses are possible as well and are called rectangular pulse deposition. Care must be taken to ensure that the total charge passed in the cathodic direction is larger than the anodic direction or no material will deposit in a reversible system.

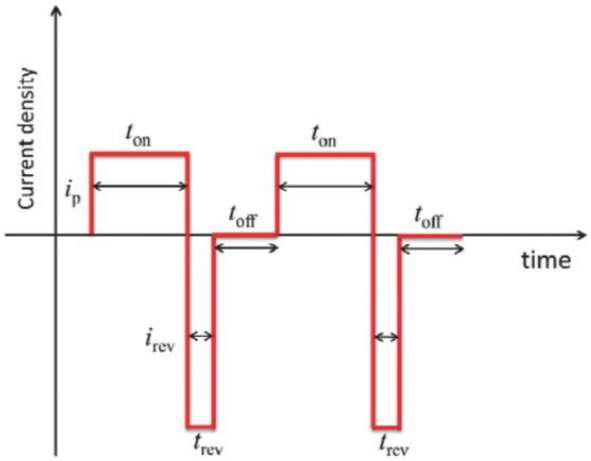

Figure 37. Example waveform for a reverse pulse deposition method for deposition of Cu in a through hole on a printed circuit board.[145]

One significant advantage to pulse current deposition methods is that the applied current can be orders of magnitude larger than i_d as there is now an off period where the consumed metal species can diffuse back into the boundary layer and replenish the depleted surface concentration. While this prevents an increased deposition rate as the average current of the pulse deposition must still be below the limiting current, other benefits can be observed. The higher current density increases the nucleation rate forming fine grained, smooth deposits. Reverse pulses can be quite useful for cleaning the surface of reaction products or particles which may be incorporated into the materials.[142] The shape of the pulse has also been shown to impact the deposition results. For AC pulses square wave was shown to perform better than sine shaped signal for filling AAO membranes.[55] Triangular pulse deposition has been shown to provide better adhesion and film density for Zn coatings on Mg alloys when compared with square, sine, and sawtooth pulses.[146] Platinum deposition for fuel cells providing low Pt loading and suitable performance.[144]

Electrodeposition of 1D Nanostructures

Electrodeposition is an attractive route for 1D nanomaterial synthesis as there is a wide range of materials that can be deposited[147] however these depositions do not tend to

intrinsically form 1D structures. This can be overcome using hard templates such as anodized alumina membranes, zeolites, and soft templates such as metal organic frameworks, or patterned polymers which allow careful control of the pore size of the template which translates to a monodisperse nanowire diameter.[14] Hard carbons in particular have shown popular use due to the ease of control of the pore diameter and ability to withstand etching processes. Additionally electrodeposition can be used to coat a conductive 1D material in an easily controlled manor which is common for CNTs and CNFs. Many 1D nanomaterials have been produced for LIB applications using a porous alumina template to deposit Cu nanorods which were subsequently electrodeposited with Fe_3O_4 , NiSn, Bi, Sb, or Sn.[54] Templated galvanostatic and pulsed electrodeposition was also used to deposit Al nanowires onto Al current collectors where the pulse condition was shown to provide better height control and a (111) growth direction.[54]

Electrodeposition of Conductive Polymers

Traditionally, metals have been heavily studied for electrodeposition applications, however, deposition of intrinsically conductive polymers has received renewed interest for sensor and energy storage applications. Electrodeposition of polymers provides advantages of chemical polymerization as it allows for stoichiometric control of the amount of material deposited through charge passed according to faraday's law, control of the location of that deposited material to conductive surfaces, and control of the initiation and termination step of the polymerization.[148] This is important as many polymers, such as PANI, require a minimum molecular weight to become conductive. Also because the polymerization is initiated with electron transfer, there are no residual oxidizing materials which need to be removed.

A typical reaction mechanism for the electrodeposition of a conductive polymer is described as follows. Polymerization typically is initiated by the formation of monomer radicals, where the radical site can vary among many locations on the polymer due to

resonance. Following the radical formation, subsequent or simultaneous protonation or deprotonation may occur depending on the pH of the solution producing a variety of intermediate species. These species couple, forming small chain polymers which are slightly soluble and are able to subsequently oxidize to form radicals and continue coupling to form larger molecular weight polymers. It is common during this process for anions to bind to the charge centers which leads to charge neutrality.[88] An example of this polymerization process is shown in Figure 38 for PANI.

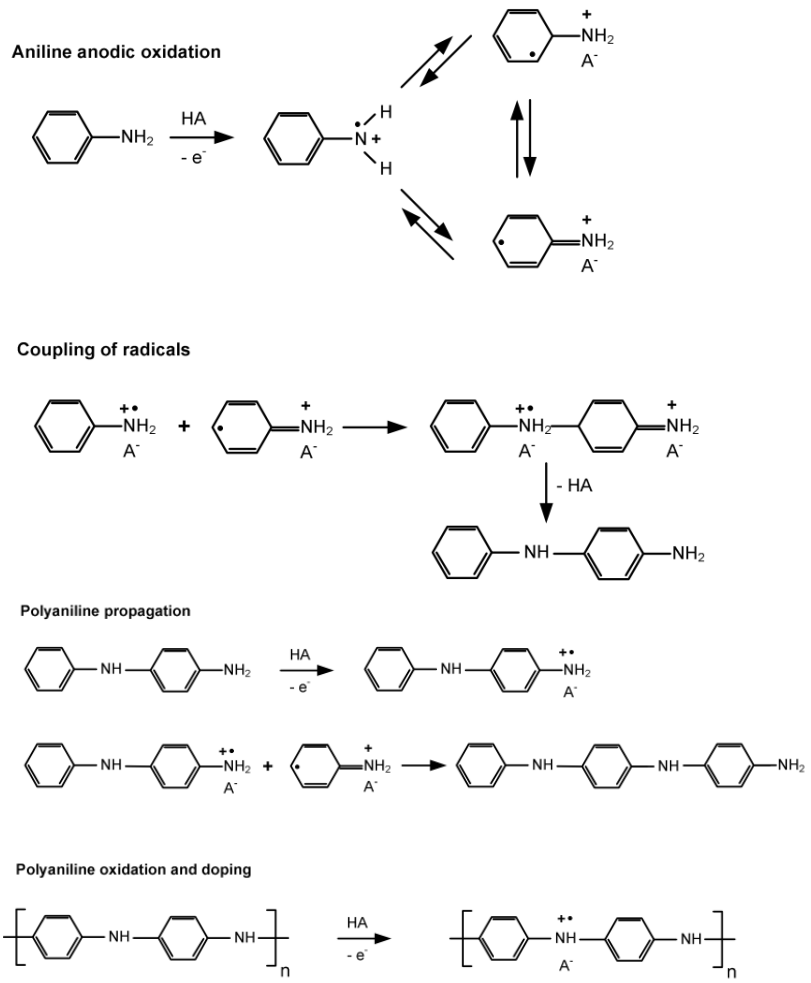

Figure 38. Typical conductive polymer electrochemical reaction path including radicle formation, coupling, and propagation.[88]

While chemical reduction methods are also possible, electrochemical reduction has many benefits, including higher monomer utilization, larger achievable molecular

weights, controllable deposit thicknesses, high density films, better conformality, and higher electrical conductivities. Polymerization kinetic studies of polyaniline have been performed using quartz crystal microbalance experiments which show the reaction rates are dependent on the mobility of the anion species in the polymer and the monomeric solubility in solution with HCl solutions showing the fastest growth kinetics as well as the highest polymer film conductivities.[149] For the mass transfer controlled early stage of polyaniline growth in a DC type deposition system, a compact conformal surface layer is typically observed with filament type growths observed at longer time periods or where the current density is increased. Pulse current and pulse voltage deposition methods have been shown to improve the conformality of the initial surface coverage layer and extend the conformal growth regime to create thicker films.[88]

For deposition of thick films the adherence is often poor leading to particulate growth and detachment from the surface at thickness >10 μm. Adhesion and conformality is typically good for thin films <1 μm and is possible on many substrate materials including commonly used current collector and reference electrodes such as glassy carbon, Pt, Au, SS, Cu, Ti, and even Fe in the correct electrolyte systems.[150] Proper electrolyte-substrate systems were important as the pH of different solutions can cause substrate dissolution before the polymerization potentials can be reached. Initial attempts to electrodeposit conductive polymers were attempted in non-aqueous electrolytes due to the higher monomer solubility. This allowed for faster polymerization rates and helped prevent the anodic dissolution of the deposition surface.

For processes such as energy storage, where free standing 1D nanowires are not needed and electrical conductivity is a priority, electrodeposition onto 1D conductive carbons such as carbon fiber, nanofiber, and nanotubes are ideal as the π-conjugated polymers tend to have high bond strength with the graphite structure.[151]

2.5 Multifunctional Energy Storage

The traditional approach to building a structure is to address the mechanical demands first and then deal with the other functional requirements separately. This results in duplicate weight and add on attachments that cause a further penalties. Multifunctional design is an approach which attempts to solve all of the functional needs in one material. The unmanned aerial vehicle is an example where the weight restrictions are severe and where a mechanical and energy storage multifunctionality from incorporating a battery into the wing surface could provide better performance than having them be separate.[11] Almost by definition these materials need to be composites and especially for energy storage purposes nanocomposites have become attractive options. Of the nanomaterials which supply mechanical support, CNTs show the most promise in this field and their conductivity and chemical compatibility make them a likely candidate for attempts to create multifunctional energy storage devices.

Introduction to Composite Mechanics

A composite is a material that is composed of one or more materials with complementary properties (typically mechanical) that have better characteristics than any single component. Traditionally, this is done by embedding a material with high mechanical properties (the reinforcement) into a matrix material of lower mechanical properties but good fracture properties or lower cost. These composite materials generally benefit from having an fiber reinforcement however this makes predicting the mechanical properties more complicated as they are a function of the filler orientation and amount as well as the intrinsic mechanical properties of the filler and matrix alone. In order to maintain the composite's electrochemical multifunctionality, electrolyte must have easy access to the active materials. Until structural solid state electrolytes are better developed, high porosity composites such as non-woven fabrics can be used as energy storage composites.

Matrix Reinforced Composites

This was first studied for a perfectly aligned, infinite length, reinforced composite using a simple approach based on continuum mechanics type calculation. This approach also assumes perfect bonding between the filler and the matrix and results in the classic "rule of mixtures" relationship for the modulus or strength of the composite in the direction of reinforcement alignment.

$$E_{11}^{c} = E_f V_f + E_M V_M \tag{65}$$

where E_{11}^{c} is the composite's longitudinal elastic modus, E_f, and E_M are the modulus of the fiber, and matrix respectively, and V_f and V_M are the volume fraction of fiber and matrix respectively.[112,152,153] For composites reinforced with nanomaterials, they are almost exclusively non-continuously reinforced due to the limited length of the 1D materials to typically 0.1-10 mm. Additionally, they tend to also not be well oriented and in some cases (air laid and vacuum filtered) are completely randomly oriented. In these cases modifications to the rule of mixtures have been suggested by the Cox-Krenchel model,

$$E_{11}^{c} = \eta_\theta \eta_l E_f V_f + E_M V_M \tag{66}$$

where η_θ is a fiber orientation distribution factor ($\eta_\theta = 3/8$ for completely random distribution),[154] and η_l is the fiber length distribution factor (<1 for chopped strands and nanofiber fillers). Work by Shaffer in 1999 observed much lower predicted fiber lengths by applying the Cox-Krenchel model than the observed nanotube length suggesting large decreases in observed properties due to nanotube curvature, reduced shear stress transfer, and CNT telescoping.[155] Fortunately, the mechanics of these types of reinforcement can be predicted well using the empirically based Halpin-Tsai equations at low volume fractions, however large deviations have been observed at large fiber reinforcement for CNT filler.[112,153]

Nonwoven Fabric Mechanics

These equations all assume good load transfer from reinforcement into a solid matrix, however this solid matrix may be undesirable for an electrochemically active composite. In such a situation, a nonwoven fabric may be more desired. Nonwoven fabrics are textile products that are manufactured from continuous or discontinuous fibers into sheets, webs, or mats. These fibers can be randomly oriented or directional and are bonded together by either friction, cohesion, or adhesion.[59] Typically these materials have a large degree of porosity (>50% with samples around 80% being typical) which is attractive for electrolyte access and subsequent active material deposition needed for ECSDs such as pseudocapacitor, battery, or separator applications.

Backer and Petterson first pioneered a fiber network theory to help describe the load/stress transfer in a non-woven fabric without binders.[156] This work assumes the fibers are completely straight, the bond strength between fibers is high enough for failure to initiate by fiber failure, and the shear stress and strain are negligible. It also makes use of a fiber orientation distribution function (FOD, or Ω(β)) which is typically measured using XRD or SANS or assumed to be random depending on the processing parameters.

$$\sigma(\theta) = E_f \varepsilon_\theta \int_{-\pi/2}^{\pi/2} (\cos^4 \beta - v(\theta) \sin^2 \beta \cos^2 \beta) \Omega(\beta) d\beta \tag{67}$$

where E_f is the fiber modulus, ε_θ is the fabric strain, $v(\theta)$ is the poisson's ratio in the direction of applied stress, β is the angle between the fiber and the direction of the applied stress, If we evaluate this for a completely random fiber orientation distribution function Ω(β)=1/π, and $v(\theta) = 1/3$, the relationship evaluates to, $\sigma \sim 0.35 E_f \varepsilon_\theta$.[157] This result provides a useful upper estimate for the stress of a randomly oriented non-woven fabric however does not include important parameters such as fiber curvature, fiber slippage, high strains, fabric density variations, and fiber length/aspect ratio which will all decrease the observed properties.

As mentioned previously, porous non-wovens have showed interest to the MF materials for electrochemical energy storage due to their increased surface area and strength compared to traditional electrode designs however non-wovens alone have not shown high enough strength and conductivity to produce comparable structural properties. One approach to increasing these non-wovens mechanical properties involves the infiltration with a structural solid state electrolyte to allow better stress transfer between fibers. Development of solid electrolytes to use in multifunctional materials have begun to address these issues. Current efforts to find high ionic conductive room temperature solids have begun with limited success and results often show an inverse relationship between mechanical properties and ionic conductivity as shown in Figure 39.[158]

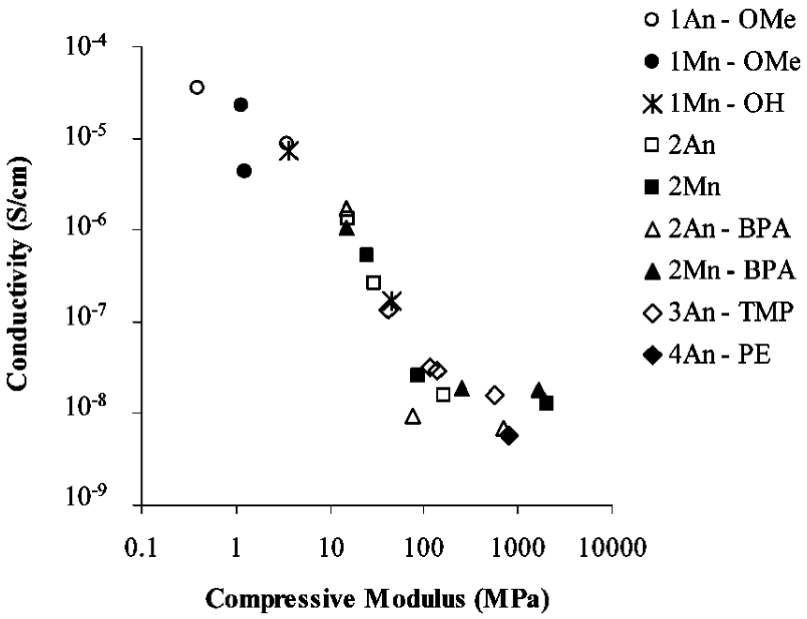

Figure 39. Room temperature ionic conductivity for a variety of potential electrolyte polymers *vs.* their compressive modulus.[158]

Carbon Fiber Multifunctional Anodes *vs.* Carbon Nanotubes

Caron fiber is an attractive material to use in multifunctional batteries due to its combination of high strength and the intercalation behavior of lithium ions into graphitic carbons. They are created by carbonizing polymer fibers (typically polyacrylonitrile,

rayon, or pitch) which are typically drawn mechanically to help align the polymer molecules. This helps oriented the resulting graphite planes along the length of the fiber thus increasing modulus. Carbonization occurs under tension at 2500 ºC in an inert atmosphere to drive off all non-carbon components leaving highly oriented graphite behind. These graphitic domains range from 6 nm wide to 200 nm long and run parallel to the fiber axis.[159] The carbon fiber industry is well developed with ready sources of materials and high reproducibility and mass production. Unfortunately, the industrially available carbon fibers typically have polymeric surface coatings called sizing that increase stress transfer between the fiber and the polymer matrix and to protect the fibers during manufacture and handling. These sizing layers prevent the fibers from accessing lithium ions from the electrolyte and while removal is possible it has not been shown to help performance.[158,160] The usage of carbon fiber as an active material has limitations as the lithiation of a structural material often severely reduces its mechanical property and can even cause exfoliation which is an even larger issue due to the micron size diameter common in these carbon fibers.[22,39,40]

Carbon Nanotube Composites

Carbon nanotubes can be described as seamless tubes made from rolling graphitic sheets having diameters from 1-100's of nanometers and lengths up to a few cm. They can be found in two different types based on the number of concentric graphitic tubes with single tubes called single walled carbon nanotubes (SWCNT) and multiple layered tubes being called multiwalled carbon nanotubes (MWCNT). First discovered in 1991 by Iijima,[161] carbon nanotubes show large promise for mechanical properties due to the C=C bond being one of the strongest found in nature. This allows them to have an extremely high modulus (~270-1200 GPa for SWCNT and 11-200 GPa for MWCNT from measurement and simulation).[162] This modulus coupled with their high flexibility (reversible bending with a radius of curvature of as low as 25 nm)[163] made them an ideal

fiber reinforcement. Furthermore these mechanical properties are dependent on the different levels of impurities and defects which is in turn dependent on the production method of the CNTs. CVD produced MWCNTs show an order of magnitude lower modulus than similar arc-discharge produced MWCNTs but much of this decreased mechanical strength can be recovered by thermally annealing the CNTs.[112]

With the increased production rate of these materials, utilization of high volume fractions of CNTs in composites is becoming more economically feasible. Their application as structural reinforcements however face a large difficulty due to the small lengths, thus requiring their use in composites (typically polymer composites). This makes the ability to transfer load efficiently between the composite matrix and the nanowire of utmost importance for their incorporation into a structural material. Typical CNT lengths from PVD/HiPCO/CVD/carbon arc are on the order of 1-10 μm however these aspect ratios are not high enough to provide efficient load transfer to a matrix and often produce fragile free standing CNT films and composites.[164,165] Interestingly, simply increasing the CNT length is not sufficient to increase the mechanical and electrical properties of the resulting composites as the processing can often shorten the tubes and disrupt bonding.[166] Some work has been done using longer (>1 mm) CNTs for producing composites from solution with less success since they still require dispersing and vacuum filtration.[167] The most promising CNT buckypaper and resultant composite results appear for samples prepared without solution processing.[168,169] New materials such as Miralon™ tapes and sheets are being produced with CNT lengths exceeding 1 mm which allows for higher mechanical properties not only due to shear transfer into a matrix but also due to CNT entanglement.[46] There are also reports of CVD grown CNTs with lengths of 550 mm though bulk mechanical properties have not been measured yet.[170]

Including CNTs into composites has traditionally been difficult due to their tendency to agglomerate upon mixing into the polymer matrix at volume fractions larger than 1-2%. This agglomeration is driven by the high surface area and high aspect ratio

combined with the van der Waals' forces between tubes in solution thus is more severe for the higher performance SWCNTs.[112] Further degradation during dispersal using ultrasonication or high shear mixing can often occur. Many approaches to overcome these issues have been attempted with the formation of free standing CNT films and subsequent infiltration/coating. These free standing CNT films are typically made through vacuum filtration using a Buckner filtration system thus giving the nickname "buckypaper".[153] Solvent free methods have shown higher performance due to the avoidance of bundle formation and agglomeration which occurs during dispersion in solution. Once these buckypapers are produced, infiltration can be performed using many different methods including precipitation, in-situ polymerization, mechanical/vacuum infiltration, chemical vapor deposition, and even electrodeposition.

The failure modes for multiwalled CNTs (MWCNTs) under tensile stresses are bending/buckling, sliding/telescoping normal to the bundle axis, or twisting.[33] Composite strength is due to interfacial strength which due to the smooth surface can be low. Surface functional groups are typically used to increase shear transfer to the matrix and this can be done by oxidation or polymer grafting. Because these functional groups are covalently bonded to the CNTs, they inherently introduce defects into the graphite structure by changing the carbon bonding from sp^2 to sp^3 hybridization. These defects can in turn reduce the reinforcement capability of the tubes significantly.

Past mechanical testing on high volume fraction (>70% by vol.) was disappointing as the strength and modulus of buckypapers and initial composites were many orders of magnitude lower than theoretical. In many of these tests the mechanical properties are surprisingly low with strengths of less than 50 MPa being common and pure buckypaper samples showing even worse behavior.[48] More commonly tests are performed at mass loading around 1-20 wt. % with a variety of polymer composites: Poly(p-phenylene benzobisoxazole) (PBO) (>10 wt. % SWCNT),[171] polymethyl methacrylate (PMMA, 20 wt. %),[172] and polyethyl and methyl methacrylate (PMMA-co-

EMA) (1,5,10 wt. % MWCNT).[173] Many of these reports are unable to accurately measure their CNT lengths due to agglomeration and solution processing, however this parameter has been shown to be critical for increased strength of CNT composites.[168] Due to the availability of short ~100 μm long CNTs which are easily dispersed and filtered to form buckypaper there are many mechanical tests with low results. Buckypapers with substantial strength increases have been observed when the CNT length exceeds ~1.3 mm.[166,167]

Design of Multifunctional Systems

Multifunctional materials can offer significant advantages in energy storage and mechanical functionally particularly in situations that are mass sensitive such as aerospace (particularly unmanned aerial vehicles) and transportation. In order to develop a metric to measure the benefit of these multifunctionalities for supercapacitor applications O'Brien developed a multifunctional efficiency term (η_{mf}) which is based on the assumption that the system design criteria must remain met and the total system mass must be lowered,[174]

$$\eta_{mf} = \eta_e + \eta_s > 1 \tag{68}$$

where the electrical $\eta_e$and mechanical $\eta_s$efficiency terms are additive and for positive weight savings $\eta_{mf} > 1$. The electrical and mechanical efficiency terms are defined in relation to the component that is being replaced with the multifunction component. For design criteria based on energy storage capacity and modulus these efficiency terms are as follows,

$$\eta_e = \frac{U_{mf}}{U_o} \; ; \eta_s = \frac{E_{mf}}{E_o} \tag{69}$$

With U_{mf} energy storage capacity for the multifunctional material, U_o being the energy storage capacity for the currently used device (~120 mAh/g for a typical LIB), E_{mf} being the modulus of the multifunctional material, and E_o being the modulus of the

structural component the multifunctional battery will replace. This provides a convenient estimate of the system mass savings simply by comparing the electrical and mechanical performance of the multifunctional components with the usual components.

Interestingly, the additive property of these separate multifunctional efficiencies allows for substantial reduction of the multifunctional properties with respect to the fully optimized properties while still achieving weight savings. This is demonstrated by comparing a multifunctional composite which only achieves 60% of the electrical and mechanical performance of the original component (η_e=$\eta_s = 0.6$) which leads to a 20% increase in total multifunctional efficiency. This process can similarly be applied to other multifunctionalities that scale with mass such as volumetric and gravimetric battery capacity and capacitor capacitance, as well as mechanical stiffness or strength. In order to achieve these efficiencies drastic changes must be made to the traditional cathode, anode, capacitor electrodes as current design is based on particles embedded in a polymer binder applied to a soft metal (Al, Cu) current collector.[175] Current attempts to make multifunctional battery materials have not succeeded in achieving positive multifunctional efficiencies however structural supercapacitors have been able to provide beneficial.[174] For batteries the most success has been achieved by simply embedding commercially available battery systems into the structure and using the battery packaging itself as mechanical reinforcement. This has resulted in a 26% increase in flight time for a UAV without changing the weight of the system.[11,176]

CHAPTER 3

ALUMINUM NANOWIRE SYNTHESIS FOR SUPERCAPACITOR SUBSTRATES

3.1 Introduction and Motivation

Potential use of metal nanowires (NWs) is rapidly growing. Earlier studies of metal NWs were largely motivated by fundamental studies of the effects of constrained dimensions on electrical and thermal conductivities in one dimensional (1D) conductors[177-179] and magnetic properties of transition metals.[180-182] The size-dependent breakdowns of superconductivity in small diameter NWs draw a particular interest in the last decade.[177-179] Other important potential applications include sensors,[183] ultra-high-density magnetic recording and spintronics,[184] interconnects,[185] transparent current collectors (charge collectors) for touch screens and organic solar cells,[186] catalysis,[187,188] fuel cells,[188] active anodes for Li-ion batteries,[31,189] hydrogen storage,[190] current collectors for Li-ion batteries,[9,191] supercapacitors,[19,192] and capacitors.[193]

Currently, conductive carbon nanotubes (CNTs) mass-produced by chemical vapor deposition (CVD) are explored in some of the discussed above applications. However, the CNT structure suffers from the lack of surface sites available for the formation of chemical bonds with the deposited functional layers (such as metal oxide coatings).[9,19,191-193] While surface oxidation of multi-walled CNTs allows for the

formation of defects and carboxylic surface groups on their outer walls, the concentration of the functional groups on a CNT surface is significantly smaller than what is available on the metal surfaces. As a result, the quality of a CNT/metal oxide interface is generally inferior to that of a metal/metal oxide one.[194] More importantly, due to the low concentration of free electrons in CNT, the dc electrical conductivity of CNT is orders of magnitude smaller than that of Cu, Al, Au or Ag. Therefore, for most applications requiring high surface area conductors [9,19,185,191-193] with low resistance and high concentration of bonding cites on their surface, NWs of low-cost lightweight highly conductive metals (such as Al) may provide superior performance than CNTs.

The most common route for synthesis of metal NWs is electrodeposition.[9,177-183,191] The use of porous alumna templates attached to the conductive substrate surface has become a routine approach for the growth of aligned NWs.[9,177-179,191] The slow deposition rate and the need of tubular templates, however, prevent large-scale commercial synthesis of metal NWs using electrodeposition approaches. Several promising wet chemistry approaches have also been explored for metal NW synthesis inside the pores of self-assembled organic nanotubes.[195,196] Yet, the lack of sufficient control over the NW dimensions and limited yield prevented successful commercialization of these synthesis routes. Similar shortcomings are also present in another interesting approach - a glancing angle deposition (GLAD), in which a metal is sputtered on a target at a large incident angle.[189] The random initial nuclei formed on the substrate act as seeds for NW growth, while the growth at other areas is restricted by the shadowing of those initially grown nanocrystals.[189]

The rapid growth and large scale synthesis capability of CVD combined with a high precision in controlling the metal NW dimensions makes CVD one of the most promising approaches for metal NW synthesis. Surprisingly, in contrast to the significant progress achieved in CVD growth of CNTs and semiconductor nanowires, very limited studies report the template-free CVD growth of metal NWs.[135,136,197-200] The literature

search revealed only reports on CVD growth of Mo NWs on Si, Al_2O_3 and steel, [197] Pt NWs on SiO_2, Ni alloy, and $SrTiO_3(100)$; [198] Ni NWs on SiO_2, [199] Cu NWs on SiO_2 and Si [135,136] and Fe NWs on SiO_2. [200] However, for use of metal NWs in energy storage devices, [9,19,31,189,191-193] an abundant, low-cost, highly conductive, corrosion-resistant and lightweight Al could be of higher demand. Particularly, if AlNWs are grown on conductive metal foil substrates in order to establish a good electrical contact within an electrode. To the best of our knowledge, however, there have been no reports on AlNW growth by CVD on any substrate. Furthermore, we were unable to find reports on the patterned CVD growth of metal NWs, needed for discreet device fabrication.[193]

In this manuscript we report for the first time a patterned growth of freestanding AlNWs on Ni, Fe, and Cu surfaces using trimethylamine alane (TMAA) as an organometallic CVD precursor. We further demonstrate that the deposition of metal oxides on AlNW surface allows one to achieve one of the highest specific capacitances reported to date for supercapacitor applications. In our proof-of-concept studies we utilized vanadium oxide (VO_x) as a coating material due its chemical stability, wide availability, and the large potential window for oxidation/reduction reactions to occur.[73-80] In order to synthesize AlNW – VO_x composite electrodes we employed atomic layer deposition (ALD) to uniformly deposit VO_x onto AlNW substrates. To the best of our knowledge, ALD technique has never been employed for supercapacitor applications and the achieved gravimetric capacitance of up to 887 F/g (based on the mass of Al nanowires and a metal oxide) is higher than the specific capacitance of 601 F/g recently demonstrated in MnO_2 - nanoporous gold nanocomposite.[192] The VO_x coated Al nanowire electrodes with 30-50% of the pore volume available for electrolyte access show volumetric capacitance of 1390-1950 F/cc, which exceeds the volumetric capacitance of porous carbons and many carbon-metal oxide composites by more than an order of magnitude. [65,189,201-206]

3.2 Results and Discussion

Synthesis and Characterization

The uniform large area (tens of cm^2) deposition of AlNWs was successfully achieved on Ni, steel, and Cu foils (Figure 40a) at temperatures as low as 125 °C. Most of the produced NWs had smooth surface with no crystalline facets visible, were 20-120 nm in diameter and had multiple branches, as visible from scanning electron microscopy (SEM) analyses (Figure 40b). The overall morphology of the NWs was highly tortuous with frequent irregular bends (Figure 40b). The length of the straight segments of the NWs rarely exceeded 300 nm. This wormlike structure of the NWs was observed in all experiments, independent of the substrate employed. SEM image analysis revealed a high volume of pores between the NWs (> 93 %). Energy dispersive spectroscopy (EDS) studies confirmed the composition of AlNWs and detected a trace amount of oxygen (Figure 40c), likely from the presence of a native oxide on the Al surface. Importantly, no carbon contaminates were detected at temperatures below 150 ºC (Figure 40c).

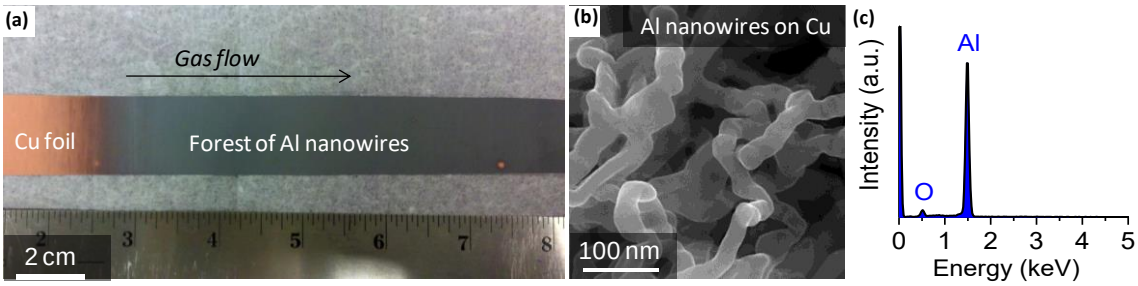

Figure 40. AlNWs grown on a rough Cu foil at 125 °C: a) optical micrograph showing uniform large-area deposition of AlNWs, b) SEM micrograph showing a high resolution image of curved AlNWs produced, and c) a typical EDS spectrum taken at a region containing AlNWs.[32]

Deposition temperature was found to have a profound effect on the NW growth rate. CVD deposition at 100 ºC was very slow with only isolated Al nuclei observed on the metal substrates after 1 h synthesis (Figure 41a). The successful growth of the NWs was achieved on all substrates within the temperature range of 125 – 300 ºC (Figure 41b-

e). However, increasing synthesis temperature above 200 ºC caused noticeable co-deposition of carbon, likely due to the pyrolysis of the trimethylamine component of TMAA. At the highest synthesis temperature of 400 ºC the amount of the deposited C reached ~50 at. % according to EDS analysis and the non-porous nanocrystalline film formed instead of NWs (Figure 41f).

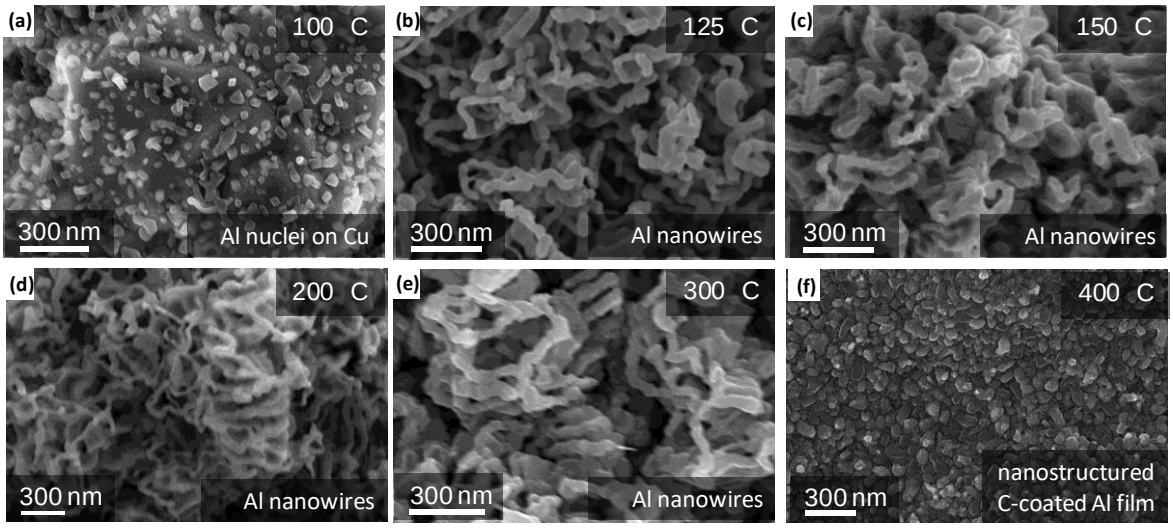

Figure 41. SEM micrographs of CVD deposition of AlNWs onto rough Cu foils at different temperatures: a) 100 °C, b) 125 °C, c) 150 °C, d) 200 °C, e) 300 °C, and f) 400 °C.[32]

The maximum growth rate was commonly observed at temperatures between 100 and 200 ºC (Figure 42a). Temperature of 100 ºC and below was too low to provide thermal energy sufficient to overcome the energy barrier needed for the rapid nucleation and growth of Al from the vapor phase. Significant decrease in the Al growth kinetics at temperatures above 300 ºC (Figure 42a) was hypothesized to be linked to the C co-deposition. The choice of metal substrates was also found to affect the AlNW growth kinetics. For example, the peak in the AlNW growth rate on Cu and Ni foil substrates takes place at slightly different temperatures, at 125 °C for Ni and 150 °C for Cu (Figure 42a). The slight difference is explained by the differences in the energies of the Ni/gas, Ni/Al, Cu/gas and Cu/Al interfaces, which should affect the nucleation barrier.

Additionally, we cannot exclude a possible effect of the H_2 absorption by Ni on the NW nucleation and growth. Hydrogen desorption is known to be the rate-controlling step in TMAA decomposition and the increased removal of surface H_2 due to its absorption by Ni may similarly explain the increased growth kinetics observed at lower temperatures.[207]

In contrast to our initial expectations rationalized by the higher mobility of surface atoms at elevated temperatures, increasing the synthesis temperature did not increase the average diameter of NWs. In contrast, this temperature increase, in fact, reduced the average diameter of NWs grown on metal substrates (Figure 42b). The observed decrease in the diameter could be related to the smaller size of stable nuclei, expected at higher temperatures where the nucleation barrier is lower. Figure 3c shows a typical NW diameter distribution with an average diameter of 63 nm and a standard deviation of 17 nm, as measured using SEM image analysis. Very similar distributions with average diameters of 45-87 nm and standard deviations of 25% were observed in all substrates and deposition parameters.

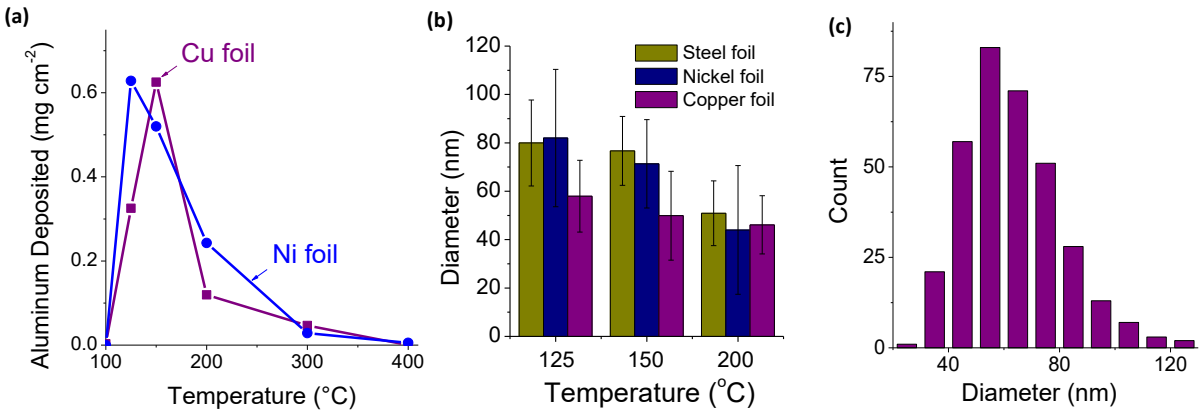

Figure 42. Diameter and deposition rate of Al nanowires on metal foil substrates: a) mass of Al nanowires deposited on metal foil substrates at different temperatures for 1h, b) average diameter of Al nanowires grown on several metal substrates as a function of deposition temperature; c) diameter distribution of Al nanowires deposited on Cu foil at 125 °C.[32]

The virtually no dependence of the average NW diameter on the length of the deposition process or on the distance from the metal foil substrate suggests that incorporation of Al takes place primarily on the NW tips and not onto the sidewalls of the NWs. This was surprising because no metal catalyst was used and, therefore, one may expect that a sticking coefficient of atoms onto different Al surfaces should not demonstrate very large differences. We propose two possible explanations: either the growth process is self-catalytic or there is a large TMAA concentration gradient at the gas/ALNW forest interface. This concentration gradient may arise if the decomposition of the TMAA on the AlNW surface is so fast that only a small fraction of the TMAA molecules diffuse into the depth of the AlNW forest. Alternatively, a self-catalytic growth may take place when a freshly-formed Al layer on the tip has sufficiently lower energy barrier (in other words, it has a higher surface energy because of the higher nanoscale roughness or higher concentration of defects at the NW tip) than the sidewalls of the NWs. We should additionally note that the NW tips may have higher local temperature because of the heat released upon the exothermic decomposition of TMAA.[207] This higher temperature at the tips may significantly reduce the energy barrier and support the tip-based growth.

The transmission electron microscopy (TEM) studies showed the crystalline structure and dense (no voids) morphology of the NWs (Figure 43a, b). In spite of the tortuous shape of the NWs, TEM studies demonstrated most of the NWs to be free from extended defects. This indicates a stress relaxation (commonly by slipping of extended defects to the NW surface) either during or after the growth. We found only a few mirror-like twin boundaries in AlNWs, commonly in those having larger diameters (Figure 43a, b). Although twinning is an important and quite common mechanism for plastic deformation in metals, pure bulk Al very rarely undergoes twinning due to its very high stacking fault energy (SFE).[204,208]

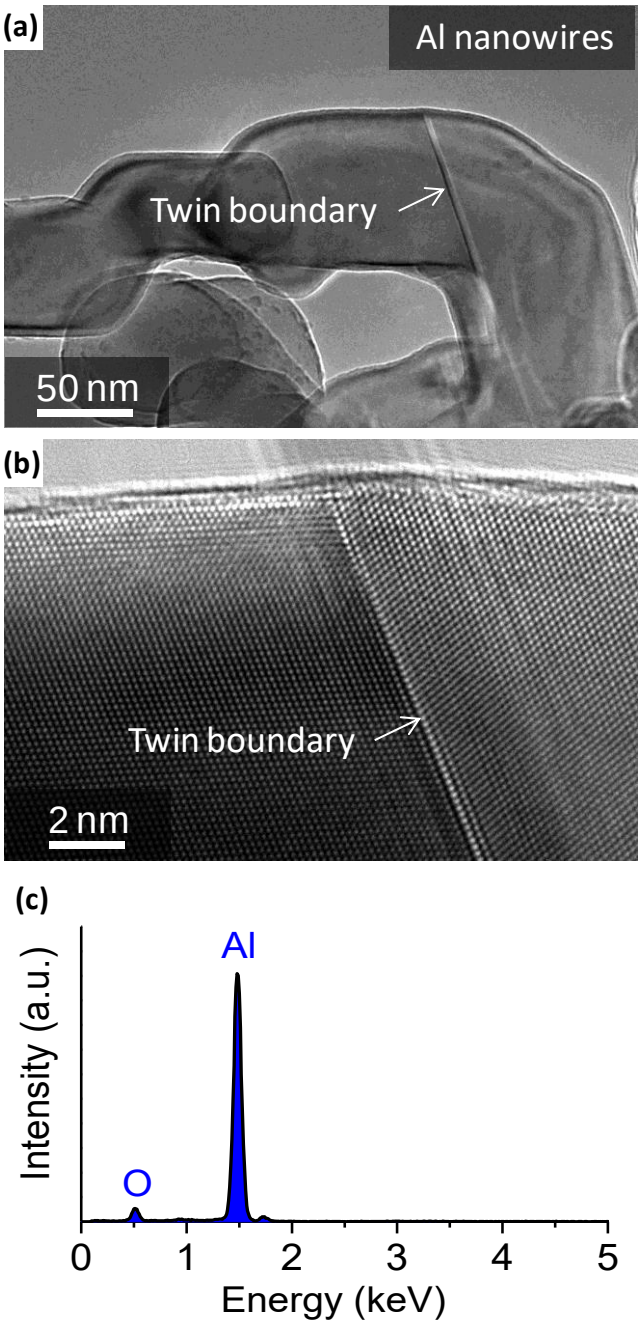

Figure 43. a) Low and b) high resolution TEM micrographs showing a twin boundary within an AlNW grown on the Cu surface at 125 °C; c) EDS spectra taken from a single AlNW.[32]

According to Warner *et al.* [208] twinning during deformations were never observed experimentally in Al, and only happened at high strain rates in computer simulations or in nanocrystals that deform under very high stresses at low temperatures.[209,210] Therefore,

our observation of twin boundaries in AlNWs in fact suggests significant stresses during their synthesis. We postulate that these stresses were caused by the local temperature variations caused by the exothermic nature of the TMAA precursor surface decomposition process.[211] EDS performed on individual NWs (Figure 43c) showed spectra identical to that of the NW forest (Figure 40c), confirming high purity and uniform oxide content in the produced NWs.

Surface Patterning Capability

In support to our hypothesis on the negative effect of carbon on the NW nucleation and growth (Figure 41f), we found various carbon and polymer coatings on the metal foils' surface to efficiently prevent formation and growth of AlNWs. Due to the low synthesis temperature and the absence of oxygen in our system (Ar is used as a carrier gas), most polymers remain intact or carbonize during the NW deposition. In contrast to native oxide - coated metal surfaces, polymers' presence prevents formation of the stable Al nuclei, emphasizing the importance of the substrate-Al interactions. Using this simple polymer coating method we successfully produced patterned AlNW forest on Cu foils (Figure 44). We expect the patterned growth to be important for some of the future device applications.

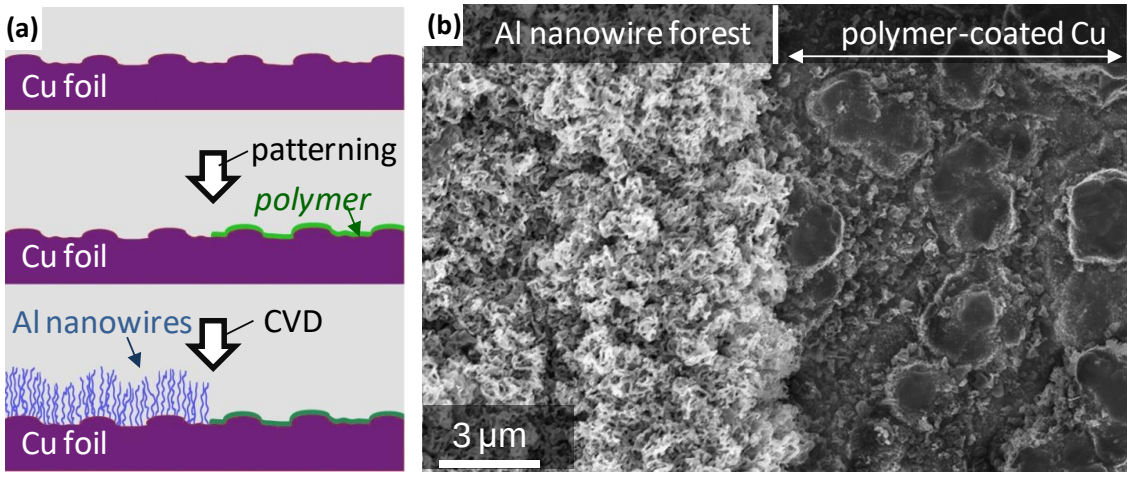

Figure 44. Patterned Al nanowire growth: a) schematic of the process, b) SEM micrograph of a patterned Al nanowire growth on a rough Cu foil at 125 °C. In this case the growth on a portion of the Cu foil was prevented by the deposition of a thin layer of a methylmethacrylate-based polymer.[32]

X-ray diffraction (XRD) analysis was used to independently investigate the crystallinity of the synthesized AlNWs on the variety of substrates and to confirm the lack of crystalline aluminum oxide and aluminum carbide impurities (Figure 45). A brief Williamson-Hall analysis estimated the grain size to be in the range of 40-100 nm, which agrees well with the values for the NW diameters observed in SEM and TEM studies (Figure 41-Figure 43). This analysis also suggested microstrain of up to 9 %. The intensity profile for AlNW diffraction pattern matches that for powder diffraction, as expected from the unaligned nature of the synthesized AlNW forests (Figure 40b, Figure 41b-e).

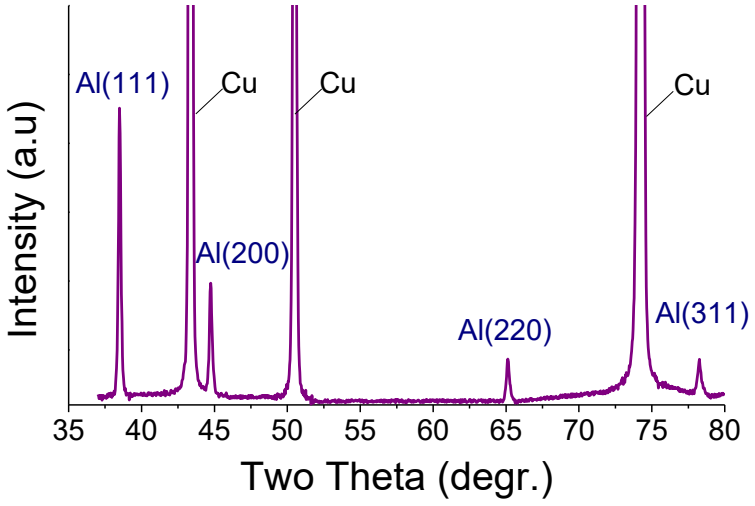

Figure 45. XRD pattern of Al nanowires grown on a rough Cu foil at 125 °C.[32]

High Surface Area Current Collector for VOx Capacitors

To evaluate the electrochemical activity of the grown AlNWs we compared cyclic voltammetry experiments performed on the NWs with that on 17 µm Al foil samples. The experiments were performed within the voltage range of 1 to 0.01 V *vs.* Li/ Li^+ at a scan rate of 1 mV/s. These results showed an order of magnitude higher Li ion insertion and extraction current densities for the NW sample than that for the plain Al foil (Figure 46), confirming significantly higher electrochemically active surface area of AlNWs.

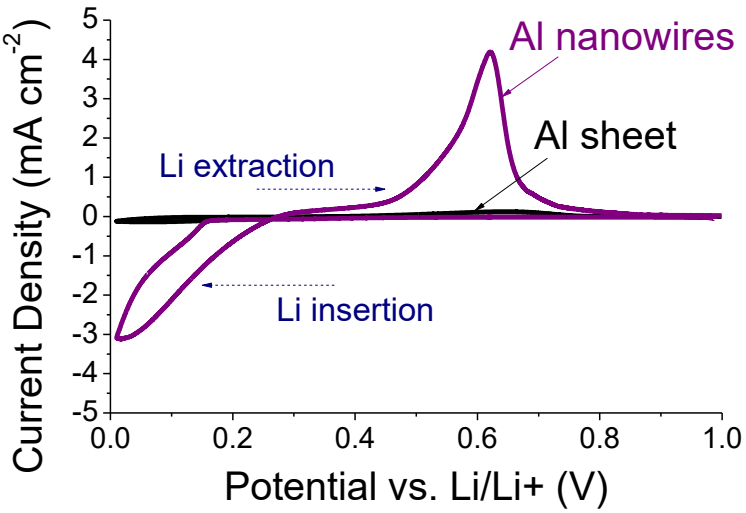

Figure 46. Electrochemical activity of Al nanowires in Li half cells: cyclic voltammetry recorded at 1 mV/s showing reversible electrochemical interaction of Li^+ ions with Al nanowire electrodes and flat Al sheets.[32]

Electrodes produced by the atomic layer deposition (ALD) of vanadium oxide (VO_x) on the surface of AlNWs were evaluated for supercapacitor applications to provide an experimental demonstration or a proof-of-concept for the AlNW application. In our view the 1D geometry of nanostructured NWs may offer some unique advantages, including higher thermal and electrical conductivity and higher power density of the NW-based energy storage devices.[212] In an ideal case of perfectly straight and aligned NWs (Figure 47a), the pores between them would allow for the shortest ion transport distance within the electrode, thus contributing to minimizing the charging or discharging time. In fact, in our prior studies on pure carbon supercapacitors we demonstrated that changing the pores within individual porous carbon particles from tortuous to straight can reduce the charging time by three orders of magnitude.[65] When nanopores are not straight but relatively large (> 2 nm) (Figure 1f), very high rate performance can still be achieved.[203,206]

Both SEM and TEM studies of the VO_x ALD-deposited on the surface of the selected AlNW samples showed high degree of coating uniformity (Figure 47 b,c). TEM studies additionally showed highly disordered nature of the deposited oxide, while SEM

analyses detected reduction of the remaining VO_x-coated AlNW electrode porosity to below 50% (Figure 8b). EDS studies, in turn, confirmed high purity of the deposited VO_x layer (Figure 8d). TEM studies as well as SEM image analysis before and after VO_x depositions were used to estimate the coating thicknesses.

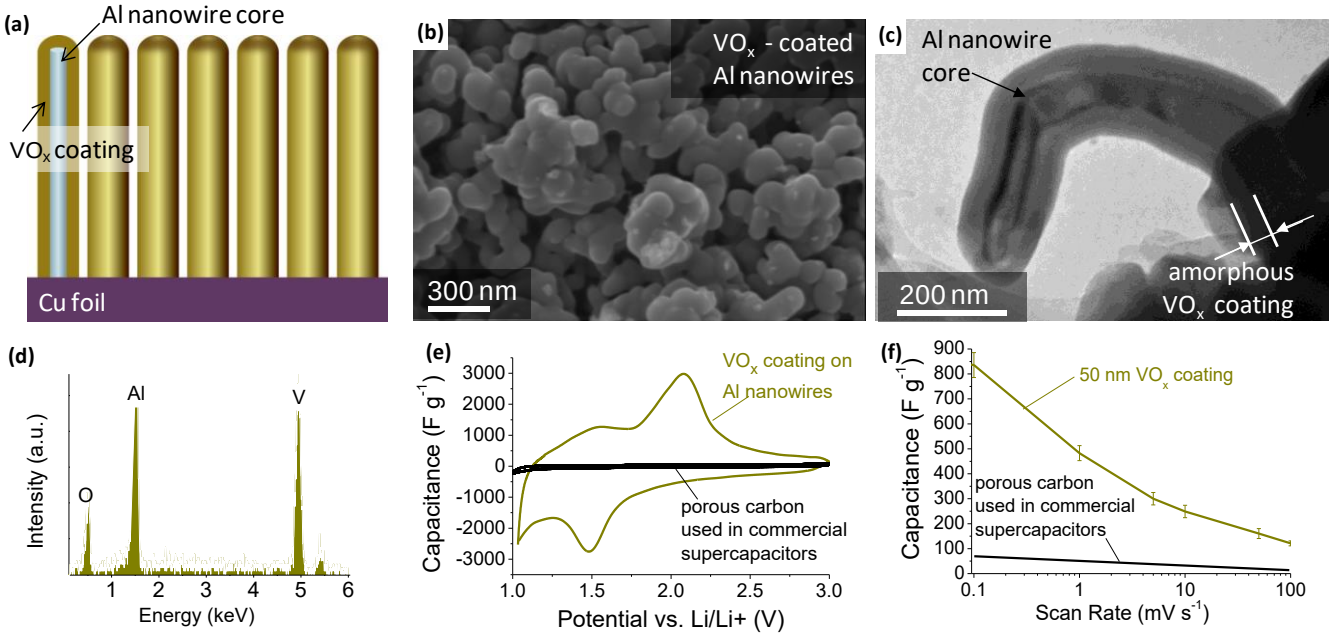

Figure 47. Al nanowire - based supercapacitor: a) simplified schematic of the electrode; b) SEM and c) TEM micrographs of VO_x-coated Al nanowires; d) EDS spectrum of VO_x-coated Al nanowires; e) cyclic voltammetry recorded at 0.1 mV/s for VO_x-coated Al nanowire electrode in comparison to that of porous carbon (capacitance is normalized by the active mass); f) average capacitance as a function of a slew rate for 50 nm VO_x coatings in comparison to that of activated carbon.[32]

An electrochemically active VO_x offers some of the highest capacitance ever demonstrated in organic electrolytes[73-80] (also Figure 47e), but suffers from very low electrical conductivity. The use of lightweight highly conductive AlNW (Figure 47a) overcomes this key limitation. At a very slow slew rate of 0.01 $mV \cdot s^{-1}$ the specific (gravimetric) capacitance of the 50 nm coating approaches 964 $F \cdot g^{-1}$, but it drops to 836 $F \cdot g^{-1}$ and further to 483 $F \cdot g^{-1}$ at 0.1 and 1 $mV \cdot s^{-1}$, respectively. The obtained values are moderately high as compared to 620-2150 $F \cdot g^{-1}$ reported in aerogels and xerogels when

measured with a ”sticky carbon” technique needed to overcome their low electrical conductivity during measurements.[77] In spite of the relatively large oxide thickness, gravimetric capacitance advantage over activated carbon used in commercial devices can be maintained even at high sweep rates (Figure 47f) and even when the mass of Al is taken into account. Indeed, assuming a density of 3.3 g cc^{-1} for VO_x and 2.7 g cc^{-1} for Al, we can easily calculate that the relative weight of Al in a core-shell NW (Figure 47a) composed of a 45 nm diameter Al core and a 50 nm VO_x shell is only 8 wt. %. This is a typical contribution of either a binder or conductive carbon additives in commercial activated carbon – based supercapacitors. The key advantage of the proposed technology over conventionally used porous carbons, however, is significantly higher density and thus volumetric capacitance. Indeed, assuming the true density of the discussed above core-shell NW to be 3.2 $g \cdot cc^{-1}$ and the remaining electrode porosity to be 30-50 vol. % (Figure 47b), the volumetric capacity of the NW electrode reaches 1390-1950 $F \cdot cc^{-3}$, which is 10-100 times higher than the volumetric capacitance of various porous carbon electrodes.[65,189,201-206] This demonstrates the high potential of the AlNW technology for supercapacitor and other energy storage applications. We expect that if we maintain the same core-shell ratio and decrease the shell thickness while optimizing the VO_x microstructure and electrolyte composition, we will increase both the rate capability and the overall capacitance of the supercapacitor electrodes. Similar techniques of the AlNW growth and ALD oxide deposition could be applicable for the fabrication of electrolytic and regular capacitors as well as electrodes for regular and 3D Li-ion batteries.

3.3 Conclusions

A catalyst-free, low-temperature method of producing high purity AlNWs on various metal foil substrates using low pressure CVD technique has been demonstrated. The lack of droplet at the tip suggested a vapor-solid growth mechanism. The presence of twin boundaries in the formed NWs suggested significant plastic deformation during

growth. Various factors affecting and explaining the NW growth have been discussed including substrate material and temperature. Thin polymer coatings were found to be highly effective in suppressing the NW growth, thus opening multiple opportunities to produce controlled patterns of Al NWs. The ALD technique experimentally demonstrated the opportunity to form uniform oxide coatings on the NW surface for use in various energy storage devices. Our future studies will be directed towards the size-controlled growth of aligned Al NWs using catalyst-assisted deposition.

3.4 Experimental Details

Our choice of solid TMAA ($H_3AlN(CH_3)_3$, >95 % purity, Gelest, USA) as an Al precursor[213] was motivated by prior studies of CVD deposition of aluminum films for applications in semiconductor industry, where other organoaluminum precursors, such as trimethylaluminum (TMA), tri-isobutylaluminum (TIBA), and dimethylaluminum hydride (DMAH) showed tendencies for aluminum carbide contamination.[211,214] For CVD synthesis we used a low-pressure (2 Torr) hot-walled horizontal quartz tube reactor having 44 mm inner diameter. Ultra-high purity (UHP) Ar (99.999 %, Air Gas, USA) was used to carry the TMAA vapors to the reaction zone by flowing through a packed bed of TMAA powder at the flow rate of 50 cc min^{-1}. The low pressure in the reactor was maintained using a mechanical pump and monitored using a convection gauge. CVD deposition experiments were performed at 100, 125, 150, 200, 300 and 400 ºC for 1 hour periods respectively. Substrates were prepared of Ni, Cu and 304 stainless steel foils (Alfa Aesar, USA). In addition, rough Cu foil with the coarse surface produced by electrodepositing Cu on Cu (Fukuda, Japan) was employed to study the effects of surface roughness on Al nanowire deposition rate and morphology. Similarly the surface chemistry was studied using smooth Cu foils with a 10 nm layer of thermally evaporated ultra-high purity (99.999%) Fe. The mass of these samples was measured before and after deposition using an analytical balance having 0.01 mg precision.

ALD deposition was done in a custom-built ALD system consisting of a quartz tube heated in a furnace to 200 °C through which precursor vapors were introduced alternatively. Vanadium tri-n-propoxide oxide (Gelest, Inc, USA) and 18 MΩ de-ionized H_2O were used as precursors and were heated to 100°C during the deposition. High purity Ar (99.999 %, Air Gas, USA) was used as both carrier and purging gas and the residence and purging periods were 12 s and 1 s, respectively for the H_2O precursor and 2 s each for the vanadium precursor. All the precursor gas lines were maintained at 100°C during the deposition process. The pressure of the system was maintained at 4 Torr throughout the deposition by means of a rotary vacuum pump.

X-ray diffraction (XRD) experiments using Cu-K_α radiation were performed with a X'Pert PRO Alpha-1 diffractometer (Panalytical, USA) equipped with a monochromator. Scanning electron microscopy (SEM) and energy dispersive spectroscopy (EDS) measurements of the nanowire morphology, diameter and composition were performed using a LEO 1550 microscope (LEO Electron Microscopy Group, DE). ImageJ software was employed for the SEM image analysis to determine the nanowire diameter distributions.[215] Transmission electron microscopy (TEM and STEM) experiments were done on FEI *Titan* 80-300 microscope with field emission gun equipped a CEOS probe-side aberration corrector, HAADF detectors, Gatan Tridiem system an energy-dispersive X-ray (EDX) system. Point-to-point resolution of this microscope is 2.45 Å in TEM mode and 0.8 Å in STEM mode. All TEM experiments were done at 200 kV.

For electrochemical testing the working electrodes were spot welded to 2016 coin cells and assembled in an Ar dry box (<2 ppm H_2O) using a 2325 Celgard (Celgard, USA) separator. The counter and reference electrode was 0.75 mm thick battery grade metallic Li (Alfa Aesar, USA). We selected 1 M $LiPF_6$ salt solution in dimethyl, diethyl, and ethylene carbonate solvents 1:1:1 by volume (Novolyte Technologies, USA) as an electrolyte. Electrodes of 17 μm Al foil were cleaned by acetone and ethanol before

assembly, while Al NW, and VO_x-coated Al NW electrodes were used as produced. Commercial carbon electrodes were produced using 90% wt. activated carbon (Sanwa Components, USA) and 10% wt. PVDF binder (Kureha, Japan). Cyclic voltammetry was performed using a Solartron 1480A (Solartron Analytical, UK) with the potential being swept from the open circuit potential (OCV) to 0.01 V *vs.* Li at a scan rate of 1-0.01 mV/s. Capacitance measurements were performed on as produced VO_x coated AlNW using cyclic voltammetry with the potential being swept from 3-1 V *vs.* Li at a scan rate of 100-0.01 mV/s.

CHAPTER 4

ALUMINUM OXIDE NANOWIRE SEPARATORS FROM AL-LI ALLOYS

Reproduced with permission from D. Lei, J. Benson, A. Magasinski, G. Berdichevsky, and G. Yushin. *Transformation of Bulk Alloys to Oxide Nanowires.* **In Preparation, 2016.**

4.1 Introduction

Advanced energy storage and energy harvesting devices, catalyst support, sensors, flexible electronic devices, lightweight structural composites, building materials, insulation, cutting tools and membranes are examples of the important and rapidly growing applications of one dimensional (1D) dielectric and semiconductor (ceramic) nanomaterials.[216-222] Nanowires, nanowhiskers, nanofibers, nanotubes and other 1D nanostructures have demonstrated truly remarkable abilities for enhancing electrical, optical, thermal and mechanical properties of a broad range of functional materials and composites.[152,223-225] Such performance enhancements significantly exceed that offered by the additions of micron-sized or nano-sized particles, even when 1D nanostructures are utilized at substantially lower mass loadings in composites.

Unfortunately, the vast majority of the synthesis routes to produce 1D nanomaterials, such as catalyst-assisted vapor deposition, physical vapor deposition, hydrothermal synthesis, the use of sacrificial templates and others,[226-229] are relatively expensive and difficult to scale. It is not uncommon for the price difference between particles and 1D structures made of the same material and having the same diameter to exceed 100 and even 1,000 times. This high price and elaborate synthesis process severely limit the opportunities offered by current technologies to satisfy the growing industrial demands of low-cost 1D ceramic nanostructures with controlled dimensions.

Since the discovery of graphene synthesis by exfoliation of graphite particles,[230] a broad range of 2D nanomaterials have been produced by similar routes, where 2D structures are produced by the separation of individual layers in layered bulk crystals.[231-234] Such processes may theoretically be inexpensive and highly scalable, but the separated 2D layers tend to stack back together creating scientific and engineering challenges, which significantly increase cost and reduce production capacity normalized by the reactor volume. Furthermore, in many applications 1D materials may be more attractive than their 2D counterparts. But in contrast to thousands of papers on 2D materials, examples of the formation of 1D materials from the bulk are very rare. In one interesting example, small nanowires of TiO_2 and VO_x have been produced from 2D layers.[235,236] In spite of the promise, this approach involves exfoliation from layered $Na_2Ti_3O_7$ and V_2O_4, which increases synthesis complexity. In another fascinating example, dense carbon nanotube (CNT) arrays were produced by ultra-high temperature vacuum annealing-induced evaporation of Si from the surface of single-crystalline SiC wafers[237] Unfortunately, the use of a similar methodology with low-cost SiC particles did not yield CNTs.[238]

Here we report for the first time a direct conversion of bulk materials into arrays of nanowires at room temperature. In our process an alloy of a reactive material, lithium (Li), and a nonreactive material, aluminum (Al) is exposed to alcohols, which produce soluble Li alkoxides and aligned Al alkoxide nanowires. Because no catalysts are used in the synthesis process and because the value of the produced byproducts (Li alkoxide) is high, the cost of the produced 1D nanostructures may approach that of Al metal. The produced alkoxide nanowires may be further converted into 1D Al_2O_3 nanostructures by heating in air.

4.2 Conversion of aluminum to alkoxide nanowires

Exposure of β-AlLi alloy to dry alcohols at low temperatures (20-60 °C) results in alloy delithiation (Figure 48). Li component of the alloy reacts with alcohols, thus forming Li alkoxides. These exhibit high solubility in alcohols and dissolve from the surface. The remaining Al atoms may re-organize and/or react with alcohols or impurities. In case of smaller alcohol molecules (e.g., methanol, CH_3OH, ethanol, C_2H_5OH, or isopropanol, C_3H_7OH) formation of Al alkoxides was found to take place (Figure 48) according to the following reaction:

$$AlLi + 4ROH \rightarrow Al(OR)_3 + LiOR + 2H_2 \uparrow \quad (70)$$

The solubility of most Al alkoxides in alcohols is very low, in contrast to Li alkoxides.[239,240] As such, they tend to remain in a solid phase. While bulk Al is known not to be reactive with alcohols without a catalyst,[241,242] the fresh Al atoms with unsatisfied bonds formed upon Li dissolution from AlLi particles are evidently sufficiently reactive to induce formation of alkoxides.

As the Li out-diffusion and dissolution proceeds from the surface of the particles to the core, more fresh Al atoms become available for the reaction with alcohol, provided Al atoms and alcohol molecules are in proximity. The later mostly depends on the diffusion of alcohol molecules through the formed surface layer, which, in turn, depends on the morphology of such a layer, size of the alcohol molecules and temperature (Al^{3+} is significantly less mobile than Li^+ in the β-AlLi phase).[243] In addition, the reaction of porous Al with alcohols with the formation of Al alkoxides induces significant volume expansion and the associated strain energy, which should slow down the reaction rate. Higher mobility of smaller alcohol molecules and smaller volume changes accompanying smaller Al alkoxide formation may explain their significantly higher reactivity (Figure 48).

a

Solvent	25 °C	60 °C
H_2O	Porous Al & AlLi	Porous Al & AlLi
MeOH	Porous Al& AlLi	Alkoxide Powder
EtOH	Alkoxide NW	Alkoxide NW
i-PrOH	Porous Al & AlLi	Alkoxide NW
t-BuOH	Porous Al & AlLi	Alkoxide NW & Porous Al
PhOH	n/a*	Porous Al & AlLi
1-BuOH	Porous Al & AlLi	--
1-HxOH	Porous Al & AlLi	--
1-OcOH	Porous Al & AlLi	--
EG	Porous Al & AlLi	--

b

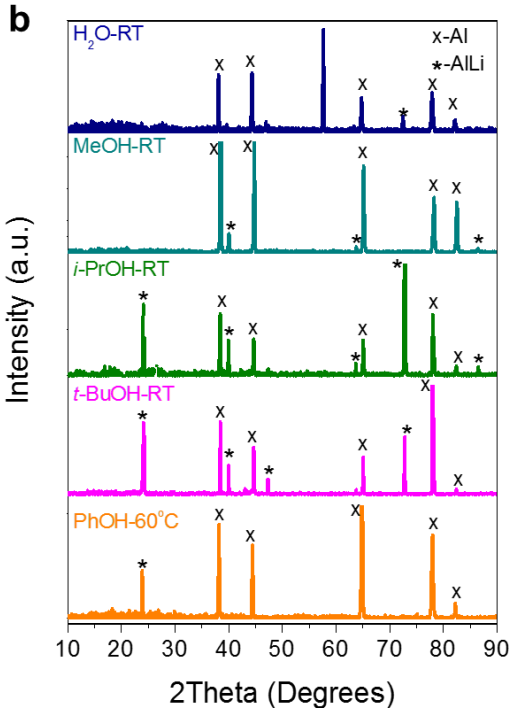

Figure 48. Qualitative summary of the experimental results: a) formation products upon exposure or β-AlLi alloys to water and selected alcohols, NW stands for nanowire morphology of the samples; b) selected XRD spectra of the produced samples, showing formation of Al and remaining AlLi alloy for H_2O, MeOH, *i*-PrOH, t-BuOH, and PhOH solvents. *Phenol is solid at RT thus delithiation was only performed at 60 °C.

One fascinating observation we made in our experiments is the formation of Al alkoxides in the shape of aligned 1D (nano)wires in case of the reaction of Al with ethanol. These structures initiated at the surface of the alloy grain and grew oriented perpendicular to the surface into the center of the grain. Their length gradually increased as the reaction proceeded to the point when the β-AlLi alloy particles were completely converted to Al alkoxide nanowires. Figure 49 shows schematic of this process and representative SEM images in case of the room temperature reaction of the alloy with ethanol and the corresponding formation of Al ethoxide, $Al(EtO)_3$. After 24 h the β-AlLi alloy is completely converted into the nanowires (Figure 49d). By controlling the size of the β-AlLi grains one may control the length of the nanowires. Because identical nanowires were formed from AlLi alloys produced from 99.999 % pure Li and both 99.999 % pure Al and 1145 Al alloy (comprising 99.5 % Al and 0.5 % of Si, Fe, Zn, Cu,

Mg, Mn and other alloying elements) we conclude that their formation was likely neither catalyzed nor strongly influenced by impurities.

High resolution transmission electron microscopy (TEM) studies also confirmed a lack of catalysts at the tips of the formed wires. TEM and X-ray diffraction (XRD) additionally revealed their amorphous microstructure (Figure 50a, c). Selected area electron diffraction (SAED) showed a diffuse pattern, similarly indicative of the amorphous nature of the nanowires (Figure 50a). Energy dispersive spectroscopy (EDS) analysis confirmed the expected chemical composition and the lack of detectable impurities, although it picked up a Cu signal from the TEM sample holder.

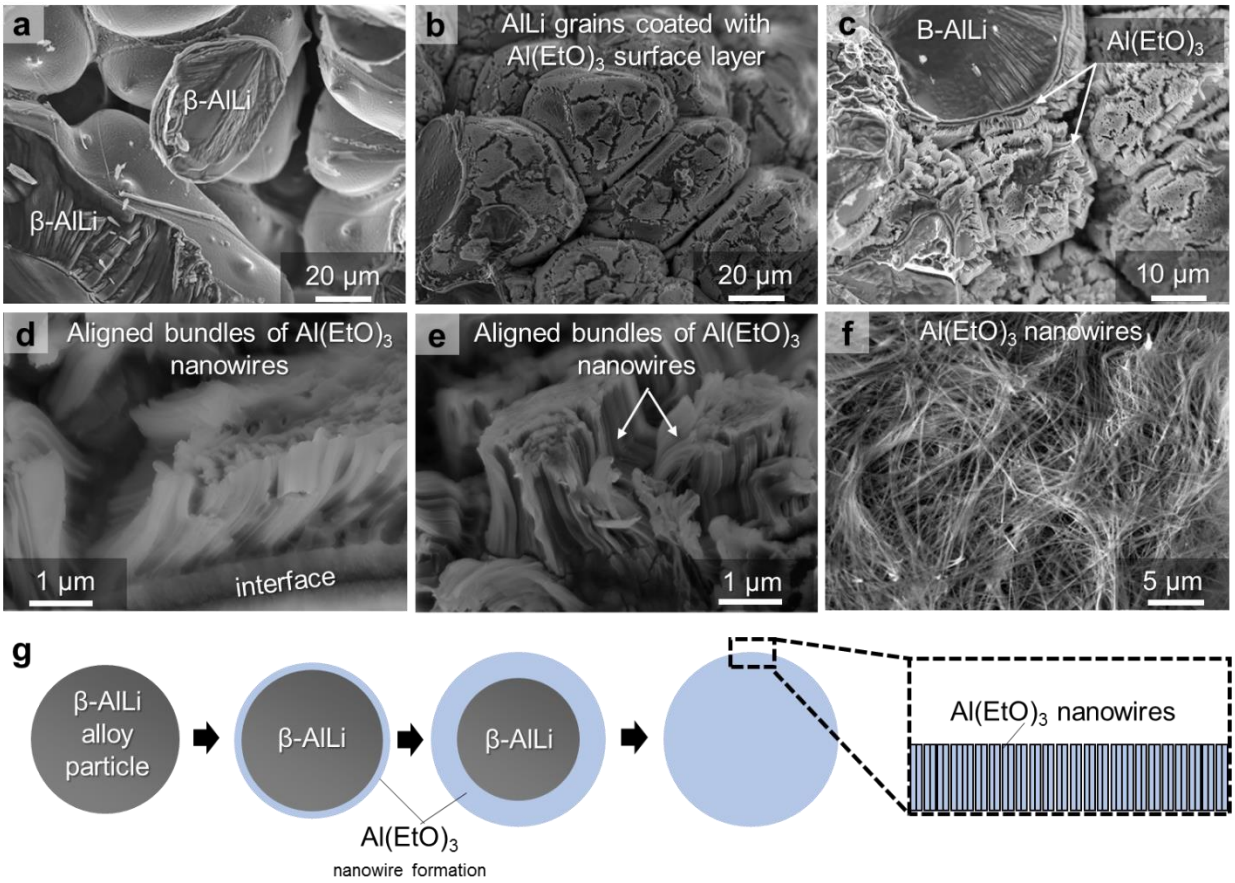

Figure 49. Formation of Al ethoxide nanowires: SEM micrographs showing a) the initial grain structure of the as produced β-AlLi alloy, b-d) low and high resolution SEM micrographs showing formation of the aligned $Al(EtO)_3$ nanowire forest on the surface of the β-AlLi particles after exposure to dry ethanol at room temperature for 30 sec; f) misaligned re-dispersed $Al(EtO)_3$ nanowires produced after completion of the conversion reaction; g) schematic representation of the nanowire formation.

As might be expected from the low melting point $Al(EtO)_3$, the heat generated during TEM imaging (300 kV) was inducing visible damages and shape distortion of nanowires, preventing us from recording high-resolution micrographs during longer collection scans and also possibly affecting the electron diffraction.[244] Thus, XRD was additionally conducted. In order to avoid hydrolysis from air interactions and possible crystallinity changes during drying the produced $Al(EtO)_3$ nanowires, we conducted XRD studies on the samples not exposed to air and suspended in ethanol using a specialized sample holder.

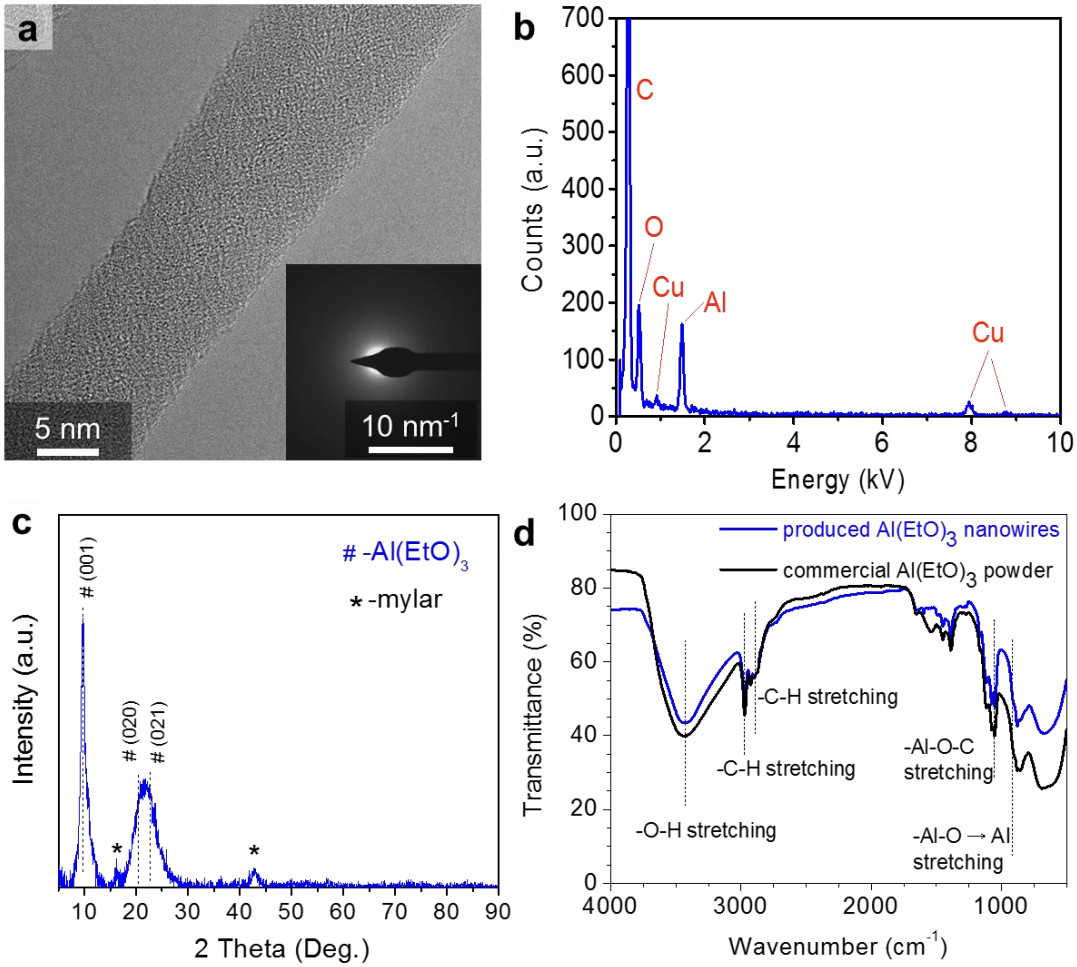

Figure 50. Characterization of Al ethoxide nanowires produced at room temperature: a) HR-TEM micrograph and SAED pattern showing their amorphous structure, b) EDS spectrum, showing its elemental composition, c) XRD spectrum of the nanowires suspended in EtOH (with the background subtracted), d) FTIR spectra of as-produced nanowires (blue) and commercial $Al(EtO)_3$ powder (black), showing identical vibrational modes.

While the literature agree on the monoclinic $P2_1/m$ structure of $Al(EtO)_3$, there is still a debate on the correct lattice and unit cell size[245,246] due to the known difficulty of producing high quality crystalline $Al(EtO)_3$ samples. Yet, according to a reference pattern, very broad peaks at around 10 and 22 degr. could be assigned to diffraction on (001) (10.3 degr.), (020) (20.35 degr.) and (021) (22.7 degr.) planes of $Al(EtO)_3$ (Figure 50c). Their large full width at half maximum gives an estimate of the grain size of only ~ 1.5 nm for the (001) peak, which is considered to be X-ray amorphous. The mostly amorphous nature of the produced $Al(EtO)_3$ is very typical, according to literature.[246,247] Fourier transform infrared spectroscopy (FTIR) analysis conducted on both the nanowire samples and the commercially produced materials additionally confirmed the $Al(EtO)_3$ composition of the nanowires (Figure 50d). The shift and broadening of the 3340 cm^{-1} and 935 cm^{-1} peaks to higher and lower frequencies, respectively, are typical of $Al(EtO)_3$ samples and suggests a partial hydrolysis during FTIR analysis.[239,248]

4.3 Alkoxide nanowire growth mechanism

Formation of the aligned solid nanowires via a non-catalytic, non-epitaxial process at room temperature is quite remarkable and deserves further discussion. As nanowires form uniformly around the crystalline grains (Figure 49), there is evidently no dependence of nanowire formation kinetics on β-AlLi grain orientation and no preferential growth on specific crystallographic planes. This is in contrast to the previously observed dramatic dependence of CNT formation on SiC wafer orientation,[237] a rare example of a somewhat related process where new 1D structures form upon preferential extraction of one component of the material. This suggests that the formation kinetics is controlled via mass transport (diffusion). As the nanowire formation process involves both the extraction of Li from the β-LiAl alloy (with the associated tensile stresses at both the surface layer and the interface with the unreacted alloy) and the insertion of EtO groups (with the associated compression stresses) according to (70), we

propose that interfacial stresses are responsible for the 1D shape of produced $Al(EtO)_3$ products.

The tensile stresses may induce intermediate formation of nanosized cracks within the thin Al layer on the β-AlLi surface and the resultant (crack-separated) nanosized islands. Such islands would transform into $Al(EtO)_3$ and serve as stable nuclei for further nanowire growth. The anisotropic swelling of the islands during this chemical transformation reaction by promoting vertical expansion while suppressing lateral expansion, previously observed in case of Si island lithiation,[249] is expected in case of the formation of a sharp boundary between the transformed (expanded) and untransformed amorphous segment,[249] exactly as observed in our experiments (Figure 49d). In order to minimize strain energy at the $Al/Al(EtO)_3$ interface, the transformation-induced strain will align with the direction normal to this interface, as previously shown.[249] As the β-AlLi de-lithiation and transformation of $Al \rightarrow Al(EtO)_3$ proceeds the strain energy minimization leads to the $Al(EtO)_3$ expansion in the vertical direction, leading to the formation of $Al(EtO)_3$ nanowires (Figure 49d, e). Figure 51a shows the schematic of the proposed formation mechanism and Figure 51b illustrates details of the morphological evolution of β-AlLi-Al surface region into $Al(EtO)_3$ nanowires *via* strain energy minimization at the reaction boundary.

The large pores between the individual nanowires assist with EtOH diffusion towards the unreacted β-AlLi surface and increase the rate of the out-diffusion of Li^+ and the reaction products, H_2 and LiEtO. Because of the significant (~ 600 %) overall volume increase upon transformation of β-AlLi alloy into $Al(EtO)_3$,[250] the particles increase in diameter.

Formation and size of both the Al and Al alkoxide nuclei (Figure 51a) depends on the interplay between the strain energy release upon the crack formation and increase in the interfacial energy. As such, the morphology of the Al alkoxide surface layer should be influenced by the alcohol composition. Interestingly, exposure of β-AlLi to smaller

methanol molecules at room temperature unexpectedly resulted in the formation of a passivating layer (Figure 48). This may be related to the prevention of nano-island (nuclei) formation in the surface layer due to faster reaction of delithiated Al with smaller methanol molecules and thus reduced fracture-inducing surface tensile stresses.

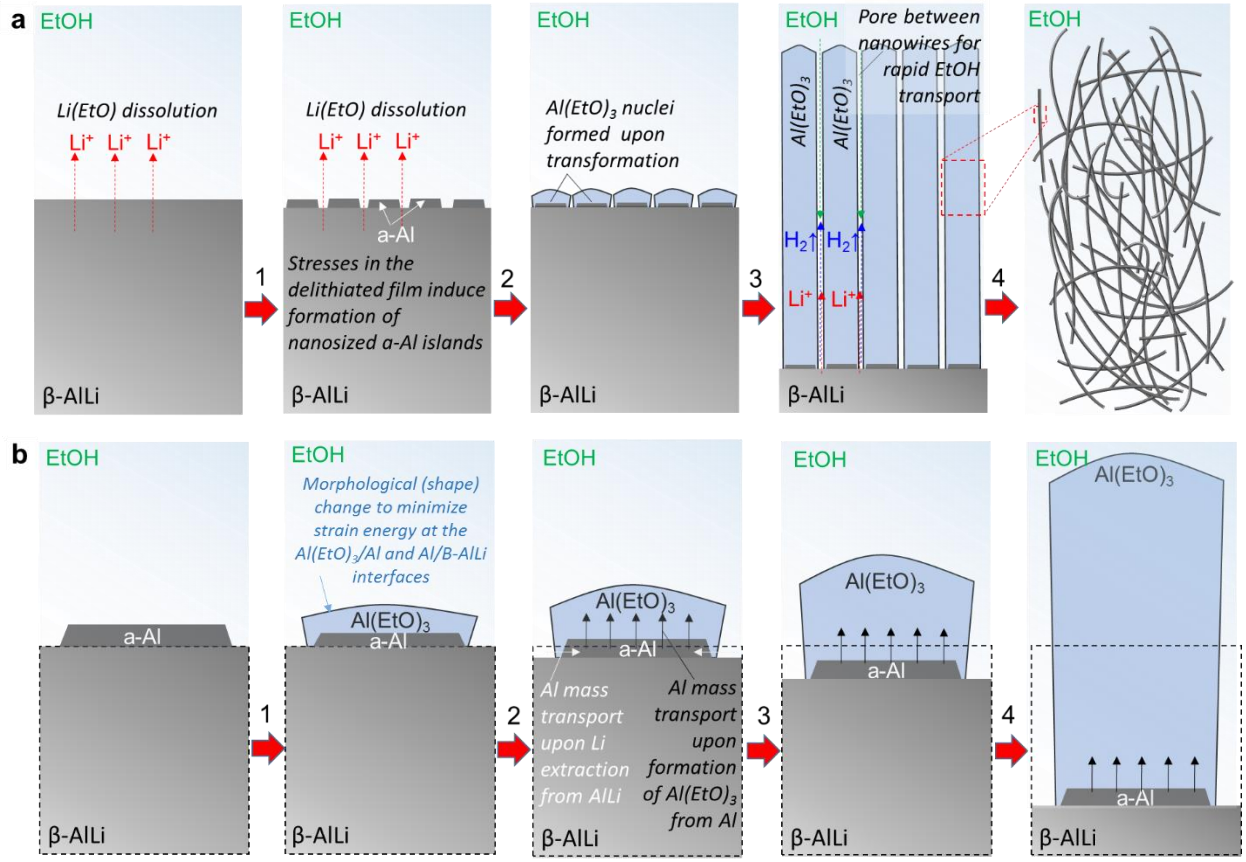

Figure 51. Schematic of the proposed $Al(EtO)_3$ nanowire formation mechanism: a) major process steps, such as (a.1) selective oxidation of Li from the β-AlLi alloy and its dissolution in ethanol resulting in the formation of strained delithiated Al surface layer, the stresses in which induce formation of nano-islands of amorphous Al, separated by surface cracks; (a.2) chemical transformation of the Al nano-islands into $Al(EtO)_3$ inducing formation of nucleation cites for (a.3) further growth of $Al(EtO)_3$ nanowires upon continuous dissolution of Li from β-AlLi alloy until (a.4) all β-AlLi is consumed and transformed into suspended $Al(EtO)_3$ nanowires; b) detailed initial steps of the $Al(EtO)_3$ nanowire formation, such as (b.1) shape change in Al upon formation of the initial $Al(EtO)_3$ nuclei and (b.2-b.4) $Al(EtO)_3$ nanowire growth caused by minimization of the strain energy at the $Al(EtO)_3$/Al (and possibly Al/AlLi) boundaries, which aligns the transformation-induced expansion with the direction normal to these boundaries.

Because mobility of Al^{3+} ions and Al alkoxide molecules increase at higher temperature, the size of the nuclei and the resultant nanowire diameter should be

temperature-dependent. To test this hypothesis we conducted synthesis experiments at moderately elevated temperature of 60 °C. This relatively moderate temperature was selected to avoid boiling of multiple alcohols tested. Similarly to the room temperature case, exposure of β-AlLi alloy to larger molecular weight alcohols resulted in the passivation of the surface layer and the formation of porous aluminum with varying degrees of residual β-AlLi. Smaller EtOH and now both MeOH, *i*-PrOH, and *t*-BuOH yielded Al alkoxides. Interestingly, Al methoxide ($Al(MeO)_3$) sample was in the form of a crystalline powder (Figure 48 and 52), while $Al(EtO)_3$, Al isopropoxide ($Al(i\text{-}Pro)_3$) , and Al tert-butoxide ($Al(t\text{-}BuO)_3$) formed nanowires (Figure 51, 48, and 53). High degree of crystallinity in $Al(MeO)_3$ produced at 60 °C may result in the formation of cracks or openings at grain boundaries and prevent the surface passivation. The lack of $Al(MeO)_3$ nanowires in this experiment may be related to their pulverization due to insufficiently high ductility and elasticity of $Al(MeO)_3$ required to accommodate chemical transformation-induced interface stresses of the relatively large (up to ~ 1 µm) diameter crystals (Figure 52c).

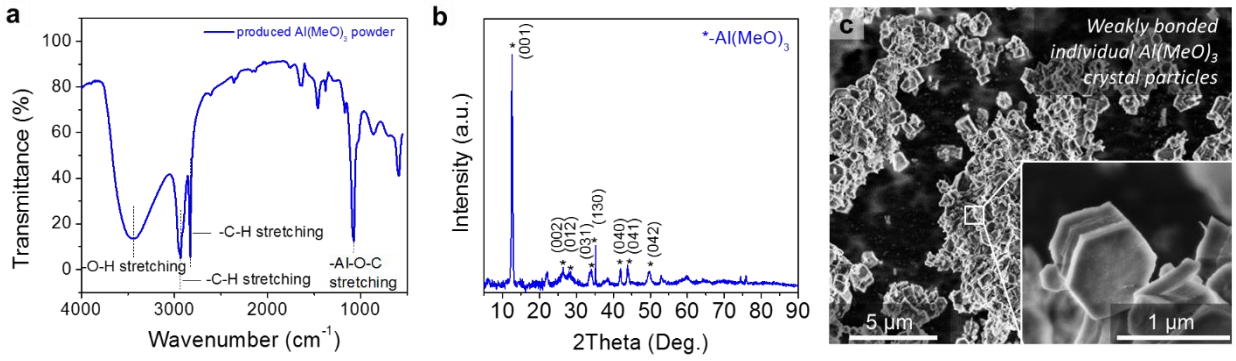

Figure 52. Selected characterization of the $Al(MeO)_3$ powder produced upon exposure of β-AlLi alloy to MeOH at 60 °C: a) FTIR, b) XRD (with the background subtracted), c) SEM micrographs recorded at low and high magnifications.

Higher temperature also allowed reaction of delithiated Al with larger isopropanol molecules, which successfully converted to 1D $Al(i\text{-}PrO)_3$ (Figure 48, 53) nanostructures of ~ 1.1 µm diameter (Figure 54d,e, 53c). Faster diffusion of still

moderately sized isopropanol molecules allowed this transformation reaction to proceed. In spite of the relatively large diameter of Al(*i*-PrO)$_3$ 1D structures, they did not pulverize into smaller crystals. This may be related to (i) partial dissolution of Al(*i*-PrO)$_3$ into *i*-PrOH (due to its significantly higher solubility in alcohols compared to that of Al(MeO)$_3$ and Al(EtO)$_3$)[251] and associated accommodation of the interface stresses by the dissolution-induced pores, to (ii) different growth direction and smoother surface (and thus reduced probability of surface crack formation and propagation)[252] or to (iii) their slower reaction rate when compared to that of Al(MeO)$_3$ (and thus lower stress-loading rate, which should lead to higher fracture toughness).[252]

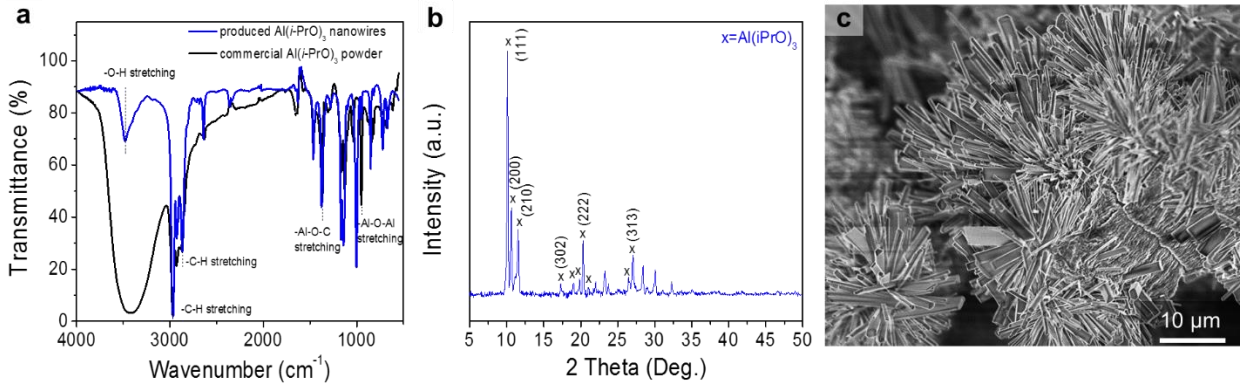

Figure 53. Selected characterization of the Al(*i*-PrO)$_3$ nanowires produced upon exposure of β-AlLi alloy to *i*-PrOH at 60 °C: a) FTIR in comparison with that of the commercial Al(*i*-PrO)$_3$ powder, b) XRD (with the background subtracted), c) SEM micrograph.

Increasing temperature from 20 to 60 °C approximately doubled the average diameter of the Al(EtO)$_3$ nanowires from 41 to 78 nm (Figure 54a,b,e). These experiments emphasize flexibility of our approach to produce 1D nanostructures of tunable diameter. The discovered formation of nanowires and other 1D structures *via* an interplay of the surface tensile stresses upon the dissolution of one of the alloy component and strain energy minimization at the chemical transformation reaction boundary (Figure 51) may be applicable for a broad range of chemistries, thus providing a new methodology for the low-cost synthesis of 1D (nano)materials.

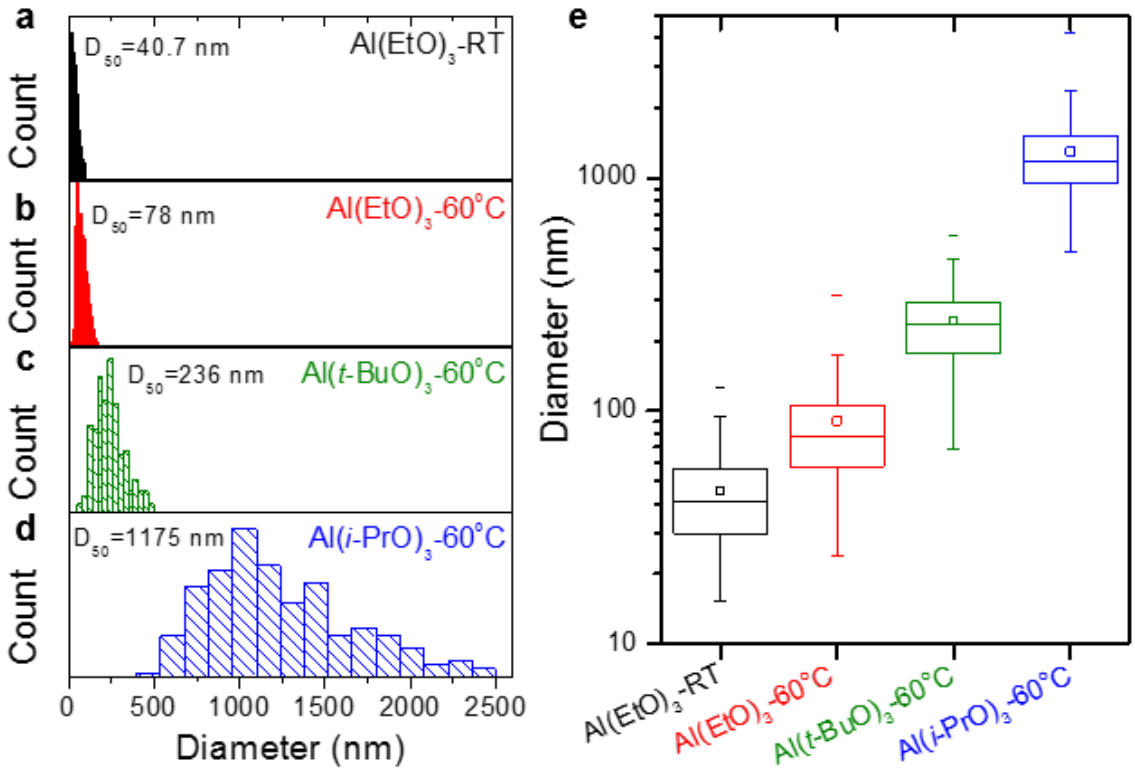

Figure 54. Diameter of nanowires tunable by synthesis temperature and alcohol used: a,b,c,d) image analysis of nanowire diameter distribution, e) average nanowire diameter for four synthesis conditions.

4.4 High performance battery separator synthesis

As an example practical application we produced flexible binder-free nonwoven fabric composed of γ-Al_2O_3 nanowires (AONWs) using a simple tape casting of the initial $Al(EtO)_3$ nanowire suspension in ethanol, followed by a heat-treatment in air (Figure 55). Heat treatment of $Al(EtO)_3$ nanowires in air at atmospheric pressure converts them into AONWs. *In-situ* X-ray diffraction (XRD) was used to show the gradual phase transformation of $Al(EtO)_3$ to Al_2O_3 by heating on a Si wafer substrate from room temperature to 1000 °C (Figure 55a). We used grazing incidence techniques in order to reduce the X-ray penetration depth to <50 μm to avoid measurements of the Al_2O_3 heating stage. The amorphous starting materials transform to γ-Al_2O_3 at around 750-800 °C, in agreement with the previously reported results.[247] SEM images of the γ-AONWs produced by heat-treatment at 1000 °C do not show any signs of pulverization or

significant microstructure changes compared to the initial $Al(EtO)_3$ samples (Figure 55b). Such morphology retention is an important aspect of AONW synthesis for practical applications.

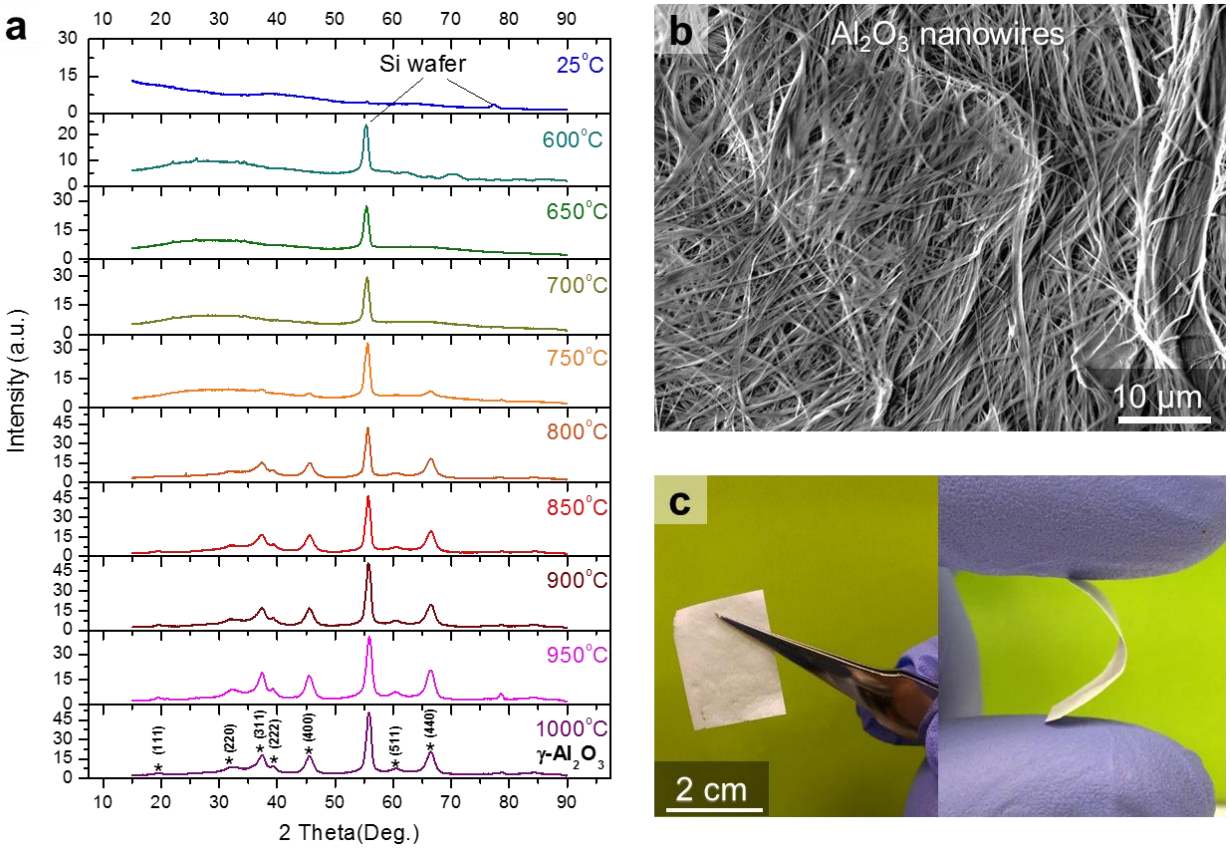

Figure 55. Transformation of $Al(EtO)_3$ nanowires into AONWs: a) *in-situ* HT-GIXRD study of $Al(EtO)_3$ nanowires upon heating in air at the heating rate of 4 ^oC/min; b) SEM micrograph of free-standing nonwoven Al_2O_3 fabric produced upon annealing of $Al(EtO)_3$ nanowires at 800 °C for 2 h and c) its optical images. Diffraction spectrum from the amorphous $Al(EtO)_3$ nanowires is weak and thus is almost not visible.

The overall morphology of the fabric is somewhat similar to that of a paper with cellulose fibers replaced here with stronger and stiffer γ-AONWs. Due to the fibrous nature of thus produced free-standing films and the small diameter of the γ-AONWs, they exhibit good flexibility (Figure 55c). This is in sharp contrast to anodized Al_2O_3 membranes of comparable thickness that are known to be extremely brittle and difficult to handle.

The produced nonwoven γ-Al_2O_3 fabric and related materials may find multiple applications in polymer-, metal- and ceramic composites with enhanced wear resistance, strength and thermal stability, catalyst support and battery separators,[253] among others. Due to the rapidly growing adoption of the environmentally-friendly battery-powered electric vehicles, the development of safer and higher energy Li-ion batteries (LIBs) becomes particularly important. A porous separator is an inactive but very important LIB component that has a major impact on cell safety. A separator should be sufficiently strong to withstand stresses during the battery assembling and operation, provide small resistance to ion transport and, in an ideal case, exhibit excellent thermal stability to prevent shrinking during self-heating (particularly in large format automotive and utility LIBs) which may induce formation of internal short circuits and lead to thermal runaway.[58] Commercial polymer separators suffer from low thermal stability, limited mechanical strength and, in many cases, allow poor wetting of many electrolytes.[56,58] Formation of ceramic-polymer composites only can improve performance to a limited degree.[56,58]

Figure 56 compares results of simple wetting tests on commonly used commercial olefin (polypropylene, PP) separator (top), a less common cellulose fiber (CF) separator (middle row) and nonwoven γ-AONW separator produced in our study (bottom row). In this experiment 5 μL of commonly used commercial electrolyte (1 M solution of $LiPF_6$ in carbonates) was dropped onto separators and the wetted area was measured as a function of time. The wetting rate of the γ-Al_2O_3 separator is significantly higher, as determined by both the final wetting area and the speed of wetting (Figure 57). Additionally, the uniformity of wetting is increased (Figure 56a) because the as-produced γ-AONW nonwoven membrane material is non-directional. Thermal stability tests were performed starting at room temperature and increasing to 800 °C with separator samples placed into the furnace for 2 minutes at each temperature (Figure 56b).

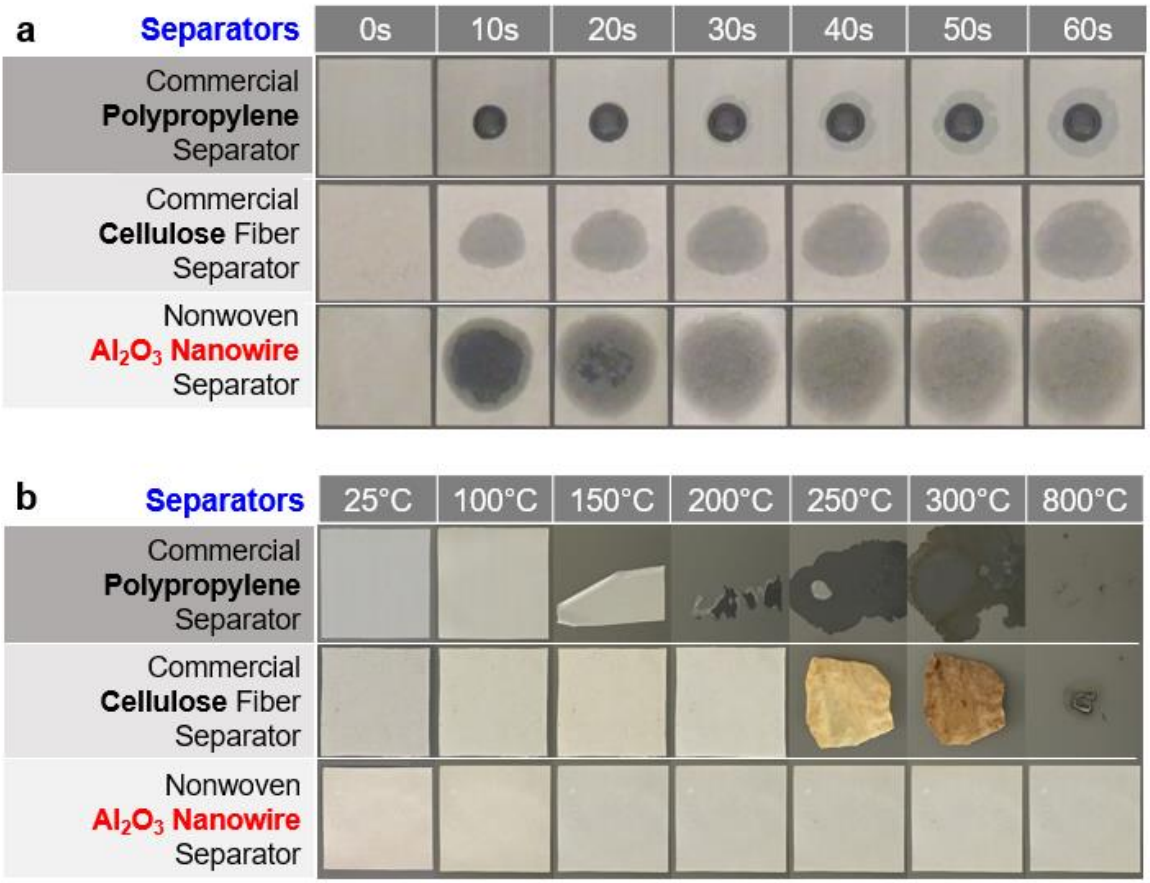

Figure 56. Selected tests conducted on AONW separator in comparison to that of commercial polypropylene and cellulose separators: a) wettability test showing time-resolved optical images of a 5 µl drop of 1M $LiPF_6$ in EC:DEC:DMC (1:1:1) on the separator surface and revealing faster and more uniform electrolyte wetting on AONW separator; b) thermal stability test showing optical images of the separators after 2 min exposure to selected temperatures in the range from 25 to 800 °C and demonstrating dramatically higher thermal stability of the of AONW separator.

The results effectively demonstrate the clear advantage of having a flexible porous ceramic separator with operating temperatures in excess of 800 °C. In contrast, the most commonly used olefin separators typically start melting at around 120 °C and oxidize at around 300 °C.[56] Finally, the strength of ceramic fibers is known to significantly exceed that of the olefins, which should eventually allow formation of thinner separators in automotive LIBs without sacrifice of their mechanical properties. This, in turn, will increase cell energy density. For example, reduction in separator

thickness from 25 to 5 μm shall lead to 13-15 % increase in cell energy density, which typically translates into a similar reduction in the cell cost on the cost-per energy basis.

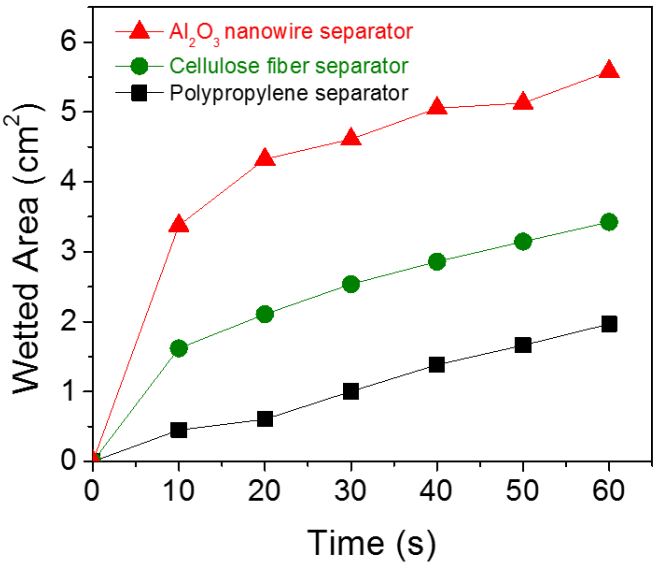

Figure 57. Electrolyte wetted area in AONW separator as a function of time in comparison with that of commercial cellulose fiber and polypropylene separator (as shown in Figure 56).

Figure 58 shows the electrochemical performance of full cells with graphite anode, lithium iron phosphate (LFP) cathode and all three types of separators. While cells with all three types of separators exhibited comparable performance at low (0.1C to 0.5C) current densities, the cells with AONW separators show significantly higher capacities retained at high (1C to 5C) discharge rates (Figure 58a). The lack of detectable oxidation during cell charging to 4.2 V (Figure 58b, d) showed the chemical compatibility of the AONW separator was similar to the commercially available separators. Figure 58b show noticeably smaller 0.5C charge-discharge hysteresis in cells with AONW separator. Such a difference in hysteresis became even more apparent at higher current densities (Figure 58d), suggesting better transport properties and lower cell polarization provided by the AONW separator. Independent electrochemical impedance spectroscopy (EIS) testing of these three separators using symmetric coin cells with stainless steel working and counter electrodes showed consistently higher conductivity of AONW separators (Figure 58c), thus demonstrating their additional advantage in LIB applications.

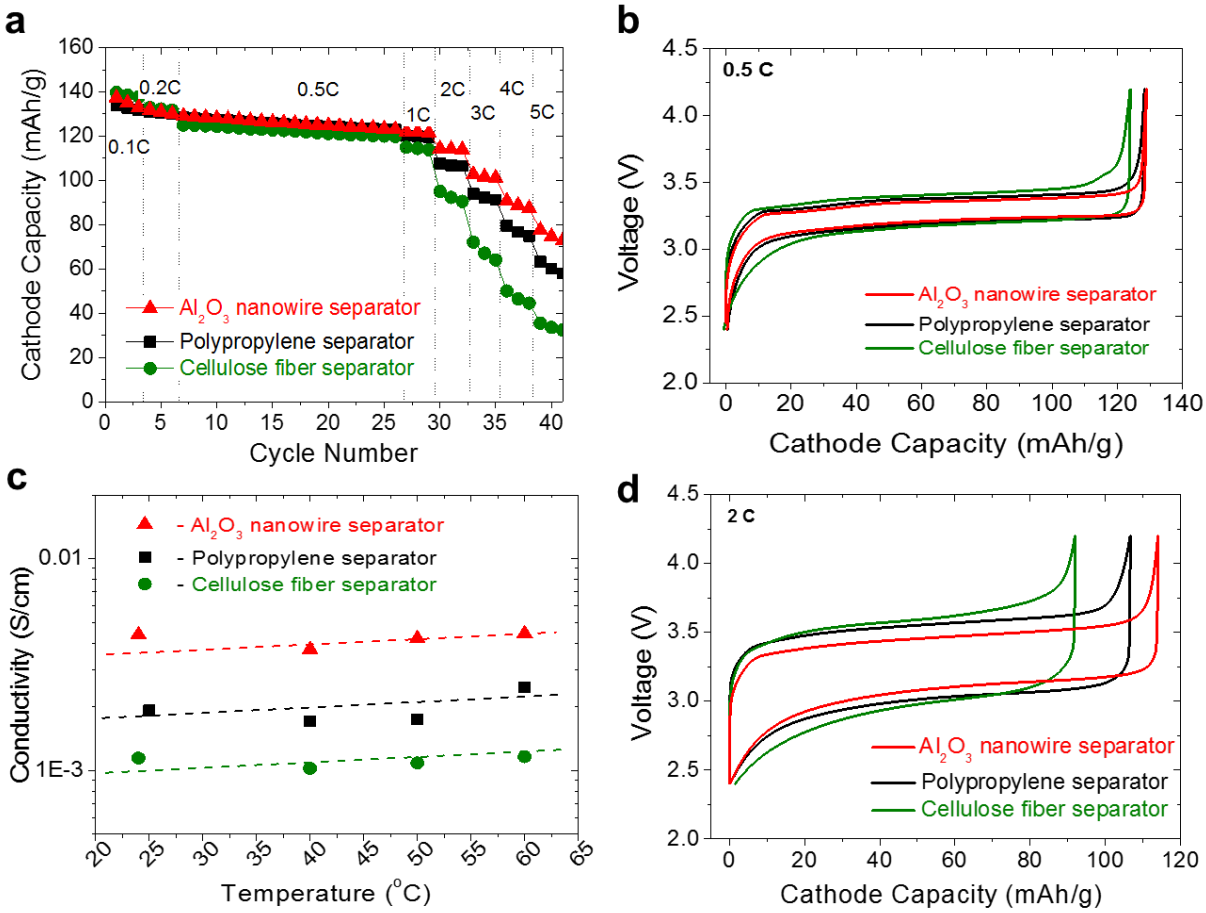

Figure 58. Selected electrochemical characterization of the AONW separator in comparison with that of commercial propylene and cellulose fiber separators: a) rate performance and b, d) typical charge-discharge profile of a full cell comprised of identical graphite anode and $LiFePO_4$ (LFP) cathode in 1 M $LiPF_6$ / EC:DEC:DMC electrolyte at 0.5C and 2C rates; c) ionic conductivity of the separators filled with 1 M $LiPF_6$ / EC:DEC:DMC electrolyte, as measured in symmetric stainless steel-stainless steel cells using an electrochemical impedance spectroscopy technique.

4.5 Conclusions

In summary, by using an example β-AlLi alloy for the formation of Al alkoxides, we have demonstrated a novel methodology for catalyst-free synthesis of organometallic compounds of nonreactive metals by selective dissolution of reactive metal(s) in metal alloys. More importantly, we additionally discovered a promising mechanism for the formation of 1D nanostructures from bulk materials. Such a mechanism is based on minimization of the strain energy at the boundary of chemical transformation reaction

front, which aligns the transformation-induced expansion with the direction normal to this boundary. This novel low-cost synthesis route may be applicable to a very broad range of chemistries. As such, the reported findings provide completely new avenues for scalable synthesis of metalorganic nanowires, which may be transformed into various ceramic nanowires and, in many cases, further reduced to metallic nanowires, thus covering a majority of the applications of nanotechnology. As an example, we have demonstrated formation of flexible thermally stable AONW-based separator for safer Li-ion batteries. Other chemistries and applications will be explored in our future studies.

4.6 Experimental Details

Materials

Battery grade 0.75 mm Li (Sigma Aldrich) and two types of Al (1145 alloy or 99.999 % pure, Sigma Aldrich) sheets were used as alloying materials. Approximately 20 wt.% (50 at.%) of Li was used to produce β-AlLi and was layered between aluminum foil to provide better mixing during melting.[254] Samples were rapidly heated to 750 °C at a heating rate of ~895 °C/min in a graphite crucible with an induction heater (Fluxeon Roy1500, USA). Temperature and heating rate was measured using an optical pyrometer (Calex PyroUSB 2.2, USA). After reaching 750 °C the heating was stopped and the molten sample was immediately flattened inside the crucible using a graphite plunger and allowed to cool in Ar (cooling rate of ~150 °C/min). During chemical delithiation experiments all pellets were placed in 20 mL of anhydrous solvent for the designated time (<24 h for full reaction) without stirring/agitation. After initial reaction the samples were decanted and washed with 10 mL of anhydrous solvent to remove soluble Li alkoxides. All organic solvents were anhydrous and were used as received.

Characterizations

SEM images were collected on a field-emission (FE) LEO 1530 microscope (Zeiss, Germany) at an accelerating beam voltage of 5 kV and a working distance of 5 mm. Image analysis was performed using ImageJ software.[215] Nanowire diameter measurements were performed on at least 150 particles for each sample type. TEM studies were conducted on JEOL TEM 4000EX (JEOL, Japan) operating at 300 kV. XRD studies were performed using a Panalytical MPD (Netherlands) while the high temperature (HT) grazing incidence (GIXRD) studies were conducted using an Anton Parr HTK-1200 hot stage (Austria). GIXRD samples used a constant incidence angle of ω=5°, which provides a penetration depth of approximately 15-30 μm based on mass absorption calculations. A heating rate of 4 °C/min was used with a 5 minute soak and 30 minute X-ray collection period in 50 °C increments from 600-1000 °C. A Cu Kα x-ray source was used with applied voltage of 45 kV and current of 40 mA and the 2θ angles ranged from 20 to 85°. For $Al(EtO)_3$ nanowires suspended in ethanol a XRD was performed in transmission geometry with mylar sample holder and a traditional 2θ-ω geometry in order to increase the diffracted volume. FTIR was conducted with a Thermo Scientific Nicolet iS50 (USA) with an optical velocity of 0.6329 and resolution of 4 cm^{-1}. Thirty two scans were collected to average for both sample and background signals. FTIR samples were prepared in KBr inside an Ar glovebox and analyzed under air.

Electrochemical measurements

Electrochemical studies were performed using commercial carbonate-based electrolyte (1 M $LiPF_6$, ethylene carbonate : diethyl carbonate : dimethyl carbonate (EC:DEC:DMC) mixture, 1:1:1 by vol.) in 2032 coin cells. Graphite anodes were purchased from MTI (USA) and LFP cathodes were obtained from Sila Nanotechnologies Inc. (USA). Charge-discharge tests were conducted using Arbin battery system (USA). Electrochemical measurements were additionally performed in

symmetric stainless steel-stainless steel coin cells using electrochemical impedance spectroscopy (EIS) technique on a Gamry Reference 600+ (USA) with a 10 mV amplitude in the frequency range from 1 MHz to 100 Hz. Temperature was controlled during EIS to an accuracy of ±0.2 °C using a Tenney environmental control chamber.

CHAPTER 5

PANI-CNT COMPOSITES FOR MULTIFUNCTIONAL SUPERCAPACITOR APPLICATIONS

5.1 Introduction and Motivation

A large market push to develop high-performance materials has been observed in mobile structural applications and the energy storage sector. Unmanned aerial vehicles (UAVs), aerospace and space exploration vehicles, satellites, energy-efficient aircraft and ground vehicles, smart textiles and flexible electronics demand both strong and light-weight structural materials and high capacity energy storage.

Most of the improvements in electrochemical energy storage materials have been focused on increasing their ion-storage capacity and cycle life.[83] In spite of the world-wide efforts, rather moderate increase in the energy storage has been demonstrated (~10%/year or less) a trend that does not follow Moore's Law.[255] Weight and volume sensitive applications have traditionally relied on increasing the gravimetric and volumetric energy density of their energy storage materials. Increasingly multifunctional materials have attracted attention as a solution to reduce weight and volume on a system wide level by combining the functions of multiple components using conventional electrode materials.[11,256] Many different modes of multifunctional material implementations are possible, but the most immediately benefits come from combining

structural functions, such as strength, stiffness, fracture toughness, and damping, with non-structural functions, such as electrical and/or thermal conductivity, energy storage, electromagnetic interference (EMI) shielding, radiation shielding and others.

Carbon nanotubes (CNTs) are well known for their good structural properties. [257] Their high strength and modulus combined with low density and the dampening properties of a composite layup, provide a robust multifunctional mechanical response. When used as fillers in polymer composites, CNT must be uniformly dispersed within the polymer matrix and the CNT-polymer interface should be carefully engineered to achieve the transfer of the mechanical load to individual nanotubes.[258-263] Strong chemical bonding between with CNT and the polymer matrix is critically important for achievement of high strength and modulus. Traditional synthesis methods employed to achieve good CNT dispersion rely either on chemical modification or grafting macromolecules onto the CNT surface. The majority of the reported processing methods, however, allow introduction of only small volume fractions of CNTs into the polymer matrix, which does not allow sufficiently high mechanical property values to be attained.[263]

Li-ion batteries (LIB) and supercapacitors are both among the most promising electrochemical energy storage devices with complementary characteristics: LIBs offer high energy density and moderate power density, while supercapacitors offer at least 20 times less energy per unit volume but 20-100 times more power. [264] Early work on structural energy storage devices simply embedded traditional LIB cells into the carbon fiber layup.[265] This provided serious design problems for mechanical compatibility between the host composite and the inserted cells, and made electrical wiring and maintenance difficult. More recently structural batteries used the carbon fiber of the layup as the anode material.[160] Unfortunately, this design was complicated by the polymer sizing used for enhancing the fiber-matrix interface and the mechanical property mismatch between the transition metal oxide cathodes and the polymeric matrix. Several

recent studies explored the deposition of active materials on carbon nanotubes, carbon and polymer fibers, metal nanowires and other structural materials.[32,212,266-272] The reported results provide good examples of multi-functionality demonstrations, but rarely show enhancements of composite mechanical properties after the deposition of active material on the fiber surfaces. In some cases, a reduction of mechanical performance is observed. For example, the CNT-reinforced anode for LIBs demonstrated specific strength of ~100 $kN \cdot m \cdot kg^{-1}$,[212] which showed a great promise for the application of CNTs in multifunctional composites. But, unfortunately, the active vapor-deposited ceramic coating on the CNT surface limited the maximum elongation to less than ~ 1% (*vs.* > 6 % in CNTs before the coating deposition) and the modulus of toughness to only ~ 1 $MJ \cdot m^{-3}$.

In this work, we have used electrodeposition of high-strength, low-cost electrically conductive polymer, polyaniline (PANI), onto the nonwoven CNT fabric to achieve a remarkable combination of high strength and toughness. When tested for supercapacitor and capacitive deionization (CDI) applications, the produced flexible composites showed very rapid ion adsorption and specific capacitances significantly exceeding that of commercial activated carbon powders. These properties translate into high energy and power densities. This approach additionally offers longer cycle life, higher CNT mass loading and makes use of the CNT interconnectivity to reduce electrode resistance. By carefully controlling porosity and coating thickness to optimize volumetric capacity and power characteristics, a smooth electrode surface is achieved which allows thinner separators, elimination of a binder and heavy metal foil current collectors. Elimination of the metal foils also eliminates galvanic coupling which can cause degradation of the device.

5.2 Pulsed Electrodeposition of PANI on CNT Fabrics

According to our approach, we first produced a high-strength binder-free CNT-based nonwoven fabric. In contrast to the majority of CNT film synthesis routes, we utilized a commercial-scale continuous chemical vapor deposition (CVD) process that allows rapid manufacturing of uniform high-strength CNT sheets with tunable mechanical properties. We used ~ 15 μm thick CNT fabric for polymer electrodeposition.

We have selected PANI due to its high conductivity, good environmental stability, tailorable nanostructure, and good mechanical properties.[269,273-275] The strong interaction between polyaniline and CNT through the π–π conjugation of the quinoid rings in polyaniline and the benzenoid rings of CNT results in strong chemical bonding and thus high interfacial shear strength, which tends to be a problem for other CNT polymer systems.[148,151,276] Compared to other traditional supercapacitor active materials PANI is unique in that the ion exchange process by which the polymer equilibrates with acid solutions also imposes the anion into the polymer. This has been the basis for the use of PANI as an anion exchange polymer for mixtures of halide ions and can be used for desalination applications using capacitive deionization (CDI).[148,277-279]

Pulsed electrodeposition was utilized to allow control over the morphology, uniformity and the amount of PANI deposited. Here we report the effect of different peak current densities (2, 4, and 16 $mA \cdot cm^{-2}$) on the composite microstructure and performance. To minimize the effect of other parameters, both the total deposition charge and the total deposition time was kept constant, while the lengths of pulse and relaxation time periods varied to maintain equal charge passed. Active mass was calculated after this drying step and was found to be 31±3 wt.% PANI in all samples.

After the PANI deposition the CNT fabrics not only remained flexible, but have become more resistant to permanent wrinkle formations during handling, as shown in Figure 59a,b. The lowest current density of 2 $mA \cdot cm^{-2}$ resulted in the deposition of a rather homogeneous PANI coating. However, increasing the deposition current resulted

in the evident reduction of the deposition conformality and closed some of the pores (compare Figure 59a,b with d,e). Interestingly, the highest current density of 16 $mA \cdot cm^{-2}$ additionally triggered the growth of elongated PANI nanoparticles (short PANI nanowires) on the CNT surface. After deposition the density of the PANI composite was ~ 1.34 $g \cdot cc^{-1}$, which indicates a significant amount of the remaining porosity (~26 %) since the theoretical density of a fully dense composite exceeds 1.8 $g \cdot cc^{-1}$.

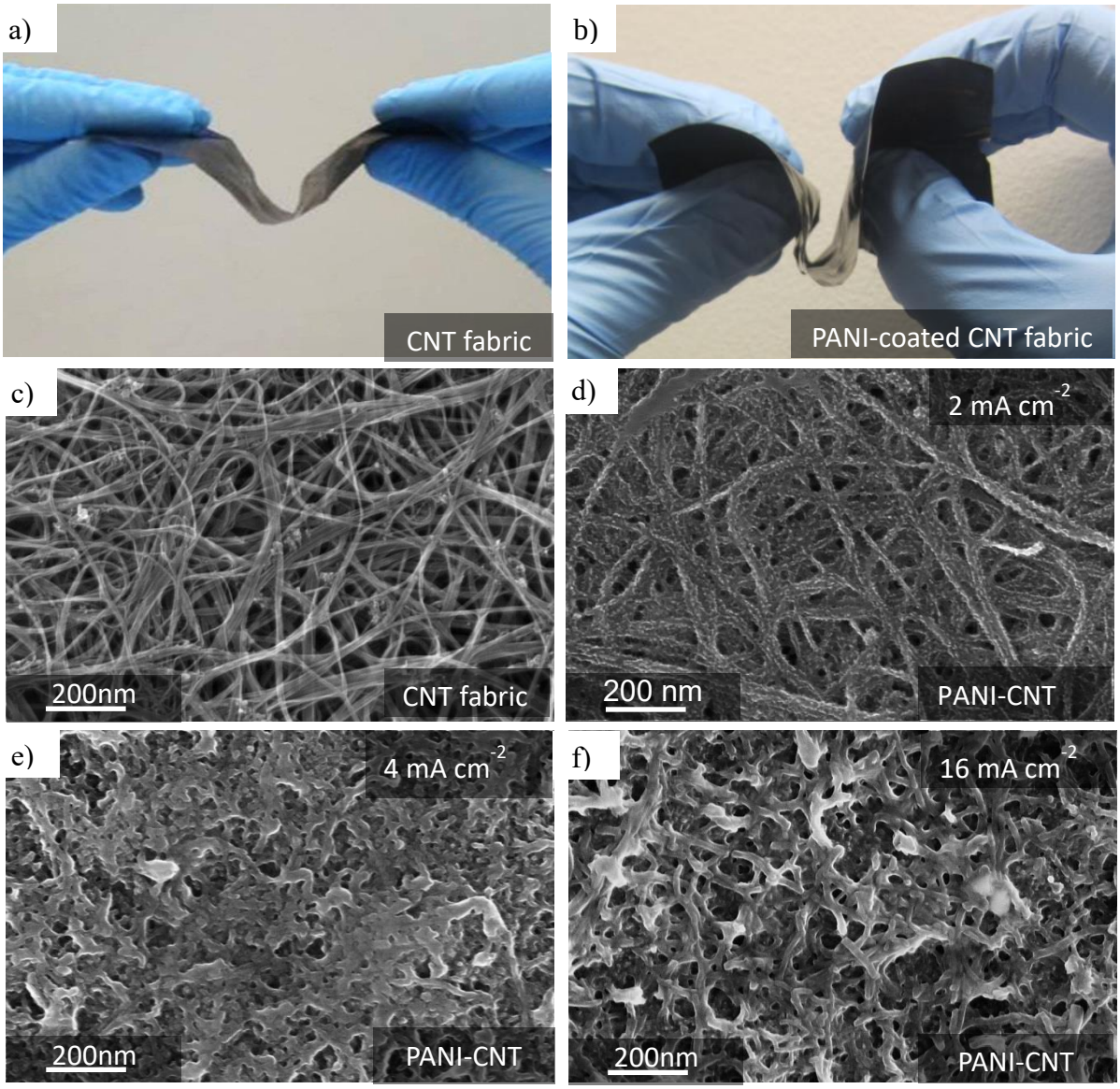

Figure 59. Photographic and SEM images of CNT fabric before (a,c) and after (b, d-f) coating with PANI electro-deposited at different current densities.[280]

Energy dispersive spectroscopy (EDS) revealed low concentration of contaminants (Figure 60a). As expected, ~91 at. % was observed to be from carbon in the CNT and PANI polymer with smaller amounts of N, Cl, and Fe. The presence of N was attributed to the PANI backbone. In order to increase the conductivity of the deposited PANI, we used a Cl dopant through the introduction of HCl during the electrodeposition. Fe is a byproduct of the CNT synthesis process. Raman analyses showed typical PANI spectra (Figure 60b).[281] The 1000-300 cm^{-1} region show conformation-dependent features. The 416 cm^{-1} peak is indicative of C-N-C out of plane deformation modes, the 565 cm^{-1} peak is related to the deformation mode of protonated amine groups, and the 813 cm^{-1} peak results from a mixture of various torsion angles between the two aniline rings of the PANI structure. In the 1700-1000 cm^{-1} range, bands that are sensible to the PANI oxidation state can be found. For example, the peak at 1509 cm^{-1} is due to an N-H bending deformation band of protonated amine. The peak at 1589 cm^{-1} is indicative of the C-C deformation band of benzoid ring. Finally, the peak at 1170 cm^{-1} is attributed to the C-H deformation band of the benzoid ring. The presence of the bands at 1589 and 1170 cm^{-1} suggests that the deposited PANI film is fully oxidized.[281]

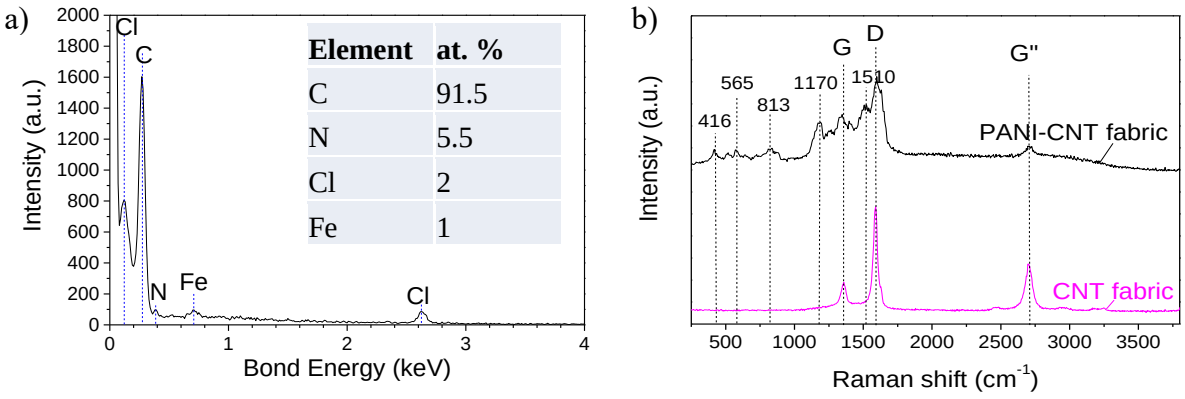

Figure 60. Chemical characterization of the deposited PANI: a) energy dispersive spectroscopy of a PANI-coated CNT and b) typical Raman spectra of CNT and PANI-coated CNT fabrics.[280]

5.3 PANI-CNT Fabrics as Supercapacitor Electrodes

The deposition of PANI on the surface of a preformed CNT fabric allows one to maintain the high conductivities of the fabric because the low resistance CNT-CNT junctions can be preserved. 1 M H_2SO_4 electrolyte was selected as most common in commercial low-cost aqueous supercapacitors. All tests have been performed in fully symmetric configurations. As we discussed in our prior publication,[282] the specific capacitance of PANI-containing electrodes strongly depends on the measurement technique. A three-electrode cell configuration commonly results in 3-to-4 time higher capacitance than the same electrodes measured in a symmetric two-electrode cell configuration.[283,284] The potential window in our electrochemical tests was maintained within the -0.6 to 0.6 V range to avoid the conversion of emeraldine to pernigraniline, which leads to subsequent dissolution of PANI in H_2SO_4 electrolyte.

The generated cyclic voltammograms (CV) (Figure 61a) revealed excellence performance of the PANI-CNT nanocomposite electrodes and a clear dependence of the reduction-oxidation (redox) peaks on the PANI deposition conditions. The highest capacitance was observed in the CNT electrode that was most uniformly covered with PANI (Figure 60b). The capacitance of 240 $F \cdot g^{-1}$ (Figure 61a-d) corresponds to ~700 $F \cdot g_{PANI}^{-1}$ (Figure 61e, f), which is one of the highest capacitances ever observed in symmetric tests on various PANI-containing composites as reported in prior studies[282-293] and indicates excellent ionic and electronic access to the redox reaction sites. Increasing the sweep rate from 10 to 2,000 $mV \cdot s^{-1}$ showed a very high capacitance retention for the utilized capacitance loading (~0.7 $F \cdot cm^{-2}$). The shape of the CV curves remain nearly rectangular at a very high 1 $V \cdot s^{-1}$ sweep rate (Figure 61b). Figure 61c summarizes the capacitance retention of the nanocomposite electrodes at increasing sweep rates and shows the best rate capability of the PANI electrode pulse-deposited at the lowest current density of 2 $mA \cdot cm^{-2}$.

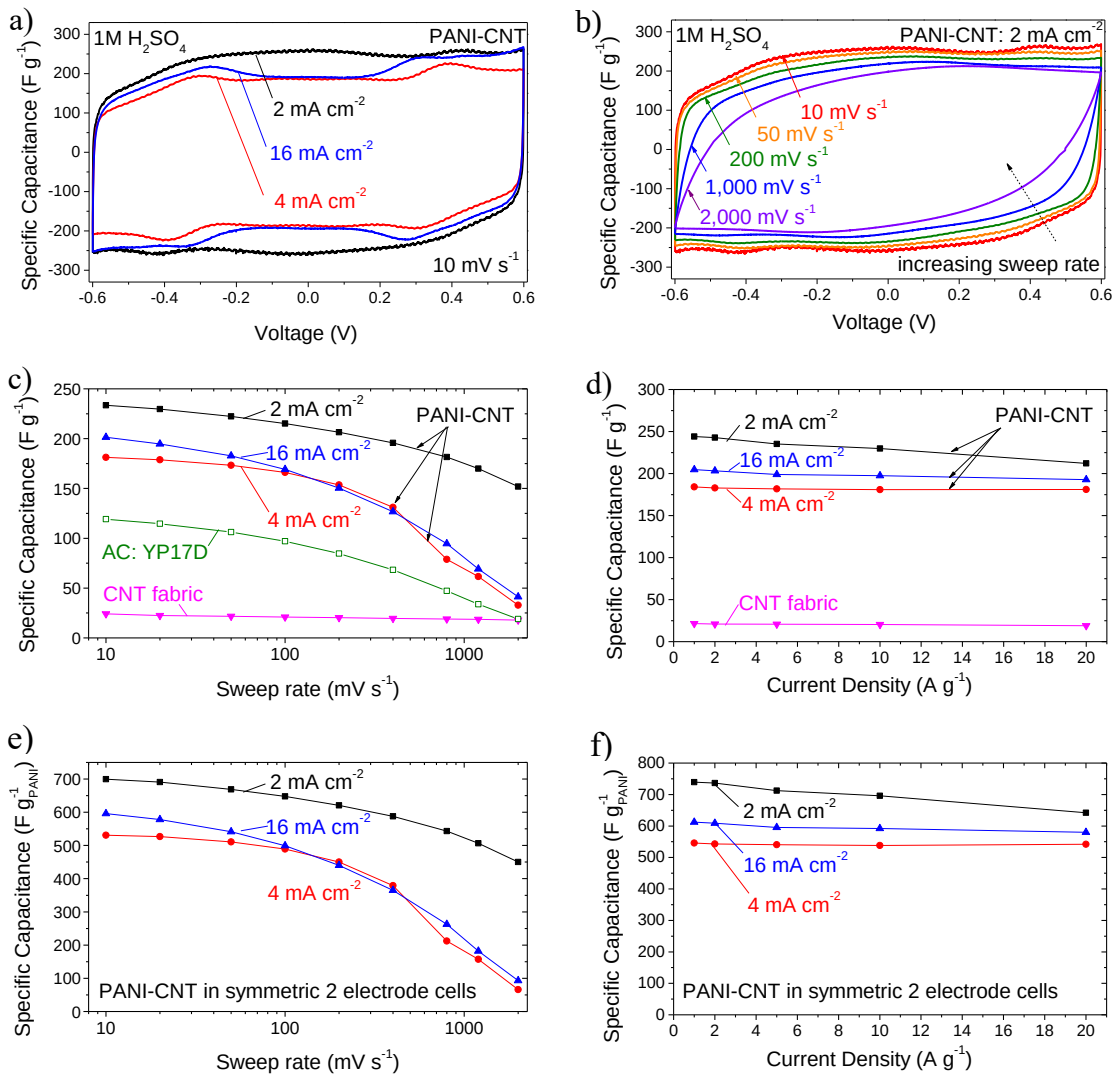

Figure 61. Electrochemical characterization of PANI-coated CNT fabrics in 1 M H_2SO_4 electrolyte in symmetric two-electrode cells: a) cyclic voltammetry of the CNT fabric samples with PANI deposited at different current densities, b) effect of sweep rate on the capacitance retention for the sample produced at 2 mA cm-2 current density, c) effect of the sweep rate on the capacitance retention of PANI-CNT samples in comparison with a commercial activated carbon YP17-D and as-produced CNT fabric, d) effect of the current density in charge-discharge tests on the specific capacitance of PANI-CNT samples in comparison with as-produced CNT fabric, e-f) specific capacitance of the PANI component of the composite as a function of sweep rate and current density.[280]

When compared to the initial CNT fabric, PANI deposition increased its capacitance ten-fold. An “industry-standard” activated carbon, YP-17D, produced from coconut shell precursors and utilized in the majority of commercial devices due to its combination of high capacitance and rapid ion transport rates, clearly showed inferior

performance at the identical capacitance loading (Figure 61c). The volumetric performance of PANI/CNT composites is even more impressive – the achieved volumetric capacitance of ~308 $F \cdot cm^{-3}$ is 3-5 times higher than that of commercial activated carbon electrodes as well as electrodes produced from other high-performance porous carbons utilized in supercapacitor devices.[65,264,294-297]

Galvanostatic charge-discharge (CD) measurements confirmed the capacitance values estimated from the CVs (Figure 61d) and demonstrated capacitance in excess of 200 $F \cdot g^{-1}$ (>260 F cc^{-1}) retained at a very high current density of 20 $A \cdot g^{-1}$. These results corroborate an attractive combination of high-power and high-energy capabilities of the supercapacitor devices built with the produced composite materials.

Electrochemical impedance spectroscopy (EIS) recorded in the 0.001-1000 Hz range provides complimentary characterization and can be used for the estimation of the frequency response of the assembled devices. The initial CNT fabric show remarkable frequency response due to the very high rate of a double layer formation on the external CNT surface. When operated at a characteristic frequency (f_m) of ~50 Hz such a capacitor can charge to 50 % of its maximum capacitance (Figure 62a). The slower redox reactions responsible for the pseudocapacitance in PANI reduce the rate performance to the f_m of ~2.5 Hz in the best performing composite sample. When charged within 1 s this device can store up to 80 % of its maximum energy, which is still quite impressive compared to the activated carbon electrodes operating nearly an order of magnitude slower (Figure 62a).

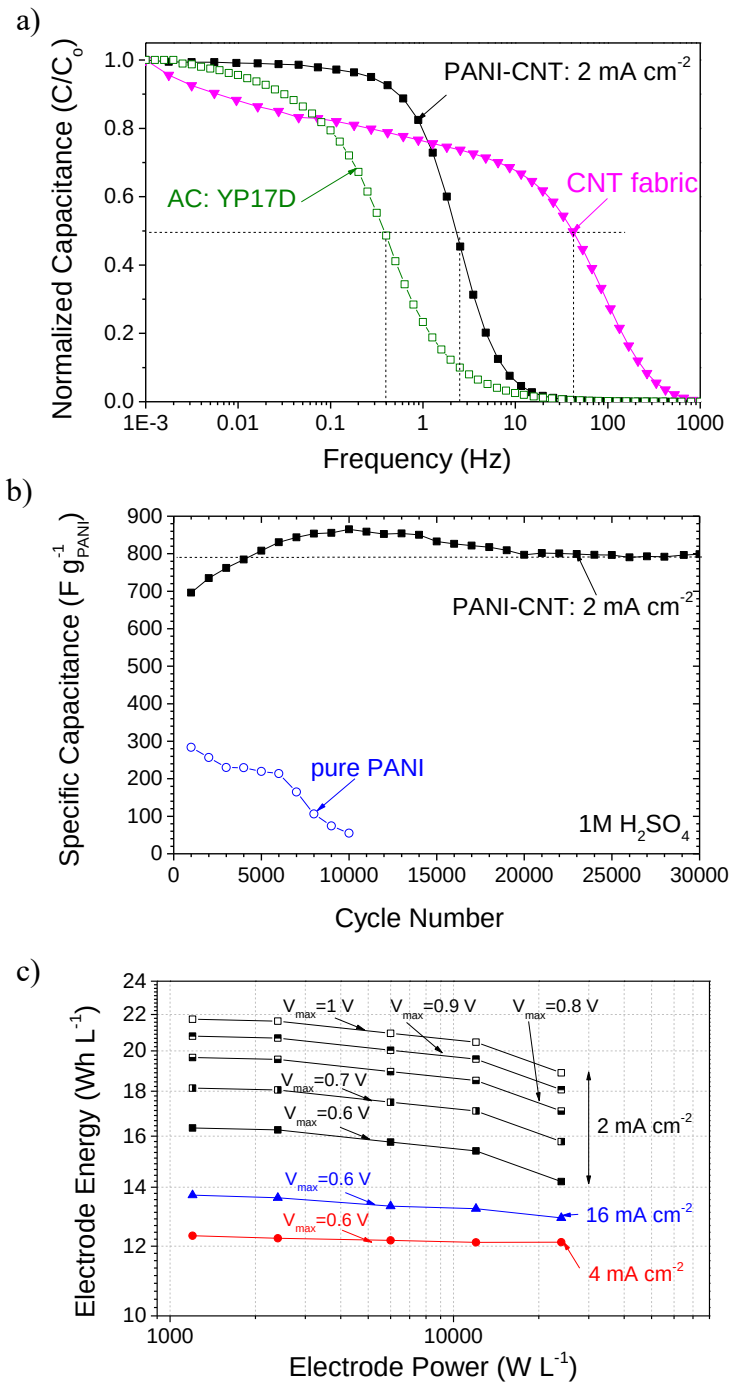

Figure 62. Electrochemical characterization of PANI-coated CNT fabrics in comparison with other materials in 1 M H_2SO_4 electrolyte in symmetric two-electrode cells: a) frequency response of the PANI-CNT electrodes in comparison with a commercial activated carbon YP17-D and as-produced CNT fabric, b) cycle stability of a PANI-CNT electrode produced at 2 mA·cm^{-2} current density in comparison with that of pure PANI (chemically synthesized) electrode in charge-discharge testes performed in the voltage range from -0.6 to +0.6 V, c) energy and power density of PANI-CNT electrodes discharged from different maximum voltages.[280]

The redox reactions occurring during charging and discharging of the supercapacitor, are known to cause swelling and contraction of PANI, which commonly lead to the continuous electrode disintegration, the loss of the electrical contact between the electrode particles and the eventual capacity loss with cycling.[282-292] For example, the chemically synthesized PANI-CNT composite showed 4-10 % degradation after 1500-3000 cycles,[269,283,291] PANI-porous carbon composites 10 % degradation after 1000 cycles,[298] and dense PANI film deposited on planar carbon substrate showed as high as 75 % degradation after 1200 cycles.[293] In contrast, the PANI-CNT composites we produced demonstrate outstanding stability showing no significant degradation for over 30,000 cycles, in contrast to rapidly degrading pure PANI (Figure 62b). The robust electrically interconnected CNT network and strong interactions between the electrodeposited PANI and CNT are likely responsible for such an excellent cycle stability. The estimated energy and power densities of the PANI-CNT composite electrodes tested at different operating voltages of the fully symmetric cells are summarized in Figure 62c. A lower than expected energy density upon charging the cells to higher voltages is due to the reduced capacitance of such cells. Note that the energy and power density on the device level should be lower than what is shown in this figure. Building asymmetric cells (optionally with an organic electrolyte) is a route towards attaining higher energy density characteristics of PANI-based electrodes.

5.4 PANI-CNT Fabric as Capacitive Desalination (De-Ionization) Electrodes

The simplicity of a CDI recently triggered a significant interest to this approach as an alternative method to a reverse osmosis for both static and mobile water desalination and purification applications. It does not require an installation of a large, heavy and expensive high-pressure system, which is the primary drawback of reverse osmosis systems. An ideal CDI electrode shall rapidly adsorb and desorb high content of ions

from salt solutions, possess high electrical and ionic conductivity (for low-loss operation) and exhibit sufficient structural integrity for the prolonged operation under flow.

We believe the produced PANI-CNT composites, therefore, shall be well suited for this purpose. Indeed, these composites show high specific capacitance (200 $F \cdot g^{-1}$, 260 F cc^{-1}) in aqueous NaCl solutions, as confirmed from both CV (Figure 63a) and CD (Figure 63b-f) measurements. The capacitance stays above that of commercial activated carbon fabrics such as YP-17D even at extremely rapid scan rates, which is important for maximizing water desalination efficiency via CDI. Similar to previous tests (Figure 61) the most uniform sample (Figure 59d) showed the most promising performance. The performance of the PANI sample deposited at 16 $mA \cdot cm^{-2}$ was better than previously observed in a H_2SO_4 electrolyte. Small variations in the performance, however, could be expected. The PANI-CNT sample produced at 4 $mA \cdot cm^{-2}$ current density and showing partially plugged outer surface (Figure 59e) demonstrated the lowest capacitance and worst rate performance, as could be expected. The galvanostatic cycling in 1 M NaCl electrolyte did not reveal any significant degradation (Figure 63d, f).

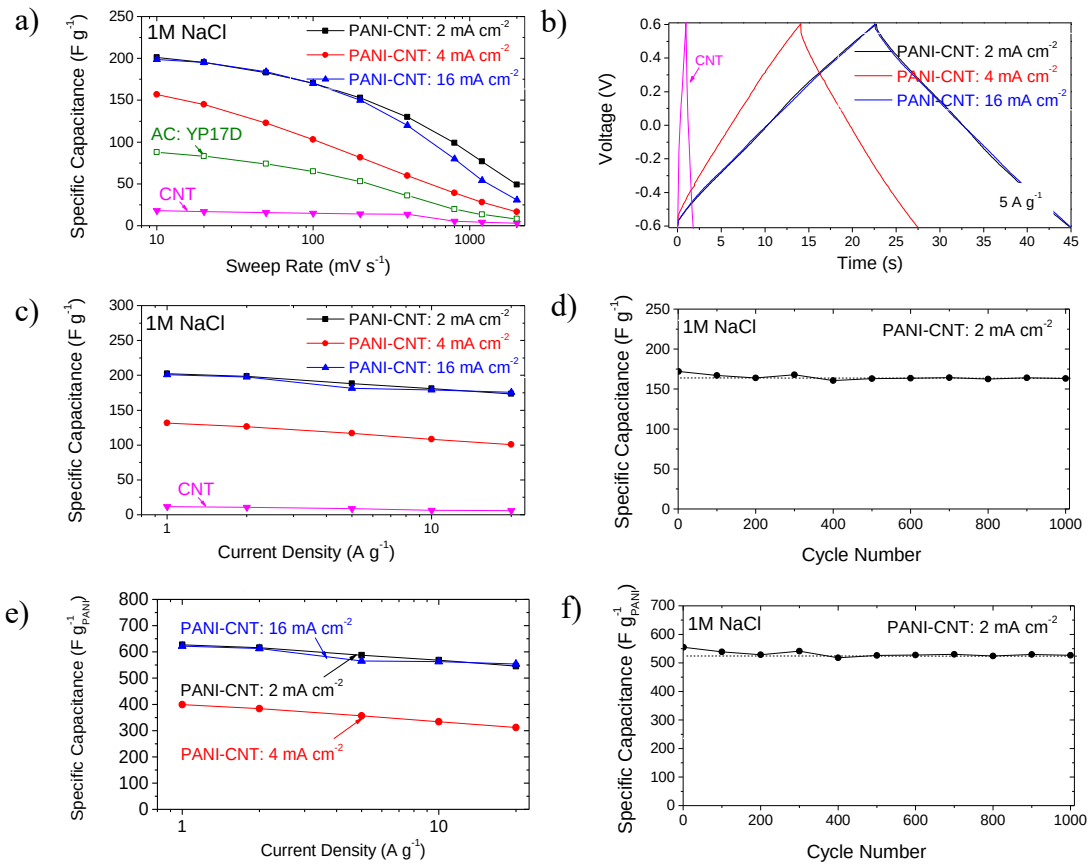

Figure 63. Electrochemical characterization of PANI-coated CNT fabrics in 1 M NaCl electrolyte in symmetric two-electrode cells: a) effect of sweep rate on the capacitance retention for the sample produced at 2 mA cm^{-2} current density, b) typical shape of the charge-discharge profiles, c, e) effect of the current density in charge-discharge tests on the specific capacitance of PANI-CNT samples and the PANI component of these samples in comparison with as-produced CNT fabric, d, f) cycle stability of a PANI-CNT electrode and the PANI component of this sample produced at 2 mA·cm^{-2} current density.[280]

5.5 Static and Dynamic Mechanical Properties

The majority of the composite samples produced demonstrate remarkable mechanical properties. Tensile tests results show dramatic improvements in strength and ductility of the CNT fabric after PANI deposition (Figure 64a). The average ultimate tensile strength of the best sample (PANI deposited at 2 $mA \cdot cm^{-2}$) was 484±65 MPa with an elastic modulus of 19 GPa using the elastic 0-0.5% strain region. The relatively light weight of the PANI-CNT composites leads to the specific ultimate tensile strength (SUTS) up to ~385 $kN \cdot m \cdot kg^{-1}$ (Figure 64b). This value shows a large improvement compared to PANI-CNT films previously reported [285] and compare well with epoxy-SWCNT composites, many strong natural fibers and tissues, various steels, aerospace-grade aluminum and titanium alloys, aluminum-matrix composites and many other structural materials of interest.[289,299-309] Interestingly, the constant stirring of electrolyte during the PANI deposition increased the maximum strain-to-failure to over 20% (Figure 64a). Since the SEM micrographs and electrochemical characterization didn't reveal any significant changes for this sample (compared to a deposition using a static electrolyte), we assume that electrolyte agitation further improved the uniformity of the PANI deposition within CNTs and allowed the observed improvement in the mechanical properties. The mechanical response to temperature of these composites was studied using a dynamic mechanical analysis (DMA) performed on a temperature ramp from 30 to 200 °C in air at a 3 °C min^{-1} heating rate (Figure 64b). These results show remarkable high temperature stability in air with very small decreases of storage modulus. Even at the maximum temperature of 200 °C the storage modulus was found to be above 40 GPa for samples produced using the lowest peak current density, which compares very favorably to fiberglass and carbon fiber epoxy composites. The high strain to failure combined with high ultimate tensile strength of the selected PANI-CNT composite fabric samples resulted in the very high modulus of toughness (Figure 64d) compared to various lightweight structural materials and composites.

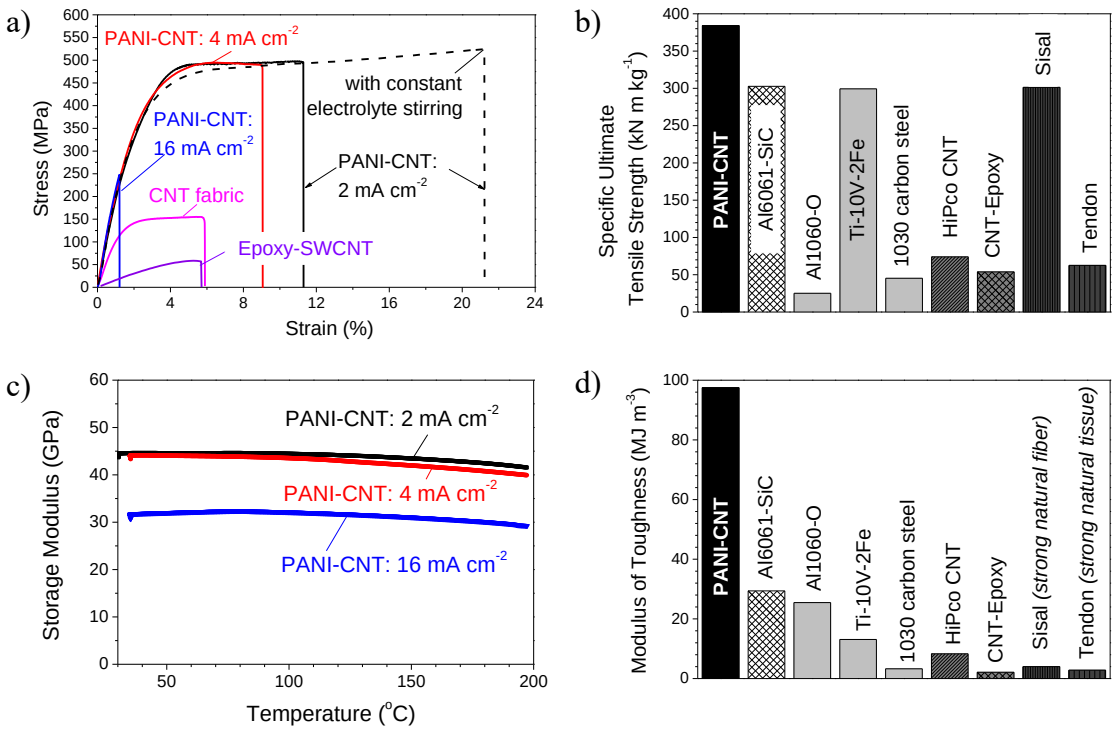

Figure 64. Mechanical characterization of PANI-coated CNT fabrics: a) tensile tests, b) specific ultimate strength, c) storage modulus and d) modulus of toughness of PANI-CNT in comparison with other materials.[280]

5.6 Conclusions

Flexible PANI-CNT composite fabrics produced by pulsed electro-deposition on CNT pre-formed matrix make a promising multifunctional material system for a variety of important applications ranging from energy storage to water desalination to durable structural composite materials. A comparison of the different peak current densities shows that the PANI deposited at a 2 mA·cm^{-2} pulse peak current has the best combination of electrochemical and mechanical properties. This attractive combination of properties could be attributed to the increased shear transfer from π-π bonds in the PANI-CNT structure, which additionally would improve the electrical charge transfer. The lowest peak current density additionally allows for higher uniformity of PANI deposition through the thickness of the samples. This best performing sample exhibits volumetric capacitance of up to ~300 F·cc^{-1} in low-cost aqueous electrolytes and salt solutions,

which is significantly higher than that of both commercial and advanced porous carbons. The high power characteristics of this composite are demonstrated by retaining more than 80% of such a high capacitance when the current density is increased to 20 $A \cdot g^{-1}$ or when the supercapacitor operates at a very high (for comparable capacitance loading) frequency of 1 Hz. In contrast to many other PANI-containing composites, the good structural characteristics of the produced sample allow for a stable performance during more than 30,000 galvanostatic cycles at high current densities. The specific tensile strengths of PANI-CNT fabrics are comparable to or exceed that of lightweight titanium and aluminum alloys as well as some metal matrix composites. More importantly for many structural applications the produced PANI-CNT fabrics demonstrate an outstandingly values of the modulus of toughness, which are higher than the majority of other light-weight structural materials. All of these benefits coupled with the applications of low-cost materials and ambient temperature processing conditions make the PANI-CNT composite an attractive candidate for a wide variety of mobile applications and may offer a great solution for weight and volume reduction on a system level if such a system requires a combination of structural and energy storage functions. Our future studies will be focused on further material optimization and studies of other functionalities of these composites, such as sensing.

5.7 Experimental Details

Materials

CNT fabrics were produced at Nanocomp Technologies (USA) using a chemical vapor deposition process. These underwent a thermal treatment at a temperature of 450 °C in argon atmosphere for 2 hours. Pulsed electrodepositions were performed using a custom plating holder and graphite foil current collectors (Alpha Aesar, USA). Aniline monomer (0.5 M, 99.5% Sigma Aldrich, USA) and HCl (1 M) were used as the plating

solution to ensure proper Cl doping to enhance the conductivity. Proper mixing was ensured via stirring and ultrasonication. Pulsed electrodeposition was carried out at using a peak current density of 2, 4 and 16 $mA \cdot cm^{-2}$ with the pulse length varied from 3.75 to 30 s to maintain the same total charge 120 $mAs \cdot cm^{-2}$ for all samples. After synthesis, the resulting material was washed with 18 MΩ DI water and ethanol. The resulting fabric was dried in an oven overnight and final drying was done in a vacuum oven at a temperature of 80 °C. For comparison of electrochemical properties we utilized activated carbon YP-17D (Kuraray, Japan) mixed with a polytetrafluoroethylene binder (10 wt. %).

Electrochemical Characterization

Cyclic voltammetry, charge discharge, and impedance spectroscopy was performed on the as produced electrode materials in a symmetric configuration using H_2SO_4 (1 M) or NaCl (1 M) as the electrolyte, and gold foil as the current collector and PTFE Gore® separator (23 µm thick, WL Gore & Associates, USA) in a beaker cell design. Cyclic voltammetry was performed using a Solartron 1480A (AMETEK Advanced Measurement Technology, USA) with the potential being swept from -0.6 V to +0.6 V at scan rates of 5–1000 $mV \cdot s^{-1}$. The integrated-average gravimetric capacitance of each electrode was calculated from the CV data according to:

$$C_{electrode} = \frac{2I}{m\left(\frac{dV}{dt}\right)}\left\{\int_{-0.6}^{0.6} I(V)dV - \int_{0.6}^{-0.6} I(V)dV\right\} * \frac{1}{2 * 1.2} \qquad (71)$$

where *dV/dt* is the scan rate, m is the mass of each electrode in a symmetric cell, and *I(V)* is the total current. The C–D tests were carried out using an Arbin SCTS supercapacitor testing system (Arbin Instruments, TX, USA) between -0.6 V and +0.6 V at charge/discharge current densities between 1000 and 20,000 $mA \cdot g^{-1}$, based on the mass

of a single electrode. The gravimetric capacitance, $C_{electrode}$ ($F \cdot g^{-1}$), of each electrode was calculated according to:

$$C_{electrode} = \frac{2I}{m(\frac{dV}{dt})} \tag{72}$$

where I is the current (A), dV/dt is the average slope of the discharge curve ($V \cdot s^{-1}$), and m is the mass of each electrode (g) in a symmetric cell. Capacitance of PANI component of the PANI-CNT was calculated as:

$$C_{PANI} = \frac{C_{electrode} - f_{CNT} * C_{CNT}}{1 - f_{CNT}} \tag{73}$$

where f_{CNT} is a weight fraction of the CNT in the composite and C_{CNT} is a gravimetric capacitance of CNT. The energy E ($Wh \cdot L^{-1}$) and power P ($W \cdot L^{-1}$) densities of the PANI-CNT electrodes were estimated as:

$$E = \frac{C_{electrode} * V^2}{2} * \frac{1000(g\ kg^{-1})}{3600(s\ h^{-1})}(Wh\ J^{-1})\rho_{electrode} \tag{74}$$

$$P = \frac{2I(0.6V - IR)}{m} * \frac{1000(g\ kg^{-1})}{3600(s\ h^{-1})}\rho_{electrode} \tag{75}$$

where I is the discharge current (A), $\rho_{electrode}$ is the electrode density ($kg \cdot L^{-1}$), and m is the mass of each electrode (g) in a symmetric cell.

EIS measurements were performed on a Gamry Potentiostat from 100 kHz to 1 mHz at 1 V scanning amplitude. The gravimetric capacitance, $C_{electrode}$ ($F \cdot g^{-1}$), was calculated according to:

$$C_{electrode} = \frac{2\mathrm{Im}(Z)}{2\pi f[\mathrm{Im}(Z)^2 + \mathrm{Re}(Z)^2]m} \quad (76)$$

where *f* is the operating frequency (Hz), *Im(Z)* and *Re(Z)* are the imaginary and real parts of the total device resistance (Ohm), and *m* is the mass of carbon in each electrode (g). All supercapacitors were tested in the following order to ensure reproducibility and accuracy: CV followed by C–D then EIS.

Mechanical Testing

Mechanical properties were studied using a tensile test frame (MTS Insight 2, USA) with at a strain rate of 10% min^{-1} and a 200 N load cell. Five sample specimens from each were cut in accordance to ASTM D882 and were tested with a gauge length of 40 mm and a sample width of 5 mm. Sample thickness was measured via micrometer and was found to be 16-17 µm. Sample edges were inspected optically before testing to avoid damaged samples. A TA Instruments DMA Q800 was used to perform temperature ramp DMA with the samples being 5 x 15 mm and tightened to 7 in·lb for reproducibility. Samples were heated at a constant rate of 3 °C min^{-1} in air from 30-200 °C. During this test the strain amplitude was 0.2% and the frequency was fixed to 2 Hz.

CHAPTER 6

COBALT FLUORIDE-CNT COMPOSITES AS MULTIFUNCTIONAL CONVERSION CATHODES

6.1 Introduction

Due to their large energy density, lithium ion batteries (LIBs) have been extensively studied to satisfy the ever increasing need of power sources.[6,264,310-312] In order to further increase functionality or operational time of LIB-powered devices, two general strategies could be considered: (i) development of multifunctional LIBs (such as structural LIBs, which may carry mechanical load and be a part of the structure) with the potential to minimize the device weight and volume on a system level, even when such batteries offer energy density comparable or slightly lower than state-of-the-art and (ii) development of new materials that increase energy density in LIBs.

Currently, only a few studies have reported on the development of high strength electrodes for LIBs and other energy storage devices,[158,260,268,280,313-317] mostly focusing on the structural anode or supercapacitor development. Some of the most promising performance characteristics were recently achieved in electrodes utilizing carbon nanotubes (CNTs): these demonstrated high strength, flexibility, high thermal and electrical conductivities.

Significant effort has been placed on the development of alloying-type anode materials with extremely high capacity, including Si and Sn.[6,212,318-327] At the same time, the state-of-the-art cathode materials, namely $LiCoO_2$ (LCO), $LiNi_xMn_yCo_{1-x-y}O_2$ (NMC) and $LiNi_xCo_yAl_{1-x-y}O_2$ (NCA), cannot match both the gravimetric and, more importantly, volumetric capacity of Si anodes.[328-333] Such imbalance of capacity constitutes a major challenge for fabricating advanced LIBs that target larger energy density. In order to overcome this issue, the number of studies of various high capacity conversion-type cathode materials has been rapidly increasing in the last few years.

Chalcogen-based cathodes (mostly sulfur, S) have received the most attention due to their high theoretical capacities of up to ~ 1.9 Ah cm^{-3}.[264,334-341] Their low average potential (theoretical ~ 2.2 V *vs.* Li/Li^+), however, limit the cell energy density. More recently, metal fluorides (MF), a sub-class of conversion-type transition metal halides cathodes, has showed potential on achieving high-capacity and high energy density. The full utilization of the oxidation state in the corresponding metal (M) becomes possible in MF, resulting in higher theoretical volumetric capacity (up to ~ 2.2 Ah cm^{-3}) and higher theoretical potential (up to ~ 3.5 V *vs.* Li/Li^+)[342-346] than that in S cathodes. Nevertheless, among MF's, cobalt (II) fluoride (CoF_2), with the theoretical specific capacity of 553 mAh g^{-1}, is rarely studied because of its extremely poor cycling stability. Somewhat stable cycling performance of thin film CoF_2 was achieved through a deposition of a protective coating by a pulsed laser deposition (PLD) process, which made the CoF_2 hard to be utilized for rechargeable LIBs.[347] The reason for the extremely low stability of CoF_2 was attributed to its poor conductivity and slow kinetics. Therefore, the research focus shifted to size reduction because nanostructures would reduce the Li ion diffusion paths and hence, improve the ion insertion rate. One of the highest capacities was demonstrated in hierarchical CoF_2 spheres synthesized using a supercritical fluid method.[348] Unfortunately, while this unique structure delivered high initial capacity, it rapidly dropped to ~50 mAh.g^{-1} after 10 cycles. More recently, fast capacity degradation was

also reported with nano-sized CoF_2 by Teng et.al.[349] All these reports indicated that there might be other unrevealed reasons for the fast capacity degradation of CoF_2.

In order to synergistically enhance electrical conductivity and load-bearing properties of CoF_2 cathodes, a novel electrode preparation method was employed, where we incorporate CoF_2 nanoparticles within a porous, high strength CNTs fabric. As a result of the innovative proposed electrode a theoretical capacity under 10 mA g^{-1} current density was achieved with a capacity of ~360 mAh g^{-1} under a relatively high (for this system) current density of 100 mA g^{-1}. Under a very high current density of 1000 mA g^{-1}, over 50 % of the initial capacity was retained after 10,000 cycles. Furthermore, the fabricated CoF_2/CNT nonwoven fabrics demonstrated a high strength which suggests the promise of MF_x-based materials for their application in multifunctional batteries with load-bearing capabilities.

6.2 Synthesis and Characterization

The overall process flow utilized for the CoF_2/CNTs composite fabrication is shown in Figure 65. As a starting material for this project, we introduced binder-free CNT-based nonwoven fabric (Figure 65a) produced on a commercial scale.[268] The CNT fabric was produced by continuous chemical vapor deposition (CVD) for a high-throughput, low-cost manufacturing of a uniform high-strength CNT material.

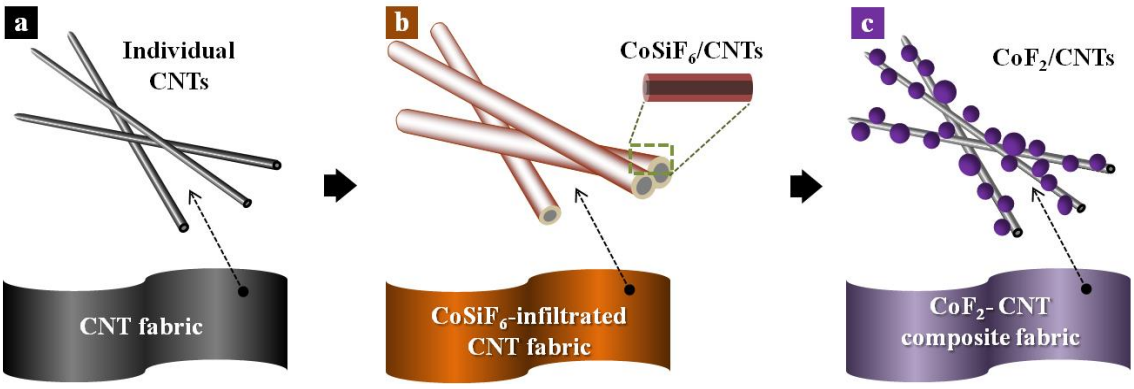

Figure 65. Schematics of CoF_2/CNTs composite fabrication.[350]

The next step involved the infiltration of the CNTs with an aqueous precursor solution of $CoSiF_6$. Surfactant of Triton X-100 was utilized to improve the wetting property of highly hydrophobic CNTs surface. A uniform coating of the CNTs with the $CoSiF_6$ layer was achieved after drying (Figure 65b). Subsequently, post-annealing step was conducted at 400 ^oC for 6 h in argon (Ar) atmosphere to chemically transform $CoSiF_6$ into CoF_2 (Figure 65c), according to:[351]

$$CoSiF_6 \xrightarrow{\Delta 400\ ^oC} CoF_2 + SiF_4 \uparrow \quad (77)$$

Figure 66 shows the selected morphological characterization of the produced CoF_2/CNTs composite. With high flexibility, the produced composite fabric can be rolled, cut and directly used as binder-free electrodes in LIBs (Figure 66a inset). SEM studies showed that the produced samples exhibited uniform distribution of well-dispersed CoF_2 nanoparticles without any large agglomerates visible (Figure 66a). Note that without surfactant, however, such a result could not be achieved and high aggregation of CoF_2 was observed. High-resolution SEM showed CoF_2 nanoparticles on the top surface of the electrode to be spherical in shape and have a diameter in the range from ~30 to 50 nm (Figure 66b). TEM studies further verified the size and shape of CoF_2 nanoparticles coated on the top layer of the CNT fabric (Figure 66c).

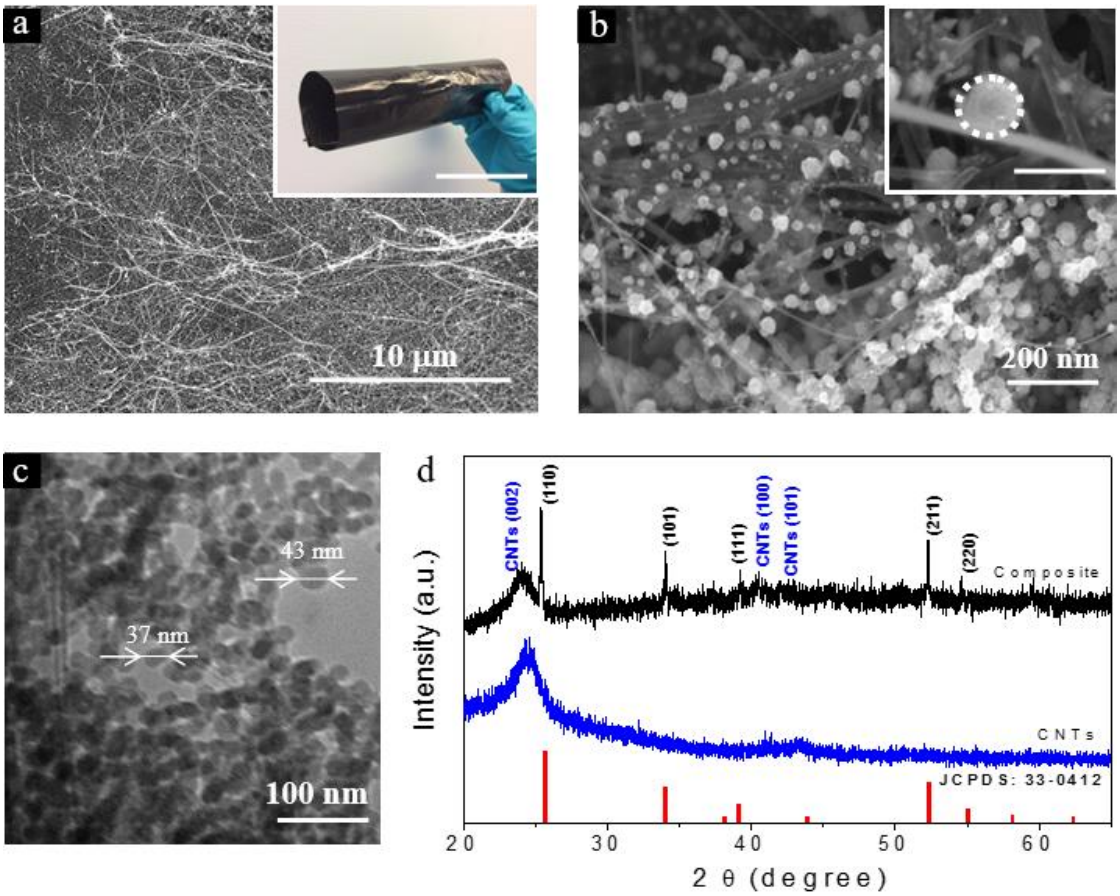

Figure 66. The morphology and structural characteristics of the CoF_2/CNTs composite fabric: a) SEM micrograph of the composite surface (inset-photograph of the composite, scale bar of 5 cm); b) high resolution SEM micrograph of the interface of CoF_2-decorated CNTs with a close-up of a single CoF_2 nanoparticle on a CNT (inset, scale bar of 50 nm); c) TEM micrograph of the CoF_2-decorated CNTs; d) XRD spectrum of the composite.[350]

In order to confirm the composition of the nanoparticles, XRD (Figure 66d), EDS and XPS tests were additionally conducted (Figure 68). XRD spectra revealed typical CoF_2 diffraction peaks indexed to the (110), (101), (111), (211), (202) and (301) crystal planes associated with the tetragonal-phase CoF_2, according to the database JCPDS No. 33-0417. Additional peaks at ~26°, 41° and 43° are associated with the nanostructured carbon of the CNTs substrates (Figure 66d).[352] By conducing Scherer analysis on the strongest (110) peak we estimated the average crystal size to be ~ 45 nm. We propose that the bulk of the electrode (not easily accessible by SEM and TEM due to high strength of the fabric) comprise particles larger than what we observe on the surface.

Indeed, these larger particles located between the CNTs thin layers could be observed by the cross-section SEM images (Figure 67).

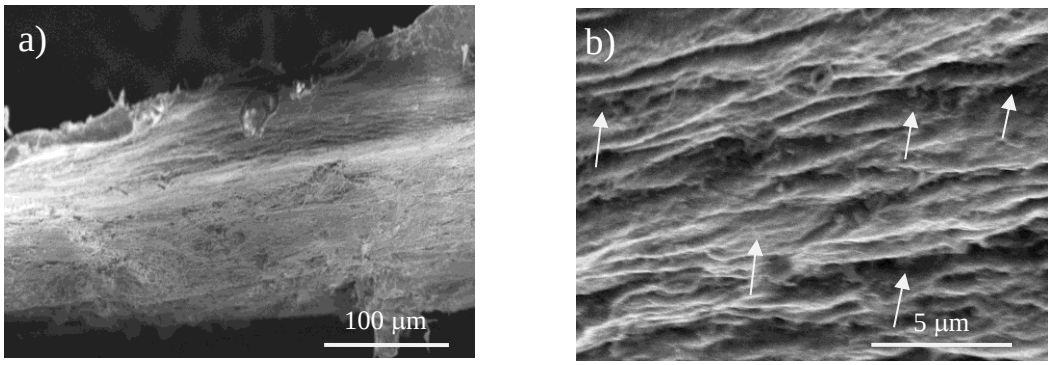

Figure 67 Cross-section images of prepared CoF_2-CNTs nanocomposite: a) SEM image of layer-by-layer structure of the composite and b) SEM image of CoF_2 large aggregation between layers.[350]

EDS studies showed the presence of cobalt (Co), fluorite (F) (with the atomic ratio of Co to F being ~1:2) (Figure 68a), further confirming the formation of CoF_2. EDS also revealed the presence of small amount of Si and O impurities. The likely origin of Si is the incomplete conversion of the precursor, while O may originate from the CNTs and the moisture adsorbed during sample handling. The XPS studies (Figure 68b) further confirmed the presence of Co, F, and Si which was expected for CoF_2.

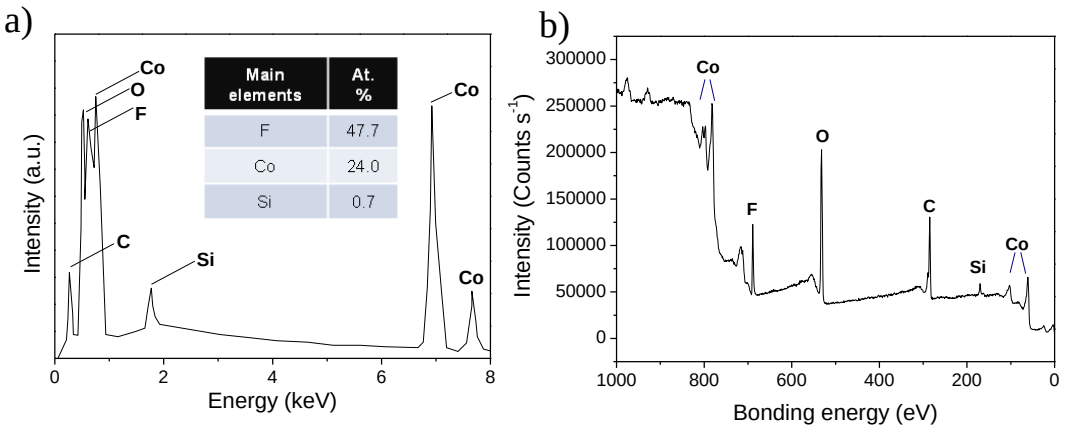

Figure 68 Component analysis of CoF_2/CNTs nanofibrous composite: a) EDS analysis and b) XPS survey, showing the presence of cobalt, fluoride and slight impurity of silicon from absorbed silicon fluoride gas.[350]

The results of tensile tests (Figure 69) demonstrated the modulus of toughness of the composite (which is a measure of the energy of mechanical deformation per unit volume prior to fracture) of 97.5 MJ m^{-3}, which was higher than that for the initial CNT fabric (75.5 MJ m^{-3}) and showed clear advantages compared to various commonly-used structural materials, including lightweight metals and metal matrix composites (Figure 69c). These tests also show an increase of the ultimate stress to 267 MPa after the decoration of CoF_2 nanoparticles (Figure 69a) compared with the one of 219 MPa for the CNT fabric alone. We propose that the deposition of CoF_2 at the CNT junctions and at the boundary between the individual tubes enhance the mechanical properties of the composite and improve their pull-out behavior. This further suggests the SiF_4 vapors generated during the annealing step do not adversely impact the mechanical properties of the CNT composite. Such a high ultimate tensile strength was even comparable to that of pure metals (Figure 69b). This indicates a promise of these composite materials for applications in flexible, structural (and thus multifunctional) batteries.

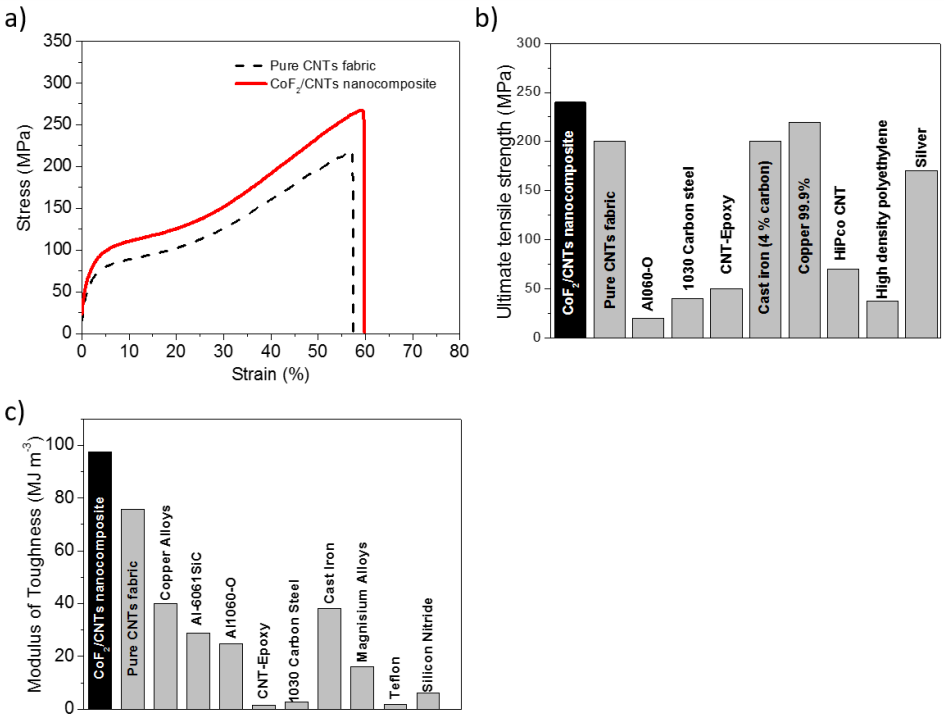

Figure 69. Selected mechanical characteristics of the CoF_2/CNTs composite fabric: a) tensile test results and a comparison of the produced material with selected materials for b) the specific ultimate tensile strength, and c) the modulus of toughness.[350]

Specific surface area (SSA) of the composite was measured by the Brunauer–Emmett–Teller (BET) analysis of N_2 sorption isotherm collected at 77 K. It revealed a BET SSA of ~230 $m^2 g^{-1}$ compared with the pure CNTs of 220 $m^2 g^{-1}$. Thermal gravimetric analysis (TGA) was performed in air to determine the composition of CoF_2 (40 wt. %) in the as produced composite (Figure 70).

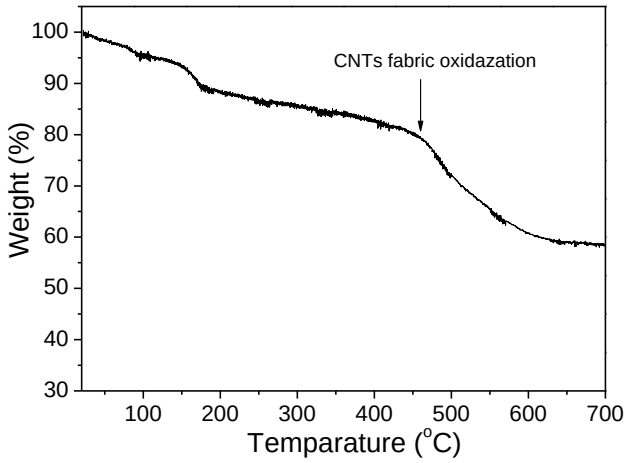

Figure 70. TGA analysis of prepared CoF_2-CNTs nanocomposite in air from room temperature to 700 °C, indicating the content of CoF_2 to be 40 wt. %. The heating rate is 2 °C min^{-1}.[350]

6.3 Electrochemical Testing

The most common electrolyte utilized in CoF_2 and in most other cathode studies has been 1 M $LiPF_6$ salt solution in a ternary mixture of carbonate solvents, such as ethylene carbonate, dimethyl carbonate and diethyl carbonate (EC/DMC/DEC). In such electrolytes, EC forms a favorable solid electrolyte interphase (SEI) on a graphite anode and provides high salt solubility due to its high dielectric constant. The addition of DEC to the electrolyte mixture greatly improves the electrolyte performance at low temperature due to its low melting point (-43 °C),[353] but at the expense of reducing SEI stability. Other solvents (such as DMC) are commonly required as additives to improve the miscibility of DEC with EC, particularly at low temperatures. Unfortunately, the commonly used electrolyte (EC/DMC/DEC) leads to unsatisfactory performance for

metal fluoride cathodes. Such poor performance triggered our investigation of alternative electrolytes comprising fluoroethylene carbonate (FEC), which has recently demonstrated a more stable SEI on the anode surface than EC. Furthermore, while prior studies made great effort on reducing the characteristic dimensions of CoF_2 to improve the rate capability and initial capacity, little improvement of cycling stability was achieved. This inspired us to find other issues attributed to the cell instability, such as transition metal dissolution (Co in the case of CoF_2) during cycling of high energy CoF_2/Li cells, which may negatively affect the SEI on both CoF_2 cathode and the Li anode.[354] As a low melting point co-solvent we selected ethyl methyl carbonate (EMC) due to its excellent miscibility with FEC without any additional co-solvents needed. Keeping two solvents in the electrolyte simplifies analysis of the obtained results. As an additional bonus, EMC is known to form a superior SEI than DMC. By using an electrolyte composed of FEC/EMC 3:7 and 1 M $LiPF_6$, stable performance and near theoretical capacity utilization was achieved when cycled at a current density of 10 mA g^{-1} (Figure 71a). This was attributed to the SEI stability which prevented transition metal dissolution. Thereafter, this electrolyte composition was utilized to determine the effectiveness of the CNT fabric as a current collector.

It should be pointed out that even though the electrode capacity retention at increasing current density was clearly not as fast as that of most conventional intercalation-type electrodes,[355,356] it was still a significant upgrade for a MF system. The high initial capacity achieved suggests excellent electrical connectivity of CoF_2 in the composite, as expected by the employment of CNTs. In Figure 71b, typical charge/discharge profiles at 100 mA g^{-1} showed a high (over 1.3 V) voltage hysteresis. While the origin(s) of the hysteresis is under investigation, it is commonly observed in MFs[343,345] and is certainly undesirable as it reduces the energy efficiency of the cell. On a positive note, since some of our studies demonstrated the opportunity to dramatically reduce the hysteresis in MF's, we are optimistic that this negative factor could be greatly

diminished. Furthermore, in some applications, such as for using structural batteries in drones or sensors powered by solar cells, rapid charging is not needed and slow charging capability (e.g. within 4 h or more) is sufficient.

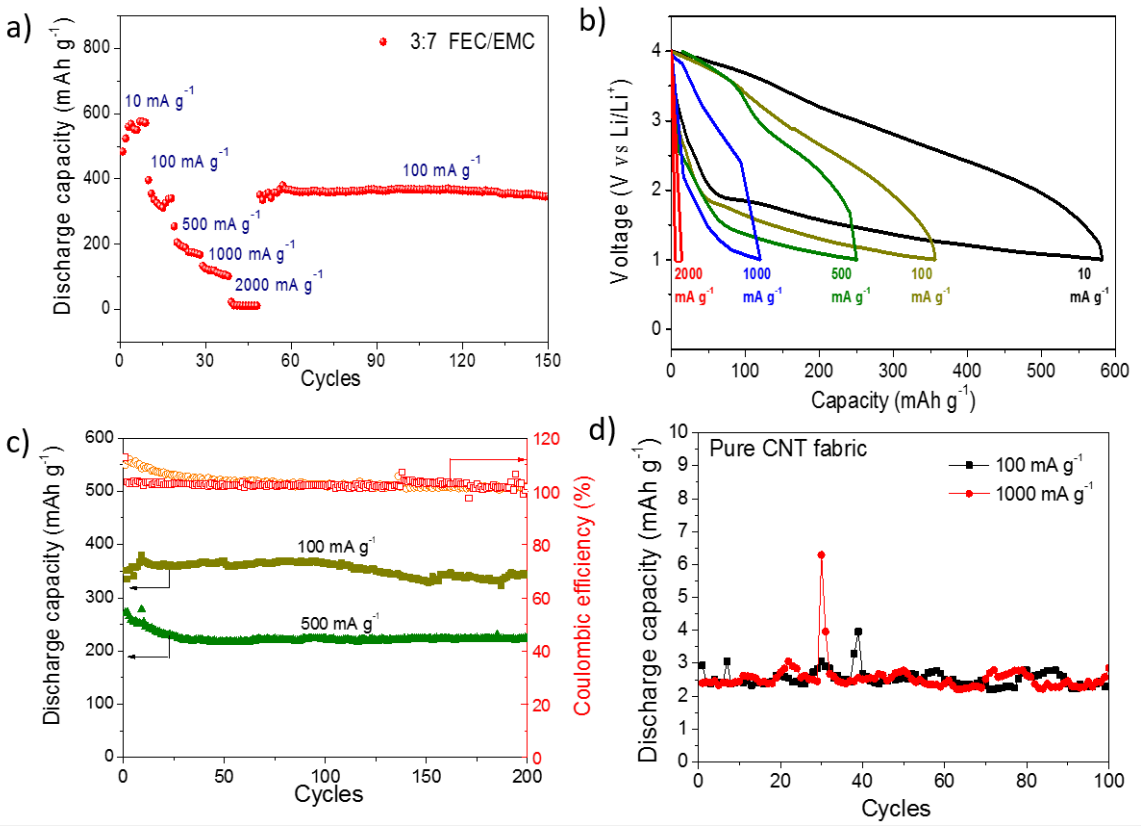

Figure 71. Rate performance and cycle stability of CoF_2/CNT composites in 1 M $LiPF_6$, FEC/EMC (3:7) electrolyte. a) charge discharge performance and complete capacity recovery, b) the charge/discharge profiles at different current densities, c) capacity retention and columbic efficiency at current density of 100 and 500 mA g^{-1}, d) Capacity contribution from CNT fabric at different current densities.[350]

As previously discussed, prior studies on CoF_2 reported very poor cycle stability.[347,349] In contrast, here we demonstrate excellent electrochemical stability in constant-current galvanostatic tests conducted at 100 and 500 mA g^{-1} (Figure 71c). When tested at a moderately high current densities of 100 and 500 mA g^{-1}, the composite electrodes showed initial capacity of $260\text{-}360\,\mathrm{mAh\,g}_{CoF_2}^{-1}$, and showed a good stability with a remarkable capacity retention (93 % for 100 mA g^{-1}) in 200 cycles (Figure 71c). In

order to reveal the contribution of CNTs to the electrode capacitance, charge discharge tests of CoF_2-free CNT fabric electrodes were performed in the same potential range and at the same current densities. The observed capacity was only ~ 3 mAh/g, and could almost be neglected (Figure 71d). The CNT electrodes were pre-cycled for 10 times prior to the test in order to discount small initial electrolyte decomposition on the CNT surface.

Figure 72 emphasizes the important role of the nanofibrous electrode structure on CoF_2 cycling stability, capacity, and impedance. By the comparison of the CoF_2/CNT nanocomposite fabric composite with an electrode comprising a CoF_2/CNTs mixture (both with optimized FEC/EMC electrolyte), noticeably superior capacity utilization and cycle stability of the composite were observed (Figure 72a). The conventionally prepared electrode showed a maximum capacity of ~ 200 mAh $g_{CoF_2}^{-1}$ during charge-discharge tests at a moderate current density of 100 mA g^{-1}, followed by a relatively fast capacity fading to 100 mAh $g_{CoF_2}^{-1}$ after 50 cycles, presumably due to the formation of SEI that breaks electrical contact between CoF_2 particles and the CNTs. In contrast, the CoF_2/CNTs composite, where each CoF_2 particle was bonded to a CNT, exhibited capacity of $\sim 360\ mAh\ g_{CoF_2}^{-1}$ for the same current density, which remained unchanged during the next cycles (Figure 72a).

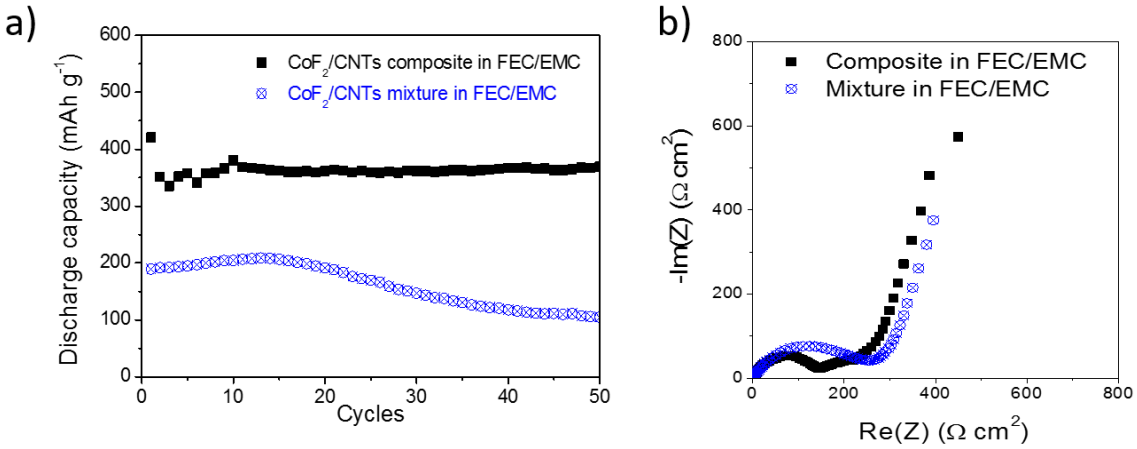

Figure 72. Impact of electrode morphology for the stability, capacity, and impedance of the CoF_2-based composite cathodes: a) comparison of cycling stability of CoF_2/CNT

composite *vs.* CoF_2/CNT mixture with a current density of 100 mA g^{-1}, b) EIS spectrum (0.01 Hz to 100 kHz) comparing half cells of CoF_2-CNT fabric with CoF_2-CNT mixture.

In order to gain further insights of how the proposed electrode microstructure improved the electrochemical properties of CoF_2 electrodes, we have conducted EIS tests to compare the electrochemical charge transfer resistance (R_{ct}) of the cells with different electrode structures (Figure 72b). The R_{ct} (diameter of the semicircle) for the cells with the nanocomposite fabric electrode is ~ 50 % less than that for the cells with the regular slurry-based CoF_2/CNT electrodes. Clearly, the CoF_2-anchored CNTs nanofibrous electrode was superior to slurry-based on power capability. These comparisons provide further evidence for the importance of the electrode microstructure to effectively reduce R_{ct} , which correlate well with the results of cycling performance (Figure 71).

6.4 Post-Mortem Analysis

Post-mortem SEM and EDS analysis of surface characteristics of both cathode (CoF_2) and anode (Li foil) electrodes provided insights on the cycle stability of the CoF_2 and the major degradation mechanism. We characterized the morphology and chemical composition of cycled Li metal anodes (Figure 73). The SEM micrograph of the Li anode cycled in FEC/EMC-based electrolyte showed smooth (at a low magnification) Li surface with only a few salt residues visible (Figure 73a). The corresponding EDS spectrum showed the presence of C from the SEI, F from the $LiPF_6$ and FEC, O from the EMC, FEC and unintentional oxidation during the sample transfer to the SEM chamber, and P from the $LiPF_6$ (Figure 73b). No traces of Co could be observed, suggesting that no significant CoF_2 dissolution took place during lithiation/delithiation processes. For the FEC/EMC electrolyte cells, visual inspection showed both the separator and electrolyte looked nearly identical to the original ones- the separator was clean and the electrolyte clear and transparent.

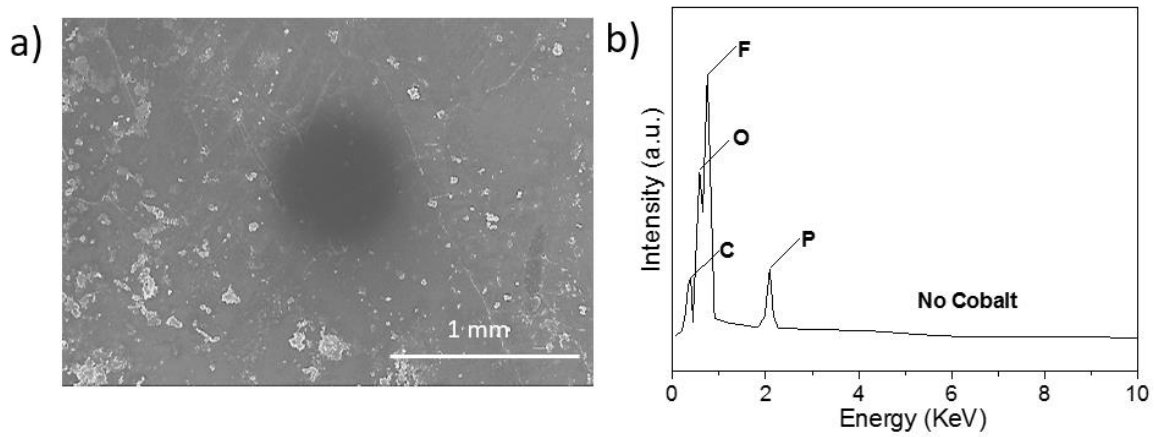

Figure 73. Morphology and composition of the cycled Li anodes: a) SEM micrograph and b) EDS spectrum of the anode foil in 1 M $LiPF_6$, FEC/EMC (3:7) electrolyte, showing smooth morphology as well as a lack of Co precipitates.[350]

6.5 Conclusion

The CoF_2/CNTs nanocomposite was successfully produced via continuous CVD synthesis of CNT non-woven fabric followed by a surfactant-assisted aqueous infiltration of Co precursor and its transformation to 30-50 nm CoF_2 nanoparticles uniformly distributed on the CNT surface. The flexible CoF_2/CNTs nanocomposite exhibited an improvement on composite strength and a remarkable modulus of toughness, an important feature as a binder-free multifunctional electrode for LIBs. The uniform and small size of CNT-linked CoF_2 allowed the produced composite to demonstrate near theoretical capacity of $\sim 550\,\text{mAh}\ g_{CoF_2}^{-1}$ at a small current density, $\sim 360\,\text{mAh}\ g_{CoF_2}^{-1}$ at a medium current density of 100 mA g^{-1} and $\sim 130\,\text{mAh}\ g_{CoF_2}^{-1}$ at a high current density of 1000 mA g^{-1}. Electrolyte solvent composition was found to have a major impact on electrochemical stability of the composite. Attractive mechanical properties of the composite in combination with its high specific capacity demonstrate promise for the formation of high strength flexible fluoride-comprising cathodes for multifunctional battery applications.

6.6 Experimental Details

Materials

Cobalt hexafluorosilicate ($CoSiF_6$) solution was prepared from cobaltous carbonate ($CoCO_3$, 99.9 %, Sigma Aldrich) and hexafluorosilicic acid (99.9%, aqueous solution, Sigma Aldrich). The surfactant Triton X-100 was purchased from Alfa Aesar and the MWCNT fabric was from Nanocomp Technologies Inc. The CNTs fabric was pre-washed with ethanol and acetone, and annealed in argon for 12 h at 450 ºC to remove any residual polymers.

Preparation of CoF_2-infiltrated CNTs

The in-situ construction of CoF_2/CNT nanofibrous cathode was carried out through a surfactant-assistant aqueous deposition process. In a typical synthesis, a 1.2 × 1.2 cm CNTs membrane was immersed into 0.05 M $CoSiF_6$ solution. Because the surface of CNTs is highly hydrophobic, 0.1 (V/V) % Triton X-100 was added into the precursor solution in order to increase the precursor wetting. After infiltration and 12 h drying in a 70 ^oC oven, the samples underwent 400 ^oC post annealing treatment in argon for 6 h. By varying the concentration of $CoSiF_6$ solution from 0.05 M to 0.5 M, the mass fraction of CoF_2 in the CoF_2/CNT composites (demonstrated from ~30 to ~70 wt.% in our experiments) could be controlled and quantitatively measured by mass difference before/after loading. In order to compare the battery performance of pure CoF_2, CoF_2/CNTs mixture and CoF_2/CNTs nanofibrous composite, the pure CoF_2 nanopowder was synthesized using the same procedure (without addition of CNTs). And the CoF_2/CNTs mixture was fabricated by the simply blending CNTs and CoF_2 powder together with the same amount of CoF_2 as that in CoF_2/CNTs composite.

Characterizations

The morphology of samples was characterized by using field-emission scanning electron microscope (FESEM; Hitachi, SU8010, Japan) and transmission electron microscopy (TEM; FEI, Tecnai 30, Holland). The crystallinity of these samples was analyzed by X-Ray diffraction (XRD; Panalytical, X'Pert PRO□□-1 diffractometer, Netherland). The surface area of CoF_2/CNTs composite was determined by the isotherms of N_2 gas adsorption, collected at 77 ºK using an ASAP 2020 Surface Area and Porosimetry Analyzer (Micromeritics Inc., USA). The cell was disassembled for *ex-situ* energy dispersive spectroscopy (EDS) and X-ray photoelectron spectroscopy (XPS) tests. The cycled anode (lithium metal) was directly used for the EDS (Zeiss, Ultra 60, Germany) tests for the determination of Co content. The cycled cathode was washed with EMC or DMC to remove any lithium hexafluorophosphate ($LiPF_6$) and dried in argon atmosphere naturally. After cleaning, these cathode was tested by the X-ray photoelectric spectroscopy (XPS; Kratos Analytical Ltd, Japan) and Ar filled sample transfer chamber was used to prevent air exposure of the electrodes. The CoF_2 electrode fabric comprising with ~60 wt. % CNT (no other conductive additives and no binder) was selected for both electrochemical and mechanical tests. An electrode comprising CoF_2 nanopowder milled with CNT (similar CoF_2:C ratio, ~40 wt. %) and additionally containing 5 wt. % polyvinylidene fluoride (PVDF) binder was used for benchmark comparison.

Mechanical Properties Measurement

Mechanical properties were measured using a tensile test frame (MTS Insight 2, USA) with at a strain rate of 10% min^{-1} and a 100 N load cell. Strain was measured without a strain gauge or extensometer due to the large displacements achieved in accordance with ASTM D882-12. Five sample specimens from each

were cut into a length of ~10 cm and width of 5 mm. Actual sample width and thickness was measured via micrometer and was found to be 5.5 mm and 33 μm.

Electrochemical Measurements

The electrochemical properties were evaluated by using 2016 coin cells with Li metal disks as the counter and reference electrodes. The prepared CoF_2/CNTs composite was directly cut into electrode disks (10 mm diameter) and assembled using a polypropylene membrane (Celgard, 2500) as a separator. The electrolyte used was 1 M $LiPF_6$ dissolved in 1:1:1 (V/V/V %) ethylene carbonate/dimethyl carbonate/diethyl carbonate (EC/DMC/DEC) solvents. As for the CoF_2/CNTs mixture, 5 (wt.) % of polyvinyliene fluoride (PVDF) was added as the binder to the 1-Methyl-2-pyrrolidinone (NMP) solution to make the slurry on an aluminum (Al) foil. The rest of the preparation procedure of CoF_2/CNTs mixture electrode was the same with that of CoF_2/CNTs composite electrode. The electrode mass loading was ~ 1 mg cm^{-2} in all tests. The cyclic voltammetry (CV) of CoF_2/CNTs composite was tested using a Solartron potentiostat (AMATEK Inc., USA) within the potential window of 1-4 V (*vs.* Li^+/Li) and the galvanostatic charge-discharge properties were evaluated on an Arbin battery system (Arbin Instrument, USA) with the same potential window as in CV tests. The electrochemical impedance spectroscopy (EIS) was conducted by using a Gamry EIS system (Gamry Instruments, USA) from 10^5 to 0.01 Hz with an amplitude of 10 mV.

CHAPTER 7

CONCLUSIONS

7.1 Research Impact

The research presented herein has contributed broadly to the knowledge of synthesizing and implementing 1D nanomaterials into a variety of energy storage devices. The multifunctionality of these devices was also examined.

A novel catalyst-free, low-temperature method of producing high purity Al NWs on metal foil substrates (Fe, Ni, Cu) using low pressure and temperature (100-300 ºC) CVD technique has been demonstrated. The lack of droplet at the tip suggested a vapor-solid growth mechanism. The presence of twin boundaries in the formed NWs suggested significant plastic deformation during growth. Various factors affecting and explaining the NW growth have been discussed including substrate material and temperature. Thin polymer coatings were found to be highly effective in suppressing the NW growth due to the surface selectivity of the CVD precursor. This opens multiple opportunities to produce controlled patterns of Al NWs which may be useful in system on a chip applications. The Al NWs were used as a high performance current collectors upon which 50 nm conformal film of VOx was deposited using ALD technique. The resulting pseudocapacitor was tested electrochemically and was determined to have a high capacitance (1400 F cm^{-3}) and good rate capability. Future studies will be directed towards the size-controlled growth of aligned Al NWs using catalyst-assisted deposition.

In addition to the development of the Al NW synthesis method, a novel scalable method of producing AONWs was developed. First Al alkoxide nanowires were formed using a catalyst-free alcohol based delithiation of a β-AlLi alloy. These alkoxide nanowires were shown to be able to be controlled in size through temperature variation and alcohol selection with smaller molecular weights forming smaller dimensions and

higher temperatures causing larger dimensions with sizes ranging from 40-1700 nm observed. More importantly this process allows the formation of 1D nanostructures from bulk materials. This novel low-cost synthesis route may be applicable to a very broad range of chemistries. As such, the reported findings provide completely new avenues for scalable synthesis of metalorganic nanowires, which may be transformed into various ceramic nanowires and, in many cases, further reduced to metallic nanowires, thus covering a majority of the applications of nanotechnology. As an example, flexible thermally stable AONW-based separators for safer Li-ion batteries were created and characterized for temperature stability and electrochemical performance. Other nanowire chemistries and applications will be explored in the future studies.

Fabrics produced from CNTs having lengths >1 mm were demonstrated to be effective current collectors for increasing the cycle stability of traditionally low stability capacitor and battery active materials. The mechanical properties of non-woven CNT composites could be greatly increased by deposition of active materials which was driven by the increase in CNT-CNT bonding. PANI was shown to allow higher strength than CoF_2 due to the π- π bonding between the CNT and conjugated polymer backbone and the uniform deposition enabled by pulsed electrodeposition. CoF_2 showed a much higher strain to fail and lower strength than the PANI-CNT composites due to the low interfacial energy between the CNT and CoF_2 nanoparticles which allowed for greater pullout behavior. These CNT-active material composites showed higher strength, strain to failure, and modulus of toughness than both the initial CNT fabric and comparable current collectors (Al, Cu) while providing a low weight (0.6 g cm^{-3}) high surface area current collector. The CNT capacity/capacitance contribution was repeatedly shown to be negligible (~3 mAh g^{-1} and <20 F g^{-1} respectively) in these systems.

The CoF_2/CNTs nanocomposite was successfully produced via a surfactant-assisted aqueous infiltration of Co precursor and its transformation to 30-50 nm CoF_2 nanoparticles uniformly distributed on the CNT surface. The flexible CoF_2/CNT

nanocomposite exhibited an improvement on composite strength and a remarkable modulus of toughness, an important feature as a binder-free multifunctional electrode for LIBs. The uniform and small size of CNT-linked CoF_2 allowed the produced composite to demonstrate near theoretical capacity of $\sim 550\,\text{mAh}\,g_{CoF_2}^{-1}$ at a small current density, ~ $360\,\text{mAh}\,g_{CoF_2}^{-1}$ at a medium current density of 100 mAh g^{-1} and $\sim 130\,\text{mAh}\,g_{CoF_2}^{-1}$ at a high current density of 1000 mAh g^{-1}. Electrolyte solvent composition was found to have a major impact on electrochemical stability of the composite.

7.2 Recommendations

This research has demonstrated the important contributions 1D nanomaterials can have in non-active material roles in an energy storage device. The synthesis techniques developed will also help enable further research into these fields by providing simple low cost, scalable synthesis methods for interesting nanomaterials. Continued investigation of the synthesis methods and the potential uses for the produced materials will need to be performed to fully develop this technology into a useful device component. For all nanowire deposition methods more research is needed to better control the diameter distribution and ensure doing so maintains control of the nanowire diameters. For AlNW this could be accomplished by implementing a VLS growth method instead of the self-catalytic VS method used currently. Suggestions for catalyst compounds include low melting point materials such as indium or gallium which form eutectics easily with aluminum. This should simultaneously improve the crystallinity, length, and orientation of the AlNWs. Due to the toxicity of vanadium it also may be beneficial to experiment with testing the high surface area AlNW current collectors with other less hazardous pseudocapacitor materials such as MnO_2, etc. which still suffer from electrical resistivity issues.

Separator materials have proven to be a large concern for the safety and performance of modern LIB with the likely hood of unscheduled thermal events growing

as energy and power density increases. The free standing AONW membranes developed in this thesis provide a unique solution to many of these safety issues however further development is likely needed to ensure these materials comply with current manufacturing systems. While the produced films have good flexibility for porous ceramic membranes an improvement will be needed to allow roll to roll processing which is required for mass manufacturing. This can likely be achieved through binder addition through infiltration or applying the AONW film to a thin free standing membrane for additional mechanical support or as a carrier layer. An alternate route would be the incorporation of these high aspect ratio AONWs as structural supports and low temperature conductivity enhancers for polymer electrolytes such as PEO. While the synthesis methods of producing nanowires from bulk aluminum have been demonstrated, the same reaction mechanism could possibly be applied to other material systems and work is currently being done to validate this mechanism with materials such as Mg, Cu, and Ag.

CNT composites have been widely studied however only recently have production quantities and quality been high enough to enable usage in large format electrochemical storage devices. These developments led to the usage in high performance current collectors for a wide variety of active material based devices. While we have shown the potential benefits of these materials for enabling flexible devices and potential structural multifunctionality, more work is needed to prepare complete devices. Current structural applications are limited by a lack of solid electrolyte with both good mechanical properties and ionic conductivity.

REFERENCES

1 Singh, R. Lithium-Ion Battery Market by Material Type (Cathode, Anode, Electrolytic solution, Foils, Binders, Separators) and Industry Vertical (Smartphones, UPS, Cars, Aircraft, Busses, Trucks, Mining equipment, Smart Grid, Games, Gardening tools) - Global Opportunity Analysis and Industry Forecast, 2015-2022. 110 (Allied Market Research, 2016).

2 Park, J.-K. *Principles and applications of lithium secondary batteries*. (John Wiley & Sons, 2012).

3 Conway, B. E. *Electrochemical supercapacitors: scientific fundamentals and technological applications*. (Springer Science & Business Media, 2013).

4 Zhang, Y. *et al.* Progress of electrochemical capacitor electrode materials: A review. *Int. J. Hydrogen Energy* **34**, 4889-4899, doi:10.1016/j.ijhydene.2009.04.005 (2009).

5 Song, M.-K., Park, S., Alamgir, F. M., Cho, J. & Liu, M. Nanostructured electrodes for lithium-ion and lithium-air batteries: the latest developments, challenges, and perspectives. *Materials Science and Engineering: R: Reports* **72**, 203-252 (2011).

6 Nitta, N. & Yushin, G. High-Capacity Anode Materials for Lithium-Ion Batteries: Choice of Elements and Structures for Active Particles. *Particle & Particle Systems Characterization* **31**, 317-336 (2014).

7 Nitta, N., Wu, F., Lee, J. T. & Yushin, G. Li-ion battery materials: present and future. *Mater. Today* **18**, 252-264, doi:10.1016/j.mattod.2014.10.040 (2015).

8 Buchmann, I. *Batteries in a Portable World: A Handbook on Rechargeable Batteries for Non-engineers*. (Cadex Electronics, 2016).

9 Taberna, P.-L., Mitra, S., Poizot, P., Simon, P. & Tarascon, J.-M. High rate capabilities Fe3O4-based Cu nano-architectured electrodes for lithium-ion battery applications. *Nat. Mater.* **5**, 567-573 (2006).

10 Fischer, A. E., Pettigrew, K. A., Rolison, D. R., Stroud, R. M. & Long, J. W. Incorporation of homogeneous, nanoscale MnO2 within ultraporous carbon structures via self-limiting electroless deposition: implications for electrochemical capacitors. *Nano Lett.* **7**, 281-286 (2007).

11 Thomas, J. P. & Qidwai, M. A. The design and application of multifunctional structure-battery materials systems. *JOM* **57**, 18-24, doi:10.1007/s11837-005-0228-5 (2005).

12 Mullen, J. in *CNN* (CNNMoney, Hong Kong, 2016).

13 Bard, A. J. & Faulkner, L. R. *Electrochemical methods: fundamentals and applications*. (Wiley, 2001).

14 Zhang, L. L. & Zhao, X. S. Carbon-based materials as supercapacitor electrodes. *Chem. Soc. Rev.* **38**, 2520-2531, doi:10.1039/B813846J (2009).

15 Japan, T. C. S. *Advanced Ceramic Technologies & Products*. (Springer Japan, 2012).

16 Simon, P. & Gogotsi, Y. Materials for electrochemical capacitors. *Nat. Mater.* **7**, 845-854 (2008).

17 Gu, W., Wang, X. & Yushin, G. Nanostructured Activated Carbons for Supercapacitors. *Nanocarbons for Advanced Energy Storage* **1** (2015).

18 Whittingham, M. S. Materials challenges facing electrical energy storage. *MRS Bull.* **33**, 411-419 (2008).
19 Portet, C., Taberna, P. L., Simon, P. & Laberty-Robert, C. Modification of Al current collector surface by sol-gel deposit for carbon-carbon supercapacitor applications. *Electrochim. Acta* **49**, 905-912, doi:10.1016/j.electacta.2003.09.043 (2004).
20 Braithwaite, J., Nagasubramanian, G., Gonzales, A., Lucero, S. & Cieslak, W. Corrosion of Current-Collector Material in Li-Ion Cells. *Lithium Polymer Batteries*, 44-51 (1997).
21 Zhu, J., Feng, J. & Guo, Z. Mechanical properties of commercial copper current-collector foils. *RSC Advances* **4**, 57671-57678, doi:10.1039/C4RA07675C (2014).
22 Yazici, M., Krassowski, D. & Prakash, J. Flexible graphite as battery anode and current collector. *J. Power Sources* **141**, 171-176 (2005).
23 Taheri, P., Mansouri, A., Schweitzer, B., Yazdanpour, M. & Bahrami, M. Electrical constriction resistance in current collectors of large-scale lithium-ion batteries. *J. Electrochem. Soc.* **160**, A1731-A1740 (2013).
24 Kim, S. W. & Cho, K. Y. Current Collectors for Flexible Lithium Ion Batteries: A Review of Materials. *Journal of Electrochemical Science and Technology* **6**, 1-6 (2015).
25 Daniel, C. & Besenhard, J. O. *Handbook of Battery Materials*. (Wiley, 2012).
26 Myung, S.-T., Hitoshi, Y. & Sun, Y.-K. Electrochemical behavior and passivation of current collectors in lithium-ion batteries. *J. Mater. Chem.* **21**, 9891-9911 (2011).
27 Myung, S.-T., Sasaki, Y., Sakurada, S., Sun, Y.-K. & Yashiro, H. Electrochemical behavior of current collectors for lithium batteries in non-aqueous alkyl carbonate solution and surface analysis by ToF-SIMS. *Electrochim. Acta* **55**, 288-297 (2009).
28 Morita, M., Shibata, T., Yoshimoto, N. & Ishikawa, M. Anodic behavior of aluminum in organic solutions with different electrolytic salts for lithium ion batteries. *Electrochim. Acta* **47**, 2787-2793 (2002).
29 Melendres, C. A. Kinetics of Electrochemical Incorporation of Lithium into Aluminum. *J. Electrochem. Soc.* **124**, 650-655 (1977).
30 Winter, M. & Besenhard, J. O. Electrochemical lithiation of tin and tin-based intermetallics and composites. *Electrochim. Acta* **45**, 31-50 (1999).
31 Hamon, Y. *et al.* Aluminum negative electrode in lithium ion batteries. *J. Power Sources* **97-98**, 185-187 (2001).
32 Benson, J., Boukhalfa, S., Magasinski, A., Kvit, A. & Yushin, G. Chemical Vapor Deposition of Aluminum Nanowires on Metal Substrates for Electrical Energy Storage Applications. *ACS Nano* **6**, 118-125, doi:10.1021/nn202979y (2011).
33 Saito, R., Dresselhaus, G. & Dresselhaus, M. S. *Physical Properties of Carbon Nanotubes*. (Imperial College Press, 1998).
34 Mattia, D. *et al.* Effect of graphitization on the wettability and electrical conductivity of CVD-carbon nanotubes and films. *The Journal of Physical Chemistry B* **110**, 9850-9855 (2006).
35 Pollock, M. Grafoil Engineering Design Manual. (2002).

36 Spahr, M. E. *et al.* Exfoliation of Graphite during Electrochemical Lithium Insertion in Ethylene Carbonate-Containing Electrolytes. *J. Electrochem. Soc.* **151**, A1383-A1395-A1383-A1395 (2004).
37 Jiang, Z., Pei, B. & Manthiram, A. Randomly stacked holey graphene anodes for lithium ion batteries with enhanced electrochemical performance. *Journal of Materials Chemistry A* **1**, 7775-7781 (2013).
38 Ohzuku, T., Iwakoshi, Y. & Sawai, K. Formation of Lithium-Graphite Intercalation Compounds in Nonaqueous Electrolytes and Their Application as a Negative Electrode for a Lithium Ion (Shuttlecock) Cell. *J. Electrochem. Soc.* **140**, 2490-2498, doi:10.1149/1.2220849 (1993).
39 Liu, Y. *et al.* Lithiation-induced embrittlement of multiwalled carbon nanotubes. *ACS Nano* **5**, 7245-7253 (2011).
40 Basu, S. *et al.* Synthesis and properties of lithium-graphite intercalation compounds. *Materials Science and Engineering* **38**, 275-283 (1979).
41 Besenhard, J. The electrochemical preparation and properties of ionic alkali metal-and NR4-graphite intercalation compounds in organic electrolytes. *Carbon* **14**, 111-115 (1976).
42 Imanishi, N. *et al.* Charge-Discharge Characteristics of Mesophase-Pitch-Based Carbon Fibers for Lithium Cells. *J. Electrochem. Soc.* **140**, 315-320 (1993).
43 Mattia, D. & Gogotsi, Y. Review: static and dynamic behavior of liquids inside carbon nanotubes. *Microfluidics and Nanofluidics* **5**, 289-305 (2008).
44 Sugime, H. *et al.* Low temperature growth of ultra-high mass density carbon nanotube forests on conductive supports. *Appl. Phys. Lett.* **103**, 073116, doi:10.1063/1.4818619 (2013).
45 Thess, A., Lee, R., Nikolaev, P. & Dai, H. Crystalline ropes of metallic carbon nanotubes. *Science* **273**, 483 (1996).
46 Syngellakis, S. *Composites: Advances in Manufacture and Characterisation*. (WIT Press, 2015).
47 de las Casas, C. & Li, W. A review of application of carbon nanotubes for lithium ion battery anode material. *J. Power Sources* **208**, 74-85, doi:10.1016/j.jpowsour.2012.02.013 (2012).
48 Berhan, L. *et al.* Mechanical properties of nanotube sheets: Alterations in joint morphology and achievable moduli in manufacturable materials. *J. Appl. Phys.* **95**, 4335-4345, doi:10.1063/1.1687995 (2004).
49 Peigney, A., Laurent, C., Flahaut, E., Bacsa, R. & Rousset, A. Specific surface area of carbon nanotubes and bundles of carbon nanotubes. *Carbon* **39**, 507-514 (2001).
50 Kaempgen, M., Chan, C. K., Ma, J., Cui, Y. & Gruner, G. Printable thin film supercapacitors using single-walled carbon nanotubes. *Nano Lett.* **9**, 1872-1876 (2009).
51 Hu, L. *et al.* Highly conductive paper for energy-storage devices. *Proceedings of the National Academy of Sciences* **106**, 21490-21494, doi:10.1073/pnas.0908858106 (2009).
52 Kim, Y.-L., Sun, Y.-K. & Lee, S.-M. Enhanced electrochemical performance of silicon-based anode material by using current collector with modified surface morphology. *Electrochim. Acta* **53**, 4500-4504 (2008).

53 Park, M.-H. *et al.* Flexible high-energy Li-ion batteries with fast-charging capability. *Nano Lett.* **14**, 4083-4089 (2014).
54 Oltean, G., Nyholm, L. & Edström, K. Galvanostatic electrodeposition of aluminium nano-rods for Li-ion three-dimensional micro-battery current collectors. *Electrochim. Acta* **56**, 3203-3208, doi:10.1016/j.electacta.2011.01.053 (2011).
55 Gerein, N. J. & Haber, J. A. Effect of ac electrodeposition conditions on the growth of high aspect ratio copper nanowires in porous aluminum oxide templates. *The Journal of Physical Chemistry B* **109**, 17372-17385 (2005).
56 Huang, X. Separator technologies for lithium-ion batteries. *J. Solid State Electrochem.* **15**, 649-662 (2011).
57 Weber, C. J., Geiger, S., Falusi, S. & Roth, M. in *REVIEW ON ELECTROCHEMICAL STORAGE MATERIALS AND TECHNOLOGY: Proceedings of the 1st International Freiberg Conference on Electrochemical Storage Materials.* 66-81 (AIP Publishing).
58 Zhang, S. S. A review on the separators of liquid electrolyte Li-ion batteries. *J. Power Sources* **164**, 351-364, doi:10.1016/j.jpowsour.2006.10.065 (2007).
59 Arora, P. & Zhang, Z. Battery separators. *Chem. Rev.* **104**, 4419-4462 (2004).
60 Baldwin, R. S., Bennet, W. R., Wong, E. K., Lewton, M. R. & Harris, M. K. Battery Separator Characterization and Evaluation Procedures for NASA's Advanced Lithium-Ion Batteries. (2010).
61 Doeff, M. M. in *Batteries for Sustainability: Selected Entries from the Encyclopedia of Sustainability Science and Technology* (ed J. Ralph Brodd) 5-49 (Springer New York, 2013).
62 Vetter, J. *et al.* Ageing mechanisms in lithium-ion batteries. *J. Power Sources* **147**, 269-281 (2005).
63 Gu, W. & Yushin, G. Review of nanostructured carbon materials for electrochemical capacitor applications: advantages and limitations of activated carbon, carbide-derived carbon, zeolite-templated carbon, carbon aerogels, carbon nanotubes, onion-like carbon, and graphene. *Wiley Interdisciplinary Reviews: Energy and Environment* **3**, 424-473, doi:10.1002/wene.102 (2014).
64 Chmiola, J. *et al.* Anomalous increase in carbon capacitance at pore sizes less than 1 nanometer. *Science* **313**, 1760-1763 (2006).
65 Kajdos, A., Kvit, A., Jones, F., Jagiello, J. & Yushin, G. Tailoring the Pore Alignment for Rapid Ion Transport in Microporous Carbons. *J. Am. Chem. Soc.* **132**, 3252 (2010).
66 Brousse, T., Bélanger, D. & Long, J. W. To Be or Not To Be Pseudocapacitive? *J. Electrochem. Soc.* **162**, A5185-A5189, doi:10.1149/2.0201505jes (2015).
67 Augustyn, V., Simon, P. & Dunn, B. Pseudocapacitive oxide materials for high-rate electrochemical energy storage. *Energy & Environmental Science* **7**, 1597-1614 (2014).
68 Yang, C. *et al.* Polymer nanocomposites for energy storage, energy saving, and anticorrosion. *Journal of Materials Chemistry A* **3**, 14929-14941, doi:10.1039/C5TA02707A (2015).

69 Reddy, Y. V. & Mergel, D. Structural and electrical properties of RuO2 thin films prepared by rf-magnetron sputtering and annealing at different temperatures. *Journal of Materials Science: Materials in Electronics* **17**, 1029-1034 (2006).
70 Zheng, J. & Jow, T. High energy and high power density electrochemical capacitors. *J. Power Sources* **62**, 155-159 (1996).
71 Ghodbane, O., Pascal, J.-L. & Favier, F. Microstructural effects on charge-storage properties in MnO2-based electrochemical supercapacitors. *ACS applied materials & interfaces* **1**, 1130-1139 (2009).
72 Wei, W., Cui, X., Chen, W. & Ivey, D. G. Manganese oxide-based materials as electrochemical supercapacitor electrodes. *Chem. Soc. Rev.* **40**, 1697-1721 (2011).
73 Sun, D. *et al.* The relationship between nanoscale structure and electrochemical properties of vanadium oxide nanorolls. *Adv. Funct. Mater.* **14**, 1197-1204, doi:10.1002/adfm.200400056 (2004).
74 Sudant, G., Baudrin, E., Dunn, B. & Tarascon, J. M. Synthesis and electrochemical properties of vanadium oxide aerogels prepared by a freeze-drying process. *J. Electrochem. Soc.* **151**, A666-A671, doi:10.1149/1.1687427 (2004).
75 Sakamoto, J. S. & Dunn, B. Vanadium oxide-carbon nanotube composite electrodes for use in secondary lithium batteries. *J. Electrochem. Soc.* **149**, A26-A30, doi:10.1149/1.1425791 (2002).
76 Rolison, D. R. & Dunn, B. Electrically conductive oxide aerogels: new materials in electrochemistry. *J. Mater. Chem.* **11**, 963-980, doi:10.1039/b007591o (2001).
77 Dong, W., Rolison, D. R. & Dunn, B. Electrochemical properties of high surface area vanadium oxide aerogels. *Electrochem. Solid-State Lett.* **3**, 457-459 (2000).
78 Shembel, E., Apostolova, R., Nagirny, V., Aurbach, D. & Markovsky, B. Synthesis, investigation and practical application in lithium batteries of some compounds based on vanadium oxides. *J. Power Sources* **80**, 90-97, doi:10.1016/s0378-7753(99)00165-2 (1999).
79 Chen, Z. *et al.* High-Performance Supercapacitors Based on Intertwined CNT/V2O5 Nanowire Nanocomposites. *Adv. Mater.* **23**, 791–795, doi:10.1002/adma.201003658 (2011).
80 Dong, W., Sakamoto, J. & Dunn, B. Electrochemical properties of vanadium oxide aerogels and aerogel nanocomposites. *J. Sol-Gel Sci. Technol.* **26**, 641-644 (2003).
81 Rata, A. *et al.* Growth and properties of strained VO x thin films with controlled stoichiometry. *Phys. Rev. B* **69**, 075404 (2004).
82 Stringer, J. The vanadium-oxygen system—a review. *Journal of the Less Common Metals* **8**, 1-14 (1965).
83 Arico, A. S., Bruce, P., Scrosati, B., Tarascon, J.-M. & van Schalkwijk, W. Nanostructured materials for advanced energy conversion and storage devices. *Nat Mater* **4**, 366-377 (2005).
84 Thomberg, T., Jänes, A. & Lust, E. Energy and power performance of vanadium carbide derived carbon electrode materials for supercapacitors. *J. Electroanal. Chem.* **630**, 55-62 (2009).

85 Cohen, Y. S. & Aurbach, D. Surface films phenomena on vanadium-pentoxide cathodes for Li and Li-ion batteries: in situ AFM imaging. *Electrochem. Commun.* **6**, 536-542 (2004).
86 Skotheim, T. A. & Reynolds, J. *Handbook of Conducting Polymers, 2 Volume Set*. (CRC Press, 2007).
87 Lvovich, V. F. *Impedance Spectroscopy : Applications to Electrochemical and Dielectric Phenomena*. (Wiley, 2012).
88 Gvozdenović, M., Jugović, B., Stevanović, J., Trišović, T. & Grgur, B. in *Electropolymerization* (ed Ewa Schab-Balcerzak) 77-96 (InTech, 2011).
89 Cullity, B. D. *Elements of X-ray Diffraction*. (Addison-Wesley Publishing Company, 1978).
90 Williamson, G. & Hall, W. X-ray line broadening from filed aluminium and wolfram. *Acta Metall.* **1**, 22-31 (1953).
91 Birkholz, M. *Thin Film Analysis by X-Ray Scattering*. (Wiley, 2006).
92 Birkholz, M. in *Thin Film Analysis by X-Ray Scattering* 1-40 (Wiley-VCH Verlag GmbH & Co. KGaA, 2006).
93 Zhou, W. & Wang, Z. L. *Scanning microscopy for nanotechnology: techniques and applications*. (Springer science & business media, 2007).
94 Zhou, W., Apkarian, R., Wang, Z. L. & Joy, D. in *Scanning Microscopy for Nanotechnology: Techniques and Applications* (eds Weilie Zhou & Zhong Lin Wang) 1-40 (Springer New York, 2007).
95 *An Introduction to electron microscopy*. (FEI Inc., 2010).
96 Nicholson, R. S. & Shain, I. Theory of Stationary Electrode Polarography. Single Scan and Cyclic Methods Applied to Reversible, Irreversible, and Kinetic Systems. *Anal. Chem.* **36**, 706-723, doi:10.1021/ac60210a007 (1964).
97 Dolin, P. & Ershler, B. The kinetics of discharge and ionization of hydrogen adsorbed at Pt-electrode. *Acta Physicochim. URSS* **13**, 747 (1940).
98 Randles, J. E. B. Kinetics of rapid electrode reactions. *Discussions of the faraday society* **1**, 11-19 (1947).
99 Taberna, P., Simon, P. & Fauvarque, J.-F. Electrochemical characteristics and impedance spectroscopy studies of carbon-carbon supercapacitors. *J. Electrochem. Soc.* **150**, A292-A300 (2003).
100 Randviir, E. P. & Banks, C. E. Electrochemical impedance spectroscopy: an overview of bioanalytical applications. *Analytical Methods* **5**, 1098-1115, doi:10.1039/C3AY26476A (2013).
101 Scholz, F. *Electroanalytical Methods: Guide to Experiments and Applications*. (Springer Berlin Heidelberg, 2009).
102 Macdonald, D. D. Reflections on the history of electrochemical impedance spectroscopy. *Electrochim. Acta* **51**, 1376-1388 (2006).
103 Boukamp, B. A. Practical application of the Kramers-Kronig transformation on impedance measurements in solid state electrochemistry. *Solid State Ionics* **62**, 131-141, doi:10.1016/0167-2738(93)90261-Z (1993).
104 Lide, D. R. *CRC Handbook of Chemistry and Physics, 85th Edition*. (Taylor & Francis, 2004).
105 Gaikwad, A. M. *et al.* A High Areal Capacity Flexible Lithium-Ion Battery with a Strain-Compliant Design. *Advanced Energy Materials* **5** (2015).

106 Miccoli, I., Edler, F., Pfnür, H. & Tegenkamp, C. The 100th anniversary of the four-point probe technique: the role of probe geometries in isotropic and anisotropic systems. *J. Phys.: Condens. Matter* **27**, 223201 (2015).
107 Valdes, L. B. Resistivity Measurements on Germanium for Transistors. *Proceedings of the IRE* **42**, 420-427, doi:10.1109/JRPROC.1954.274680 (1954).
108 Smits, F. Measurement of sheet resistivities with the four-point probe. *Bell System Technical Journal* **37**, 711-718 (1958).
109 Ashby, M. F. *Materials Selection in Mechanical Design*. (Elsevier Science, 2004).
110 Amutha, K. *A Practical Guide to Textile Testing*. (WPI India, 2016).
111 IPS Testing. ASTM Test Methods Performed by IPS. (2016). <www.ipstesting.com/find-a-test/astm-test-methods/>.
112 Mallick, P. K. *Fiber-Reinforced Composites: Materials, Manufacturing, and Design, Third Edition*. (CRC Press, 2007).
113 Wu, J. & Pan, N. Grab and strip tensile strengths for woven fabrics: An experimental verification. *Textile research journal* **75**, 789-796 (2005).
114 Menard, K. P. *Dynamic mechanical analysis: a practical introduction*. (CRC press, 2008).
115 Wei, Y. *et al.* Thermal transitions and mechanical properties of films of chemically prepared polyaniline. *Polymer* **33**, 314-322 (1992).
116 Kuchibhatla, S. V. N. T., Karakoti, A. S., Bera, D. & Seal, S. One dimensional nanostructured materials. *Progress in Materials Science* **52**, 699-913, doi:10.1016/j.pmatsci.2006.08.001 (2007).
117 Byrappa, K. & Adschiri, T. Hydrothermal technology for nanotechnology. *Prog. Cryst. Growth Charact. Mater.* **53**, 117-166, doi:10.1016/j.pcrysgrow.2007.04.001 (2007).
118 Karabacak, T., Singh, J. P., Zhao, Y. P., Wang, G. C. & Lu, T. M. Scaling during shadowing growth of isolated nanocolumns. *Phys. Rev. B* **68** (2003).
119 Alagoz, A. S. & Karabacak, T. Fabrication of Crystalline Semiconductor Nanowires by Vapor-Liquid-Solid Glancing Angle Deposition (VLS-GLAD) Technique. *MRS Online Proceedings Library Archive* **1350**, mrss11-1350-ee1303-1341 (1356 pages), doi:10.1557/opl.2011.1005 (2011).
120 Robbie, K. & Brett, M. J. Sculptured thin films and glancing angle deposition: Growth mechanics and applications. *Journal of Vacuum Science & Technology A* **15**, 1460-1465, doi:10.1116/1.580562 (1997).
121 Pierson, H. O. *Handbook of Chemical Vapor Deposition (CVD): Principles, Technology, and Applications*. (Noyes Publications, 1992).
122 Welty, J. R., Wicks, C. E., Rorrer, G. & Wilson, R. E. *Fundamentals of momentum, heat, and mass transfer*. (John Wiley & Sons, 2009).
123 Park, J. H. & Sudarshan, T. S. *Chemical Vapor Deposition*. (ASM International, 2001).
124 Leskelä, M. & Ritala, M. Atomic layer deposition (ALD): from precursors to thin film structures. *Thin Solid Films* **409**, 138-146 (2002).
125 Pauleau, Y. *Chemical Physics of Thin Film Deposition Processes for Micro- and Nano-Technologies*. (Springer Netherlands, 2012).

126 Wang, X. & Yushin, G. Chemical vapor deposition and atomic layer deposition for advanced lithium ion batteries and supercapacitors. *Energy & Environmental Science* **8**, 1889-1904, doi:10.1039/C5EE01254F (2015).
127 Wagner, R. S. Vapor-Liquid-Solid Mechanism of Single Crystal Growth. *Appl. Phys. Lett.* **4**, 89 (1964).
128 Kolasinski, K. W. Catalytic growth of nanowires: Vapor-liquid-solid, vapor-solid-solid, solution-liquid-solid and solid-liquid-solid growth. *Current Opinion in Solid State and Materials Science* **10**, 182-191, doi:10.1016/j.cossms.2007.03.002.
129 Inoue, Y. *et al.* One-step grown aligned bulk carbon nanotubes by chloride mediated chemical vapor deposition. *Appl. Phys. Lett.* **92**, 213113-213113 (2008).
130 Philippe, R. *et al.* Catalytic Production of Carbon Nanotubes by Fluidized-Bed CVD. *Chem. Vap. Deposition* **13**, 447-457 (2007).
131 Liu, Y. & Liu, M. Growth of Aligned Square-Shaped SnO2 Tube Arrays. *Adv. Funct. Mater.* **15**, 57-62 (2005).
132 Pan, Z. W., Dai, Z. R. & Wang, Z. L. Nanobelts of semiconducting oxides. *Science* **291**, 1947-1949 (2001).
133 Mohammad, S. N. Self-catalysis: A contamination-free, substrate-free growth mechanism for single-crystal nanowire and nanotube growth by chemical vapor deposition. *The Journal of chemical physics* **125**, 094705 (2006).
134 Wang, N., Cai, Y. & Zhang, R. Q. Growth of nanowires. *Materials Science and Engineering: R: Reports* **60**, 1-51, doi:10.1016/j.mser.2008.01.001 (2008).
135 Kim, C. *et al.* Copper nanowires with a five-twinned structure grown by chemical vapor deposition. *Adv. Mater.* **20**, 1859–1863, doi:10.1002/adma.200701460 (2008).
136 Choi, H. & Park, S. H. Seedless growth of free-standing copper nanowires by chemical vapor deposition. *J. Am. Chem. Soc.* **126**, 6248-6249, doi:10.1021/ja049217 (2004).
137 Yoshimura, M. & Byrappa, K. Hydrothermal processing of materials: past, present and future. *Journal of Materials Science* **43**, 2085-2103 (2008).
138 Rabenau, A. The Role of Hydrothermal Synthesis in Preparative Chemistry. *Angewandte Chemie International Edition in English* **24**, 1026-1040, doi:10.1002/anie.198510261 (1985).
139 Byrappa, K. & Yoshimura, M. *Handbook of hydrothermal technology*. (William Andrew, 2012).
140 Brown, P. W. & Constantz, B. *Hydroxyapatite and Related Materials*. (Taylor & Francis, 1994).
141 Bashford, D. & Case, D. A. Generalized Born Models of Macromolecular Solvation Effects. *Annu. Rev. Phys. Chem.* **51**, 129-152, doi:10.1146/annurev.physchem.51.1.129 (2000).
142 Gamburg, Y. D. & Zangari, G. *Theory and Practice of Metal Electrodeposition*. (Springer New York, 2011).
143 Chandrasekar, M. S. & Pushpavanam, M. Pulse and pulse reverse plating—Conceptual, advantages and applications. *Electrochim. Acta* **53**, 3313-3322, doi:10.1016/j.electacta.2007.11.054 (2008).

144 Karimi, S. Pulse Current Electrodeposition of Nanocatalysts Using Different Waveforms for Use in PEMFCs. *ECS Transactions* **53**, 59-67 (2013).
145 Shen, F.-Y. *et al.* Periodic Pulse Reverse Cu Plating for Through-Hole Filling. *ECS Electrochemistry Letters* **2**, D23-D25, doi:10.1149/2.003305eel (2013).
146 Dai, J., Wang, W., Liang, J., Chu, Q. & Zhen, Z. Influence of pulse waveforms on electrodeposition of Zn coating. *Surf. Eng.* **29**, 500-506 (2013).
147 Pang, Y.-T. *et al.* Electrochemical synthesis of ordered alumina nanowire arrays. *J. Solid State Electrochem.* **7**, 344-347, doi:10.1007/s10008-002-0333-0 (2003).
148 Syed, A. A. & Dinesan, M. K. Review: Polyaniline—A novel polymeric material. *Talanta* **38**, 815-837, doi:10.1016/0039-9140(91)80261-W (1991).
149 Torresi, R. M. & Maranhao, S. L. D. Anion and solvent exchange as a function of the redox states in polyaniline films. *J. Electrochem. Soc.* **146**, 4179-4182 (1999).
150 Beck, F. Electrodeposition of polymer coatings. *Electrochim. Acta* **33**, 839-850, doi:10.1016/0013-4686(88)80080-X (1988).
151 Ding, L. *et al.* Modification of glassy carbon electrode with polyaniline/multi-walled carbon nanotubes composite: Application to electro-reduction of bromate. *J. Electroanal. Chem.* **668**, 44-50, doi:10.1016/j.jelechem.2011.12.018 (2012).
152 Ruoff, R. S. & Lorents, D. C. Mechanical and Thermal-Properties of Carbon Nanotubes. *Carbon* **33**, 925-930, doi:10.1016/0008-6223(95)00021-5 (1995).
153 Coleman, J. N., Khan, U., Blau, W. J. & Gun'ko, Y. K. Small but strong: A review of the mechanical properties of carbon nanotube–polymer composites. *Carbon* **44**, 1624-1652, doi:10.1016/j.carbon.2006.02.038 (2006).
154 Krenchel, H. *Fibre Reinforcement: Theoretical and Practical Investigations of the Elasticity and Strength of Fibre-reinforced Materials*. (Akademisk forlag, 1964).
155 Shaffer, M. S. & Windle, A. H. Fabrication and characterization of carbon nanotube/poly (vinyl alcohol) composites. *Adv. Mater.* **11**, 937-941 (1999).
156 Backer, S. & Petterson, D. R. Some principles of nonwoven fabrics. *Textile Research Journal* **30**, 704-711 (1960).
157 Russell, S. J. *Handbook of Nonwovens*. (Elsevier Science, 2006).
158 Snyder, J. F., Wong, E. L. & Hubbard, C. W. Evaluation of Commercially Available Carbon Fibers, Fabrics, and Papers for Potential Use in Multifunctional Energy Storage Applications. *J. Electrochem. Soc.* **156**, A215-A224, doi:10.1149/1.3065070 (2009).
159 Tang, L. G. & Kardos, J. L. A review of methods for improving the interfacial adhesion between carbon fiber and polymer matrix. *Polym. Compos.* **18**, 100-113 (1997).
160 Snyder, J. *et al.* Multifunctional structural composite batteries. (DTIC Document, 2007).
161 Iijima, S. & Ichihashi, T. Single-shell carbon nanotubes of 1-nm diameter. (1993).
162 Hussain, F., Hojjati, M., Okamoto, M. & Gorga, R. E. Review article: Polymer-matrix Nanocomposites, Processing, Manufacturing, and Application: An Overview. *J. Compos. Mater.* **40**, 1511-1575, doi:10.1177/0021998306067321 (2006).
163 Falvo, M. R. *et al.* Bending and buckling of carbon nanotubes under large strain. *Nature* **389**, 582-584 (1997).

164 Zhang, J., Jiang, D., Peng, H.-X. & Qin, F. Enhanced mechanical and electrical properties of carbon nanotube buckypaper by in situ cross-linking. *Carbon* **63**, 125-132, doi:10.1016/j.carbon.2013.06.047 (2013).
165 Qian, D., Dickey, E. C., Andrews, R. & Rantell, T. Load transfer and deformation mechanisms in carbon nanotube-polystyrene composites. *Appl. Phys. Lett.* **76**, 2868-2870 (2000).
166 Che, J., Chen, P. & Chan-Park, M. B. High-strength carbon nanotube buckypaper composites as applied to free-standing electrodes for supercapacitors. *Journal of Materials Chemistry A* **1**, 4057-4066, doi:10.1039/C3TA01421E (2013).
167 Sakurai, S., Kamada, F., Futaba, D. N., Yumura, M. & Hata, K. Influence of lengths of millimeter-scale single-walled carbon nanotube on electrical and mechanical properties of buckypaper. *Nanoscale Res Lett* **8**, 546-546, doi:10.1186/1556-276X-8-546 (2013).
168 Wang, X. *et al.* Effect of carbon nanotube length on thermal, electrical and mechanical properties of CNT/bismaleimide composites. *Carbon* **53**, 145-152 (2013).
169 Liu, W. *et al.* Producing superior composites by winding carbon nanotubes onto a mandrel under a poly (vinyl alcohol) spray. *Carbon* **49**, 4786-4791 (2011).
170 Zhang, R. *et al.* Growth of half-meter long carbon nanotubes based on Schulz–Flory distribution. *ACS Nano* **7**, 6156-6161 (2013).
171 Kumar, S. *et al.* Synthesis, Structure, and Properties of PBO/SWNT Composites&. *Macromolecules* **35**, 9039-9043 (2002).
172 Hwang, G. L., Shieh, Y. T. & Hwang, K. C. Efficient Load Transfer to Polymer-Grafted Multiwalled Carbon Nanotubes in Polymer Composites. *Adv. Funct. Mater.* **14**, 487-491, doi:10.1002/adfm.200305382 (2004).
173 Yang, J., Hu, J., Wang, C., Qin, Y. & Guo, Z. Fabrication and Characterization of Soluble Multi-Walled Carbon Nanotubes Reinforced P(MMA-co-EMA) Composites. *Macromolecular Materials and Engineering* **289**, 828-832, doi:10.1002/mame.200400049 (2004).
174 O'Brien, D., Baechle, D. & Wetzel, E. Design and performance of multifunctional structural composite capacitors. *J. Compos. Mater.* **45**, 2797-2809 (2011).
175 Liu, P., Sherman, E. & Jacobsen, A. Design and fabrication of multifunctional structural batteries. *J. Power Sources* **189**, 646-650 (2009).
176 Thomas, J. P. & Qidwai, M. A. Mechanical design and performance of composite multifunctional materials. *Acta Mater.* **52**, 2155-2164, doi:10.1016/j.actamat.2004.01.007 (2004).
177 Zgirski, M., Riikonen, K. P., Touboltsev, V. & Arutyunov, K. Size dependent breakdown of superconductivity in ultranarrow nanowires. *Nano Lett.* **5**, 1029-1033, doi:10.1021/nl050321e (2005).
178 Zgirski, M., Riikonen, K. P., Touboltsev, V. & Arutyunov, K. Y. Quantum fluctuations in ultranarrow superconducting aluminum nanowires. *Phys. Rev. B* **77**, doi:10.1103/PhysRevB.77.054508 (2008).
179 Ozer, M. M., Thompson, J. R. & Weitering, H. H. Hard superconductivity of a soft metal in the quantum regime. *Nat. Physics* **2**, 173-176, doi:10.1038/nphys244 (2006).

180 Guo, Y. G. *et al.* Ordered Ni-Cu nanowire array with enhanced coercivity. *Chem. Mater.* **15**, 664-667, doi:10.1021/cm0208962 (2003).
181 Bao, J. C. *et al.* Template synthesis of an array of nickel nanotubules and its magnetic behavior. *Adv. Mater.* **13**, 1631-1633 (2001).
182 Ferre, R., Ounadjela, K., George, J. M., Piraux, L. & Dubois, S. Magnetization processes in nickel and cobalt electrodeposited nanowires. *Phys. Rev. B* **56**, 14066-14075 (1997).
183 McGary, P. D. *et al.* Magnetic nanowires for acoustic sensors (invited). *J. Appl. Phys.* **99**, doi:10.1063/1.2167332 (2006).
184 Sellmyer, D. J., Zheng, M. & Skomski, R. Magnetism of Fe, Co and Ni nanowires in self-assembled arrays. *J. Phys.: Condens. Matter* **13**, R433-R460 (2001).
185 Kim, T. H. *et al.* Large Discrete Resistance Jump at Grain Boundary in Copper Nanowire. *Nano Lett.* **10**, 3096-3100, doi:10.1021/nl101734h (2010).
186 Granqvist, C. G. Transparent conductors as solar energy materials: A panoramic review. *Sol. Energy Mater. Sol. Cells* **91**, 1529-1598, doi:10.1016/j.solmat.2007.04.031 (2007).
187 Huber, G. W., Shabaker, J. W. & Dumesic, J. A. Raney Ni-Sn catalyst for H-2 production from biomass-derived hydrocarbons. *Science* **300**, 2075-2077 (2003).
188 Lee, E. P. *et al.* Growing Pt nanowires as a densely packed array on metal gauze. *J. Am. Chem. Soc.* **129**, 10634–10635, doi:10.1021/ja074312e (2007).
189 Au, M. *et al.* Free standing aluminum nanostructures as anodes for Li-ion rechargeable batteries. *J. Power Sources* **195**, 3333-3337, doi:10.1016/j.jpowsour.2009.11.102 (2010).
190 Sakintuna, B., Lamari-Darkrim, F. & Hirscher, M. Metal hydride materials for solid hydrogen storage: A review. *Int. J. Hydrogen Energy* **32**, 1121-1140, doi:10.1016/j.ijhydene.2006.11.022 (2007).
191 Shaijumon, M. M. *et al.* Nanoarchitectured 3D Cathodes for Li-Ion Microbatteries. *Adv. Mater.* **22**, 4978–4981, doi:10.1002/adma.201001922 (2010).
192 X. Lang, A. Hirata, T. Fujita & Chen, M. Nanoporous metal/oxide hybrid electrodes for electrochemical supercapacitors. *Nat. Nano.* (2011).
193 Banerjee, P., Perez, I., Henn-Lecordier, L., Lee, S. B. & Rubloff, G. W. Nanotubular metal-insulator-metal capacitor arrays for energy storage. *Nat. Nano.* **4**, 292-296, doi:10.1038/nnano.2009.37 (2009).
194 Centi, G. *et al.* The role of mechanically induced defects in carbon nanotubes to modify the properties of electrodes for PEM fuel cell. *Catal. Today* **147**, 287-299, doi:10.1016/j.cattod.2009.07.080 (2009).
195 Reches, M. & Gazit, E. Casting metal nanowires within discrete self-assembled peptide nanotubes. *Science* **300**, 625-627 (2003).
196 Hong, B. H., Bae, S. C., Lee, C. W., Jeong, S. & Kim, K. S. Ultrathin single-crystalline silver nanowire arrays formed in an ambient solution phase. *Science* **294**, 348-351 (2001).
197 Zhou, J. *et al.* Growth of large-area aligned molybdenum nanowires by high temperature chemical vapor deposition: Synthesis, growth mechanism, and device application. *J. Phys. Chem. B* **110**, 10296-10302, doi:10.1021/jp061213z (2006).

198 Lo Nigro, R., Malandrino, G., Fiorenza, P. & Fragala, I. L. Template-free and seedless growth of Pt nanocolumns: Imaging and probing their nanoelectrical properties. *ACS Nano* **1**, 183-190, doi:10.1021/nn700068u (2007).
199 Chan, K. T. *et al.* Oriented Growth of Single-Crystal Ni Nanowires onto Amorphous SiO2. *Nano Lett.* **10**, 5070-5075, doi:10.1021/nl103301x (2010).
200 Bien, D. C. S. *et al.* Multiple Self-Aligned Iron Nanowires by a Dual Selective Chemical Vapor Deposition Process. *Electrochem. Solid-State Lett.* **10**, H251-H253 (2007).
201 Korenblit, Y. *et al.* High-Rate Electrochemical Capacitors Based on Ordered Mesoporous Silicon Carbide-Derived Carbon. *ACS Nano* **4**, 1337-1344 (2010).
202 Chmiola, J., Largeot, C., Taberna, P. L., Simon, P. & Gogotsi, Y. Monolithic Carbide-Derived Carbon Films for Micro-Supercapacitors. *Science* **328**, 480-483, doi:10.1126/science.1184126 (2010).
203 Pech, D. *et al.* Ultrahigh-power micrometre-sized supercapacitors based on onion-like carbon. *Nat. Nano.* **5**, 651-654, doi:10.1038/nnano.2010.162 (2010).
204 Al-Samman, T. Comparative study of the deformation behavior of hexagonal magnesium-lithium alloys and a conventional magnesium AZ31 alloy. *Acta Mater.* **57**, 2229-2242 (2009).
205 Hulicova-Jurcakova, D., Seredych, M., Lu, G. Q. & Bandosz, T. J. Combined Effect of Nitrogen- and Oxygen-Containing Functional Groups of Microporous Activated Carbon on its Electrochemical Performance in Supercapacitors. *Adv. Funct. Mater.* **19**, 438-447, doi:10.1002/adfm.200801236 (2009).
206 Portet, C., Yushin, G. & Gogotsi, Y. Electrochemical performance of carbon onions, nanodiamonds, carbon black and multiwalled nanotubes in electrical double layer capacitors. *Carbon* **45**, 2511-2518 (2007).
207 Dubois, L. H., Zegarski, B. R., Gross, M. E. & Nuzzo, R. G. Aluminum thin film growth by the thermal decomposition of triethylamine alane. *Surf. Sci.* **244**, 89-95 (1991).
208 Warner, D. H., Curtin, W. A. & Qu, S. Rate dependence of crack-tip processes predicts twinning trends in f.c.c. metals. *Nat. Mater.* **6**, 876-881, doi:10.1038/nmat2030 (2007).
209 Chen, M. W. *et al.* Deformation twinning in nanocrystalline aluminum. *Science* **300**, 1275-1277, doi:10.1126/science.1083727 (2003).
210 Liao, X. Z., Zhou, F., Lavernia, E. J., He, D. W. & Zhu, Y. T. Deformation twins in nanocrystalline Al. *Appl. Phys. Lett.* **83**, 5062-5064, doi:10.1063/1.1633975 (2003).
211 Carlsson, J.-O. & Jansson, U. Progress in chemical vapor deposition. *Prog. Solid State Chem.* **22**, 237-292 (1993).
212 Evanoff, K. *et al.* Towards Ultrathick Battery Electrodes: Aligned Carbon Nanotube – Enabled Architecture. *Adv. Mater.* **24**, 533-537 (2012).
213 Beach, D. B., Blum, S. E. & LeGoues, F. K. Chemical vapor deposition of aluminum from trimethylamine-alane. *J. Vac. Sci. Technol., A* **7**, 3117-3118 (1989).
214 Hinnen, C., Imbert, D., Siffre, J. M. & Marcus, P. An in situ XPS study of sputter-deposited aluminium thin films on graphite. *Appl. Surf. Sci.* **78**, 219-231 (1994).

215 Abramoff, M. D., Magelhaes, P. J. & Ram, S. J. Image Processing with ImageJ. *Biophotonics International* **11**, 36-42 (2004).
216 Xia, Y. N. *et al.* One-dimensional nanostructures: Synthesis, characterization, and applications. *Adv. Mater.* **15**, 353-389, doi:10.1002/adma.200390087 (2003).
217 Stuart, M. A. C. *et al.* Emerging applications of stimuli-responsive polymer materials. *Nat. Mater.* **9**, 101-113, doi:10.1038/nmat2614 (2010).
218 Sanchez, F. & Sobolev, K. Nanotechnology in concrete - A review. *Construction and Building Materials* **24**, 2060-2071, doi:10.1016/j.conbuildmat.2010.03.014 (2010).
219 Wang, Z. L. Zinc oxide nanostructures: growth, properties and applications. *Journal of Physics-Condensed Matter* **16**, R829-R858, doi:10.1088/0953-8984/16/25/r01 (2004).
220 Tian, B. *et al.* Coaxial silicon nanowires as solar cells and nanoelectronic power sources. *Nature* **449**, 885-U888, doi:10.1038/nature06181 (2007).
221 Zhang, M. *et al.* Strong, transparent, multifunctional, carbon nanotube sheets. *Science* **309**, 1215-1219, doi:10.1126/science.1115311 (2005).
222 Ibrahim, I. A., Mohamed, F. A. & Lavernia, E. J. Particulate Reinforced Metal Matrix Composites - A Review. *Journal of Materials Science* **26**, 1137-1156, doi:10.1007/bf00544448 (1991).
223 Hassan, S. F. & Gupta, M. Enhancing physical and mechanical properties of Mg using nanosized Al2O3 particulates as reinforcement. *Metallurgical and Materials Transactions A* **36**, 2253-2258, doi:10.1007/s11661-005-0344-4 (2005).
224 Balandin, A. A. Thermal properties of graphene and nanostructured carbon materials. *Nature Materials* **10**, 569-581, doi:10.1038/nmat3064 (2011).
225 De Volder, M. F. L., Tawfick, S. H., Baughman, R. H. & Hart, A. J. Carbon Nanotubes: Present and Future Commercial Applications. *Science* **339**, 535-539, doi:10.1126/science.1222453 (2013).
226 Peng, X. S. *et al.* Photoluminescence and Infrared Properties of α-Al2O3 Nanowires and Nanobelts. *The Journal of Physical Chemistry B* **106**, 11163-11167, doi:10.1021/jp026028+ (2002).
227 Tang, C. C., Fan, S. S., Li, P., Chapelle, M. L. d. l. & Dang, H. Y. In situ catalytic growth of Al2O3 and Si nanowires. *Journal of Crystal Growth* **224**, 117-121, doi:10.1016/S0022-0248(01)00852-1 (2001).
228 Zhao, Q. *et al.* Catalyst-free growth of single-crystalline alumina nanowire arrays. *Appl. Phys. A* **79**, 1721-1724, doi:10.1007/s00339-004-2911-8 (2004).
229 Kim, Y. *et al.* Robust Superhydrophilic/Hydrophobic Surface Based on Self-Aggregated Al2O3 Nanowires by Single-Step Anodization and Self-Assembly Method. *ACS Applied Materials & Interfaces* **4**, 5074-5078, doi:10.1021/am301411z (2012).
230 Geim, A. K. & Novoselov, K. S. The rise of graphene. *Nat. Mater.* **6**, 183-191, doi:10.1038/nmat1849 (2007).
231 Mashtalir, O. *et al.* Intercalation and delamination of layered carbides and carbonitrides. *Nature Communications* **4**, doi:10.1038/ncomms2664 (2013).
232 Radisavljevic, B. & Kis, A. Mobility engineering and a metal-insulator transition in monolayer MoS2. *Nat. Mater.* **12**, 815-820, doi:10.1038/nmat3687 (2013).

233 Ma, R. & Sasaki, T. Nanosheets of Oxides and Hydroxides: Ultimate 2D Charge-Bearing Functional Crystallites. *Adv. Mater.* **22**, 5082-5104, doi:10.1002/adma.201001722 (2010).
234 Chhowalla, M. *et al.* The chemistry of two-dimensional layered transition metal dichalcogenide nanosheets. *Nat. Chem.* **5**, 263-275, doi:10.1038/nchem.1589 (2013).
235 Wei, M., Konishi, Y., Zhou, H., Sugihara, H. & Arakawa, H. A simple method to synthesize nanowires titanium dioxide from layered titanate particles. *Chem. Phys. Lett.* **400**, 231-234, doi:10.1016/j.cplett.2004.10.114 (2004).
236 Wei, M. D., Sugihara, H., Honma, I., Ichihara, M. & Zhou, H. S. A New Metastable Phase of Crystallized V2O4·0.25H2O Nanowires: Synthesis and Electrochemical Measurements. *Adv. Mater.* **17**, 2964-2969, doi:10.1002/adma.200501608 (2005).
237 Kusunoki, M., Rokkaku, M. & Suzuki, T. Epitaxial carbon nanotube film self-organized by sublimation decomposition of silicon carbide. *Appl. Phys. Lett.* **71**, 2620-2622, doi:10.1063/1.120158 (1997).
238 Cambaz, Z. G., Yushin, G. N., Gogotsi, Y., Vyshnyakova, K. L. & Pereselentseva, L. N. Formation of carbide-derived carbon on beta-silicon carbide whiskers. *J. Am. Ceram. Soc.* **89**, 509-514, doi:10.1111/j.1551-2916.2005.00780.x (2006).
239 Wilhoit, R. C., Burton, J. R., Kuo, F.-t., Huang, S.-R. & Viquesnel, A. Properties of aluminium ethoxide. *J. Inorg. Nucl. Chem.* **24**, 851-861, doi:10.1016/0022-1902(62)80106-7 (1962).
240 Gladstone, J. & Tribe, A. I.—Aluminium alcohols. Part I. Their preparation by means of the aluminium-iodine reaction. *Journal of the Chemical Society, Transactions* **39**, 1-12 (1881).
241 Cuomo, J. J., Leary, P. A. & Woodall, J. M. (US Patent US4745204, 1988).
242 Mehrotra, R. & Singh, A. Recent trends in metal alkoxide chemistry. *Prog. Inorg. Chem.* **46**, 239-454 (1997).
243 Kishio, K. & Brittain, J. O. Defect structure of [beta]-LiAl. *J. Phys. Chem. Solids* **40**, 933-940 (1979).
244 Tsai, M.-Y., Yu, C.-Y. & Perng, T.-P. Synthesis and Photoluminescence of Amorphous Ca5Ge2O9 Nanowires. *Journal of Nanoscience and Nanotechnology* **8**, 6376-6380, doi:10.1166/jnn.2008.383 (2008).
245 Rogova, T., TUROVA, N. & Novoselova, A. The Structure of Polymeric Alcoholates of Trivalent Aluminum, Chromium, and Iron. *Doklady Akademii Nauk SSSR* **285**, 896-901 (1985).
246 Amma, E. L. Single crystal data of some tetrameric aluminium alkoxides. *J. Inorg. Nucl. Chem.* **25**, 779-781, doi:10.1016/0022-1902(63)80361-9 (1963).
247 Seri, O. & Sasaki, D. Preparation of Aluminumtriethoxide by Application of Aluminum Corrosion. *Materials transactions* **50**, 1964-1968 (2009).
248 Mehrotra, R. C. Alkoxides and alkylalkoxides of metals and metalloids. *Inorganica Chimica Acta Reviews* **1**, 99-112, doi:10.1016/0073-8085(67)80023-8 (1967).
249 Wang, J. W. *et al.* Two-Phase Electrochemical Lithiation in Amorphous Silicon. *Nano Lett.* **13**, 709-715, doi:10.1021/nl304379k (2013).

250 Turova, N. Y., Turevskaya, E. P., Kessler, V. G. & Yanovskaya, M. I. *The chemistry of metal alkoxides*. (Springer Science & Business Media, 2002).
251 Turova, N. Y. *et al.* Physicochemical and Structural Investigation of Aluminum Isopropoxide. *Journal of Inorganic & Nuclear Chemistry* **41**, 5-11, doi:10.1016/0022-1902(79)80384-x (1979).
252 J.M. Gere, B. J. G. *Mechanics of Materials*. (Cengage Learning 2009).
253 Lu, Y. Y., Tu, Z. Y. & Archer, L. A. Stable lithium electrodeposition in liquid and nanoporous solid electrolytes. *Nat. Mater.* **13**, 961-969, doi:10.1038/nmat4041 (2014).
254 McAlister, A. The Al−Li (Aluminum−Lithium) system. *Journal of Phase Equilibria* **3**, 177-183 (1982).
255 Wolsky, S. P. & Taylor, A. H. *The 23rd International Battery Seminar & Exhibit: Primary & Secondary Batteries-small Fuel Cells-other Technologies : March 13-16, 2006*. (Florida Educational Seminars, 2006).
256 Thomas, J. P., Keennon, M. T., DuPasquier, A., Qidwai, M. A. & Matic, P. 289-292 (ASME).
257 Foroughi, J. *et al.* Torsional Carbon Nanotube Artificial Muscles. *Science* **334**, 494-497, doi:10.1126/science.1211220 (2011).
258 Thostenson, E. T., Ren, Z. & Chou, T.-W. Advances in the science and technology of carbon nanotubes and their composites: a review. *Compos. Sci. Technol.* **61**, 1899-1912, doi:10.1016/s0266-3538(01)00094-x (2001).
259 Chou, T.-W., Gao, L., Thostenson, E. T., Zhang, Z. & Byun, J.-H. An assessment of the science and technology of carbon nanotube-based fibers and composites. *Compos. Sci. Technol.* **70**, 1-19, doi:10.1016/j.compscitech.2009.10.004 (2010).
260 Gibson, R. F. A review of recent research on mechanics of multifunctional composite materials and structures. *Compos. Struct.* **92**, 2793-2810, doi:10.1016/j.compstruct.2010.05.003 (2010).
261 Coleman, J. N., Khan, U. & Gun'ko, Y. K. Mechanical Reinforcement of Polymers Using Carbon Nanotubes. *Adv. Mater.* **18**, 689-706, doi:10.1002/adma.200501851 (2006).
262 Mamedov, A. A. *et al.* Molecular design of strong single-wall carbon nanotube/polyelectrolyte multilayer composites. *Nat Mater* **1**, 190-194 (2002).
263 Spitalsky, Z., Tasis, D., Papagelis, K. & Galiotis, C. Carbon nanotube–polymer composites: Chemistry, processing, mechanical and electrical properties. *Prog. Polym. Sci.* **35**, 357-401, doi:10.1016/j.progpolymsci.2009.09.003 (2010).
264 Choi, N.-S. *et al.* Challenges Facing Lithium Batteries and Electrical Double-Layer Capacitors. *Angew. Chem. Int. Ed.* **51**, 9994-10024, doi:10.1002/anie.201201429 (2012).
265 Pereira, T., Guo, Z., Nieh, S., Arias, J. & Hahn, H. T. Embedding thin-film lithium energy cells in structural composites. *Compos. Sci. Technol.* **68**, 1935-1941, doi:10.1016/j.compscitech.2008.02.019 (2008).
266 Bae, J. *et al.* Fiber Supercapacitors Made of Nanowire-Fiber Hybrid Structures for Wearable/Flexible Energy Storage. *Angew. Chem. Int. Ed.* **50**, 1683-1687, doi:10.1002/anie.201006062 (2011).

267 Shirshova, N. *et al.* Structural composite supercapacitors. *Composites Part A: Applied Science and Manufacturing* **46**, 96-107, doi:10.1016/j.compositesa.2012.10.007 (2013).
268 Evanoff, K. *et al.* Ultra-Strong Silicon-Coated Carbon Nanotube Nonwoven Fabric as Multifunctional Lithium Ion Battery Anodes. *ACS Nano*, doi:10.1021/nn303393p (2012).
269 Huang, F. & Chen, D. Towards the upper bound of electrochemical performance of ACNT@polyaniline arrays as supercapacitors. *Energy & Environmental Science* **5**, 5833-5841, doi:10.1039/C1EE01989A (2012).
270 Boukhalfa, S., Evanoff, K. & Yushin, G. Atomic layer deposition of vanadium oxide on carbon nanotubes for high-power supercapacitor electrodes. *Energy & Environmental Science* **5**, 6872-6879, doi:10.1039/C2EE21110F (2012).
271 Gaikwad, A. M. *et al.* Highly Stretchable Alkaline Batteries Based on an Embedded Conductive Fabric. *Adv. Mater.* **24**, 5071-5076, doi:10.1002/adma.201201329 (2012).
272 Gaikwad, A. M., Whiting, G. L., Steingart, D. A. & Arias, A. C. Highly Flexible, Printed Alkaline Batteries Based on Mesh-Embedded Electrodes. *Adv. Mater.* **23**, 3251-3255, doi:10.1002/adma.201100894 (2011).
273 Gajendran, P. & Saraswathi, R. in *Pure and Applied Chemistry* Vol. 80 2377 (2008).
274 Gangopadhyay, R. & De, A. Conducting Polymer Nanocomposites: A Brief Overview. *Chem. Mater.* **12**, 608-622, doi:10.1021/cm990537f (2000).
275 De Paoli, M.-A. & Gazotti, W. A. Conductive polymer blends: preparation, properties and applications. *Macromolecular Symposia* **189**, 83-104, doi:10.1002/masy.200290008 (2002).
276 Sainz, R. *et al.* Soluble Self-Aligned Carbon Nanotube/Polyaniline Composites. *Adv. Mater.* **17**, 278-281, doi:10.1002/adma.200400921 (2005).
277 Syed, A. A. & Dinesan, M. K. Polyaniline: Reaction stoichiometry and use as an ion-exchange polymer and acid/base indicator. *Synth. Met.* **36**, 209-215, doi:10.1016/0379-6779(90)90053-N (1990).
278 Diniz, F. B., de Freitas, K. C. S. & de Azevedo, W. M. Ion exchange properties of polyaniline: potentiometric measurements on membranes and coated wire electrodes. *Electrochim. Acta* **42**, 1789-1793, doi:10.1016/S0013-4686(96)00378-7 (1997).
279 Yan, C., Zou, L. & Short, R. Single-walled carbon nanotubes and polyaniline composites for capacitive deionization. *Desalination* **290**, 125-129, doi:10.1016/j.desal.2012.01.017 (2012).
280 Benson, J. *et al.* Multifunctional CNT-Polymer Composites for Ultra-Tough Structural Supercapacitors and Desalination Devices. *Adv. Mater.* **25**, 6625-6632, doi:10.1002/adma.201301317 (2013).
281 Tagowska, M., Pałys, B. & Jackowska, K. Polyaniline nanotubules—anion effect on conformation and oxidation state of polyaniline studied by Raman spectroscopy. *Synth. Met.* **142**, 223-229, doi:10.1016/j.synthmet.2003.09.001 (2004).

282 Kovalenko, I., Bucknall, D. G. & Yushin, G. Detonation Nanodiamond and Onion-Like-Carbon-Embedded Polyaniline for Supercapacitors. *Adv. Funct. Mater.* **20**, 3979-3986, doi:10.1002/adfm.201000906 (2010).
283 Frackowiak, E., Khomenko, V., Jurewicz, K., Lota, K. & Béguin, F. Supercapacitors based on conducting polymers/nanotubes composites. *J. Power Sources* **153**, 413-418, doi:10.1016/j.jpowsour.2005.05.030 (2006).
284 Khomenko, V., Frackowiak, E. & Béguin, F. Determination of the specific capacitance of conducting polymer/nanotubes composite electrodes using different cell configurations. *Electrochim. Acta* **50**, 2499-2506, doi:10.1016/j.electacta.2004.10.078 (2005).
285 Yang, J. *et al.* Polyaniline/polypropylene film composites with high electric conductivity and good mechanical properties. *J. Appl. Polym. Sci.* **56**, 831-836, doi:10.1002/app.1995.070560708 (1995).
286 Wang, H., Hao, Q., Yang, X., Lu, L. & Wang, X. Graphene oxide doped polyaniline for supercapacitors. *Electrochem. Commun.* **11**, 1158-1161, doi:10.1016/j.elecom.2009.03.036 (2009).
287 Meng, C., Liu, C. & Fan, S. Flexible carbon nanotube/polyaniline paper-like films and their enhanced electrochemical properties. *Electrochem. Commun.* **11**, 186-189, doi:10.1016/j.elecom.2008.11.005 (2009).
288 Ramamurthy, P. C. *et al.* Polyaniline/single-walled carbon nanotube composite electronic devices. *Solid-State Electronics* **48**, 2019-2024, doi:10.1016/j.sse.2004.05.051 (2004).
289 Dong, B., He, B.-L., Xu, C.-L. & Li, H.-L. Preparation and electrochemical characterization of polyaniline/multi-walled carbon nanotubes composites for supercapacitor. *Materials Science and Engineering: B* **143**, 7-13, doi:10.1016/j.mseb.2007.06.017 (2007).
290 Gupta, V. & Miura, N. Influence of the microstructure on the supercapacitive behavior of polyaniline/single-wall carbon nanotube composites. *J. Power Sources* **157**, 616-620, doi:10.1016/j.jpowsour.2005.07.046 (2006).
291 Gupta, V. & Miura, N. Polyaniline/single-wall carbon nanotube (PANI/SWCNT) composites for high performance supercapacitors. *Electrochim. Acta* **52**, 1721-1726, doi:10.1016/j.electacta.2006.01.074 (2006).
292 Jiao, S. Q., Zhou, H. H., Chen, J. H., Luo, S. L. & Kuang, Y. F. Influence of the preparation conditions on the morphology of polyaniline electrodeposited by the pulse galvanostatic method. *J. Appl. Polym. Sci.* **94**, 1389-1394, doi:10.1002/app.20983 (2004).
293 Fan, L. Z. *et al.* High Electroactivity of Polyaniline in Supercapacitors by Using a Hierarchically Porous Carbon Monolith as a Support. *Adv. Funct. Mater.* **17**, 3083-3087, doi:10.1002/adfm.200700518 (2007).
294 Korenblit, Y. *et al.* In Situ Studies of Ion Transport in Microporous Supercapacitor Electrodes at Ultralow Temperatures. *Adv. Funct. Mater.* **22**, 1655-1662, doi:10.1002/adfm.201102573 (2012).
295 Wei, L., Sevilla, M., Fuertes, A. B., Mokaya, R. & Yushin, G. Hydrothermal Carbonization of Abundant Renewable Natural Organic Chemicals for High-Performance Supercapacitor Electrodes. *Advanced Energy Materials* **1**, 356-361, doi:10.1002/aenm.201100019 (2011).

296 Rose, M. *et al.* Hierarchical Micro- and Mesoporous Carbide-Derived Carbon as a High-Performance Electrode Material in Supercapacitors. *Small* **7**, 1108-1117, doi:10.1002/smll.201001898 (2011).
297 Presser, V., Heon, M. & Gogotsi, Y. Carbide-Derived Carbons – From Porous Networks to Nanotubes and Graphene. *Adv. Funct. Mater.* **21**, 810-833, doi:10.1002/adfm.201002094 (2011).
298 Chen, W.-C. & Wen, T.-C. Electrochemical and capacitive properties of polyaniline-implanted porous carbon electrode for supercapacitors. *J. Power Sources* **117**, 273-282, doi:10.1016/S0378-7753(03)00158-7 (2003).
299 McDanels, D. Analysis of stress-strain, fracture, and ductility behavior of aluminum matrix composites containing discontinuous silicon carbide reinforcement. *Metallurgical and Materials Transactions A* **16**, 1105-1115, doi:10.1007/BF02811679 (1985).
300 Gordon, J. E. *Structures: Or Why Things Don't Fall Down*. (Da Capo Press, 2009).
301 Mamalis, A. G., Branis, A. S. & Manolakos, D. E. Modelling of precision hard cutting using implicit finite element methods. *J. Mater. Process. Technol.* **123**, 464-475, doi:10.1016/S0924-0136(02)00133-4 (2002).
302 Geng, H. z. *et al.* Fabrication and Properties of Composites of Poly(ethylene oxide) and Functionalized Carbon Nanotubes. *Adv. Mater.* **14**, 1387-1390, doi:10.1002/1521-4095(20021002)14:19<1387::AID-ADMA1387>3.0.CO;2-Q (2002).
303 Chand, N. & Hashmi, S. a. R. Mechanical properties of sisal fibre at elevated temperatures. *Journal of Materials Science* **28**, 6724-6728, doi:10.1007/BF00356422 (1993).
304 Ahmad Ibrahim, A. *Aspect Ratio Effect of Functionalized/Non-Functionalized Multiwalled Carbon Nanotubes on the Mechanical Properties of Cementitious Materials*, Texas A&M University, (2011).
305 Wang, Q., Dai, J., Li, W., Wei, Z. & Jiang, J. The effects of CNT alignment on electrical conductivity and mechanical properties of SWNT/epoxy nanocomposites. *Compos. Sci. Technol.* **68**, 1644-1648, doi:10.1016/j.compscitech.2008.02.024 (2008).
306 Abbadi, M., Hähner, P. & Zeghloul, A. On the characteristics of Portevin–Le Chatelier bands in aluminum alloy 5182 under stress-controlled and strain-controlled tensile testing. *Materials Science and Engineering: A* **337**, 194-201, doi:10.1016/S0921-5093(02)00036-9 (2002).
307 Kanagaraj, S., Varanda, F. R., Zhil'tsova, T. V., Oliveira, M. S. A. & Simões, J. A. O. Mechanical properties of high density polyethylene/carbon nanotube composites. *Compos. Sci. Technol.* **67**, 3071-3077, doi:10.1016/j.compscitech.2007.04.024 (2007).
308 Coleman, J. N. *et al.* Improving the mechanical properties of single-walled carbon nanotube sheets by intercalation of polymeric adhesives. *Appl. Phys. Lett.* **82**, 1682-1684, doi:10.1063/1.1559421 (2003).
309 Dettlaff-Weglikowska, U. *et al.* Effect of SOCl2 Treatment on Electrical and Mechanical Properties of Single-Wall Carbon Nanotube Networks. *J. Am. Chem. Soc.* **127**, 5125-5131, doi:10.1021/ja046685a (2005).

310 Kang, K., Meng, Y. S., Bréger, J., Grey, C. P. & Ceder, G. Electrodes with High Power and High Capacity for Rechargeable Lithium Batteries. *Science* **311**, 977-980, doi:10.1126/science.1122152 (2006).
311 Tarascon, J. M. A. M. Issues and challenges facing rechargeable lithium batteries. *Nature* **414**, 359 (2001).
312 Bruce, P. G., Scrosati, B. & Tarascon, J.-M. Nanomaterials for rechargeable lithium batteries. *Nanomaterialien für wiederaufladbare Lithiumbatterien*, 2930, doi:10.1002/anie.200702505 (2008).
313 Sun, L. *et al.* High-strength all-solid lithium ion electrodes based on Li4Ti5O12. *J. Power Sources* **196**, 6507-6511 (2011).
314 Zheng, H., Zhang, L., Liu, G., Song, X. & Battaglia, V. S. Correlationship between electrode mechanics and long-term cycling performance for graphite anode in lithium ion cells. *J. Power Sources* **217**, 530-537, doi:10.1016/j.jpowsour.2012.06.045 (2012).
315 Li, X. *et al.* Novel approach toward a binder-free and current collector-free anode configuration: highly flexible nanoporous carbon nanotube electrodes with strong mechanical strength harvesting improved lithium storage. *J. Mater. Chem.* **22**, 18847-18853, doi:10.1039/C2JM33297C (2012).
316 Zhang, M., Atkinson, K. R. & Baughman, R. H. Multifunctional carbon nanotube yarns by downsizing an ancient technology. *Science* **306**, 1358-1361, doi:10.1126/science.1104276 (2004).
317 Bae, J. *et al.* Fiber Supercapacitors Made of Nanowire-Fiber Hybrid Structures for Wearable/Flexible Energy Storage. *Angewandte Chemie-International Edition* **50**, 1683-1687, doi:10.1002/anie.201006062 (2011).
318 Kovalenko, I. *et al.* A Major Constituent of Brown Algae for Use in High-Capacity Li-Ion Batteries. *Science* **334**, 75-79, doi:10.1126/science.1209150 (2011).
319 Zhang, G. *et al.* Rapid communication: Tin quantum dots embedded in nitrogen-doped carbon nanofibers as excellent anode for lithium-ion batteries. *Nano Energy* **9**, 61-70, doi:10.1016/j.nanoen.2014.06.030 (2014).
320 Fan, X. *et al.* Rapid communication: SnLi4.4 nanoparticles encapsulated in carbon matrix as high performance anode material for lithium-ion batteries. *Nano Energy* **9**, 196-203, doi:10.1016/j.nanoen.2014.07.020 (2014).
321 Liu, R. *et al.* Rapid communication: Core–shell structured hollow SnO2–polypyrrole nanocomposite anodes with enhanced cyclic performance for lithium-ion batteries. *Nano Energy* **6**, 73-81, doi:10.1016/j.nanoen.2014.03.010 (2014).
322 Magasinski, A. *et al.* High-performance lithium-ion anodes using hierarchical bottom-up approach. *Nat. Mater.* **9**, 353-358 (2010).
323 Elazari, R. *et al.* Rechargeable lithiated silicon-sulfur (SLS) battery prototypes. *Electrochem. Commun.* **14**, 21-24, doi:10.1016/j.elecom.2011.10.020 (2012).
324 Huggins, R. A. Lithium alloy negative electrodes. *J. Power Sources* **82**, 13-19 (1999).
325 Chan, C. K. *et al.* High-performance lithium battery anodes using silicon nanowires. *Nat. Nano.* **3**, 31-35, doi:10.1038/nnano.2007.411 (2008).

326 Li, W. *et al.* Core–Shell Si/C Nanospheres Embedded in Bubble Sheet-like Carbon Film with Enhanced Performance as Lithium Ion Battery Anodes. *Small* **11**, 1345-1351, doi:10.1002/smll.201402072 (2015).
327 Zhou, X. S., Wan, L. J. & Guo, Y. G. Electrospun Silicon Nanoparticle/Porous Carbon Hybrid Nanofibers for Lithium-Ion Batteries. *Small* **9**, 2684-2688, doi:10.1002/smll.201202071 (2013).
328 Reddy, M. V. *et al.* Studies on Bare and Mg-doped LiCoO2 as a cathode material for Lithium ion Batteries. *Electrochim. Acta* **128**, 192-197, doi:10.1016/j.electacta.2013.10.192 (2014).
329 Isaac, D. S. *et al.* Ultrathin Coatings on Nano-LiCoO2for Li-Ion Vehicular Applications. *Nano Lett.* **11**, 414-418 (2011).
330 Röder, P. *et al.* The impact of calendar aging on the thermal stability of a LiMn2O4–Li(Ni1/3Mn1/3Co1/3)O2/graphite lithium-ion cell. *J. Power Sources* **268**, 315-325, doi:10.1016/j.jpowsour.2014.06.040 (2014).
331 Yang, F. *et al.* Nanoscale morphological and chemical changes of high voltage lithium-manganese rich NMC composite cathodes with cycling. *Nano Lett.* **14**, 4334-4341, doi:10.1021/nl502090z (2014).
332 Visbal, H. *et al.* The influence of the carbonate species on LiNi0.8Co0.15Al0.05O2 surfaces for all-solid-state lithium ion battery performance. *J. Power Sources* **269**, 396-402, doi:10.1016/j.jpowsour.2014.07.021 (2014).
333 Watanabe, S., Kinoshita, M., Hosokawa, T., Morigaki, K. & Nakura, K. Capacity fading of LiAlyNi1−x−yCoxO2 cathode for lithium-ion batteries during accelerated calendar and cycle life tests (effect of depth of discharge in charge–discharge cycling on the suppression of the micro-crack generation of LiAlyNi1−x−yCoxO2 particle). *J. Power Sources* **260**, 50-56, doi:10.1016/j.jpowsour.2014.02.103 (2014).
334 Chen, L. & Shaw, L. L. Recent advances in lithium-sulfur batteries. *J. Power Sources* **267**, 770-783, doi:10.1016/j.jpowsour.2014.05.111 (2014).
335 Wu, F., Lee, J. T., Magasinski, A., Kim, H. & Yushin, G. Solution-Based Processing of Graphene-Li2S Composite Cathodes for Lithium-Ion and Lithium-Sulfur Batteries. *Particle & Particle Systems Characterization* **31**, 639, doi:10.1002/ppsc.201300358 (2014).
336 Lee, J. T., Zhao, Y., Kim, H., Cho, W. I. & Yushin, G. Sulfur infiltrated activated carbon cathodes for lithium sulfur cells: The combined effects of pore size distribution and electrolyte molarity. *J. Power Sources* **248**, 752-761, doi:10.1016/j.jpowsour.2013.10.003 (2014).
337 Ji, X. L., Evers, S., Black, R. & Nazar, L. F. Stabilizing lithium-sulphur cathodes using polysulphide reservoirs. *Nature Communications* **2**, doi:10.1038/ncomms1293 (2011).
338 Ji, X. L., Lee, K. T. & Nazar, L. F. A highly ordered nanostructured carbon-sulphur cathode for lithium-sulphur batteries. *Nat. Mater.* **8**, 500-506, doi:10.1038/nmat2460 (2009).
339 Wu, F., Magasinki, A. & Yushin, G. Nanoporous Li2S and MWCNT-linked Li2S powder cathodes for lithium-sulfur and lithium-ion battery chemistries. *J. Mater. Chem. A*, doi:10.1039/C3TA14161F (2013).

340 Lee, J. T. *et al.* Sulfur-Infiltrated Micro- and Mesoporous Silicon Carbide-Derived Carbon Cathode for High Performance Lithium Sulfur Battery. *Adv. Mater.* **25**, 4573–4579, doi:10.1002/adma.201301579 (2013).
341 Kim, H. *et al.* Plasma-Enhanced Atomic Layer Deposition of Ultrathin Oxide Coatings for Stabilized Lithium-Sulfur Batteries. *Advanced Energy Materials* **3**, 1308-1315 (2013).
342 Liu, L. *et al.* A comparison among FeF3·3H2O, FeF3·0.33H2O and FeF3 cathode materials for lithium ion batteries: Structural, electrochemical, and mechanism studies. *J. Power Sources* **238**, 501-515, doi:10.1016/j.jpowsour.2013.04.077 (2013).
343 Wang, F. *et al.* Conversion Reaction Mechanisms in Lithium Ion Batteries: Study of the Binary Metal Fluoride Electrodes. *J. Am. Chem. Soc.* **133**, 18828-18836, doi:10.1021/ja206268a (2011).
344 Amatucci, G. G. *et al.* Formation of lithium fluoride/metal nanocomposites for energy storage through solid state reduction of metal fluorides. *J. Fluorine Chem.* **132**, 1086-1094, doi:10.1016/j.jfluchem.2011.06.033 (2011).
345 Amatucci, G. G. & Pereira, N. Fluoride based electrode materials for advanced energy storage devices. *J Fluorine Chem* **128**, 243-262, doi:10.1016/j.jfluchem.2006.11.016 (2007).
346 Badway, F., Pereira, N., Cosandey, F. & Amatucci, G. G. Carbon-metal fluoride nanocomposites - Structure and electrochemistry of FeF3 : C. *J. Electrochem. Soc.* **150**, A1209-A1218, doi:10.1149/1.1596162 (2003).
347 Fu, Z. W. *et al.* Electrochemical reaction of lithium with cobalt fluoride thin film electrode. *J. Electrochem. Soc.* **152**, E50-E55, doi:10.1149/1.1839512 (2005).
348 Armstrong, M. J., Panneerselvam, A., O'Regan, C., Morris, M. A. & Holmes, J. D. Supercritical-fluid synthesis of FeF2 and CoF2 Li-ion conversion materials. *Journal of Materials Chemistry A* **1**, 10667-10676, doi:10.1039/c3ta12436c (2013).
349 Teng, Y. T., Pramana, S. S., Ding, J., Wu, T. & Yazami, R. Investigation of the conversion mechanism of nanosized CoF2. *Electrochim. Acta* **107**, 301-312, doi:10.1016/j.electacta.2013.05.107 (2013).
350 Wang, X. *et al.* Carbon Nanotube–CoF2 Multifunctional Cathode for Lithium Ion Batteries: Effect of Electrolyte on Cycle Stability. *Small* **11**, 5164-5173 (2015).
351 Gu, W. T., Magasinski, A., Zdyrko, B. & Yushin, G. Metal Fluorides Nanoconfined in Carbon Nanopores as Reversible High Capacity Cathodes for Li and Li-Ion Rechargeable Batteries: FeF2 as an Example. *Advanced Energy Materials* **5**, 1148-1148 (2015).
352 Cao, A., Xu, C., Liang, J., Wu, D. & Wei, B. X-ray diffraction characterization on the alignment degree of carbon nanotubes. *Chem. Phys. Lett.* **344**, 13-17, doi:10.1016/S0009-2614(01)00671-6 (2001).
353 Huggis, R. A. *Advanced batter*. (Springer, 2009).
354 Zheng, H., Sun, Q., Liu, G., Song, X. & Battaglia, V. S. Correlation between dissolution behavior and electrochemical cycling performance for LiNi1/3Co1/3Mn1/3O2-based cells. *J. Power Sources* **207**, 134-140 (2012).
355 Wu, X. L., Jiang, L. Y., Cao, F. F., Guo, Y. G. & Wan, L. J. LiFePO4 Nanoparticles Embedded in a Nanoporous Carbon Matrix: Superior Cathode

Material for Electrochemical Energy-Storage Devices. *Adv. Mater.* **21**, 2710-+, doi:10.1002/adma.200802998 (2009).
356 Prakash, A. S. *et al.* Solution-Combustion Synthesized Nanocrystalline Li4Ti5O12 As High-Rate Performance Li-Ion Battery Anode. *Chem. Mater.* **22**, 2857-2863, doi:10.1021/cm100071z (2010).

VITA

James M. Benson

Jim was born in Savannah, Georgia and attended public schools in both Pooler, Georgia and Brunswick, Georgia. He received his B.A. in Materials Science and Engineering from Georgia Tech in 2009 before returning for his doctoral degree also in Materials Science and Engineering. During college, Jim studied abroad with the GT Lorraine program in Metz, France and also performed a brief internship at NASA Langley in Hampton, VA. His interest in commercializing innovative technologies led to his participating in the TI:GER fellowship in collaboration with the Georgia Tech School of Business and the Emory University School of Law to explore new desalination opportunities. When he isn't developing new battery materials, Jim enjoys playing bass clarinet and hiking with his dog, Lola.